The
University
Of
Sheffield.

CHARACTERISATION OF TWO CYTOSKELETON PROTEINS
OF
MYXOCOCCUS XANTHUS

J. M. T. So

Doctor of Philosophy

2019

CHARACTERISATION OF TWO CYTOSKELETON PROTEINS OF *MYXOCOCCUS XANTHUS*

by

Jeffery Man To So

A thesis submitted to the

Department of Molecular Biology and Biotechnology

at the

University of Sheffield

with the requirements for the degree of

Doctor of Philosophy

September 2019

Summary

Once thought to be unique to eukaryotes, cytoskeleton proteins have now been found in all prokaryotes. In fact, prokaryotes possess many more diverse cytoskeletal elements than eukaryotes, some of which are absent in most eukaryotes Recent research showed that these diverse bacterial cytoskeleton proteins play a wide range of roles. This study was aimed to characterise two different cytoskeletal proteins from *M. xanthus*. One is BacM, a member of the ubiquitously found bactofilin family reported to be crucial for cell morphology. The other is MXAN0657, a poorly characterised chain-like filamentous protein with no known function. To do this, a range of light and electron microscopy and molecular biology techniques were employed. It was found that BacM forms multiple types of structures in the cell, including highly stable cell-polar structures, and smaller motile structures. Its C-terminal tail was found to be important for function and localisation. The use of cryo-electron microscopy further confirmed that BacM filament elongation occurs along the same axis as intra-subunit β-sheet stacking. MXAN0657 was found also to be widespread among bacteria. Bundling and elongation of native filaments was found to be induced by divalent ions and change in pH values. MXAN0657 was observed to form short filaments distributed across the cell. Intriguingly, deletion of *mxan0657* caused a spore-density dependent germination deficiency. Using cryo-electron tomography, a new structural model of MXAN0657 was proposed, contradicting the existing model for subunit arrangment within a filament unit. All in all, this study has contributed towards our understanding of the complex family of bacterial cytoskeletal proteins.

Acknowledgements

The last four years has been quite the journey. I've learnt so much from so many people, so it is impossible to mention everyone I wish to thank and show my gratefulness. Nevertheless, I'll give it my best try! Egbert has been an absolutely wonderful supervisor, and I've been very lucky to be his PhD student. I have benefited so much from the knowledge and wisdom he has shared with me, and I particular enjoyed all the scientific discussions we've had late into the night. His curiosity and eagerness for knowledge was highly contagious and have helped me develop my scientific mind. I'd like to thank all my lab colleagues, past and present, especially Koen Semeijn and Dr. Christa Walther, for their encouragements, companionship, scientific discussions, and the not-so-scientific ones too! I also acknowledge the help I've received from Prof. Simon Foster and Prof. Per Bullough who were on my advisory committee. I'd like to extend a big thank you to everybody in the Imagine: Imaging Life initiative. I have learnt so much from all the seminars and discussions I took part in, and I particularly enjoyed being part of the organising teams for the Imagine symposiums and outreach activities. Members of the laboratories of Prof. Foster, Dr. Fagan, Dr. Corrigan, and Dr. Mesnage have contributed a lot to my PhD, through discussions, advice, and assistance, and also everything I've 'borrowed' from them! The members of staff from the Wolfson Light Microscopy centre have been extremely helpful, and I thank them for their advice and expertise. I cannot overstate how much I appreciate the help I've received from members of the MBB EM user group and of the facility. I would be so lost without your guidance! Speaking of EM, I owe Dr. Alasdair Steven and his group at the NIH a huge debt of gratitude. They welcomed me with opened arms and I have learnt so much in the short time I've spent with them. They are truely missed. I'd also like to thank Dr. Juan Fontana at the University of Leeds and members of staff at the EM facility of the Astbury Centre. The myxobacteria community has also contributed much to my scientific development. They were willing to share their knowledge and insight so readily, and I've had many enlightening conversations with them at the myxobacteria conferences.

Scientific development is only part of my journey of the last few years. Thanks to all my friends, I have also become a better, more wholesome person. First and foremost, I'd like to thank my dear friends Loren and Jineesha, who have blessed me with their unwavering support, and have always been there when I needed them, whether I knew it or not! I'll always remember the good times I had with Mirjam, Lea, Sarah, Tom, Sabine and Nick, and I so grateful to know you all! I am also very lucky to be part of the Sheffield University Swing Dance Society. They have been a massive part of my time here in Sheffield, and I have made oh so many good friends in the society. The fun I had with them was also incredible. I would also like to single out Thane and Daria, who have both been extremely supportive in their own ways, and have helped me scientifically, but also in my well-being mentally and physically! Special thanks to Rob, Dan, Martin, Eugene, Jodie, Hannah A, Hannah S, Faez, Oscar, David, Connor, Bardley, Arka, and Wilson who have supported me over the years, which I appreciate greatly. I am also very sorry for not keeping in touch more. A special shout-out to my Singaporean students Leanette and Cherie!

Most importantly, I wish to express my wholehearted gratitude to my family, who have nurtured me throughout my life. Even though they are half the world away, their enduring support has helped me through my hardest times, and they also somehow always find a way to take care of me as if we are living under the same roof! This is why I am dedicating this thesis to my amazing, loving family.

Dedicated to my amazing, loving family

Contents

List of figures

List of tables

Abbreviations

2D – Two Dimensional
3D – Three Dimensional
aa (#) – Amino Acid (position)
ATP – Adenylate Tri-Phosphate
BAL – 2,3-Dimercapto-1-propanol
BLAST – Basic Local Alignment Search Tool
BSA – Bovine Serum Albumin
cAMP – Cyclic Adenylate Mono-Phosphate
CAPS – N-cyclohexyl-3-aminopropanesulfonic acid
CCPEM – Collaborative Computational Project for Electron cryo-Microscopyy
CLEM – Correlative Light and Electron Microscopy
CNBr – Cyanogen Bromide
Cryo-EM – Cryo-Electron Microscopy
Cryo-ET – Cryo-Electron Tomography
CTT – Casitone Tris Media
ddH$_2$O – Double-distilled water
DED – Direct Electron Detector
DMSO – dimethyl sulfoxide
DQE – Detective Quantum Efficiency
DUF – Domain of Unknown Function
ECM – Extracellular Matrix
EDTA – Ethylenediaminetetraacetic Acid
EGTA – Ethylene glycol-bis(2-aminoethylether)-N,N,N',N'-tetraacetic acid
EM – Electron Microscopy
EMDB – Electron Microscopy Data Bank
FA – Focal Adhesion
FAS – Fatty Acid Synthase
FEG – Field Emission Gun
FlAsH-EDT$_2$ - Fluorescein Arsenical Hairpin binder-Ethanedithiol
GTP – Guanylate Tri-Phosphate

HAE-1 – Hydrophobe/Amphiphile Efflux 1

HEPES - 2-[4-(2-hydroxyethyl)piperazin-1-yl]ethanesulfonic acid

HMM – Hidden Markov Model

His – 6x histidines

IHRSR – Iterative Helical Real-Space Reconstruction

IPTG – Isopropyl β-D-1-thiogalactopyranoside

KMH – buffer with 1 mM KH_2PO_4/K_2HPO_4, 10 mM $MgSO_4$, and 10 mM HEPES

LaB_6 – Lanthanum hexaboride

MCS – Multiple Cloning Site

MS – Mass Spectrometry

NCBI – National Center for Biotechnology Information

OD_{600} – Optical Density at wavelength of 600 nm

OMV – Outer Membrane Vesicles

PAGE – Poly-Acrylamide Gel Electrophoresis

PBS – Phosphate-Buffered Salin

PBST – PBS with 0.05% Tween-20

PEG – PolyEthylene Glycol

PG – Peptidoglycan

POI – Protein-Of-Interest

PLL – Poly-L-Lysine

PSI-BLAST – Position Specific Iterative - Basic Local Alignment Search Tool

PSSM – Position-Specific Scoring Matrices

PVDF – Polyvinylidene Difluoride

ReAsH-EDT_2 – Resorufin Arsenical Hairpin binding reagent - Ethanedithiol

RND – Resistance/Nodulation/Cell Division

RPM – Revolutions Per Minute

RT – Room Temperature

SAM – Self-Assembled Monolayer

SDS – Sodium Dodecyl Sulfate

SNR – Signal-To-Noise

SPA – Single Particle Analysis

STEM – Scanning Transmission Electron Microscope

TC – Tetracysteine

TEM – Transmission Electron Microscopy

TMV – Tobacco Mosaic Virus

TPM – Tris Phosphate Magnesium starvation media

WT – Wild-type

α – Anti

β-DDM – n-Dodecyl β-D-maltoside

Chapter 1

General Introduction

1.1 The Cytoskeleton

Cytoskeleton proteins are essential to the function and survival of cells across all domains of life. In eukaryotes, there are three major, well studied classes of cytoskeleton proteins – actin filaments, intermediate filaments, and microtubules. These proteins can form networks that are highly dynamic and undergo rapid remodelling, or are relatively stable providing long-term structural support. The functions of these proteins include cell motility, scaffolding for binding proteins, mechanical support, intracellular organelle transport, and chromosomal segregation[1–3].

Intracellular filaments have long been observed in bacteria[4,5], but these have mostly been ignored and not classified as *bona fide* cytoskeletons. Moreover, due to the simple appearance of bacterial cells and the lack of clear sequence homology, it was subsequently thought that the cytoskeleton is a unique feature of the eukaryotic domain of life, and bacterial shape maintenance and cellular functions do not require one[2,6]. This view changed in the 1990s after multiple bacterial proteins were found to assemble into filaments *in vivo* and *in vitro*, and share structural homology with eukaryotic cytoskeletal proteins[7–9]. It then became clear that bacteria also possess complicated networks of cytoskeletal elements, and their diversity and range of function even surpass those of the eukaryotes.

1.1.1 Bacterial Cytoskeletal Elements with Eukaryotic Homologues

Tubulin homologs

FtsZ

The realisation that bacteria have cytoskeletal elements began with the study of FtsZ. It was known that FtsZ is essential for cell division, and is widespread across bacteria[10]. Bi and Lutkenhaus[7] discovered that FtsZ formed a constricting ring-like structure at the midcell of *Escherichia coli* during cell division (**Figure 1-1 A**). They proposed that FtsZ could form a dynamic cytoskeletal element with similar function to actin during cytokinesis in eukaryotes. Subsequent studies showed that FtsZ has a GTP-binding motif similar to that of tubulin[11], undergoes GTP-dependent polymerisation into tubules[12], and has a three-dimensional structure similar to that of tubulin, despite having low sequence similiarity[13].

The function of FtsZ has since been well studied. It forms a ring-shaped structure at the cytoplasmic side of the inner membrane, termed the Z-ring, and provides a scaffold for division related proteins. This FtsZ scaffold is attached to the membrane *via* binding with membrane-tethered protein anchors, and recruits peptidoglycan (PG)-modifying proteins to generate the new cell pole[14]. This assembly of machinery is termed the divisome. It is noteworthy that FtsZ has been found to also contribute to the proper positioning of PG synthesis during pre-division cell elongation in *E. coli* and *Caulobacter crescentus* [15,16]. In *Bacillus subtilis* and *E. coli*, the spatial regulation of FtsZ is achieved by nucleoid occlusion and negative regulation of FtsZ polymerisation at the cell poles by MinCD concentration gradients[17]. The polymerisation of FtsZ is GTP-binding dependent[18], and its self-activating GTPase activity is dependent on polymerisation.

Whether FtsZ provides the major force behind membrane constriction during division has been strongly debated. Evidence for this includes observed constriction of liposomes by FtsZ in the presence of GTP *in vitro*[19]. A recent study utilising correlative cryo-fluorescence and cryo-electron microscopy (cryo-CLEM) in *E. coli* established that FtsZ alone cannot generate enough force to constrict membranes *in vivo*, and that membrane invagination required PG ingrowth[20].

Much effort has been made to understand the exact organisation and dynamics of FtsZ at the division site. Using superresolution light microscopy techniques, the Z-ring was found to be formed by small laterally associating discontinuous filaments[21]. It has also been demonstrated in *E. coli* and *B. subtilis* that the circumferential motion of FtsZ filaments is caused by GTPase activity-dependent treadmilling, where polymerisation takes place at one end of the filament, and depolymerisation takes place at the other end (**Figure 1-1 B**). This motion was shown to guide the PG synthesis machinery, and ensures proper distribution of newly synthesised PG at the septum[22,23].

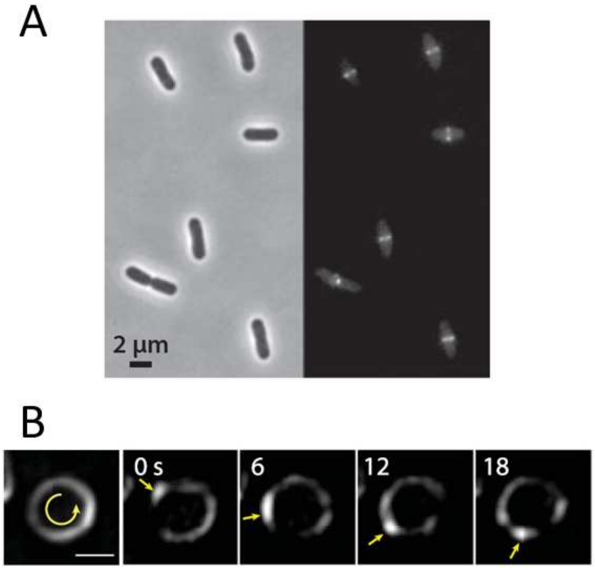

Figure 1-1 FtsZ localises to the midcell for cell division, and exhibits treadmilling activity.
(A) Conventional fluorescence microscopy of GFP-tagged FtsZ in *E. coli*, showing localisation to the midcell. Image adapted from (23). (B) Time series structured illumination microscopy projection of FtsZ viewing down the longitudinal axis of a dividing *E. coli* cell. FtsZ can be seen treadmilling around the circumference of the septum. Scale bar = 0.5 µm. Images adapted from (24).

Other tubulin homologs

Apart from FtsZ, other tubulin homologs identified include BtubA/B and TubZ. BtubA/B were discovered in *Prosthecobacter dejongeii* and share around 35% sequence identity with eukaryotic tubulin[25]. Crystal structures also showed very high similarities. BtubA and BtubB can both bind GTP and co-polymerise into filaments and bundles. Their GTPase activities induce dissembly[25]. Unfortunately, the lack of genetic tools for *Prosthecobacter* has hampered investigations into their function and architecture *in vivo*. TubZ, in contrast, shares little sequence homology with tubulin or FtsZ[26]. It was found to function as a plasmid partitioner in *Bacillus* species. Interestingly, TubZ exhibits treadmilling behaviour, and the pulling force of the depolymerising minus-end causes the segregation of target plasmid[27].

Actin Homologs

MreB

MreB was known to be important for rod cell-shape determination in *E. coli*[28], and some species possess multiple MreB paralogs. It was found to be an actin homolog by the identification of actin-superfamily motifs in its sequence[8]. By tagging MreB with GFP in *B. subtilis*, Jones *et al*[29]. discovered that MreB formed helical filaments. They also reported that MreB homologs are only present in rod-shaped bacteria but not in coccoid bacteria. The crystal structure of MreB from *Thermotoga maritima* (TmMreB), along with its filamentous polymerisation *in vitro* strengthened the arguments for a bacterial actin-like cytoskeleton[30].

MreB polymerises into anti-parallel, non-helical double protofilaments[31] and is dependent on ATP or GTP-binding[32] (**Figure 1-2 A**). Mutation of the nucleotide binding pocket and the blocking of nucleotide binding with the antibiotic A22 prevents polymerisation of MreB *in vivo*[33]. Salje *et al*[34] demonstrated that MreB can bind directly to the cytoplasmic membrane *via* a hydrophobic membrane-insertion loop, and additionally with an amphipathic helix in the case of Gram-negative bacteria.

The view of extensive helical MreB filaments in cells has recently been overturned. Light and electron microscopy studies suggested that MreB forms short, discontinuous and motile patches or filaments that move slowly around the cell circumference, orthogonal to the longitudinal axis of the cell[35–38] (**Figure 1-2 B**). This decade-long confusion was mostly due to artefacts of YFP-tag-induced helical MreB filament formation, dynamic movement of MreB filament around the cell, and over reliance on deconvoluted images[39,40]. Contrary to actin and FtsZ, the movement of MreB is not caused by treadmilling but was shown to be powered by PG synthesis[35,36] as the inhibition of PG synthesis machineries arrests MreB filament motion.

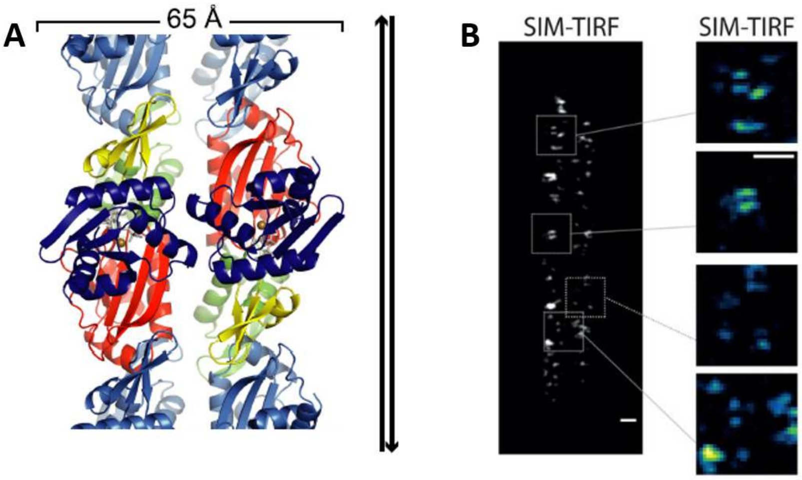

Figure 1-2 MreB forms antiparallel double filaments, and forms short filaments in the cell. (A) Ribbon diagram of MreB from *C. crescentus* forming double protofilaments arranged in an antiparallel manner, adapted from (30). (B) Superresolution micrographs of MreB from *B. subtilis*. Short filaments could be observed during active growth using SIM-TIRF (structured illumination microscopy – total internal reflection fluorescence). Scale bars = 500 nm. Images adapted from (41).

MreB is critical in rod-shaped morphology maintenance. The depletion of MreB or addition of A22 causes the formation of spherical cells and can cause cells to undergo lysis[42]. MreB filaments act as scaffolds for PG synthesis-related proteins to coordinate the location of cell wall synthesis. This assembly of machineries and cytoskeleton is termed the elongasome[36,39]. The mechanism of how it directs cylindrical PG synthesis at the side wall is partly understood. It has been observed that MreB exhibit preferential localisation to sites of zero Gaussian curvature i.e. the inside of a cylinder, and this preference can be modulated by RodZ, a transmembrane protein that links MreB to PG synthesis enzymes[43]. Not only does this property allow maintenance of the rod shape of the PG sacculus, but it also provides a mechanism for rescuing the morphology of mis-shaped cells[44].

Interestingly, although MreB is essential for the maintenance of specific cell shapes of species with well-defined shapes, some rod-shaped bacteria like members of Actinobacteria and Rhizobiales lack MreB or its homologs. Instead, these bacteria have been shown to rely on polar growth for elongation[44]. MreB has also been implicated as essential for motility of *Myxococcus xanthus*, where MreB has been shown to recruit motility-related proteins and the addition of A22 inhibits motility[45,46], an observation that will be later discussed in the text.

Other bacterial actin homologs

ParM is an actin homolog responsible for segregation of the R1 plasmid in *E. coli*. ParM can undergo bidirectional elongation and exhibits dynamic instability[24,47]. ParM filaments are stabilised only by binding to ParR/R1 plasmid complexes. Using cryo-eletron microscopy (cryo-EM), ParM filaments were revealed to consist of a pair of parallel protofilaments arranged in a left-handed helix[47]. Two of these filaments can then form anti-parallel doublet filaments and elongate at opposing ends to ensure synchronised partitioning of sister plasmids[47] (**Figure 1-3**). AlfA and AlpS are actin homologs also involved in plasmid segregation. Both exhibit treadmilling behaviour *in vitro*, and their functional mechanisms remain to be clarified[24,48].

Magnetotactic bacteria, like *Magnetospirillum magneticum*, produce intracellular magnetic iron oxide-filled organelles called magnetosomes. The alignment of these magnetosomes into a chain allows the cell to orientate along geomagnetic fields, which has been proposed to assist navigation towards favourable environments[49]. MamK, an actin homolog, is responsible for the positioning of magnetosomes. Unlike MreB, MamK has been shown to arrange in a parallel, helical manner, and exhibit treadmilling behaviour *in vivo*, which ensures the equal distribution of magnetosomes between daughter cells during cell division[50–52].

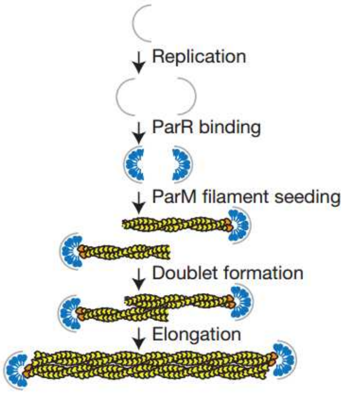

Figure 1-3 Hypothetical model of ParM/R plasmid segregation mechanism.
First, ParR (blue) binds to a specific locus on R1 plasmid (grey), forming a complex. ParM filaments (yellow) are able to elongate after stabilisation by ParM/R1 plasmid binding. Doublet filament formation aligns opposite plasmid complexes, resulting in synchronised and directionally opposed plasmid segregation. Figure adapted from (47).

Intermediate filament homologs

Crescentin

Crescentin was identified in *C. crescentus* where disruption of its gene *creS* caused the loss of crescent-shaped morphology and cell straightening[9]. It was found to share similarities in sequence and domain organisation with eukaryotic *i*ntermediate *f*ilaments (IF) forming proteins, which involves extended and repeating coiled-coil domains forming the core of the protein, with highly variable N- and C-terminal domains. Moreover, crescentin can also polymerise spontaneously *in vitro* in a nucleotide-independent fashion (**Figure 1-4 A**), like its eukaryote counterpart. In the cell, crescentin forms a stable filamentous structure located at the inner curvature of the cell where it was suggested to be tethered to the cell wall *via* MreB[53,54] (**Figure 1-4 B**). Intriguingly, crescentin is able to induce curved cell morphology in *E. coli*, but not in *Agrobacterium tumefaciens* which lacks MreB. The current model of mechanism suggests that crescentin induces unequal PG elongation through the relief of strain on one side of the cell against turgor pressure. Continual unequal PG insertion rate then causes the cell to become curved[53].

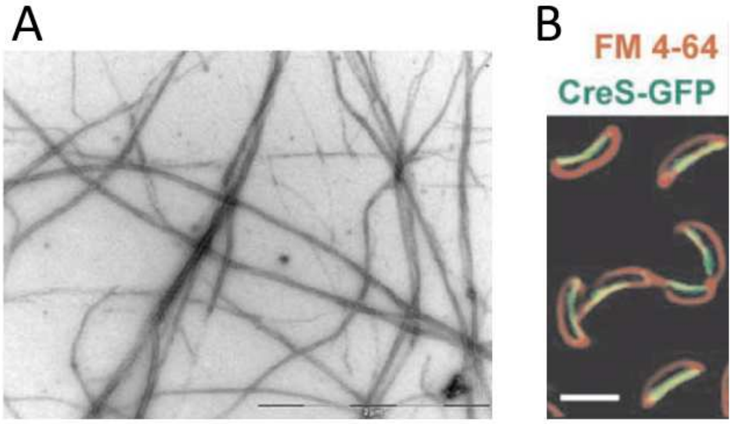

Figure 1-4 Intracellular localisation of crescentin and filament morphology in vitro.
(A) TEM micrograph of negative stained purified crescentin filaments from (9) (B) Fluorescence microscopy micrographs of GFP-tagged crescentin (green), and membrane dye (red). Crescentin localises to the inner curvature of the cells and is membrane-associated. Scale bars = 2μm. Images adapted from (55).

Other IF homologs

Recently, four IF-like *C*oiled-*c*oil-*r*ich *p*roteins (Ccrp) have been identified in *Helicobacter pylori*. Deletion of any *ccrp* causes cell morphology disruption at varying degrees, and also reduces pathogenicity and motility. IF-like domain containing proteins have also been identified in many bacterial genomes, but they have yet to be characterised[24].

Organisms that rely on apical growth suffer structural weakness problem at the tip, where nascent cell wall is continuously being built and modified. In the bacterium *Streptomyces coelicolor*, this mechanical weakness appears to be compensated by the IF-like FliP protein[56]. FliP forms a dense network *in vitro* and is likely to do so at the subpolar region where it is localised during active cell growth, providing mechanical support[56].

1.1.2 Cytoskeletal Proteins Unique to Bacteria

Bactofilins

Bactofilin was first discovered in *Proteus mirabilis*[57] where it was named *C*urved *c*ell *m*orphology (CcmA) due to the effect its disruption had on the cell (**Figure 1-5**). Later studies revealed that bactofilins can polymerise into filaments independent of nucleotides, which made it a candidate for a cytoskeletal element. Homologs were also found in most Gram-negative and positive bacteria. Although these homologs show low sequence similarity due to the highly variable N- and C-termini, they all contain the common *D*omain of *U*nknown *F*unction DUF583[58,59].

The DUF583 domain forms the core of bactofilins and acts as the polymerisation module[59]. High resolution NMR studies and protein contact prediction demonstrated that DUF583 from BacA, a bactofilin from *C. crescentus*, adopts a right-handed β-helical fold[60,61]. This is contrary to the left-handedness previously predicted for BacM from *M. xanthus*[59]. This highly stable and tightly packed core can undergo polymerisation by monomer stacking *via* hydrophobic interaction and these filaments are thought to form higher ordered structures by charge-charge interactions along the filaments[58,62].

Since their identification, a number of bactofilins have been studied and their roles implicated in a variety of cellular functions. From *C. crescentus*, BacA and BacB appeared to co-assemble into membrane-associated patches at cell poles and also at the stalked pole[58]. At the latter location, the co-polymer recruits and interacts with *p*enicillin-*b*inding *p*rotein (Pbp) C, which is involved in PG remodelling. The deletion of *bacA, bacB* and *pbpC* showed a relatively mild phenotype of reduced stalk length[58]. The role of this assembly is unclear, but has been proposed to assist in the coordination of stalk extension, or the strengthening of the stalk for mechanical stress bearing.

Two bactofilins have been identified in *B. subtilis*, originally named YhbE and YhbF, but now termed BacE and BacF respectively[63]. These were found to form dynamic membrane-associated patches that co-localised with the flagellar basal body. Deletion of either *bacE* or *bacF* completely disrupted cell motility, caused by the absence of flagellar hook and filament assembly[63] (**Figure 1-5**).

Only one bactofilin has been found in *Helicobacter pylori*, also named CcmA as its deletion caused cells to lose their distinctive helical shape and adopt a curved rod form. In two separate studies, CcmA was shown to interact with Csd5 and Csd7[64,65]. The Csd or *c*ell *s*hape-*d*etermining proteins family have a range of PG interacting or modifying enzymatic activities which are essential for the generation of the distinctive cell shape. Csd5 can also interact with the PG precursor synthase MurF, and Csd7 likely forms a complex with Csd1 and Csd2. This puts CcmA squarely in the role as a scaffold for positioning of PG-modifying assemblies to ensure maintenance of cell shape. Immunofluorescence of CcmA in *H. pylori* showed that it forms distinct spots that mostly congregate around the mid cell[66]. How this relates to its function has yet to be explored.

Most recently, five bactofilins were found in *Leptospira biflexa*, termed LbbA-E (*Leptospira biflexa* bactofilins)[67]. Further study of LbbD showed that its deletion altered cell helical morphology where cells appeared like compressed springs, and cells became more susceptible to cell-wall targeting antibiotics and osmotic stresses (**Figure 1-5**). Since cell shape and motility are closely linked in *L. biflexa*, its ability to spread as a colony and individual cell velocity were reduced[67]. Interestingly, the authors of the study proposed that LbbD provides a mechanical force to maintain the proper spacing of cell helices, and also provides the optimal cell shape for periplasmic flagella-induced motility[67].

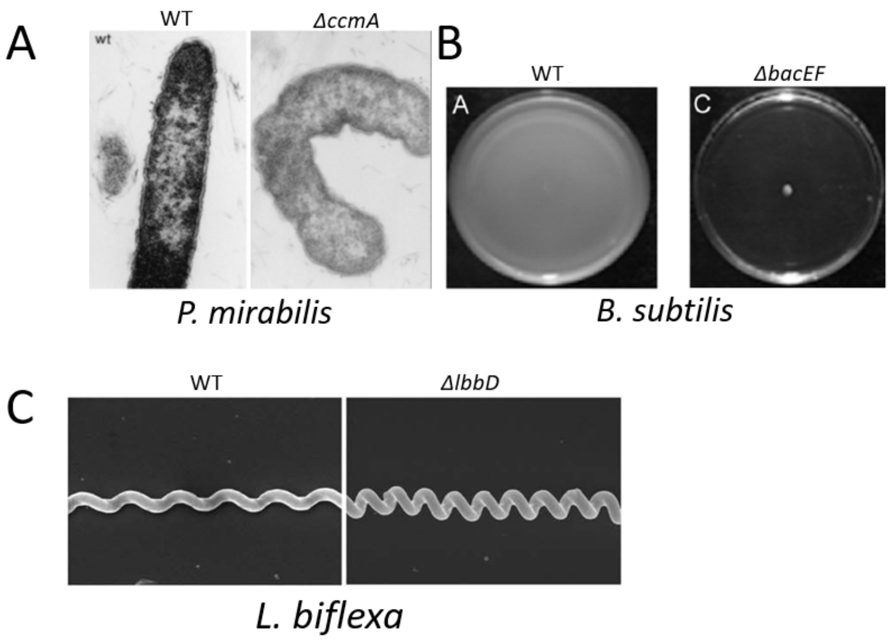

Figure 1-5 Deletion of bactofilins in different organisms has different effects.
(A) Deletion of *ccmA* in *P. mirabilis* caused a curved cell morphology. (B) Deletion of *bacEF* from *B. subtilis* caused complete lost of swarming ability on agar. (C) Deletion of *lbbD* from *L. biflexa* caused change in helical parameters of the cell. Images were adapted from (53), (63), and (67), respectively.

There are four bactofilin paralogs in *M. xanthus*. These are named BacM-P. They have been implicated in a range of functions including cell shape maintenance, chromosomal segregation, and motility. These will be discussed in **Section 2.1**.

Other bacterial cytoskeletal proteins

Studied bacteria-exclusive cytoskeletal proteins include DivIVA and PopZ[68]. DivIVA is a conserved protein among Gram-positive bacteria with diverse functions[69]. In *B. subtilis*, it forms two-dimensional lattices at the cell poles and growing septum. It then recruits the aforementioned MinCD to prevent incorrect re-initiation of cell division after cell division. DivIVA is also involved in the positioning of the chromosome to a cell pole during sporulation[68,69]. PopZ also localises at the cell poles, putatively as a mesh[70]. Together with the ParA/B system, it ensures proper chromosomal partitioning during cell division. Briefly, ParB, associated with the newly replicated centromere (*parS* locus), travels along a path of nucleoid-associated ParA towards the opposite cell pole. ParB-binding induces ATPase activity of ParA and disassembly of ParA-nucleoid complex. The ParB/*parS* complex then travels forward to the next patch of ParA-nucleoid complex. PopZ mesh traps released ParA to increase cell pole concentration of ParA, ensuring directionality of ParB/*parS* migration. Additionally, PopZ captures segregated ParB/*parS* to prevent backflow[70,71]. Interestingly, ParA was a cytoskeleton element candidate as *in vitro* filaments were observed and a filament-mediated mechanism was proposed[71]. However, this is not observed *in vivo*, and the experimentally supported model above (named the diffusion-ratchet model) argues against that concept[71].

1.1.3 Concluding remark

It is clear that bacteria have developed their own lineages of cytoskeletal proteins, playing a wide range of roles. These families of proteins can interact with each other and should not be seen as separate systems with well-defined roles. For example, FtsZ and MreB were demonstrated to interact during cell division at the Z-ring for coordination of PG synthesis[72]; crescentin localisation is dependent on MreB[54]; PopZ and ParA/B can interact[70]; the recruitment of FliP to subpolar regions relies on DivIVA[56]. There are many bacterial cytoskeletal elements yet to be studied. Investigation of their evolutionary relationships, biomechanical and biochemical mechanisms and roles will no doubt lead to interesting discoveries.

1.2 Model Organism: *Myxococcus xanthus*

M. xanthus is a Gram-negative bacterium in the delta-proteobacterial group. It is non-pathogenic to humans and is found ubiquitously in soil[73,74]. Like other myxobacteria, it is a predatory organism that preys on Gram-negative and Gram-positive bacteria, and also fungi. *M. xanthus* is a very interesting model organism because it exhibits highly social behaviour and can be thought to have transitioned into multicellular life. This is highlighted by the predation and development stages of *M. xanthus'* life cycle.

During vegetative growth, feeding is carried out in cell clusters known as 'swarms'[75]. These swarms progress outwards from the colonies and upon contact with prey, secrete a cocktail of hydrolytic enzymes, antibiotics, and secondary metabolites to carry out the lysis of prey cells[73,74,76]. Rippling response is also triggered during predation. It is described as a co-ordinated accordion-like, back and forth movement of cells and has been proposed to ensure complete uptake of prey macromolecules and maximise prey-predator contact[77].

Development is triggered by starvation, which involves the coordinated aggregation of cells leading to the formation of spore-filled mound-shaped fruiting bodies of a defined size. Sporulation involves the duplication of its chromosome without cell division[78], dismantling of PG cell wall[79], and the deposition of a thick polysaccharide spore-coat[80] making them resistant to environmental stresses. During this process, apart from sporulation, a majority of cells in fact undergo programmed cell lysis, and a small percent of cells (named peripheral rods) resists signals for development and instead remain motile at the periphery of the fruiting bodies[81]. The cell-cell signalling aspect of fruiting body formation is of great interest and debated, particularly the molecular mechanism of 'C-signalling', which co-ordinates the aggregation of cells[82–84]. When spores encounter favourable environmental conditions, they germinate *en masse* to form a new swarming population[85].

These multicellular behaviours rely on two different motility systems for co-ordinated movements: Adventurous (A-) and Social (S-) motility. *M. xanthus* has only one-dimensional control of movement i.e. when cell poles are switched which leads to directional reversal, which, surprisingly, is sufficient for the coordination of three-dimensional organisation of cells during fruiting body formation. The frequency at which cell reversal takes place is controlled by the Frz chemosensory system[75]. The Frz signal is transduced through the small Rsas-like GTPase MglA, its GTPase-activating protein MglB, and the guanine nucleotide exchange factor complex (GEF) RomR-RomX to both motility systems[75,86,87], which controls the polarity of the motile cell.

S-motility

S-motility, also called twitching motility, takes place in close cell-cell proximity. This motility involves the extension and retraction of type IV pili (T4P) at the leading cell pole, and the architecture of this machinery have recently been mapped[88]. The mechanical forces required for pili extension and retraction are provided by the ATPases PilB and PilT, respectively[88,89]. Pili have been shown to bind to the exopolysaccharide (EPS) on neighbouring cells or in the extracellular matrix (ECM)[90]. Substrate-binding triggers PilT-powered pili retraction, which pulls the cell forward. This motor is crucial for fruiting body formation, cooperative predation[91], as well as the colonisation of soft agar surfaces.

A-motilty

In contrast to S-motility, the mechanism of A-motility is much more elusive and debated, as it does not utilise any visible appendages. The first model proposed involved propulsion by slime secretion from nozzle-like organelles[92], similar to that of filamentous cyanobacteria[93]. This was supported by the observation that directional slime secretion is linked to effective A-motility[94]. However, the lack of non-slime producing mutants and protein components identified hampered studies to test this hypothesis. Furthermore, visualisation of the nanometres thin slime with wet-surface-enhanced ellipsometric contrast (wet-SEEC) microscopy suggested that slime secretion is independent of motility[95].

The current A-motility models are the "helical rotor" model[96,97] and the "focal adhesion (FA)" model[46,98,99] (**Figure 1-6 A&B**). These two models are based on the presence of motor protein complexes that remain stationary relative to the gliding surface that run along helical tracks in the cell[45,46,98,100–102]. Since the motor complexes are fixed to the substratum, the cell is pushed forward instead. Evidence include light microscopy experiments that showed A-motility related proteins remaining fixed to the substratum during gliding motiltiy[98,103] (**Figure 1-6 C**). MglA, which is essential for motility has also been found at focal adhesion sites[45,46]. Interestingly, immunofluorescence also showed MglA being associated with a helical structure[101]. More than a dozen proteins have been identified to form the FA motor complex, named the Agl-Glt motor, by genetic studies[104,105]. The motion of the motor complex is dependent on the proton motive force[96].

The helical track was initially thought to be MreB[45], as disruption of MreB with A22 inhibits A-motility. After the continuous helical MreB cytoskeleton model was challenged, it was revised that MreB only acts as a scaffold for A-motility complex assembly[102]. Most recently, MreB from *M. xanthus* (MxMreB) was reported to behave very different to other model organisms studied, whereby the majority of small MreB filaments move rapidly at low angles to the cell longitudinal axis. This observed motion was also not coupled to PG synthesis, but instead depended on the motility complex[106]. It is unclear how widespread this non-canonical behaviour of MxMreB is.

The two models differ mainly on their proposed mechanism of force transduction. For the helical motor model, the chain of A-motility complexes are hypothesised to deform the PG layer, forming "bumps" on the cell surface for traction[96,97] (**Figure 1-6 B**). However, no bumps have ever been observed in electron micrographs. For the FA model, the motility complexes extend through the PG layer and inner and outer membranes, engaging directly with the substratum[102] (**Figure 1-6 A**). This is supported by the predicted cellular locations of proteins in the motor complex[102], and also biophysical modelling and observations of the elastic response of colliding cells[99]. Slime is thought to be the adhesive in this model[95,102]. How the complexes traverse through the PG during cell movement is under speculation. A hypothesis is that parts of the motor complex can extend through the PG with their periplasmic flexible domains to transfer force to the outer-membrane components[105]. Moreover, the PG has been proposed as a candidate for the helical guidance of the motor complex[105]. There is currently no structural study of the gliding motor complex.

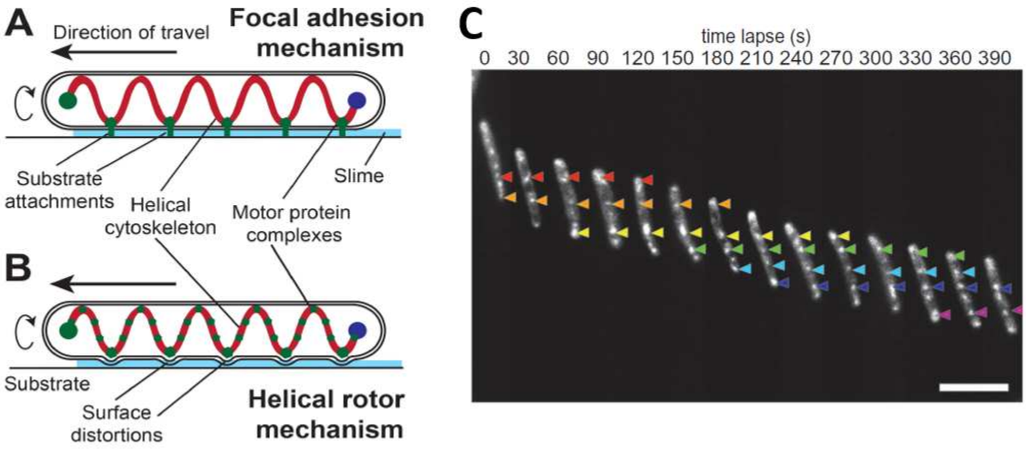

Figure 1-6 Helical rotor and focal adhesion adventurous motility models.
A) and B) Cartoon outlining the similarities and differences between the focal adhesion model and the helical rotor model, respcetively. Adapted from (99). C) Example of fluorescence microscopy images showing protein clusters remaining fixed relative to the substratum as the cell moves forwards. Fluorescence here is the AgmU-mCherry cluster. Scale bar 5μm. Adapted from (100).

1.2.1 Concluding remarks

As shown above, *M. xanthus* is a unique social bacterium to study. Another interesting social aspect not yet mentioned is *M. xanthus*' ability to exchange outer membrane material in a process called *O*uter *M*embrane *E*xchange (OME). This is performed through the TraA and TraB system[107] where direct membrane contact can repair damaged sibilings, and may also share modified LPS to induce a homogenous population response. This beneficial process is only restricted to closely related cells as TraA-TraA interaction is allele selective[107]. Myxobacteria's large repertoire of secondary metabolites has also been recognised. In *M. xanthus*, 9% of its genome is composed of secondary metabolite gene clusters[108]. Many of the compounds produced have antimicrobial activities[73,74,108], which makes *M. xanthus* and other myxobacteria very attractive for drug discovery research. All in all, *M. xanthus'* complex life cycle and highly social behaviours makes it a good model for research on cell-cell communication, motility, cell biology, drug discovery, and the evolution of multicellular life.

1.2.2 Scope of study

This study aimed to investigate and characterise two cytoskeletal proteins from *M. xanthus*. One of them was BacM, one of four paralogs of bactofilins from *M. xanthus*. The other was MXAN0657, a novel filamentous protein that has only been described in a cursory manner[109,110]. This work could be split into two parts. First, a range of methods were used to characterise the properties of the cytoskeletal elements. Aspects covered include their behaviour *in vitro* and *in vivo*, and their intracellular localisation and dynamics. The second part dealt with the structural aspects of the proteins, which were mainly performed with cryo-EM. Questions that this work aimed to address include how subunits are arranged in the polymers and what are the surfaces involved in polymerisation. The study also aimed to obtain a high resolution structure of the two proteins, either in their monomeric or polymeric states.

Chapter 2

Characterisation of BacM, a bactofilin of *Myxococcus xanthus*

2.1 Background

Bactofilins in *M. xanthus*

There are four bactofilin paralogs in *M. xanthus*: BacM, N, O, P[58]. They all contain the DUF583 bactofilin core domain, but have varying N- and C- termini (**Figure 2-1 A**). The gene *bacM* is positioned in an operon with genes encoding chromosomal segregation proteins ParA and ParB towards the chromosomal terminus, whereas *bacNOP* share the same operon with *padC* and a Lysophospholipase *agmH* positioned near the centre of the chromosome (**Figure 2-1 B**). As with bactofilins from other organisms, these bactofilins exhibit functional diversity.

BacNOP – Polar landmarks

BacP has been found to interact with the small Ras-like GTPase SofG by a pull-down experiment[89]. In the same study, the authors found that the deletion of both *bacP* and *sofG* resulted in loss of S-motility and aberrant localisation of the ATPases PilB and PilT, but not the remaining machinery for type IV pili. As mentioned earlier, PilB and PilT proteins use the hydrolysis of ATP to induce the extension and retraction of T4P, respectively. Fluorescence light microscopy experiments showed that BacP forms bipolar patches that extend to subpolar regions where SofG resides. SofG was found to 'shuttle' PilB and PilT to and from polar and subpolar regions over BacP patches in a GTPase activity-dependent fashion, but the correct polarisation of the T4P associated proteins are still dependent on MglA. The study could not determine whether SofG shuttling requires the dynamic polymerisation and depolymerisation of BacP or is the result of a Brownian ratchet-like movement of SofG along BacP polymers.

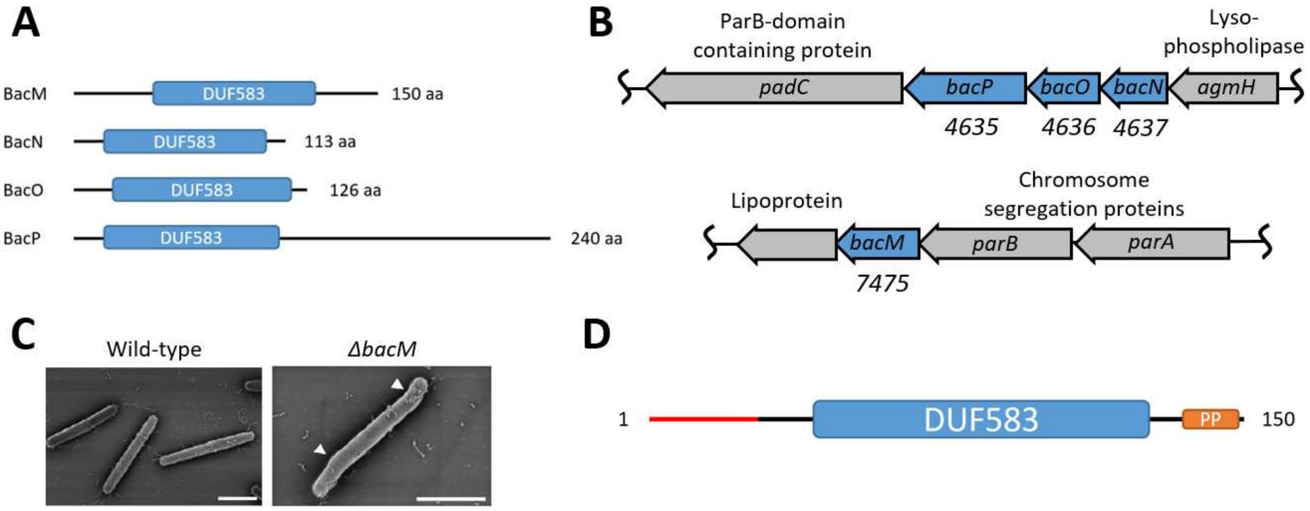

Figure 2-1 Bactofilins in *Myxococcus xanthus*.
(A) The four bactofilin paralogs in *M. xanthus*. Show in blue is the conserved bactofilin domain. (B) Chromosomal arrangement of bactofilins. The MXAN number is stated under each bactofilin gene. Note that both operons are encoded on the reverse strand. (C) Scanning electron microscopy micrographs of *ΔbacM* cells exhibiting crooked cell morphology. Micrographs adapted from (59). (D) Schematic of key-features in BacM. Cleaved N-terminal sequence is in red, with cleavage site pointed out by red arrowhead. Poly-proline region is in orange.

A subsequent study demonstrated that BacNOP co-assemble into a heteropolymeric scaffold at cell pole regions[111], with BacP appearing to form the core of this structure and BacO maintaining its position and integrity. BacN has an unknown role in this scaffold. This scaffold was reported to interact with PadC, a protein coded in the same operon (**Figure 2-1 B**), and together mediate the localisation of ParA and ParB, which are coded in a distant operon with *bacM*. The C-terminus of BacP is responsible for PadC interaction and in turn recruits ParA to the bactofilin scaffold. ParB appears to bind the ends of BacNOP structures directly. During cell division, the BacNOP-PadC complex anchors the ParABS chromosomal segregation machinery to a defined position at subpolar regions. Defects in the bactofilin complex caused abnormal distribution of DNA content and chromosomal origin arrangement.

In the light of this new study, it is unlikely that the BacNOP co-polymer depolymerises for the shuttling of SofG, as it would also affect the chromosomal segregation complex, making a Brownian ratchet mechanism more likely. The fact that BacP is able to simultaneously perform its function with SofG, PadC and the ParABS complex is a testament to the functional diversity of bactofilins.

BacM – Cell morphology maintenance

BacM is encoded in an operon containing genes coding for the putative lipoprotein MXAN7474 and chromosomal partitioning proteins ParA and ParB[59] (**Figure 2-1 B**). Surprisingly, loss of *MXAN7474* has no observable effects on BacM, and loss of *bacM* has no effects on motility, cell division and chromosome segregation[59,111]. However, *bacM* knockout cells do exhibit morphological defects, where cells no longer have a smooth, even contour, and surface deformations in the forms of 'bumps' and 'dents' could be observed, as evident in the scanning electron microscopy image in **Figure** 2-1 **C**[59]. Immunofluorescence experiments show that BacM forms cable structures that appeared to span the whole cell as well as shorter, membrane associated rods found at cell poles. Extraction and purification of these structures show that they are formed of strands of BacM filaments[62]. BacM exists in the 16kDa form and the 13kDa N-terminally cleaved form (**Figure 2-1 D**), and the latter form is the majority species in the cell and the isolated strands[59]. However, what causes this cleavage is unclear. Another effect of *bacM* deletion is increased susceptibility to PG-targeting antibiotics[59]. These observed effects suggest that BacM is involved in PG synthesis and maintenance, possibly through interaction with enzymes with such functions, as is the case for BacA and BacB in *C. crescentus*[58]. Purified BacM filaments showed remarkable resilience to chaotropic agents, pH values, detergents, and high salt concentrations, and this property is now a defining feature of bactofilins. This study aims to improve our understanding of BacM by the use of a range of microscopy techniques, to reveal its intracellular dynamics and localisation.

2.2 Materials and methods

2.2.1 Bacterial strains and culture conditions

Bacteria strains used are listed in **Table 2-1**. *M. xanthus* cultures were grown in CTT (1% tryptone, 10 mM Tris-HCl pH 8.0, 8 mM $MgSO_4$, 1 mM KH_2PO_4) liquid medium on a shaking platform at 200 revolutions per minute (RPM), or on CTT 1.5% agar (Sigma) (hard agar) or 0.5% agar (soft agar) plates, supplemented with appropriate antibiotics (Tetracycline 15 μg/ml; Kanamycin 100 μg/ml; Ampicillin 10 μg/ml) at 32°C. Where appropriate, induction of protein expression was performed with filter-sterilised vanillate at pH 8 or copper sulphate solution added into liquid media or agar. *E. coli* strains were grown in Lysogeny Broth (LB) (Sigma) liquid medium on a shaking platform at 200 RPM, or on LB 1.5% agar plates, supplemented with appropriate antibiotics (Tetracycline 10 μg/ml; Kanamycin 50 μg/ml; Ampicillin 10 μg/ml; Chloramphenicol 25 μg/ml) at 37°C. Where appropriate, induction of protein expression was performed with filter-sterilised IPTG added into liquid media.

2.2.2 PCR and plasmid construction

List of primers used for this study can be found in **Table 2-2.** PCR reactions were carried out using either Expand High FidelityPLUS PCR System (Roche), Phusion High Fidelity DNA polymerase master mix with high GC buffer (New England Biolabs), or Q5 Hot Start High Fidelity master mix (New England Biolabs) as per manufacturer's instructions. PCR reactions were supplemented with 0 – 8% DMSO or ethylene glycol where appropriate. Conventional, gradient, and touchdown PCR schemes were used. PCR products were purified using GeneJet PCR Purification kit or GeneJet Gel Extraction Kit (ThermoFisher). Restriction enzymes were all purchased from New England Biolabs. Digested products were purified with the purification kits above. Ligation reactions were performed with T4 DNA ligase (New England Biolabs) or DNA Ligation Kit Ver. 2.1 (TaKaRa). DH5α (ThermoFisher) cells were used for molecular cloning purposes. List of plasmids used are listed in **Table 2-3.**

Name	Alias	Parent strain	[Plasmid integrated]/Description	Source
M. xanthus				
DK1622	Wild-type (WT)			112
EH301	*ΔbacM*	DK1622		59
EH700	WT PcuoA BacM-mCherry	DK1622	[pDMZ169] Complementation at the chromosomal *attB* site. Expresses BacM-mCherry under control of copper-inducible promoter.	This study
EH701	WT pMR3679 BacM-Tc1	DK1622	[pJS001] Inserted into the segment between positions 8498672 and 8500048. Expresses BacM-Tc1 under control of vanillate-inducible promoter.	This study
EH702	*ΔbacM* pMR3679 BacM-Tc1	EH301	As above.	This study
EH707	WT pMR3679 BacM-Tc2	DK1622	[pJS002] Inserted into the segment between positions 8498672 and 8500048. Expresses BacM-Tc2 under control of vanillate-inducible promoter.	This study
EH708	*ΔbacM* pMR3679 BacM-Tc2	EH301	As above.	This study
EH709	WT pMR3679 BacM-Tc3	DK1622	[pJS003] Inserted into the segment between positions 8498672 and 8500048. Expresses BacM-Tc3 under control of vanillate-inducible promoter.	This study
EH710	*ΔbacM* pMR3679 BacM-Tc3	EH301	As above.	This study
EH711	WT pMR3679 BacM-Tc4	DK1622	[pJS004] Inserted into the segment between positions 8498672 and 8500048 Expresses BacM-Tc4 under control of vanillate-inducible promoter.	This study
EH712	*ΔbacM* pMR3679 BacM-Tc4	EH301	As above.	This study
EH713	WT pMR3679 BacM	DK1622	[pJS006] Inserted into the segment between positions 8498672 and 8500048. Expresses BacM under control of vanillate-inducible promoter.	This study
EH714	*ΔbacM* pMR3679 BacM	EH301	As above.	This study
EH715	WT pMR3679 mCherry	DK1622	[pJS007] Inserted into the segment between positions 8498672 and 8500048. Expresses mCherry under control of vanillate-inducible promoter.	This study
EH716	*ΔbacM* pMR3679 mCherry	EH301	As above.	This study
EH717	WT pMR3679 BacM-ΔPP	DK1622	[pJS009] Inserted into the segment between positions 8498672 and 8500048. Expresses BacM_ΔPP under control of vanillate-inducible promoter.	This study
EH718	*ΔbacM* pMR3679 BacM-ΔPP	EH301	As above.	This study
EH719	WT pMR3679 mCherry_PP	DK1622	[pJS008] Inserted into the segment between positions 8498672 and 8500048. Expresses mCherry-PP under control of vanillate-inducible promoter.	This study
EH720	*ΔbacM* pMR3679 mCherry_PP	EH301	As above.	This study
EH721	WT pMR3679 bacM-mNeonGreen	DK1622	[pJS020] Inserted into the segment between positions 8498672 and 8500048. Expresses BacM-mNG under control of vanillate-inducible promoter.	This study
EH722	*ΔbacM* pMR3679 bacM-mNeonGreen	EH301	As above.	This study
EH727	WT pMR3679 BacM-Tc5	DK1622	[pJS012] Inserted into the segment between positions 8498672 and 8500048. Expresses BacM-Tc5 under control of vanillate-inducible promoter.	This study
EH728	*ΔbacM* pMR3679 BacM-Tc5	EH301	As above.	This study
EH729	WT pMR3679 BacM-Tc6	DK1622	[pJS013] Inserted into the segment between positions 8498672 and 8500048. Expresses BacM-Tc6 under control of vanillate-inducible promoter.	This study
EH730	*ΔbacM* pMR3679 BacM-Tc6	EH301	As above.	This study
EH731	WT pMR3679 BacM-Tc7	DK1622	[pJS014] Inserted into the segment between positions 8498672 and 8500048. Expresses BacM-Tc7 under control of vanillate-inducible promoter.	This study
EH732	*ΔbacM* pMR3679 BacM-Tc7	EH301	As above.	This study
EH733	WT pMR3679 BacM-Tc8	DK1622	[pJS015] Inserted into the segment between positions 8498672 and 8500048. Expresses BacM-Tc8 under control of vanillate-inducible promoter.	This study
EH734	*ΔbacM* pMR3679 BacM-Tc8	EH301	As above.	This study
E. coli				
Rosetta(DE3)pLysS			For heterogeneous protein expression.	Novagen
BL21(DE3)			For heterogeneous protein expression.	Invitrogen
DH5α			For molecular cloning purposes.	ThermoFisher
BL21-BacMTR		BL21	[pJS030] Expresses BacMTR for TEM inspection after freeze substitution and thin section. Also for anti-BacM immmunofluorescence. IPTG-inducible promoter.	This study
Rosetta-His-BacMTR		Rosetta	[pJS025] Expresses BacMTR with N-terminal his-tag. IPTG-inducible promoter.	This study
Rosetta-BacMTR		Rosetta	[pJS030] Expresses BacMTR for BacMTR isolation. IPTG-inducible promoter.	This study
Rosetta-BacMTR-Tc1		Rosetta	[pJS026] Expresses BacMTR-Tc1 IPTG-inducible promoter.	This study
Rosetta-BacMTR-Tc6		Rosetta	[pJS027] Expresses BacMTR-Tc6 IPTG-inducible promoter.	This study
Rosetta-BacMTR-Tc7		Rosetta	[pJS028] Expresses BacMTR-Tc7 IPTG-inducible promoter.	This study
Rosetta-BacMTR-Tc8		Rosetta	[pJS029] Expresses BacMTR-Tc8 IPTG-inducible promoter.	This study

Table 2-1 List of strains used in this study.

Name	Sequence (5' to 3')
BacM_F_NdeI	ATTCACATATGGCGCTCCTTGGCG
BacM_Lumio_R_EcoRI	TACTATGAATTCCTAGCAGCAGCCCGGGCAGCACTTCTTCTCGCCACCCGG
BacM_Lum2_R_EcoRI	ATATCGAATTCTTACGGCTCCATGCAGCAGCCCGGGCAGCAGTTCAAGAACTTCTTCTCGCCACCCGG
BacM_Lum3_R_EcoRI	ATATCGAATTCTTACGGCTCCATGCAGCAGCCCGGGCAGCAGTTCAAGAAGCTGCCGCCGCCCTTCTTCTCGCCACCCGG
BacM_Lum4_R_EcoRI	TACTATGAATTCCTAGCAGCAGCCCGGGCAGCAGCTGCCGCCGCCCTTCTTCTCGCCACCCGG
BacM_R_EcoRI	GTTCAGAATTCCTACTTCTTCTCGCCACC
mCherry_F_NdeI	ATTCACATATGGTGAGCAAGGGCGAG
mCHerry_R_EcoRI	TACTATGAATTCCTACTTGTACAGCTCGTCCATGC
mCherry_PP_EcoRI	TACTATGAATTCTACTTCTTCTCGCCACCCGGAGGCGGAGGCGGGCGGCCCTTGTACAGCTCGTCCATGCC
BacM_noPP_R_EcoRI	TATATGAATTCTAGGCGCCAGCGGTGCCCAG
BacM_TC6_R_v2	ACCACAACAACCCGGACAACAACCAGCCTGGATTTCGGCCTGAACCTTG
BacM_TC6_F_v2	GGTTGTTGTCCGGGTTGTTGTGGTGGCACCGTCATCATCAACGGCCAG
BacM_TC7_R_v2	ACCACAACAACCCGGACAACAACCCTGAACCTTGGCGCCATCCCCAATG
BacM_TC7_F_v2	GGTTGTTGTCCGGGTTGTTGTGGTGCCGAAATCCAGGCTGGCACCGTCATC
Lnk_NeoG_F_EL	CCTCGCCCTTGCTCACCATGCGAGCTCGACCGAGGAG
Lnk_NeoG_R_EL	CTCCTCGGTCGAGCTCGCATGGTGAGCAAGGGCGAGG
NeoG_R_EcoRI_EL	GTACGTGAATTCTCACTTGTACAGCTCGTCCATGCC
NeoG_F_NdeI_EL	TAGTCACATATGGTGAGCAAGGGCGAGG
5_linker_mNG	ACCTCCTCGGTCGAGCTCGCATGGTGAGCAAGGGCGAGGAGG
3_linker_BacM	CGACGGGAGCGGGATCCAGCTTCTTCTCGCCACCCGGAGGC
BacMTR_pOPINF_F	AAGTTCTGTTTCAGGGCCCGTCTGGTGAGGTCCACACGCTC
BacMTR_pOPINF_R	ATGGTCTAGAAAGCTTTACTACTTCTTCTCGCCACC
BacMTR_F_XbaI	GTCCATCTAGAAATAATTTTGTTTAACTTTAAGAAGGAGATATACCATGTCTGGTGAGGTCCACACG

Table 2-2 List of primers used in this study.

Name	Alias	Parent	Description	Primers used	Source
pMR3679			*M. xanthus* 1.38-kb-PR3-4::*vanR-Pvan*-MSC_B, KanR.		113
pET28b			For expression of proteins in *E. coli.* T7 promoter and *lac* operator.		Novagen
pOPINF			For expression of proteins in E. coli.T7 promoter and *lac* operator.		PPUK
pDMZ169	PcuoA BacM-mCherry	pMAT3	*PcuoA BacM-mCherry* . Insertion at attB site.		David Zuckerman; 114
pJS001	pMR3679 BacM-Tc1	pMR3679	*Pvan - bacM* -tetracysteine tag.	BacM_F_NdeI; BacM_Lumio_R_EcoRI	This study
pJS002	pMR3679 BacM-Tc2	pMR3679	*Pvan - bacM* -enhanced tetracysteine tag.	BacM_F_NdeI; EcoRI BacM_Lum2_R_ EcoRI	This study
pJS003	pMR3679 BacM-Tc3	pMR3679	*Pvan - bacM* -GGGS- enhanced tetracysteine tag.	BacM_F_NdeI; BacM_Lum3_R_ EcoRI	This study
pJS004	pMR3679 BacM-Tc4	pMR3679	*Pvan - bacM* -GGGS-tetracysteine tag.	BacM_F_NdeI; BacM_Lum4_R_ EcoRI	This study
pJS006	pMR3679 BacM	pMR3679	*Pvan - bacM .*	BacM_F_NdeI; BacM_R_EcoRI	This study
pJS007	pMR3679 mCherry	pMR3679	*Pvan - mCherry.*	mCherry_R_EcoRI; mCherry_F_NdeI	This study
pJS008	pMR3679 mCherry-PP	pMR3679	*Pvan - mCherry* with poly-proline tail (GRPPPPPGGEKK after last native residue).	mCherry_F_NdeI; mCherry_PP_EcoRI	This study
pJS009	pMR3679 BacM-ΔPP	pMR3679	*Pvan - bacM* without poly-proline tail (last 11 aa residues removed).	BacM_F_NdeI; BacM_noPP_R_EcoRI	This study
pJS012	pMR3679 BacM-TC5	pMR3679	*Pvan - bacM* with tetracysteine tag infront of Arg 140, spaced by a glycine on both sides.	Synthesied by Thermofisher/ Invitrogen.	This study
pJS013	pMR3679 BacM-TC6	pMR3679	*Pvan - bacM* with tetracysteine tag infront of Gly 82, spaced by a glycine on both sides.	BacM_F_NdeI; BacM_R_EcoRI; BacM_TC6_R_v2; BacM_TC6_F_v2	This study
pJS014	pMR3679 BacM-TC7	pMR3679	*Pvan - bacM* with tetracysteine tag infront of Ala 77, spaced by a glycine on both sides.	BacM_F_NdeI; BacM_R_EcoRI; BacM_TC7_R_v2; BacM_TC7_F_v2	This study
pJS015	pMR3679 BacM-TC8	pMR3679	*Pvan - bacM* with tetracysteine tag infront of Ala 73 spaced by a glycine on both sides.	BacM_F_NdeI; BacM_R_EcoRI; BacM_TC8_R_v2; BacM_TC8_F_v2	This study
pJS020	pMR3679 BacM-mNeonGreen	pMR3679	*Pvan - bacM -mNeonGreen.*	BacM_F_NdeI; Lnk_NeoG_R_EL; Lnk_NeoG_F_EL; NeoG_R_EcoRI; 5_linker_mNG; 3_bacM_linker	This study
pJS025	pOPINF His-3C-BacMTR	pOPINF	*Pt7/lac - bacM* with first 27 aa removed. Preceeded by 6xhis and 3C protease site.	BacMTR_pOPINF_F; BacMTR_pOPINF_R	This study
pJS026	pET28b BacMTR Tc1	pET28b	*Pt7/lac - bacM-TC1,* untagged.	BacMTR_F_XbaI; BacM_R_EcoRI	This study
pJS027	pET28b BacMTR Tc6	pET28b	*Pt7/lac - bacM-TC6,* untagged.	BacMTR_F_XbaI; BacM_R_EcoRI	This study
pJS028	pET28b BacMTR Tc7	pET28b	*Pt7/lac - bacM-TC7,* untagged.	BacMTR_F_XbaI; BacM_R_EcoRI	This study
pJS029	pET28b BacMTR Tc8	pET28b	*Pt7/lac - bacM-TC8,* untagged.	BacMTR_F_XbaI; BacM_R_EcoRI	This study
pJS030	pET28b BacMTR	pET28b	*Pt7/lac - bacM* with first 27 aa removed.	BacMTR_F_XbaI; BacM_R_EcoRI	This study

Table 2-3 List of plasmids used in this study.

2.2.3 Transformation

For the transformation of *E. coli* cells, 10 ng of vector or ligation product was used to transform chemically competent DH5α, BL21(DE3) or Rosetta(DE3)pLysS (Novagen/Merck) strains of *E. coli* cells. Competent cells were mixed with the appropriate constructs, heat-shocked at 42°C for 60 seconds in a water-bath, recovered in LB medium and plated on LB agar supplemented with relevant antibiotics.

To transform *M. xanthus*, cells were grown to mid-log phase, washed in TPM (CTT without tryptone) and thrice in ddH_2O at room temperature (RT). Cells were concentrated to ~650x in sterile water and ~1 μg of plasmid DNA was added to 50 μl of cells. The cell suspension was contained in Gene Pulser Cuvette (Bio-Rad) with 1 mm electrode gap, and electroporated at 0.65 kV, 25 μF, 400 Ω using a Bio-Rad Gene Pulser with a capacitance extender. Cells were allowed to recover in CTT for 5-7 hrs. Cells were mixed with molten 0.5% agar (soft agar) with CTT and poured over CTT hard agar with appropriate antibiotics, and grown at 32°C.

2.2.4 Protein expression in *E. coli*

For heterogeneous protein expression in *E. coli*, either the Rosetta or BL21 strain was used. Cells were transformed with the appropriate plasmids as described above. A pre-culture was grown overnight with appropriate antibiotics. This was used to inoculate a larger culture at 1:100 dilution. Cells were grown to an optical density at 600 nm wavelength (OD_{600}) of 0.5 - 0.6 at 37°C before being chilled and added with IPTG to a final concentration of 1 mM unless otherwise stated. Expression was allowed to take place on a shaking platform at 200 RPM, at 18°C for 20 hours. Cells were then chilled on ice, and harvested by centrifugation at 5,000 x g for 5 min at 4°C. Cells were resuspended in phosphate buffered saline (PBS), and breakage was performed with a Soniprep 150 Plus ultrasonicator (MSE), using the 19 mm solid titanium probe (MSE) at amplitude setting of around 13 μm. Sample was chilled in ice slurry at all times. Cell breakage was confirmed by conventional phase contrast light microscopy.

2.2.5 Regular fluorescence light microscopy

Cells expressing fluorescent proteins were washed thoroughly in TPM (10 mM Tris-HCl pH 8, 10 mM $MgSO_4$, 1 mM KH_2PO_4/K_2HPO_4) to reduce background fluorescence. Cells were transferred onto a 1.5% TPM-agarose pad on a glass slide, covered with a coverslip, and sealed with a paraffin-petroleum jelly mixture (Price, Vaseline, respectively) before imaging. Phase contrast and fluorescence images of cells were taken on a Nikon Eclipse Ti inverted fluorescence microscope using the Nikon Plan Apo 100x Ph oil (NA 1.45) objective. This microscopy system is housed in a temperature adjustable enclosure, which was set at 32°C for live cell imaging. Excitation wavelength of 488 nm was used for mNeonGreen imaging and 561 nm for mCherry imaging. Images were captured with a Zyla sCMOS camera (Andor Technology). Image acquisition was controlled using NIS Elements Advance Research (AR) 4.2 imaging software (Nikon Instruments). Images were visualised and analysed with FIJI[115].

2.2.6 FRAP microscopy

FRAP experiments were performed on the LSM 800 with Airyscan detector (Zeiss) with a Plan-Apochromat 63x/1.4 Oil DIC II objective, controlled with ZEN Blue microscope software (Zeiss). Fluorescence imaging and bleaching was done with a 488 nm laser. For transmitted light cell detection, the T-PMT detector and the 405 nm laser was used. EH721 cells induced with 10 μM of vanillate were grown for a minimum of 18 hours to mid-log phase, washed thoroughly in TPM, and diluted to OD_{600} of 0.2. Cells were then incubated in TPM for at least 1 hr to cease vanillate-inducible production of fluorescently-tagged protein, and to reduce the proportion of motile cells. Cells were imaged on TPM-agarose pads as described above. Small regions of cells were photobleached using a laser setting of 50% and scan speed of 3. Fluorescence recovery was recorded at 1 Hz for 50 seconds. Image processing and FRAP measurements were made using Zen Blue software and FIJI[115]. Quantification of fluorescence recovery was measured as follow. Fluorescence intensities at regions targeted for photobleaching, as well as unbleached regions were measured and subtracted by the background intensities. The intensity of the corrected bleached region was normalised with the corrected unbleached region to account for overall decay in fluorescence during imaging. This normalised intensity was then presented as a fraction of the pre-bleached intensity. Intensity traces were plotted on a graph using Prism 8 software (GraphPad).

2.2.7 Immunofluorescence microscopy

M. xanthus cells of interest were grown to mid-log phase before harvest, with the induction of protein expression where appropriate. *E. coli* cells expressing BacM$_{TR}$ were harvested at the end of expression. Cells were collected and washed with 1 mM KH_2PO_4/K_2HPO_4, 10 mM $MgSO_4$, and 10 mM HEPES (KMH) at pH 8 for *M. xanthus*, or PBS for *E. coli*, and fixed with 4% formaldehyde with gentle agitation in KMH or PBS for 30 min at RT. Cells were then washed with KMH or PBS, and lysozyme was added to 1 mg/ml and gently agitate at RT. Meanwhile, 24x24 mm high precision cover-glass (Marienfeld SUPERIOR), or cover-glass for routine use (Menzel Glasër) were incubated at 37°C in a solution of 0.1 mg/ml poly-L-lysine (PLL) for 2 hours and air-dried. Cells were washed and 100 µl were pipetted onto the coated coverslips, and cells were allowed to settle onto the cover-glass for 5 – 10 minutes. Excess liquid was pipetted off, and the cover-glass were allowed to air-dry completely. After that, they were transferred to a six-well plate (StarLab), and cells were permeabilised with 0.2 % Triton X-100 in PBS with gentle agitation for 30 minutes at RT, and were blocked with PBST (PBS added with 0.01% Tween-20) with 2% BSA for 1 hour at RT. Cover-glass were removed from the wells and placed cell-face down onto a 100 µl drop of primary antibody at 1:100 to 1:400 dilutions in PBST with BSA, and were left at RT for 1 hour. The cover-glasses were placed back into the wells and washed thoroughly with PBST with BSA. The cover-glasses were then placed on a solution of AlexaFluor 488-conjugated secondary antibody (Molecular Probes/ThermoFisher) at 1:100 to 1:600 as above, and again washed thoroughly. Finally, the cover-glasses were washed in PBS and mounted onto a clean microscopy glass-slide with SlowFade Gold antifade mountant (Molecular Probes/ThermoFisher), and sealed with nail polish.

Imaging was performed with a Nikon Eclipse Ti inverted fluorescence microscope using the Nikon Plan Apo 100x Ph oil (NA 1.45) objective. This was equipped with the Andor Zyla sCMOS camera. Image acquisition was controlled using NIS Elements AR 4.2 imaging software (Nikon Instruments). Images were visualised and analysed with FIJI[115].

2.2.8 Distribution analysis

For the analysis of BacM distribution in *M. xanthus* from immunofluorescence micrographs, FIJI[115] and BacStalk[116] were used. Pre-processing was performed with FIJI, which separated phase contrast channel and fluorescence channels into two images. These were imported into BacStalk for cell segregation and intensity analysis. Plots and diagrams were also generated with BacStalk.

2.2.9 Total internal reflection microscopy

M. xanthus cells expressing BacM-mNG were grown to mid-log phase, washed thoroughly in TPM, and diluted to an OD_{600} of 0.2. Cells were then incubated in TPM for at least 1 hr to cease vanillate-inducible production of fluorescently-tagged protein, and to reduce the proportion of motile cells. Cells were imaged on TPM-agarose pads as described above. Microscope system used was the Nikon Eclipse Ti inverted fluorescence microscope with a CFI Apochromat TIRF 100XC oil (NA 1.49) objective, equipped with the Andor iXion ultra EM-CCD camera. The 488 nm laser line was used. TIRF was achieved by offsetting the incident laser until background fluorescence was minimal but signal was still retained. Image acquisition was controlled using NIS Elements AR 4.2 imaging software (Nikon Instruments). Images were visualised and analysed with FIJI[115].

2.2.10 Stochastic optical reconstruction microscopy

Cells were prepared with the same method as immunofluorescence described above, but high precision cover-glasses (Marienfeld SUPERIOR) were exclusively used, and AlexaFluor 647 conjugated antibody was used instead as the secondary antibody. Antibody concentrations used were 1:100 and 1:200 for primary and secondary antibody, respectively. GLOX buffer was used for STORM imaging and was prepared with 100 mg of glucose, 0.5 mg of glucose oxidase, 0.4 mg of catalase, 0.1 M cysteamine made to 1 ml with 10 mM NaCl and 50 mM Tris-HCl at pH 8. The cover-glass was mounted on a glass slide with a cavity measuring 15-18 mm in diameter and 0.6-0.8 mm in depth (Marienfeld SUPERIOR), using around 100 µl of GLOX buffer, and sealed with nail polish. Nikon Eclipse Ti inverted fluorescence microscope was used with a CFI Apochromat TIRF 100XC oil (NA 1.49) objective equipped with the Andor iXion ultra EM-CCD camera. The 647 nm and 405 nm laser lines were used. Image acquisition was controlled using NIS Elements Advance Research High Content 4.2 imaging software with the N-STORM module (Nikon Instruments).

Image reconstruction was performed with NIS Elements AR 4.2 software, and analysed and visualised with the ThunderSTORM[117] plugin on FIJI[115].

2.2.11 Transmission electron microscopy – negative stain

Continuous carbon grids from Electron Microscopy or from EM Resolutions were glow-discharged with an in-house glow discharger at a setting of 45 for 1 minute. Liquid samples to be visualised were applied to grids, blotted with filter paper, washed with ddH_2O and stained with 2% uranyl acetate for 1 minute, blotted again, and air dried. Grids were imaged with a 100 kV Philips CM100 electron microscope with a charge-coupled device (CCD) camera operated with the Gatan Digital Micrograph software. Micrographs were visualised and analysed with FIJI image processing software[115].

2.2.12 SDS-PAGE protein analysis

Protein samples to be analysed were mixed 1:1 with 2x sodium-dodecyl-sulfate (SDS) loading buffer (Invitrogen) with or without 8 M urea or 20 mM dithiothreitol (DTT) to reach a final concentration of 4 M and 10 mM, respectively. Cells was first centrifuged before adding 1x SDS-loading buffer, with or without urea or DTT. Samples were heated in a water-bath to 100°C before electrophoresed through a 10-well 4-20% or 10-20% Tris Glycine gels (Novex/Invitrogen) using an X-call SureLock II gel system (Novex/Invitrogen) at 150 volts until the dye front reaches the end of the gel.

For visualisation, gels were extracted and incubated with Quick Coomassie Stain (Generon) for 30 minutes or more before de-staining in ddH_2O several times. Gels were visualised with the G:BOX Chemi XX6 gel imaging system (Syngene) using the GeneSys image acquisition software (Syngene).

2.2.13 Western Blotting

Samples separated with SDS-PAGE were transferred onto a nitrocellulose membrane (GE Healthcare) by electroblotting in ice-cold Towbin buffer (25 mM Tris, 192 mM glycine, 20% methanol) with MINI-PROTEAN II cell blotting unit (Bio-Rad) at 180 V for 30 min. The transferred membrane was blocked overnight in 5% skimmed milk powder (Tesco) in PBS buffer. Primary antibody was diluted to a concentration of 1:3,000 - 1:10,000 in PBST and 1% bovine serum albumin (BSA) and incubated with the membrane for 2 hours at RT or overnight at 4°C. Membrane was then washed with PBST with 0.1% BSA thoroughly and incubated with anti-rabbit horse radish peroxidase-conjugated secondary antibody (ThermoFisher) diluted in PBST with 1% BSA at 1:3,000 - 1:20,000 for 2 hours at RT or overnight at 4°C. Membrane was washed again as before and incubated with SuperSignal West Pico PLUS chemiluminescent substrate (ThermoFisher) for 5 min at RT. Membrane was sandwiched between two pieces of transparent plastic before imaging with the ChemiDocs gel imaging system (Bio-Rad) operated with Image Lab software.

2.2.14 Freeze substitution and thin sectioning

BL21-BacMTR cells expressing $BacM_{TR}$ were cryofixed using the Leica EM PACT 2 high-pressure freezer. Substitution was performed with pure acetone containing 2% osmium tetroxide and a molecular sieve with pore diameter of 0.4 nm for 80 hours at -80°C. Temperature was increased slowly to 0°C. Excess fixative was washed away with pure acetone at RT. Samples were then infiltrated with acetone-Epon 812 mixtures at 2:1, 1:1, and 1:2 ratios for 1 hour, 1 hour, and overnight, respectively, and acetone was allowed to evaporate away. After this, samples were placed into fresh pure Epon 812 for 3 hours, embedded, and polymerised at 60°C for 36 hours. Resin blocks containing freeze-substituted samples were thin-sectioned using the Reichert-Jung Ultracut E ultramicrotome, and sections were collected by floating on water and transfered onto an EM-grid.

2.2.15 Isolation of untagged BacM

Rosetta-BacMTR cells were used and expression induced as described above. Cell were harvested and resuspended in PBS with lysozyme at 1 mg/ml and cOmplete EDTA-fee protease inhibitor (Merck) before cell breakage. Cell breakage was confirmed under the light microscope and by substantial increase in viscosity. Lysate was supplemented with sodium azide, 0.1 mg/ml DNase, 10 mM $MgSO_4$, and Triton X-100 at 0.4%. This was processed with a CsCl gradient, prepared with 0.5% β-DDM, 1 M urea, CsCl at 0.37 g/ml and 10 mM Tris for buffering at pH 8. Ultra-centrifugation was performed at 55k RPM for 15 hours at 20°C. Fractions were inspected with TEM for $BacM_{TR}$ filaments. Further purification was performed on fractions containing filaments with a second CsCl gradient, but urea was omitted. After centrifugation, a layer with a web-like network could be seen. The network was collected and dissolved in ddH_2O. Inspection by TEM and SDS-PAGE analysis showed high purity of BacM in from this fraction. Protein concentration was estimated with Bio-Rad protein assay reagent (Bio-Rad).

2.3 Results

2.3.1 Generation of mNeonGreen-tagged BacM under the vanillate-inducible promoter

Previous fluorescent microscopy studies on BacM performed by the Hoiczyk lab were carried out with the BacM-mCherry fusion protein[59] expressed under the copper-inducible promoter[114]. Expression of this fusion construct in the presence or absence of native BacM revealed that it localised very differently to native BacM structures. Bright punctate spots were seen instead of the intracellular cables and membrane-associated polar rod-like structures observed from native filaments. Moreover, when expressed in the *ΔbacM* strain, BacM-mCherry was unable to rescue these cellular morphological defects. This is unsurprising as mCherry, at 28 kDa, is more than twice the size of BacM, causing the disruption of its physiological function.

Preliminary experiments demonstrated that reduced expression of BacM-mCherry in strain DK1622[112], hereby refered to as the 'wild-type' strain, was sufficient to 'decorate' native BacM structures without disrupting its function. The fluorescent pattern seen was also comparable to that of immunofluorescence of native BacM. This effect is similar to the GFP-fusion of crescentin. When expressed alone in *Caulobacter crescentus,* crescentin-GFP was not functional. But when expressed in the wild-type background, the GFP-fusion construct was able to label the native crescentin structure[54].

There are two major drawbacks of this system, however. First, mCherry has low extinction coefficient and quantum yield, and also modest photostability, making time-lapse microscopy at low expression levels challenging[118]. Secondly, the use of copper as the inducer molecule can have deleterious effects[119] on cell growth, development, and motility[119]. In order to address these issues mNeonGreen[120], a 27 kDa fluorescent protein (FP), was chosen as a fluorescent tag for BacM, expressed by a vanillate-inducible system[113]. The fluorescent protein mNeonGreen has much higher extinction co-efficient and quantum yield than mCherry, making it much brighter. Its higher photostability also allows longer time-lapse imaging. Furthermore, its lower emission wavelength gives a slight improvement in resolution, as resolution is inversely proportionate to wavelength. The vanillate-inducible system was chosen for its robustness, tight regulation, and ease of use. Vanillate also has negligible effects on normal cellular behaviours at the concentrations used for this system[113] .

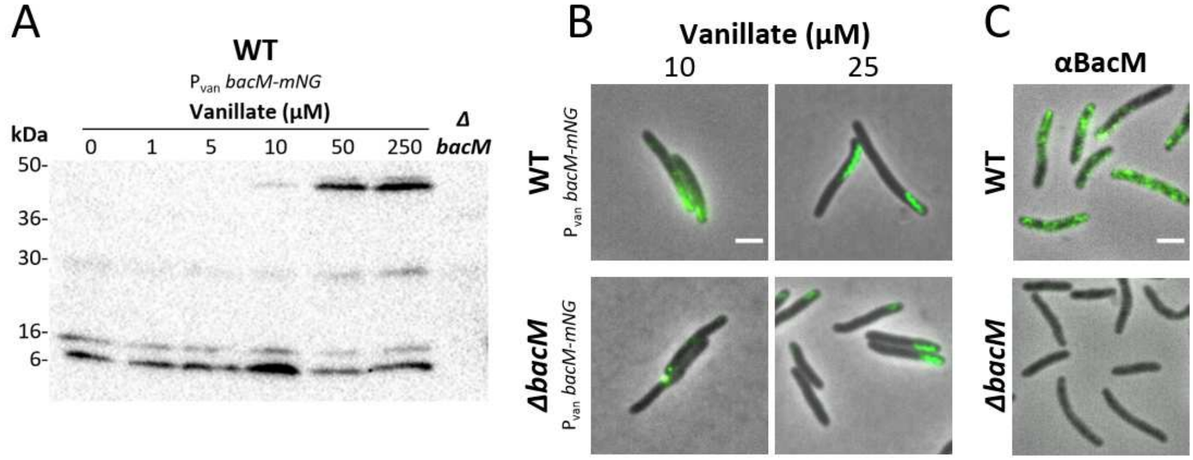

Figure 2-2 Expression of BacM-mNG under the vanillate-inducible promoter.
(A) Western blot of BacM and BacM-mNG from strains DK1622 (WT) background (EH721) using anti-BacM antibody. Concentration of vanillate used for induction is shown for each lane. BacM-mNG is present at around 42 kDa, note the presence of two populations representing the N-terminally cleaved and uncleaved forms. Two populations of native BacM can also be observed, as expected, and can be used for loading control. Faint bands at 30 kDa were off target binding. Lane representing *ΔbacM* cells is also shown. (B) Merged phase contrast and fluorescence images of WT (EH721) and *ΔbacM* (EH722) background strains expressing BacM-mNG induced with 10 μM or 25 μM vanillate. Normal BacM morphology is seen in WT at 10 μM. (C) Immunofluoresent images of BacM in fixed DK1622 and *ΔbacM* cells labelled with anti-BacM antibody and Alexafluor 488-conjugated antibody, for comparison. Scale bar = 1 μm.

To test this system, mNeonGreen (mNG) was attached to the C-terminus of BacM, and placed under the vanillate-inducible promoter (P_{VAN}) in the plasmid pMR3679[113]. This plasmid was then transformed into both DK1622 (wild-type) and EH301 (*ΔbacM*) cells, and was incorporated into an inter-genic region in the chromosome with no promoter activity by homologous recombination, generating EH721 and EH722, respectively. EH721 was induced with various concentrations of vanillate for 18 hours, and cells were analysed by Western blot with anti-BacM antibody. The bands at around 50 kDa in (**Figure 2-2 A**) shows that BacM-mNG expression can be controlled in this system, and the fusion protein remains intact. Also, the presence of a weaker band slightly higher than the major band at 40 kDa suggests that *M. xanthus* is able to cleave the N-terminus of BacM-mNG. Fluorescent imaging of EH721 and EH722 induced with various concentrations of vanillate showed that BacM-mNG localisation pattern at 10 μM of vanillate was comparable to native BacM structures (**Figure 2-2 B&C**). However, at 25 μM of vanillate, BacM-mNG adopted a polar corkscrew morphology not seen in native BacM structures, which is identical to a previous report on overexpressed BacM-mCherry (**Figure** 2-2 **B&C**). Expression of BacM-mNG alone with no native BacM in EH722 resulted in punctate spots or corkscrews, and cell morphological defect was not rescued. The concentration of vanillate chosen for all further studies was 10 µM, which provided good fluorescent signal without observable detrimental effects on BacM structures. From the Western blot (**Figure 2-2 A**), the amount of BacM-mNG was estimated to be 5% of total native BacM at 10 µM vanillate.

2.3.2 Intracellular dynamics of BacM structures

When performing *in vivo* imaging of BacM-mCherry in DK1622 background cells, subtle movements could be observed in areas of cells between bright and stable structures (**Figure 2-3**). This warranted further study into the dynamics of BacM, and with the improved qualities of BacM-mNG as stated above, this could now be investigated.

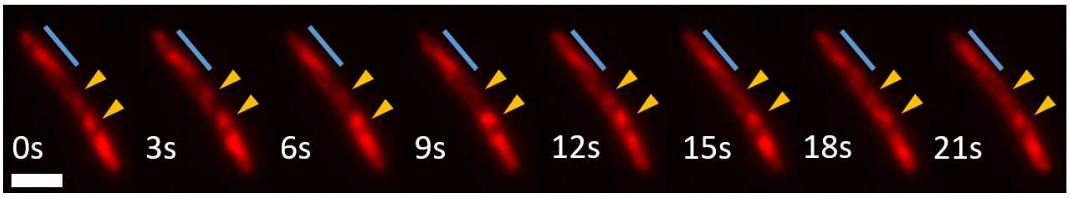

Figure 2-3 Time-lapse fluorescent images of BacM-mCherry expressed in strain DK1622 exhibits subtle intracellular movements.
Example of a cell expressing BacM-mCherry under a copper-inducible promoter. Orange arrows point to diffused patches of BacM-mCherry showing subtle movements. Blue line is adjacent to a polar structure that appears relatively stable throughout the time-lapse. Each image of the time-lapse is 3 seconds apart. Scale bar = 2 µm.

To visualise individual motile elements of BacM, total internal reflection fluorescence (TIRF) microscopy was performed. This technique utilises an evanescent excitation wave generated by a laser at high incident angle to the coverslip (**Figure 2-4 A**). This exponentially decaying wave travels through the coverslip and into the sample, selectively exciting fluorophores within approximate 200 nm from the coverslip. This technique can greatly reduce background by eliminating fluorophores outside of the focal plane from excitation.

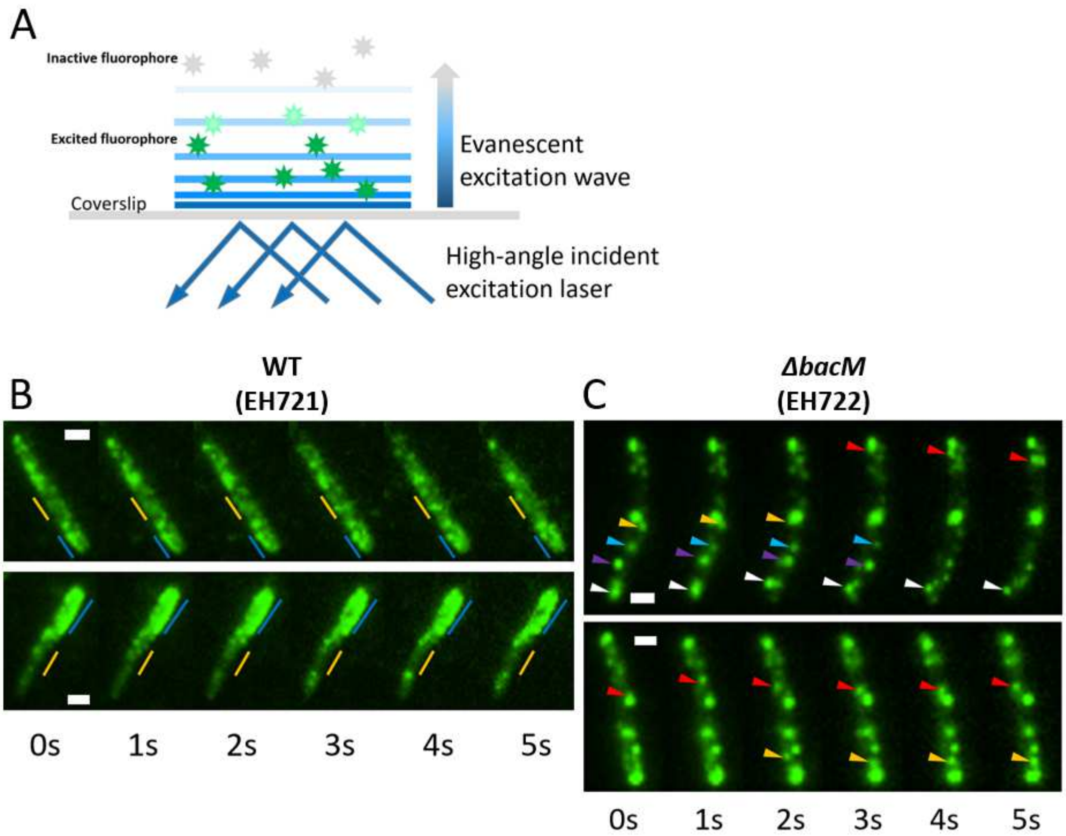

Figure 2-4 Total internal reflection fluorescence (TIRF) microscopy of BacM-mNG in DK1622 and *ΔbacM* background.
(A) Schematic describing principles of total internal reflection fluorescence (TIRF) microscopy. See text for details. BacM-mNG induced in DK1622 (B) and *ΔbacM* (C) background strains. Blue lines in (B) show stable structures, and orange lines show portion of cells with defused structures. Coloured arrowheads in (C) show positions of motile spots. Each colour follows one spot in the image sequences. Images were taken at 10 Hz, and only a subset are shown here. Images were corrected for photobleaching by histogram matching. Cells were induced with 10 µM vanillate for 18 hours before imaging on agarose. Scale bar = 1 µm.

Imaging of EH721 cells (WT background) expressing BacM-mNG showed that the prominent polar rod-like BacM structures were stationary and did not exhibit motion (**Figure 2-4 B**, blue lines). However, as observed above, the defused structures in the non-polar regions did exhibit subtle motion. They were difficult to distinguish as they were not of any fixed shape, which makes tracking difficult. In contrast, BacM-mNG in EH722 (*ΔbacM*) background form punctate spots which were highly motile (**Figure 2-4 C**). They could easily be followed through the time-lapse sequence, and unlike the bright polar structures observed in EH721, appeared to not be associated or anchored to any location in the cell. If this is the case, the movement seen was most likely normal diffusion and not active transport. Indeed, over the timeframe observed, the bright spots did not appear to have displaced towards any particular direction, and only moved erratically.

To further understand the dynamics of BacM, fluorescence recovery after photobleaching (FRAP) experiments were performed on EH721 cells. For these experiments, EH721 cells were induced for 18 hours, washed extensively to remove vanillate, and placed on starvation TPM agar for 1 hour before imaging. A small intracellular area of interest was selected and bleached with high powered excitation laser. Fluorescence of these areas were then observed and measured over time (**Figure 2-5 A**). Rapid fluorescence recovery implies highly dynamic movement of fluorescently tagged proteins, which replaces the bleached species. Conversely, the opposite is true if fluorescence recovers slowly. Moreover, the size of the fraction of fluorescence that could be seen also provides information on the proportion of mobile and non-mobile fluorescently tagged proteins.

Intracellular fluorescent BacM structures were classed into bright, polar structures and diffused non-polar structures, and were selectively bleached. A confocal microscope with an airyscan detector was chosen for this experiment as it allows accurate bleaching, provides higher signal-to-noise ratio (SNR), and improved resolution over ordinary epifluorescence and confocal microscopes. From **Figure** 2-5 **B&C**, it could be observed that the recovery of fluorescence in non-polar and polar regions was only partial, plateauing on average at around 30% and 10% of pre-bleach intensity, respectively. This suggests that the underlying BacM structures in non-polar and polar regions are non-motile, despite observed subtle movement of fluorescence in TIRF in non-polar regions. This likely also implies that very little BacM subunit exchange takes place or is very slow, which was especially evident in polar structures. On closer inspection, there were larger fluctuations in the fluorescence recovery intensity traces in the non-polar dataset than in the polar structures dataset. There are two possible reasons for this. Firstly, this could be due to individual, highly motile fluorescent structures moving through the detection area, giving peaks in intensity traces. These could be seen in the example image sequence of **Figure 2-5 D**. This is in agreement with the observed subtle movement of diffused structures in TIRF microscopy above. Whether these motile fluorescent patches represent the behaviour of native BacM cannot be verified here. Secondly, due to the lower intensities of non-polar structures, any noise-induced fluctuations would be of a higher proportion to the pre-bleach intensity than at brighter polar structures. However, inspecting absolute intensity values and also the observation of motile patches moving through FRAP sites suggests that the former scenario is more likely.

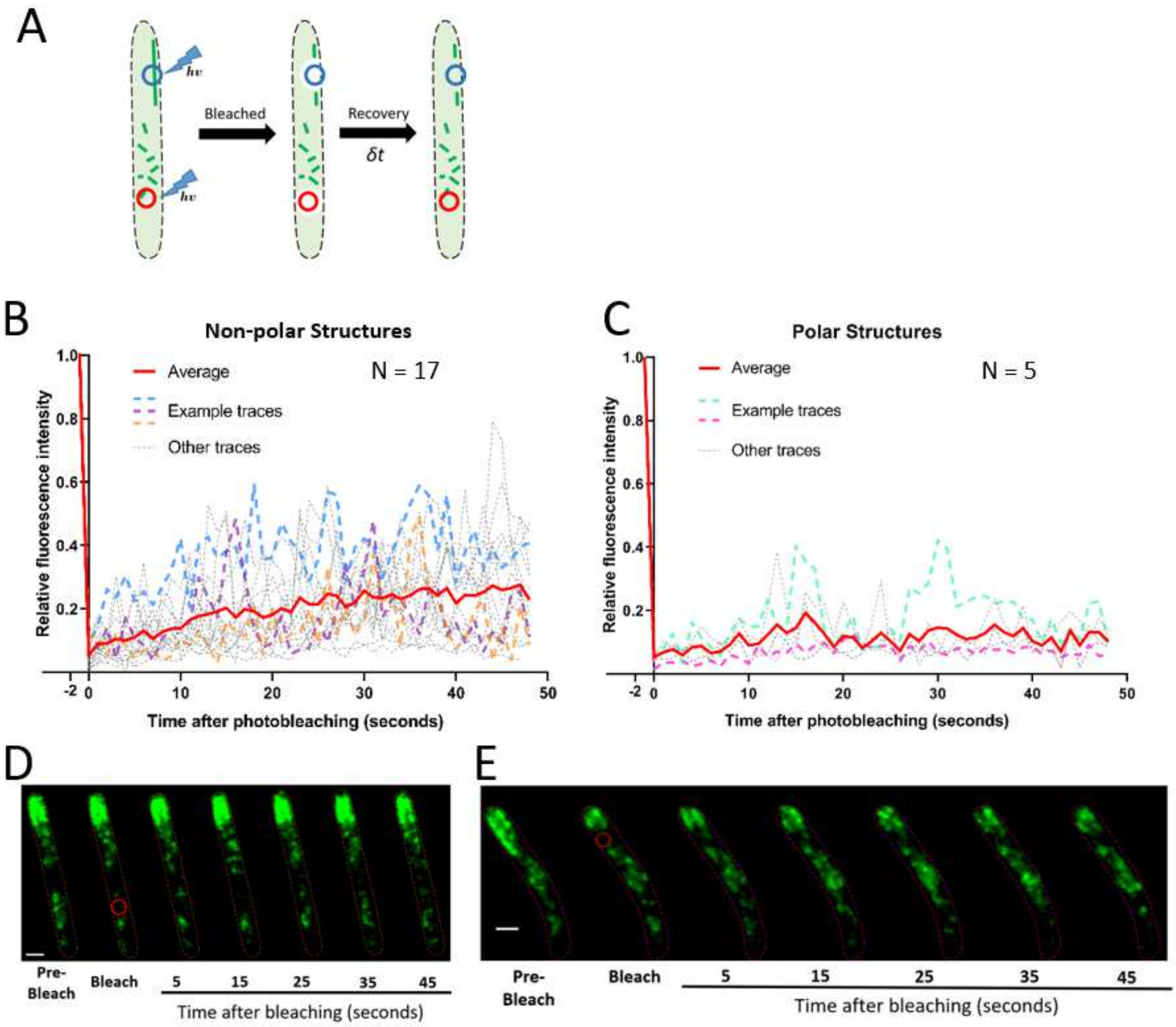

Figure 2-5 Fluorescence recovery after photobleaching (FRAP) experiment shows BacM forms stable structure inside the cell.
(A) Schematic of FRAP. Red and blue circles show area of bleaching and measurement for non-polar structures dataset and polar structures dataset, respectively. Each dataset is corrected for background and normalised for overall bleaching during measurements. Graphs presenting quantitative analysis of FRAP of non-polar (B) and polar structures (C). Averages of recovery traces are represented with solid red lines. Selected example traces are shown as dashed coloured lines, and other traces are in grey. All values are relative to pre-bleach intensities. Example fluorescent images of EH721 *M. xanthus* cells expressing low levels of BacM-mNG used for measurements for non-polar structures (D) and polar structures (E). Area of bleaching and measurement is marked with red circle. EH721 cells were induced with 10 μM of vanillate for 18 hours, washed, and mounted on TPM starvation agar for 1 hour before imaging. Images were taken at 1 Hz, only a subset are shown here. Scale bar =1 μm.

Additionally, as the intensities of polar structures were much higher than those of non-polar diffused structures (**Figure 2-5 E**), any fluctuations in intensities would be proportionally smaller in the polar structures. Three populations of BacM structures can therefore be deduced: polar structures; non-polar, non-motile structures; and non-polar, highly motile structures.

2.3.3 BacM is sensitive to tag insertions

Although informative, the experiments above could not verify whether the dynamics observed of BacM-mNG decorated BacM structures are the true characteristics of the native structures, or are partly artificially induced by BacM-mNG. A fluorescently-tagged BacM construct that could functionally replace the indigenous native BacM was required for further studies. A suitable tag for this was the tetracysteine tag (TC), which comprises of only six amino acids in its smallest form[121,122] (CCPGCC). This tag has high affinity for the membrane permeable biarsenical fluorophores FlAsH and ReAsH, which have low toxicity and can specifically label TC-tagged proteins *in vivo*. Moreover, the availability of the two dyes can be used in a pulse-chase manner to further the investigation of BacM dynamics.

A number of constructs were designed (**Figure 2-6 A&B**). The C-terminus was a selected as the predicted NMR[60] and *in silico*[62] structures of bactofilins suggested that the variable C-terminal regions of different bactofilins are unstructured. Apart from adding the simple six amino acids motif, which gave the BacM-TC1 construct, a small linker was also added, giving BacM-TC2. An optimised tetracysteine sequence was developed for mammalian cell-based studies, which consists of the twelve amino acids FLNCCPGCCMEP[123]. This optimised sequence showed higher quantum yield and improved fluorophore affinity leading to higher contrast when tested in mammalian fibroblast cells. This optimised tag was added to the C-terminus of BacM which gave BacM–TC3, and a short linker was also attached, giving BacM-TC4.

DK1622 and *ΔbacM* were transformed with these constructs under the vanillate-inducible plasmid system. These cells were induced and then incubated with FlAsH-EDT$_2$. Unbound dye was chelated and removed with the reducing agent BAL, and cells were imaged on agarose pads under an epifluorescence microscope (**Figure 2-7**). None of the BacM-TC constructs were able to rescue the cell morphological defect in *ΔbacM* cells. For both BacM-TC1 and BacM-TC2, they formed thick, bright filaments of various lengths in both backgrounds (**Figure 2-7**). The localisations of these filaments were different to that seen in immunofluorescence, and were not constrained to the poles like the polar rod-like structures. They also appeared to curve and twist down the length of the cell and detached from the membrane. The same could be observed for BacM-TC3 and BacM-TC4 in wild-type background.

However, in *ΔbacM* mutants, punctate spots throughout the cells were observed instead (**Figure 2-7**). These observations suggest that C-terminally TC-tagged BacM derivatives were able to polymerise into filaments, but their ability to form normal higher order fibres are affected, as well as their ability to localise to the correct subcellular locations.

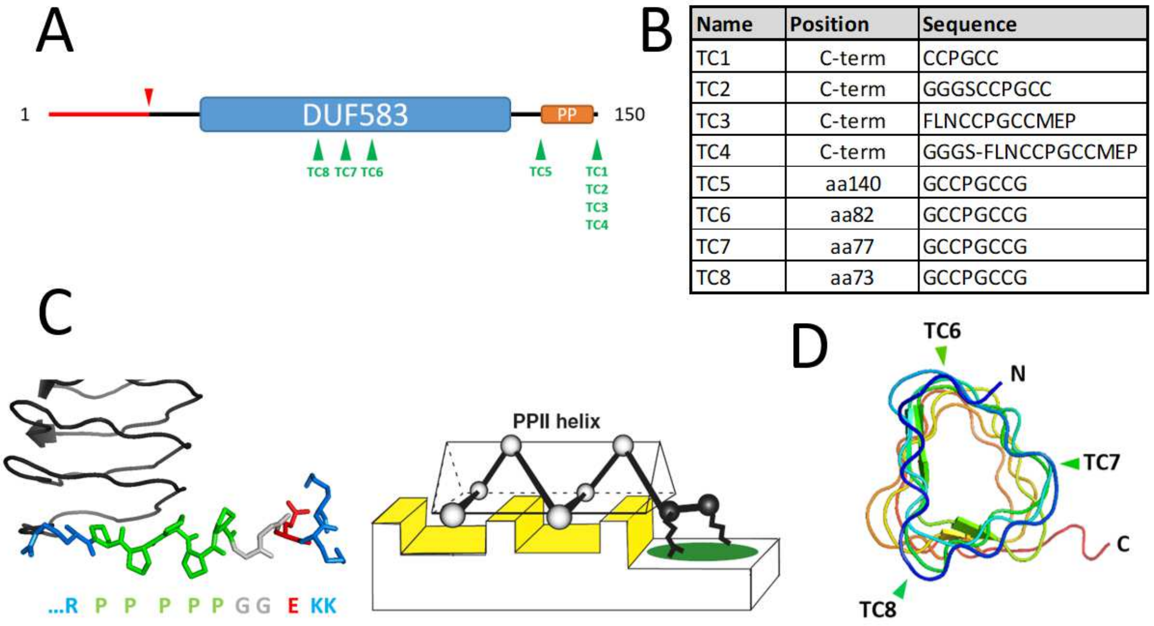

Name	Position	Sequence
TC1	C-term	CCPGCC
TC2	C-term	GGGSCCPGCC
TC3	C-term	FLNCCPGCCMEP
TC4	C-term	GGGS-FLNCCPGCCMEP
TC5	aa140	GCCPGCCG
TC6	aa82	GCCPGCCG
TC7	aa77	GCCPGCCG
TC8	aa73	GCCPGCCG

Figure 2-6 Tetracysteine tag insertion positions in BacM.
(A) Schematic of BacM with TC-tag insertion points shown by green arrowheads. The cleaved N-terminal sequence is shown in red, with cleavage site highlighted by a red arrowhead. The poly-proline region is in orange. (B) List of inserted sequence and positions of the TC-tags. aa represents amino acid position before which the tag is inserted. (C) Stick schematic of amino acids of the poly-proline region of BacM. Green represent prolines, blue represent positively charged amino acids, red represents negatively charged amino acid, and grey are uncharged residues. The corresponding symbols of amino acids are underneath. This poly-proline region of BacM is a good example of a poly-proline II (PPII) helix, which is a common motif for protein-protein interaction. Right-hand side diagram adapted from (121) (D) Top view of the ribbon diagram of BacM β-solenoid showing positions of β-arcs where TC tags were inserted. Protein backbone is coloured in rainbow spectrum.

The short C-terminus of BacM has a string of five prolines, followed by charged amino acids (**Figure 2-6 C**). This poly-proline (PP) region likely forms a poly-proline II (PPII) helix, a conformation commonly adopted by regions for protein-protein interactions[124]. The non-functionality of C-terminal FP or TC-tag fusions may in part be due to the inaccessibility of the PP region caused by steric hindrance by the tags. Therefore, the TC tag was instead inserted in front of the PP region, which gave BacM-TC5, to avoid the blocking of the PP region (**Figure 2-7**). This construct was expressed in wild-type and *ΔbacM* cells as before. Thick, short structures could be seen in the wild-type background, which are different to the long filaments observed above for BacM-TC1-4. Again, morphological defects were not rescued in the deletion mutant, and punctate spots were observed.

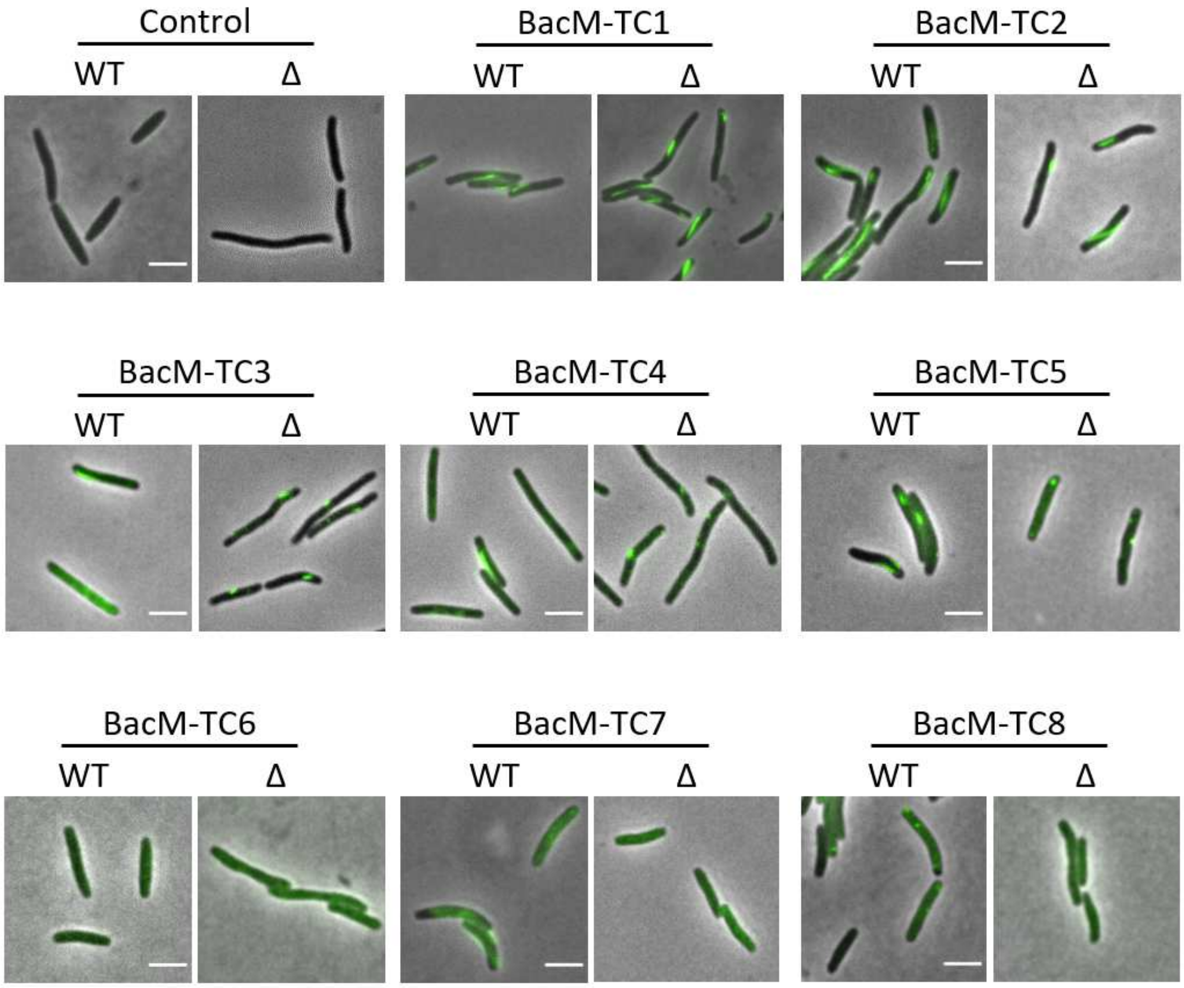

Figure 2-7 Tetracysteine-tagged BacM fail to localise correctly and rescue crooked phenotype of ΔbacM strain.
Shown here are merged fluorescence and phase contrast images of DK1622 and *bacM* deletion strains expressing BacM-tagged in various locations. Un-transformed DK1622 and *⊿bacM* strains were used as controls. Cells were induced under P_{VAN} with 25 µM of vanillate for 18 hours. Induced cells were stained in 2 µM FlAsH-EDT$_2$ before imaging on TPM agarose. Scale bar =1µm.

It became apparent that the C-terminus end of BacM is very sensitive to tag insertion. Other locations of insertion had to be considered. The N-terminus of BacM is cleaved (**Figure 2-6 A**), and *in silico* modelling of BacM predicts that the sequence immediately after the cleavage site is involved in inter-subunit interactions during polymerisation, and amino acid substitution close to this site abolished filament formation[62]. Therefore, the N-terminus would likely also be sensitive to insertions. This left the bactofilin domain as the last alternative site.

As discussed earlier, the bactofilin domain adopts the structure of a tube-like stack of parallel β-sheets, forming a β-solenoid. The 'corners', termed β-arcs, of β-solenoids are usually populated by small amino acids which allow the protein backbone to turn between β-strands[125]. Generally, the amino acids at these positions do not participate in the formation of the β-solenoids. This makes them possible sites for tag-insertion. The TC-tag was inserted into the three different corners of the bactofilin domain (**Figure** 2-6 **D**), forming BacM-TC6 – 8. Again, these constructs were expressed in wild-type and *⊿bacM* cells. Curiously, only homogenous fluorescence was seen in most cells, and no structures could be seen in either genotypes, apart from small spots in a small number of cells (**Figure 2-7**). Morphological defect was not rescued in *⊿bacM* cells. This shows that the bactofilin domain of BacM is also sensitive to tag insertions, which possibly negatively affect the folding and formation of the β-solenoid, resulting in the lack of structures observed in cells.

2.3.4 Morphology of BacM fibres is affected by tag insertions

As seen above, the addition of even a small tag affected the ability of BacM to form normal structures and localise properly *in vivo*. So far, *in vitro* studies of different isolated bactofilins have been performed with tagged constructs to aid purifications[58,62,126]. The validity of the reports could therefore be put to question. To compare isolated filament morphology between tagged and untagged BacM, constructs were expressed in *E. coli* cells, and the lysate inspected by transmission electron microscopy (TEM).

As the majority of the native BacM in *M. xanthus* has the N-terminal 27 amino acids cleaved, the BacM constructs designed and expressed here were truncated to mimic N-terminal cleavage (BacM_{TR}). The untagged BacM_{TR} found in *E. coli* lysate formed mostly thin fibres 3 – 6 nm thick. Occasionally, bigger bundles were observed, but they were loosely associated (**Figure 2-8 A**). To determine whether the observed BacM_{TR} structures remain the same when isolated, an isolation protocol (see **Section 2.2.15**) was developed to purify untagged BacM_{TR} from *E. coli*. The purified structures remained the same, comprising mostly of 3 – 6 nm thick filaments (**Figure 2-8 A**).

Next, BacM$_{TR}$ with tags inserted at either terminus were inspected (**Figure 2-8 B**). For the C-terminally tagged construct, BacM$_{TR}$-TC1 formed very thick bundles, which were not found in untagged BacM$_{TR}$. No individual thin fibres similar to the untagged BacM$_{TR}$ could be found. This is in agreement with the thick fluorescent structures observed when BacM-TC1 was expressed in *M. xanthus*. The N-terminally tagged BacM$_{TR}$ was a construct previously used for *in vitro* studies. The resulting filaments were somewhat thicker, mostly at 10 nm or more, which were similar to what was reported[58,62]. Thinner 3 nm fibres could still be seen, however.

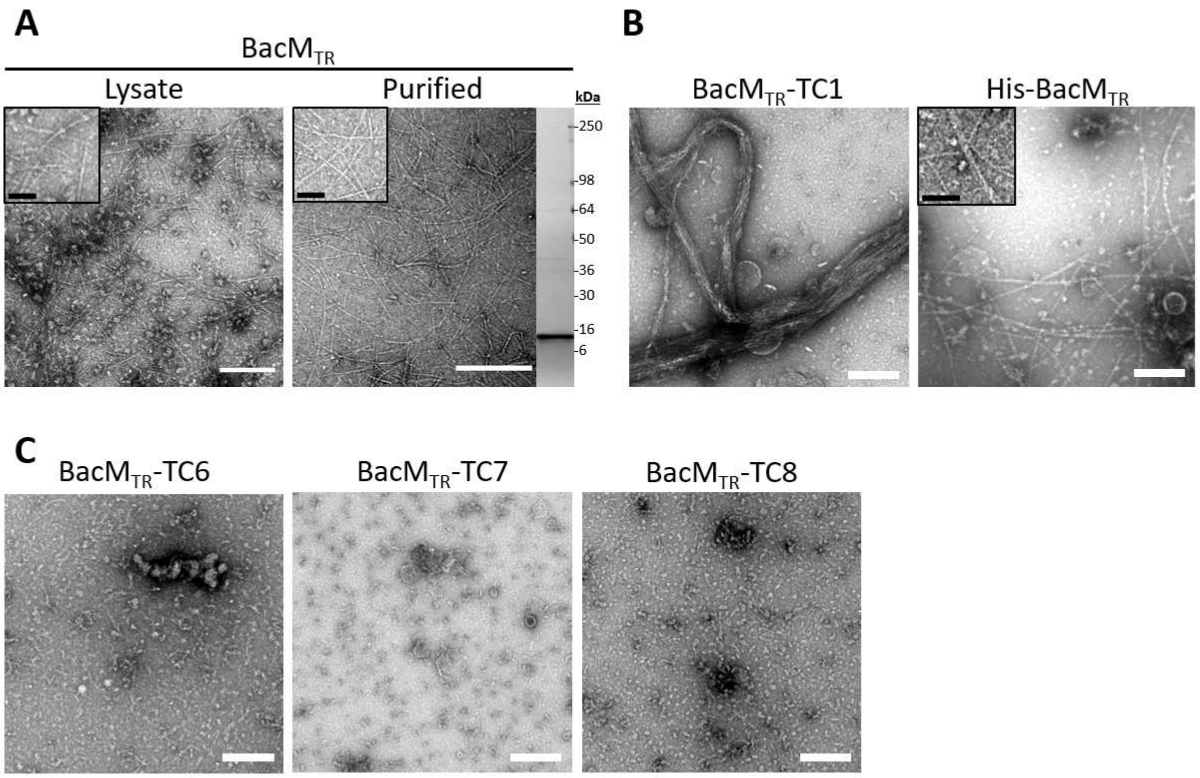

Figure 2-8 TEM micrographs of whole cell lysate of *E. coli* expressing BacMTR with tetracysteine tagged at different locations.
E. coli cells expressing BacM$_{TR}$ constructs were sonicated, and lysates were treated with 0.4% Triton X-100 to solubilise membrane fragments before imaging under TEM. (A) Left: *E.coli* lysate with untagged BacM$_{TR}$. Right: purified untagged BacM$_{TR}$, SDS-PAGE image shows purity of the sample inspected. (B) Lysate of *E. coli* cells expressing C-terminal TC-tag, or N-terminal His-tag BacM$_{TR}$. Inserts in (A) & (B) are magnified micrographs showing fibre morphology. (C) Lysate of *E. coli* cells expressing BacM$_{TR}$ with TC tags in the bactofilin domain. Scale bars = 200 nm. Scale bars in inserts = 50 nm.

To understand why no structures could be found *in vivo* in *M. xanthus* for bactofilin domain TC-tagged BacM, these were also expressed in *E. coli* as BacM$_{TR}$. No filamentous structures could be found at all in the lysate (**Figure 2-8 C**), which strongly suggests that tag insertion at these sites prevents proper folding of the bactofilin domain, hence no polymerisation could be seen, and no fluorescent filaments could be observed when expressed in *M. xanthus*.

A further interesting observation made during this investigation is that during the expression of untagged BacM$_{\text{TR}}$ in *E. coli*, many cells appeared to be unable to complete cell division, which resulted in cells being attached end to end, with up to three cells 'chained up' in a row (**Figure 2-9 A**). Probing these cells with anti-BacM antibody and performing immunofluorescence microscopy revealed that cells were filled with BacM, and it is possible that the fibres could block the resolution of cell division sites (**Figure** 2-9 **A**). These cells were cryo-substituted and thin-sectioned, and upon TEM inspection did show bundles of filaments, most likely of BacM, forming bridges between cells through the constriction sites, and preventing the resolution of septation (**Figure 2-9 B**). BacM filaments could subsequently be found in the lysate (**Figure 2-9 C**).

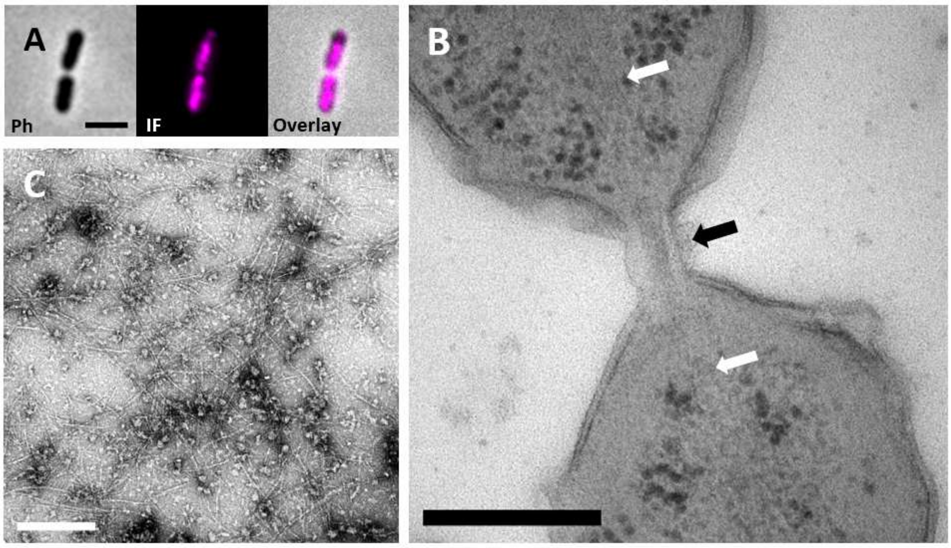

Figure 2-9 BacMTR expressing *E. coli* cells fail to complete septation.
(A) Immunofluorescence image of an *E. coli* cell expressing BacM$_{\text{TR}}$ showing arrested cell division. Fluorescence signal is location of labelled BacM$_{\text{TR}}$ structures. Ph, phase contrast; IF, immunofluorescence. Scale bar 2um. (B) TEM micrograph of thin-sectioned freeze-substituted BacM$_{\text{TR}}$ expressing *E. coli* cells. White arrows point to bundles of BacM filaments in the cytoplasm of the cell. Black arrow points to site of failed septation, arrested by BacM bundles. Scale bar 250 nm. (C) TEM micrograph of cell lysate of *E. coli* expressing BacM$_{\text{TR}}$ treated with triton X-100 to solubilise membrane fragments. Filaments can clearly be seen, along with cellular debris. Scale bar 250 nm.

2.3.5 Distribution of BacM in *Myxococcus xanthus*

During observations of the dynamics of BacM using BacM-mCherry or BacM-mNG, it could very occasionally be seen that fluorescent signal localised at early cell division sites when slight constrictions could be seen (**Figure 2-10 A**). This was also occasionally observed in immunofluorescence of fixed cells using anti-BacM antibody (**Figure 2-10 B**). To see whether BacM has a preferred pattern of distribution during the cell cycle, actively growing wild-type cells were collected at mid-log phase, labelled with anti-BacM antibody, and immunofluorescence microscopy was performed. Using the BacStalk analysis tool[116] (preprint), cells were segmented, and internal fluorescence compressed into one dimensional lines, aligned by normalised fluorescence intensity, and sorted by cell length for comparison to produce a demograph (**Figure 2-11 A**). If BacM does have a preference for localising at the mid-cell during early division, it could be predicted that as cell length increases, intensity would also increase at the middle of the cell. No such distribution could be observed, however (**Figure 2-11 A**), as no correlation between cell length and localisation could be seen. Examples of cells with slight constrictions at the mid-cells are shown in (**Figure 2-11 B**), and there was no consistent localisation at the mid-cell observed.

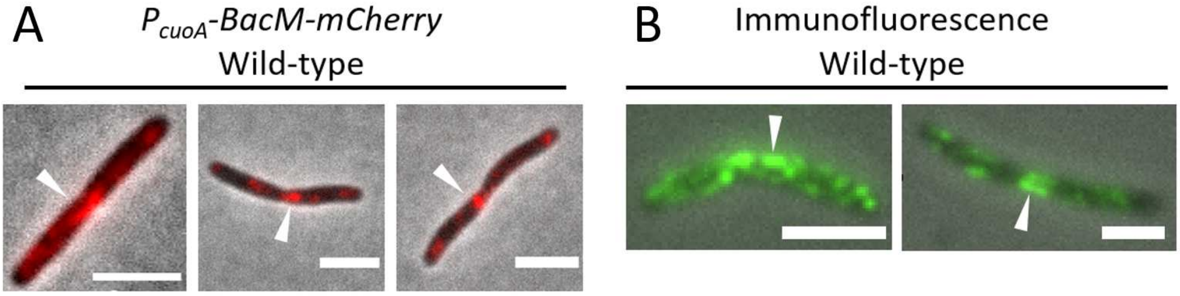

Figure 2-10 BacM can occasionally be seen to localise at early cell-division sites.
(A) Fluorescence signal of BacM-mCherry fusion protein occasionally accumulate at early division sites where slight constrictions can be observed. (B) Similar localisation can be seen from immunofluorescence images of BacM labelled with anti-BacM antibody in wild-type cells. Scale bars = 2 µm.

The demograph in **Figure 2-11 A** did show an observable preference of BacM to one particular half of the cell. This could be partially caused by the observed polar rod-like structures which only occur in one half of a cell, though only a quarter of cells at most have these rod-like structures, and there is much signal that does not extend from the pole. The reason behind this observation is unclear.

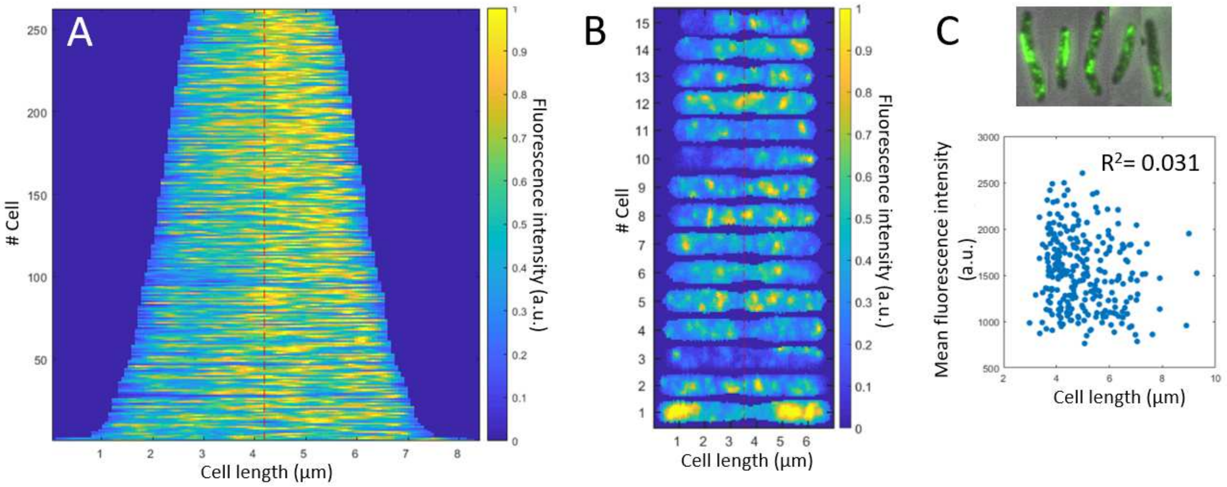

Figure 2-11 Cellular distribution of BacM measured by immunofluorescence microscopy. (A) No specific localisation of BacM can be observed when plotted against cell length, although there is a preferential localisation to one particular half of a cell. Graph generated by sorting single-cell fluorescence profiles by cell length and stacked, and orientated by intensity. Fluorescence is normalised to each individual cell. (B) Example fluorescence patterns of individual cells with slight constrictions at the septum. No consistent localisation to the septum could be observed. Fluorescence is normalised to each individual cell. (C) Scatterplot of mean cellular fluorescence intensity against cell length. Shown above are examples of cells exhibiting a range of fluorescence intensities.

The mean fluorescence signal emitted by each cells appeared to vary hugely, ranging from 760 to 2600 arbituary units between individual cells. This is demonstrated in the scatter plot in **Figure 2-11 C** and the example cells shown. The mean intensity of fluorescence in each cell varied from around 2600 units to 760 units, regardless of cell length, as shown by the low R^2 value of 0.031 This suggests that the average content of BacM is highly inconsistent, and the mechanism behind the control of BacM cellular content is unclear.

2.3.6 Superresolution microscopy of BacM in *Myxococcus xanthus*

From the light and electron microscopy results so far, BacM appears to adopt a number of forms intracellularly. Apart from the bright and clearly visible polar rod-like structures, the structures that are formed in the rest of the cell are difficult to define. So far, observations have been made using diffraction limited methods, and within the small volume of *M. xanthus*, structures are difficult to identify.

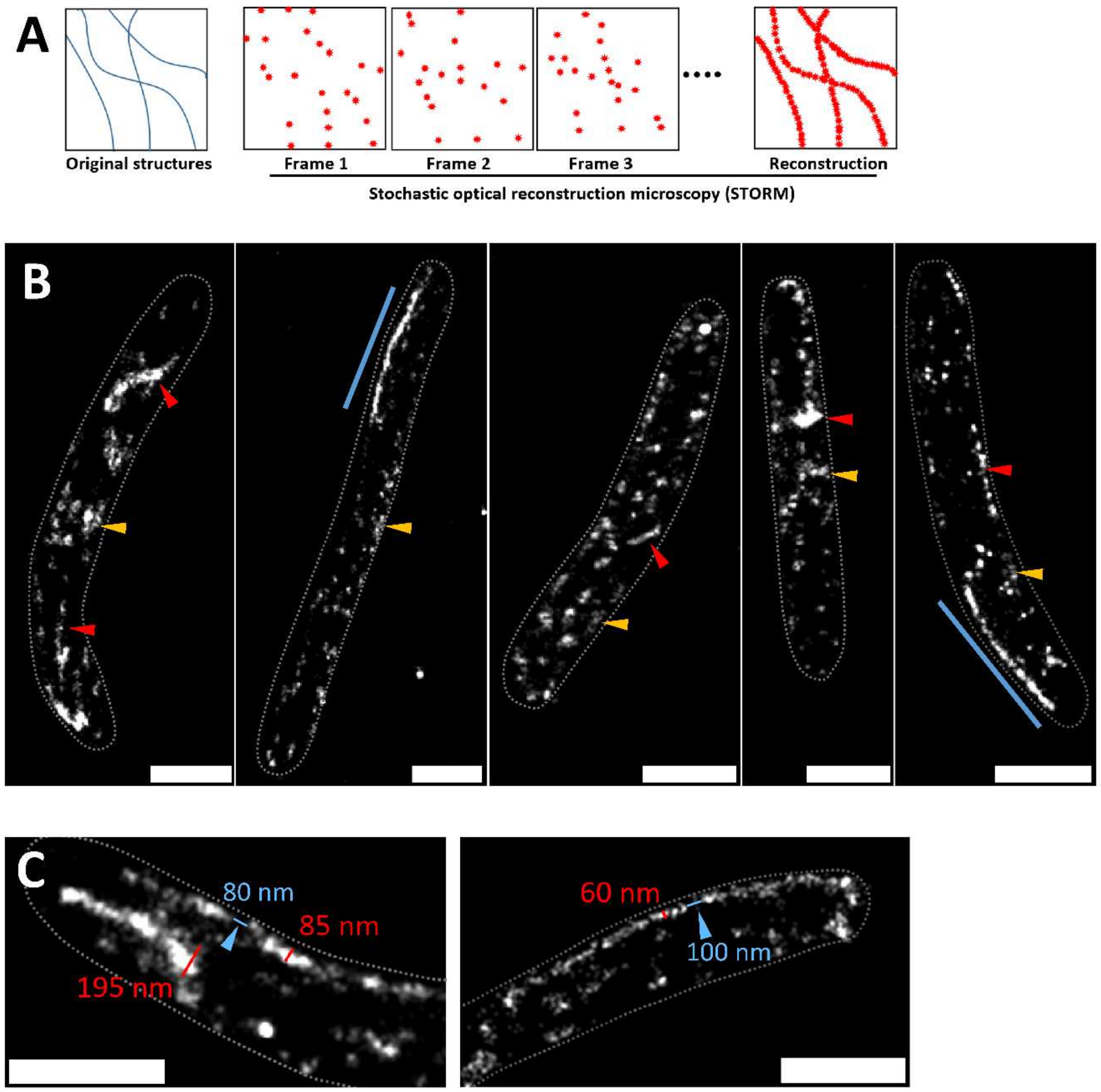

Figure 2-12 Stochastic optical reconstruction microscopy (STORM) images of immunolabelled BacM in DK1622 cells.
(A) Schematic of the mechanism of STORM. See text for details. (B) A selection of cells showing superresolution subcellular localisation of BacM. A variety of structure morphologies are indicated. Red arrowheads point to elongated structures. Orange arrowhead points to diffused structures with irregular shapes. Blue line is adjacent to 'polar-rod' structure previously reported. Many small, disjointed patches can also be seen. (C) Close-up of sub-cellular structures of BacM with measurements. Perceived thicknesses of polar rod-like structures are between 60 nm to 85 nm. Elongated structures can be up to around 200 nm in width. Blue arrowhead points to gaps in polar rod-like structures. Blue lines represent gaps seen in polar rod-like structures. Scale bars = 1 µm.

To further investigate morphology of BacM *in vivo*, stochastic optical reconstruction microscopy was performed on wild-type cells probed with anti-BacM primary antibody and AlexaFluor 647-conjugated secondary antibody. Briefly, this technique relies on the stochastic manner of rapid fluorescence blinking of the conjugated fluorophore, which is recorded over the time of data acquisition.

As these blinks at each frame are isolated and away from the signals of neighbouring fluorophores, the precise locations of each fluorophore can be accurately assigned. After many frames, the deduced locations of the fluorophores can be reconstructed into one image, which offers much higher resolution information than diffraction-limited microscopy techniques (**Figure 2-12 A**).

The reconstructed image of BacM showed a variety of structures. Most prominent were the polar rod-like filaments (**Figure 2-12 B**, blue line), which could easily be identified in widefield fluorescence microscopy. Smaller elongated structures could also be seen at different locations in the cell (**Figure** 2-12 **B**, red arrowheads). Furthermore, there were amorphous, diffuse patches of BacM, located throughout the cells (**Figure 2-12 B**, orange arrowheads). The rod-like structures had thicknesses ranging from around 50 nm to 90 nm, equating to 15 to 30 single BacM filaments thick (**Figure 2-12 C**). However, the apparent thicknesses of the structures are affected by the primary-secondary-fluorophore complex, which can increase the perceived thickness of a filament by 15 nm on each side. This means that the actual thicknesses of the rod-like structures are likely 20 nm to 75 nm – around 7 to 25 single BacM filaments thick. Gaps were also visible within some of these rod-like structures, which were up to around 100 nm wide (**Figure 2-12 C**). These gaps could be the boundaries between separate BacM filaments, or they could be caused by steric hindrance of a protein complex, blocking the binding of anti-BacM antibody. It could also be caused by the use of non-saturating concentrations of antibodies, which could leave the BacM structures unevenly labelled. Gaps in the rod-like structures remained regardless of the concentrations of primary and secondary antibody, which were used at 1:100 to 1:600, and with increasing concentrations comes the risk of non-specific labelling and increased background noise. The smaller elongated structures tended to have much more varied structures and thickness, from 30 nm to 170 nm actual (**Figure 2-12 C**). They also exhibited uneven labelling across the structures. As for the amorphous patches, they could appear as a collection of spots, or clouds of fluorescence grouped together. It is unclear whether they are part of a larger network that were not evenly labelled, or are individual patches of BacM.

2.3.7 Investigating the poly-proline region of BacM

As mentioned above, the poly-proline region at the C-terminus of BacM likely adopts a PPII helix conformation commonly found in regions responsible for protein-protein interactions. The role of this region was investigated. The sequence RPPPPPGGEKK, which corresponds to the poly-proline region of BacM, was introduced to the C-terminus of mCherry (mCherry-PP), and was expressed in *M. xanthus* cells under the vanillate promoter at a moderate level with 10 μM of vanillate. For comparison, unmodified mCherry was also expressed, which resulted in uniform intracellular fluorescence in both

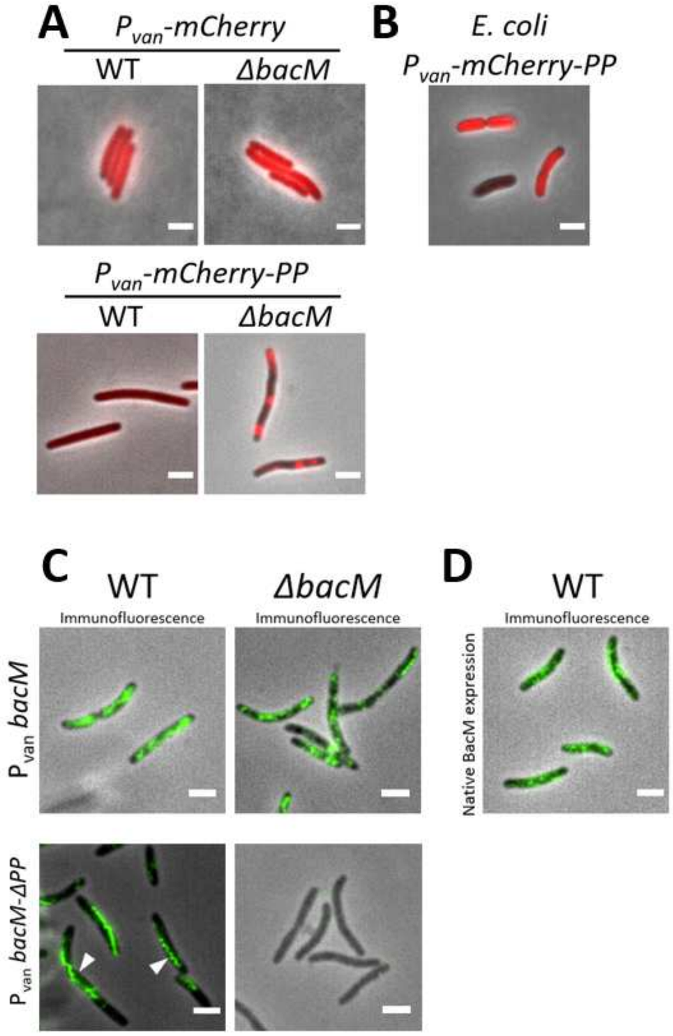

Figure 2-13 Poly-proline tail may be important for localisation of BacM.
(A) Merged phase contrast and fluorescence image of *M. xanthus* cells. Expressing mCherry results in homogenous distribution of fluorescence. However, expression of mCherry with the poly-proline (mCherry-PP) attached resulted in localisation of fluorescence in *ΔbacM* cells. (B) E. *coli* cells expressing mCherry-poly-proline fusion protein. Fluorescence is homogeneous. (C) Poly-proline tail truncated BacM (BacM-ΔPP) were overexpressed in wild-type (WT) and *ΔbacM* cells with 25 μM of vanillate. Expression of BacM-ΔPP resulted in abnormal looking structures in wild-type background (white arrowheads). (D) Immunofluorescence image of native BacM in wild-type cells for comparison. Scale bars = 2 μm.

genotypes (**Figure 2-13 A**). However, expressing mCherry-PP resulted in very weak uniform fluorescence in the wild-type background (EH719), whereas in *ΔbacM* mCherry-PP (EH720) appeared to localise to distinctive locations in the cell (**Figure 2-13 A**). This effect was not observed in *E. coli*, so is unique to *ΔbacM M. xanthus* cells (**Figure 2-13 B**). Fluorescent spots of mCherry-PP could be seen at polar regions and also near the centres of cells. It is difficult to deduce whether the localisation of mCherry-PP corresponded to the expected locations of BacM, due to the varieties of ways BacM can localise. However, it could be hypothesised that the PP tail of BacM plays a role in the localisation of BacM, and that in the wild-type cells, as the binding sites for PP tail are already occupied by native BacM, mCherry-PP are left unbound in the cytoplasm and possibly degraded.

To test the effects of the removal of the PP tail from BacM, a construct missing the poly-proline region was made (BacM-ΔPP) and expressed with the vanillate system using 25 μM of vanillate, which equated to normal cellular level of BacM. Cells were then inspected with immunofluorescence microscopy using anti-BacM antibody. For comparison, unmodified BacM was expressed also. In wild-type background (EH713), introduction of additional BacM resulted in increased levels of overall fluorescence, and there was also an increase in the length of BacM structures and the number of cells harbouring polar filamentous structures found, in line with previously reported results[59] (**Figure 2-13 C**). In *ΔbacM* background (EH714), expression of unmodified BacM restored proper cell morphology, and normal localisation of BacM was observed, as expected (**Figure 2-13 C**). Expression of BacM-ΔPP caused abnormal filament morphology in cells of wild-type background (EH717), where curls and twists could be seen in membrane-detached filamentous structures, these also appeared longer than native structures, and could occasionally be found to span the length of a cell. Dimmer fluorescence could also be seen in the rest of the cell, possibly corresponding to other forms that BacM adopts. Proper cell morphology was maintained. In *ΔbacM* mutants (EH718), little fluorescence could be seen except sporadic bright spots, and cells remained crooked. It was likely that the BacM-ΔPP was incorporated into native BacM structures when expressed in strain Dk1622, giving the twisted and curled appearance of the polar rod-like filaments. Even though cell morphology was maintained, whether these polar structures perform any function is not yet known, and other BacM structures found in the cells could be responsible for cell shape maintenance.

2.4 Discussion

From the various light microscopy experiments, it became apparent that there are distinct populations of BacM exhibiting different dynamics. The experiments suggested that the prominent polar rod-like structures are bundles of fibres that are stable, with little subunit exchange within the polar filament, with the other structures found elsewhere in the cell, and with the pool of subunits within the cytoplasm. This is very similar to the stability observed for crescentin in *C. crescentus*. The smaller BacM elements observed also had high stability in terms of subunit turnover. However, it was also observed that a subset of structures is motile, which gave the large fluctuations in the FRAP recovery. These structures may correspond to the brighter, elongated structures identified in superresolution microscopy, and that diffuse amorphous patches observed in with STORM may be the stable structures responsible for the very slow FRAP recovery at the non-polar sites. In *B. subtilis*, partially functional spots of BacE and BacF have also been found to be highly dynamic. Whether the movements seen for BacM are active or passive, i.e. directed movement or random diffusion, is unclear, and if they are active, the energy source behind it is unknown. Further experiments including using the photoswitchable nature of mNeonGreen for single particle tracking, or FRAP experiments in the presence of energy source inhibitors e.g. sodium azide and nigericin could further the understanding of the dynamics of BacM. Some of these experiments are already underway.

It is important to note that it could not be completely confirmed that the dynamics seen with BacM-mNG labelling is truly those of native BacM. The resilience of bactofilins to fluorescent tags in the forms of FP and tetracysteine tags was also reported in the other bactofilin paralogs in *M. xanthus*[111]. Interestingly, BacN fused to hemagglutinin epitope (BacN-HA) was able to localise properly when investigated with immunofluorescence with anti-HA antibody[111]. This is likely due to the observation that BacNOP form a heteropolymeric scaffold, and BacP and BacO can recruit BacN-HA in a correct manner. A possible solution is the use of fluorophore conjugated nanobodies (chromobodies). Camelid nanobodies function like antibodies, but only constitute one single heavy chain of around 15 kDa and can function in the cytoplasm as they do not require the formation of di-sulfide bonds. Chromobodies have been used in bacteria and eukaryotes for the *in vivo* labelling of intracellular structures[128,129], including the visualisation of actin dynamics[130]. Chromobodies specific to BacM could be expressed indigenously in *M. xanthus*, and label the native BacM structures *in vivo*, allowing the observation of its behaviour. There are, however, considerations. For instance, this method is expensive as it requires the selection and sequencing of monoclonal nanobodies and chromobody-tagged native BacM structures could still have their functions impaired, or dynamics altered. A well-controlled, low level of expression would be required to reduce background signal of unbound chromobodies. A similar, more novel labelling system is the use of Affimers[131]. These are non-antibody derived antigen-binding proteins of around 13 kDa, and are selected by phage display screening which is cheaper and faster than animal-inoculation-based techniques. There are as yet no reports for intracellular expression of a fluorophore-Affimer fusion in bacteria, although conceptually it is a viable method for *in vivo* investigation of intracellular protein dynamics.

It is unclear how *M. xanthus* is able to regulate the polymerisation, depolymerisation, and degradation of BacM filaments. Bactofilins have a high propensity to polymerise spontaneously, and of note the critical concentration for polymerisation of bactofilins could not yet be determined, as filaments could always be observed in TEM regardless of concentration. This presents the problematic potential for runaway polymerisation. It was previously proposed that N-terminal processing of BacM could be a mechanism of control. However, the full-length form of BacM has been shown to form filaments *in vitro*. Other cytoskeleton systems employ nucleation or recruitment factors that can temporally and spatially control polymerisation, for instance, Arp2/3 complex for actin, or PomZ for FtsZ in *M. xanthus*. It is likely that such a system would exist for bactofilins, especially when considering the wide variety of structures BacM can form in different locations of the cell.

The failed septation of BacM-overexpressing *E. coli* cells suggests that factors controlling degradation or severing of bactofilin filaments are specific to bactofilin containing organisms. Even with abnormal BacM structures, like the thick, cell-spanning filaments of BacM-ΔPP, *M. xanthus* was still able to sever the filaments and undergo cell division, pointing to a robust filament control system. In *C. crescentus,* crescentin forms a thick, continuous structure associated with the membrane at the inner curved-side of the cell, and cells are able to sever the structure at the site of division. The mechanism for this is not known. In eukaryotes, remodelling of intermediate filament involves the disassembly of filaments, promoted by phosphorylation[132]. Bactofilin and bacterial IF could utilise such a mechanism, although size shifts in SDS-PAGE in response to post-translation modifications have not been observed, apart from cleavage. Understanding the regulation and mechanism behind the deconstruction of these bacterial nucleotide-independent filaments would be highly interesting.

How BacM functions to maintain proper cell morphology is yet to be uncovered. The crookedness of *⊿bacM* cells can be described as lack of cylindrical uniformity. This phenomenon was seen in coarse-grained modelling of bacterial cell wall growth[133], when the authors input incorrect parameters on the coordination, progressivity and other properties of the peptidoglycan remodelling machinery. The deletion of RodZ in *E.coli* also resulted in loss of cylindrical uniformity, by affecting the curvature localisation, number, and length of MreB filaments[43]. This points to a possible change in peptidoglycan structure in *⊿bacM* cells. However, a recent analysis by our research group revealed no significant difference in global PG profiles between wild-type and the mutant. This on its own may not exclude the possibility of PG involvement, as the deletion of PG-interacting protein Csd5 from *H. pylori* causes straight cell morphology without significant changes in global PG content[134]. Indeed, this PG-interacting protein has been shown to interact with the bactofilin CcmA at the membrane, and BacA and BacB also interacts with the membrane bound PbpC, therefore BacM may also bind to a PG-interacting enzyme at the membrane. Evidence for this includes the observation that any BacM derivatives that fail to associate with the membrane cannot rescue the crooked cell morphology in the absence of native BacM. A very recent study showed that two conserved hydrophobic amino acids at the N-terminus allow membrane association of bactofilins[135]. These residues are lost when BacM undergoes N-terminal cleavage in *M. xanthus*, though the small amount of un-cleaved BacM could conceptually be able to tether a filament to the membrane if incorporated. Further investigations on this are warranted. The poly-proline tail is likely also to play an important role for the output pathway of BacM by interacting with downstream proteins, which also appeared to ensure the correct positioning of BacM, as seen in the localisation of mCherry-PP, and the mis-localisation of C-terminally tagged BacM. Our research group has identified a range of proteins that interact with the PP region of BacM, and investigations into these are currently taking place.

Whether the occasionally observed localisation of BacM at early cell division sites is of biological significance is unclear. The demograph from **Figure 2-11 A** showed no consistent localisation to the septum, but it does not rule out the possibility that BacM plays a role at division sites under specific circumstances that only occasionally occurs in cells. A possible role for BacM could be to control the rate of constriction at the division site. Cell size control is an important aspect of population homeostasis, and has been theorised to be controlled by a molecular clock, by reaching a size limit, and/or by constant amount of length extension before division[136]. It has recently been found that constriction rate can be regulated to influence daughter cell sizes in *E. coli* and *C. crescentus*[137]. The mechanism of regulation, or how cell measures cell size and growth parameters has not yet been identified in any bacterial organism. BacM filaments could be an agent for constriction control, as demonstrated in BacM expressing *E. coli*, where the polymer can arrest cell division even if the Z-ring has been assembled, until certain cellular parameters are satisfied. There is little evidence for this hypothesis, but is a tantalising one nonetheless. Perhaps extensive live observations of BacM behaviour using BacM-mNG-expressing cells may help reveal any possible role of BacM at division sites.

It should be noted that the wide variety of BacM distribution in individual cells and at a population level is unusual for bacterial cytoskeletons. For instance, MreB from *B. subtilis* forms rapidly moving short filaments in all cells[41]; FtsZ localises to the mid-cell in all cells undergoing division[17]; ParM forms cell spanning filaments towards opposite cell poles during plasmid segragation[24]. Even for most other bactofilins, their localisations have been specific and consistent between cells, like the stalk pole and polar patches of BacA and BacB. This suggests that BacM is required at different locations, perhaps as a scaffold for downstream proteins that perform different tasks. Additionally, polar rod-like structures may also function as a storage site for excessive BacM, as the overexpression of BacM saw an increase in their length and incident. Why the BacM content in cells varies hugely in a population is also unclear. The other cytoskeletal proteins mentioned so far have their levels regulated so that they are consistent between cells, or are changed during specific stages of the cell cycle. A transcriptome study of chemically-induced sporulation in *M. xanthus* found BacM expression was not regulated[138], and our preliminary results also showed constant levels of BacM during glycerol-induced sporulation. These obervations, together with occassionally observed septum localisation of BacM mentioned above, suggest that the factors regulating BacM expression is possibly down to the response of individual cells. The description of BacM so far has been mostly qualitative, and so finding a quantitative analysis method may help reveal the role BacM plays.

All in all, this study presents further efforts in the characterisation of BacM from *M. xanthus*, which was found to have high intra-structure stability, but could be motile within the cell. The C-terminus tail was found to be sensitive to modifications, causing altered filament morphology *in vitro*, and mis-localisation and loss-of-function *in vivo*. The distribution of BacM was heterogeneous, and highly variable within and between cells. Many open questions remain, including the output pathway of BacM, the functions of different structures seen, and how cells regulate the expression, polymerisation, degradation, and the dynamics of this member of the commonly found cytoskeleton family. The protease responsible for N-terminal cleavage is yet to be identified, and the purpose of this cleavage also need to be uncovered.

Chapter 3

Characterisation of MXAN0657, a chain-like filament

3.1 Background

A chain-like aggregate in was first described by Lünsdorf and Reichenbach[109]. The study reported the observation of proteinaceous filaments in *Myxococcus fulvus* with the appearance of periodically stacked globular ring-shaped heads (termed 'rings') linked by pairs of elongated mass, (termed 'arms') (**Figure** 3-1 **A**). They also reported that these filaments were capable of bundling and were of variable length. Due to their observation that chains appear to be able to undergo conformational change whereby the relative orientation of globular heads and arms changes (**Figure 3-1 B**), they hypothesised that this 'contraction'-like motion could be responsible for the elusive gliding motility. In a follow-up study, Freese *et al*[110] performed freeze fracture experiments where they observed patterns in the periplasmic space that may correlate with the appearance of the chain-like filaments. They then went on to hypothesise that these filaments are composed of six globular masses that forms the rings, and a pair of separate elongated elements running perpendicular through the rings. They also hypothesised that the filaments reside in the periplasm where they could exert forces by contraction to drive gliding motility (**Figure 3-1 C**). Limited by the technology of the time, they were not able to deduce more information, and the identity of the protein was not revealed.

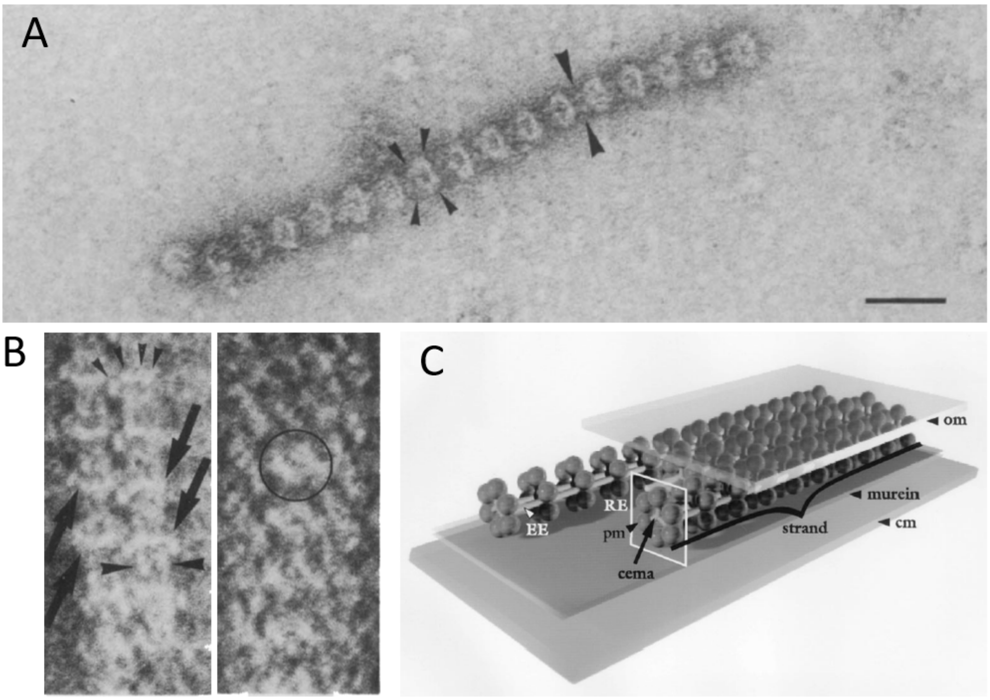

Figure 3-1 Chain-like strands described by Freese, Reichenbach, and Lünsdorf.
(A) A single chain-like strand. Large arrowheads points to arms linking the rings, shown by small arrows. Image adapted from (110). Scale bar 30 nm. (B) The different orientations of ring-shaped globular head. Left is a bundle of chain-like strands with the rings (big arrows) in the normal relative orientation to the arms (big arrowheads). Separate globular mass could be seen in the rings (small arrowheads). Right shows a different orientation adopted by a bundle of strains, where the rings are diagonal to the axis of the arms. Image adapted from (109). (C) Model presented by Freese and colleagues. The strands, formed of ring elements (RE) are linked by a pair of elongated elements (EE), and are inserted longitudinally in the periplasm. Not drawn to scale. CM, cytoplasmic membrane; OM, outer membrane; cema, central mass; pm, peripheral mass. Image adapted from (110).

These filaments were re-discovered by the Hoiczyk lab, and with improved technologies and the availability of the *Myxococcus xanthus* genome[139], they were able to identify the gene responsible for the filaments. This was carried out by performing mass spectrometry (MS) on prominent protein bands from a SDS-PAGE analysis of natively enriched filaments from *M. xanthus*. The product of gene *mxan0657* was one of the candidates identified. By creating deletion mutants of candidate genes from the MS result, it was determined that the protein product of *mxan0657*, MXAN0657, solely formed the chain-like filaments. MXAN0657 is a protein of approximately 72 kDa in size. The predicted architecture of the primary sequence is composed of a central *d*omain of *u*nknown *f*unction (DUF) 4139 that spans around three hundred amino acids, and two closely positioned C-terminal coiled-coil domains spanning around one hundred amino acids (**Figure 3-2 A**). Judging from the size of individual filament units (a term used in this study to describe the globular head with a pair of associated ar), it is apparent that MXAN0657 must oligomerise into individual filament units before polymerising into filaments, which in turn laterally associate with each other to form bundles (**Figure 3-2 B**). Each filament unit is around 17 nm in height and is 18 nm width at the largest point (**Figure 3-2 C**). Height and length are defined as the dimensions parallel to the direction of polymerisation, and width is the defined as the perpendicular dimension. The globular head is around 9 nm in height, and the arms are 8 nm in length (**Figure 3-2 C**). It is predicted that the coiled-coil domain forms the structure of the arms that extends between globular domains, as coiled-coiled domains often form elongated structures. Interestingly, the Hoiczyk lab found that native filamentous structures could only be obtained from cells grown on solid surfaces, and none could be seen from liquid-grown cultures. This was not reported in the previous studies.

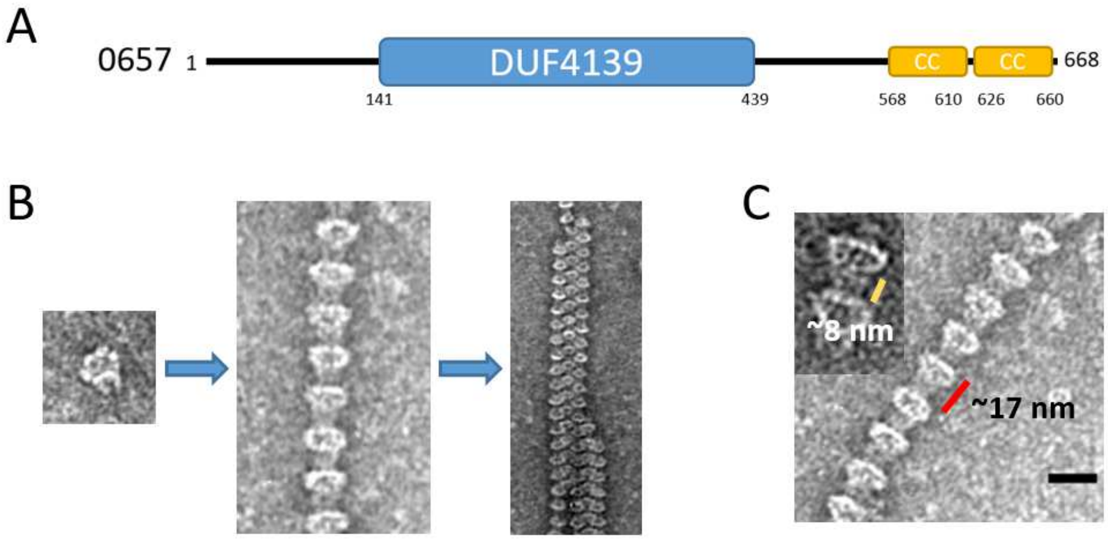

Figure 3-2 Chain-like strands are made by MXAN0657.
(A) The predicted architecture of MXAN0657. Blue boxes represent predicted DUF4139 domains. Yellow boxes represent coiled-coil domains. (B) A single filament unit is the oligomerised form of MXAN0657, which can polymerise to form single filaments, which in turn can bundle laterally. (C) Dimensions of MXAN0657 structures. Red line denotes the length of a single filament unit. Yellow line denotes length of arm.

Addressing the observations made by the authors above, the deletion of *mxan0657* had no effect on cellular motility (not published), which contradicts the functional conclusions made in the initial studies of the structure. This interpretation is further supported, as discussed in (**Section 1.2**), by the current understanding of the cellular motor for A-motility. This motor is composed of roughly a dozen different proteins and MXAN0657 is not part of this complex structure. Moreover, the conformational changes previously reported appear to be artefacts of negative staining and may not represent different conformations of the protein filaments. This is especially apparent when considering that the ‘contraction’ conformation is only visible when heavy bundling and aggregation occurs, which greatly affects contrast and how the stain is deposited onto the surfaces of filaments.

Based on the limited understanding of the structure and function of these rather enigmatic and unique looking filaments, a careful characterisation was done with the goal to establish a high-resolution structure of this novel bacterial cytoskeleton protein. Additionally, studies of mutant strains were performed to elucidate the possible function of this cytoskeleton element in *M. xanthus*.

3.2 Materials and Methods

3.2.1 Bacterial strains and culture conditions

Growth conditions for bacteria used in this chapter are identical to that described in **Section 2.2.1**. List of strains used in this chapter are listed in **Table 3-1.**

Name	Alias	Parent strain	[Plasmid integrated]/Description	Source
M. xanthus				
DK1622	Wild-type (WT)			112
DMZ30	*Δmxan0657*			David Zuckerman
EH747	WT pMR3679 MXAN_0657-Tc	DK1622	[pJS036] Inserted into the segment between positions 8498672 and 8500048. Expresses MXAN0657-Tc under control of vanillate-inducible promoter.	This study
EH748	*Δmxan0657* pMR3679 MXAN_0657-T	DMZ30	As above.	This study
EH749	WT pMR3679 Tc-MXAN_0657	DK1622	[pJS033] Inserted into the segment between positions 8498672 and 8500048. Expresses Tc-MXAN0657 under control of vanillate-inducible promoter.	This study
EH750	*Δmxan_0657* Tc-pMR3679 MXAN_06	DMZ30	As above.	This study
EH753	WT pMR3679 MXAN_0657	DK1622	[pJS031] Inserted into the segment between positions 8498672 and 8500048. Expresses MXAN0657 under control of vanillate-inducible promoter.	This study
EH754	*Δmxan0657* pMR3679 MXAN_0657	DMZ30	As above.	This study
EH755	WT pMR3679 MXAN_0657-Tc aa611	DK1622	[pJS035] Inserted into the segment between positions 8498672 and 8500048. Expresses MXAN0657-Tc aa611 under control of vanillate-inducible promoter.	This study
EH756	*Δmxan0657* pMR3679 MXAN_0657-Tc aa611	DMZ30	As above.	This study
EH757	WT MXAN0657-His aa244	DK1622	[pDMZ72] Complementation at the chromosomal *attB* site. Expresses MXAN0657-His aa244 under the *pilA* promoter.	This study
EH758	*Δmxan0657* MXAN0657-His aa244	DMZ30	As above.	This study
EH759	WT pMR3679 MXAN_0657-Tc aa244	DK1622	[pJS034] Inserted into the segment between positions 8498672 and 8500048. Expresses MXAN0657-Tc aa244 under control of vanillate-inducible promoter.	This study
EH760	*Δmxan_0657* pMR3679 MXAN_0657-Tc aa244	DMZ30	As above.	This study
E. coli				
Rosetta(DE3)pLysS			For heterogeneous protein expression.	Novagen
BL21(DE3)			For heterogeneous protein expression.	Invitrogen
DH5α			For molecular cloning purposes.	ThermoFisher
Rosetta-His-MXAN06957		Rosetta	[pJS032] For expressing N-terminal his-tagged MXAN0657.	This study
Rosetta-MXAN0657 His-construct1		Rosetta	[pJ0S42] For expressing his-tagged MXAN0657 fragments construct 1	This study
Rosetta-MXAN0657 His-construct2		Rosetta	[pJ0S41] For expressing his-tagged MXAN0657 fragments construct 2	This study

Table 3-1 List of strains used in this study.

Name	Sequence (5' to 3')
MXAN_0657_NdeI_F_v3	TCATAGCATATGACCACGAACCTGCGCATTCG
MXAN_0657_EcoRI_R_v3	GCATGAGAATTCTTACAGGTCCGCCGTGTAGCTGAG
MXAN_0657_NdeI_F_SOS_TC_v3	AGTTCTCATATGTGTTGCCCGGGCTGTTGCGGTACCACGAACCTGCGCATTCGTCG
MXAN_0657_611TC_F	ACCGCAACAACCCGGGCAACAACCCTTCAGCGACTCGATGTTGGAGCG
MXAN_0657_611TC_R	GGTTGTTGCCCGGGTTGTTGCGGTAGCGGGGCATCGCAACGCGAGCTG
MXAN_0657_244TC_F	ACCGCAACAACCCGGGCAACAACCGTCCTCGTCACCGGTGTTGTCCAC
MXAN_0657_244TC_R	GGTTGTTGCCCGGGTTGTTGCGGTTGGGTGGACGTGAAGCTGTCGCTC
MXAN_0657_EcoRI_R_EOS_TC_V3	GAATTCTTAGCAACAGCCCGGGCAACAACCCAGGTCCGCCGTGTAGCTGAGCGCCTGGATG
0657_His-339_End_F	TTGACACATATGCACCATCATCATCATCACGGTGGTGGTAGTACGACGCTCACGAAGGAGGTGG
0657_1-339-His_R	ATCATAGAATTCTTAGTGGTGATGATGGTGATGACTACCACCACCCACCGCGGCGCTCGTCTCCATG
MXAN_0657_F_XbaI	ACGTATTCTAGAAATAATTTTGTTTAACTTTAAGAAGGAGATATACCATGACCACGAACCTGCGCATTCG
MXAN_0657_R_XhoI	GATACACTCGAGTTACAGGTCCGCCGTGTAGCTG
MXAN_0657_R_339_EcoRI	ATCATAGAATTCTTACACCGCGGCGCTCGTCTCCATG
MXAN_0657_F_339_NdeI	TTGACACATATGACGACGCTCACGAAGGAGGTGG

Table 3-2 List of primers used in this study.

Name	Alias	Parent	Description	Primers used	Source
pDMZ72	PpilA - MXAN0657-His aa	pSWU30	*PpilA - MXAN0657* with 6xhis at aa224.		David Zuckerman; 140
pMR3679			*M. xanthus* 1.38-kb-PR3-4::*vanR-Pvan-* MSC_B, KanR.		113
pET28b			For expression of proteins in *E. coli.* T7 promoter and *lac* operator.		Novagen
pET DUET-1			For expression of proteins in *E. coli*. Has two MCS. T7 promoter and *lac* operator.		Novagen
pJS031	pMR3679 MXAN0657	pMR3679	*Pvan-maxn0657.*	MXAN_0657_NdeI_F_v3; MXAN_0657_EcoRI_R_v3	This study
pJS032	pET28b His-MXAN0657	pET28b	*Pt7/lac-maxn0657* with N-terminal His-tag.	MXAN_0657_NdeI_F_v3; MXAN_0657_EcoRI_R_v3	This study
pJS033	pMR3679 Tc-MXAN0657	pMR3679	*Pvan-maxn0657* with N-terminal tetracysteine tag.	MXAN_0657_NdeI_F_SOS_TC_v3; MXAN_0657_EcoRI_R_v3	This study
pJS034	pMR3679 MXAN0657-Tc aa244	pMR3679	Pvan-maxn0657 with tetracysteine tag after Asp 244, flanked by glycine on both sides.	MXAN_0657_NdeI_F_v3; MXAN_0657_EcoRI_R_v3; MXAN_0657_244TC_F; MXAN_0657_244TC_R	This study
pJS035	pMR3679 MXAN0657-Tc aa611	pMR3679	*Pvan-maxn0657* with tetracysteine tag after Lys 611, flanked by glycine on both sides.	MXAN_0657_NdeI_F_v3; MXAN_0657_EcoRI_R_v3; MXAN_0657_611TC_F; MXAN_0657_611TC_R	This study
pJS036	pMR3679 MXAN0657-Tc	pMR3679	*Pvan-maxn0657* with C-terminal tetracysteine tag.	MXAN_0657_NdeI_F_v3; MXAN_0657_EcoRI_R_EOS_TC_V3	This study
pJS041	pET Duet MXAN 0657 His-339-end	pET DUET-1	*Pt7/lac MXAN0657* in two fragments. First has aa1 to aa338. Second has His-tag-339 to aa668.	MXAN_0657_F_XbaI; MXAN_0657_R_339_EcoRI; 0657_His-339_End_F; MXAN_0657_R_XhoI	This study
pJS042	pET Duet MXAN 0657 1-339-His	pET DUET-1	Pt7/lac MXAN0657 in two fragments. First has aa1 to aa338-His-tag. Second has aa339 to aa668.	MXAN_0657_F_XbaI; 0657_1-339-His_R; MXAN_0657_F_339_NdeI; MXAN_0657_R_XhoI;	This study

Table 3-3 List of plasmids used in this study.

3.2.2 PCR and plasmid construction

Molecular cloning methods used in this chapter are identical to those described in **Section 2.2.2**. List of primers and plasmids are listed in **Table 3-2** and **Table 3-3**, respectively.

3.2.3 Native isolation of MXAN0657

The strain EH753 was used. Liquid cultures were be induced with 250 mM vanillate until reaching an OD_{600} of 0.8 -1.0, and were centrifuged at 5k x *g* for 10 minutes for harvesting. Cells were concentrated approximately 20x by resuspending in CTT with vanillate, and were spread evenly on CTT agar supplemented with vanillate and antibiotics in an industrial aluminium baking sheet (18"x13"x1", Polar Ware, Kiel). Cells were grown at 32°C for 30 – 40 hours and harvested into a solution of 100 mM NaCl and 10 mM Tris-HCl at pH 8 at 1:6 weight-to-volume ratio (wt/vol). Cells were supplemented with cOmplete EDTA-fee protease inhibitor (Merck) and ultrasonicated on ice with a Soniprep 150 Plus ultrasonicator (MSE), using the 19 mm solid titanium probe (MSE) at amplitude setting of around 13 μm. Cell breakage was confirmed by conventional phase contrast light microscopy. Cell debris was pelleted by step-wise centrifugation up to 48k x *g* at 4°C for 30 minutes or until clarification. The supernatant was supplemented with 2% polyethylene glycol (PEG) with an average molecular weight of 8,000, and 50 mM $MgCl_2$. This suspension was left at 4°C overnight, and centrifuged at 48k x *g* for 15 minutes. The pellet was resuspended with NaCl Tris buffer at 1:10 wt/vol, and supplemented with 0.25% cholic acid and 0.75% β-DDM. Solution was left on ice for 30 minutes before centrifugation at 48 k x *g* for 15 minutes. The pellet was resuspended in NaCl Tris buffer and centrifuge stepwise up to 16k x *g*. The supernatant was collected and the pellet was resuspended in ddH_2O and centrifuged again. The supernatants were pooled and added with 50 mM imidazole at pH 6.5 and left on ice for 30 minutes. This was centrifuged at 16k x *g* and the pellet was resuspended in ddH_2O. Quality of isolation was inspected under TEM and with SDS-PAGE.

3.2.4 Edman degradation analysis

Natively isolated MXAN0657 were analysed with SDS-PAGE as described in **Section 2.2.12**. Before Coomassie staining, the gel was blotted onto PVDF membrane (Millipore) described in **Section 2.2.13**. After blotting, the membrane was stained with colloidal Coomassie blue staining kit (Novex/Invitrogen) to visualise protein bands. Appropriate bands were set to TopLab, Germany, for Edman degradation analysis.

3.2.5 Isolation of His-tagged MXAN0657

Rosetta-MXAN0657-His-construct2 cells were induced as described in **Section 2.2.4**, and 100 mM NaCl and 10 mM Tris-HCl pH 8 was used instead of PBS. Cell lysate was clarified by centrifugation at 48 k x g for 15 minutes at 4°C. Supernatant was supplemented with imidazole at 10 mM pH 8, and loaded on a gravity-flow column of buffer calibrated HIS-Select HF Nickel Affinity Gel (Sigma-Aldrich). The column was then washed with NaCl Tris buffer with 20 mM imidazole thoroughly, before eluting in NaCl Tris buffer with 500 mM of imidazole. Eluate was collected and inspected with SDS-PAGE and TEM.

3.2.6 Antibody purification

Anti-serum from a rabbit inoculated with isolated native MXAN0657 was provided by Eurogentec. To perform affinity depletion of serum, 15 g of *Δmxan0657* cell pellet from a mid-log liquid culture was resuspended in 20 ml of 1 mM KH_2PO_4/K_2HPO_4, 8 mM $MgSO_4$, and 20 mM HEPES at pH 8, and added with formaldehyde to a final concentration of 4 %. This suspension was gently agitated overnight at 4°C. After fixation, cells were pelleted and washed twice with PBS, and permeabilised with PBS and 0.2% Triton X-100 (PBST) for 15 minutes at RT. Cells were then washed with PBST and blocked with PBST with 2% BSA for 20 minutes at RT and then pelleted. Anti-serum was diluted at 1:30 in PBST with 2% BSA to 17 ml total volume and added to the cell pellet and agitated for 1 hour at RT.

The suspension was clarified by centrifugation at 26k x g for 15 minutes, twice. The supernatant contains affinity depleted anti-serum.

To perform affinity purification of the affinity depleted anti-serum, approximately 10 mg of purified his-tagged MXAN0657 at 2 mg/ml was cross-linked to cyanogen bromide (CNBr)-activated sepharose beads 4B (Sigma), as per manufacturer's instructions. To do this, 0.3 grams of sepharose beads were soaked and washed thoroughly in ice-cold 1 mM HCl at pH 3, resulting in around 1 ml of bead matrix. Beads were then quickly washed in ice-cold ddH_2O, then in 20 mM HEPES at pH 8.3, before adding the protein in 20 mM HEPES at pH 8. Cross-linking was allowed to take place overnight with gentle agitation at 4°C. Afterwards, beads were washed with HEPES buffer and mixed with 1 M ethanolamine for 2 hours to block unreacted groups, washed again, and transferred into a PolyPrep gravity flow chromatography (Bio-Rad). Three millilitre of affinity depleted anti-serum was diluted 10x into Tris-HCl at pH 7.5. The matrix was calibrated with Tris buffer, before anti-serum was flowed through it. Afterwards, the matrix was washed with 500 mM NaCl in Tris buffer, before acidic elution of bound antibodies with 10 bed volume of 100 mM glycine at pH 2.5. The elute was collected in 2.5 bed volume of 1 M Tris-HCl at pH 8.8. The matrix was washed again with 10 mM Tris-HCl at pH 8.8, and basic elution was performed with 10 bed volume of 100 mM triethylamine at pH 11.5. Elution was collected in 2.5 bed volume of 1 M Tris-HCl at pH 7.5. Both eluates were concentrated to around 0.5 ml with Spectra/Gel Absorbent (Spectrum Laboratories). Eluates were tested for specificity with Western blotting of DK1622 cells and *Δmxan0657* cells. It was found that the acidic eluate was specific.

3.2.7 Immunofluorescence microscopy

Method for immunofluorescence microscopy of MXAN0657 was mostly identical to the method described in **Section 2.2.7**. However, the microscope system used was the LSM 800 with the Airyscan detector (Zeiss) Plan-Apochromat 63x Oil DIC II (NA 1.4) objective controlled with ZEN Blue microscope software (Zeiss). Fluorescence imaging was done with a 488 nm laser. For transmitted light cell detection, the T-PMT detector and the 405 nm laser was used. Image analysis was performed with ZEN Blue software.

3.2.8 Development assay of *M. xanthus* cells

M. xanthus cells were grown in CTT until reaching an OD_{600} of 1.0, and were washed thoroughly in TPM starvation medium and resuspended at 5 x 10^9 cells per ml and were spotted onto TPM hard agar at 20 µl for each spot and allowed to air-dry. Development was observed over seven days and imaged using Olympus E-PL1 camera with a M.Zuiko Digital 14-42 mm lens, and a Zeiss Imager D1 upright microscope with a 2.5x EC PLAN NEOFLUAR (NA 0.085) objective. Fruiting bodies were collected using a spatula and deposited into 500 µl of ddH_2O. These were heated to 50°C on a heat block for 30 minutes, and sonicated with a Soniprep 150 Plus ultrasonicator (MSE), with the 3 mm micro exponential probe at amplitude of 4 µm, for 6 x 5 second pulses. Phase-bright spores were counted using a haemocytometer. Concentrations of spores were equalised, and were serial diluted at 1:10 six times, and 10 µl spots of each dilution were air-dried onto CTT hard agar. Growth was observed over seven days and were imaged. Graphs were made with Prism 8 software (GraphPad).

3.2.9 MXAN0657 interaction assay

First natively isolated MXAN0657 was cross-linked to CNBr-activated Sepharose beads with a method similar to that described in **Section 3.2.6**. Approximately 1.8 mg of protein was used. As negative controls, blank HEPES buffer, and *Δmxan0657* cells lysate that had been treated as described above for native MXAN0657 isolation were also 'cross-linked'. To prepare cell lysate, DK1622 cells were grown to OD_{600} of 0.8, and spread on agar sheets, grown, harvested and lysed as described in **Section 3.2.3**, except the lysis buffer used was 200 mM NaCl, 8 mM $MgSO_4$, 1 mM KH_2PO_4/K_2HPO_4, and 20 mM Tris at pH 8 . The lysate was centrifuged at 50k x g for 30 minutes at 4°C twice. Four millilitre of the supernatant was added to the columns of sepharose matrix at 4°C and allowed to flow by gravity. Afterwards, the columns were washed with lysis buffer three times at 10 column volume each, until protein was not detected from the eluate. To analyse the bound proteins, a small metal spatula was used to scrape around 200 µl of beads from the column, and deposited in 100 µl of SDS buffer with 8 M urea and 10 mM DDT.

This was boiled for 10 minutes in a water-bath, and were centrifuged at 16k x *g* to sediment the beads. Fifty microliters of the supernatant was used for SDS-PAGE analysis. The bands of interest were identified, and the gel was set for mass-spectrometry analysis at the biOMICS Facility at the University of Sheffield.

3.2.10 Bioinformatic analysis

Homologs of proteins were identified using the protein Basic Local Alignment Search Tool (BLASTp) hosted on the Nation Center for Biotechnology Information (NCBI) website[141]. Distant homologs of MXAN0657 were searched for using Position-Specific Iterated BLAST hosted on the European Molecular Biology Laboratory – European Bioinformatics Institute (EMBL-EBI) website[142]. For genome comparison, annotated genomes sequences were obtained from NCBI, uploaded to the public CPT (Centre for Phage Technology)-Galaxy platform hosted by the Texas A&M University, and Promer genome comparison files were generated with the MUMmer tool suite[143]. Promer files were converted to Artemis Comparison Tool (ACT)-compatible format using MUMmer2ACT. For visualisation and analysis of genome comparison, ACT in Artemis was used[144]. For coiled-coil domain prediction, LOGICOIL was used[145]. Operon predictions were obtained form operonDB[146]

3.3 Results

3.3.1 Bioinformatic analysis of MXAN0657

MXAN0657 is annotated as a hypothetical protein in the NCBI protein database. In order to elucidate the possible function of MXAN0657, BLASTp was used to search for homologs that had been characterised. Remarkably, homologs were found in many phyla of bacteria, and surprisingly, some were even detected in eukaryotes (**Table 3-4**). Some species also appear to harbour multiple paralogs. Unfortunately, no annotated function was given for any of the discovered proteins. Although ubiquitous among bacteria, not all members of myxobacteria contain a homolog of MXAN0657. Investigating differences between members of myxobacteria with a homolog and those without may reveal a possible role of MXAN0657

Presence of basic characteristics of the myxobacteria were compared in **Table 3-5**, including the ability to sporulate, form fruiting bodies, glide on surfaces, undergo aerobic respiration, and cell morphology. At first glance, since the only microaerobic myxobacterium *Anaeromyxobacter dehalogenans* do not possess a homolog[147], one may postulate that MXAN0657 may be required only for obligate aerobic organsims. However, other anaerobic organisms, for instance *Syntrophobacter fumaroxidans* and *Azospirillum brasilense* also possess a homolog, making this scenario unlikely.

To investigate further, PSI-BLAST was utilised to search for clues on the function of MXAN0657. PSI_BLAST focuses on the search for regions of similarity by generating position-specific scoring matrices (PSSM) of the query protein. The PSSM is refined after every iteration of search allowing the tool to detect even distantly related proteins. Unfortunately, all five hundred proteins found were annotated as uncharacterised proteins, providing no further information on its possible role. Interestingly, LOGICOIL[145] predicted that the coiled-coil region of around a hundred amino acid long at the C-terminus is conserved in all hits found, which suggests that a coiled-coil structure is important to the functioning of MXAN0657 and its homologs.

Kingdom	Phylum	Class	Species	Orthologs	Genbank	Length	Coverage	E value	Identity	Smiliarity
Bacteria	Proteobacteria	Alphaproteobacteria	*Azospirillum brasilense*	1	CCD03386.1	705	98%	4e-62	31%	48%
		Betaproteobacteria	*Betaproteobacteria bacterium* RIFCSPLOWO2_02_FULL_65_24	1	OGA29437	638	98%	3e-126	35%	66%
		Deltaproteobacteria	*Myxococcus xanthus* DK 1622	1	SDW56963	668	100%	0.0	100%	100%
			Syntrophobacter fumaroxidans		ABK19242	701	94%	3e-95	32%	52%
			Desulfomonile tiedjei DSM 6799		AFM28063	703	97%	1e-100	31%	52%
			Deltaproteobacteria bacterium GWA2_42_85		OGP06306	697	92%	2e-93	32%	54%
		Gammaproteobacteria	*Beggiatoa* sp. 4572_84	1	OQY47989	665	99%	0.0	41%	64%
	(PVC Group) Planctomycetes	Planctomycetia	*Gemmata* sp. SH-PL17	3	AMV23022	637	99%	0.0	49%	65%
				3	AMV27922	735	97%	5e-104	31%	49%
				3	AMV29560	749	97%	1e-100	30%	49%
			Zavarzinella formosa	4	WP_020474851	729	98%	7e-98	29%	51%
				4	WP_029629943	736	98%	2e-96	30%	51%
				4	WP_020469905	731	98%	4e-93	29%	50%
				4	WP_020471217	736	98%	2e-95	29%	51%
	(PVC Group) Lentisphaerae		*Lentisphaerae bacterium* GWF2_57_35	1	OGV46314	665	98%	1e-121	34%	56%
	Armatimonadetes		*Armatimonadetes* bacterium GXS	1	CUU35718	659	98%	1e-119	35%	54%
	Acidobacteria	Solibacteres	*Candidatus Solibacter usitatus*	1	ABJ81737	675	98%	2e-109	32%	53%
			Bryobacter aggregatus	1	WP_080508053	737	97%	6e-105	32%	53%
		Acidobacteriia	*Terriglobus roseus*	1	AFL86539	740	99%	3e-95	31%	49%
	Candidatus Tectomicrobia		*Candidatus Entotheonella serta*	1	PON18212	698	97%	3e-110	34%	53%
	Nitrospirae	Nitrospira	*Nitrospira* sp. CG24D	1	PLY27609	697	98%	1e-108	32%	53%
	Spirochaetes	Spirochaetia	*Leptonema illini*		EHQ07229	655	98%	2e-89	31%	51%
	Cyanobacteria	Oscillatoriophycideae	*Leptolyngbya valderiana* BDU 20041	1	OAB58612	680	98%	3e-87	30%	52%
			Geitlerinema sp. PCC 7407	1	AFY64862	683	96%	3e-91	32%	50%
	Chloroflexi	Chloroflexia	*Roseiflexus castenholzii* DSM 13941	1	ABU59900	658	97%	1e-87	32%	52%
			Chloroflexus islandicus		OAN45891	640	98%	1e-87	33%	51%
	Rhodothermaeota	Rhodothermia	*Rubricoccus marinus*	1	OZC03113	681	98%	4e-88	32%	51%
	Fusobacteria	Fusobacteriia	*Fusobacterium ulcerans* ATCC 49185	1	WP_005977373	671	98%	1e-80	27%	50%
	(FCB group) Bacteroidetes		*Salinibacter ruber* M8	1	CBH25134	676	98%	1e-86	32%	49%
Archaea - Asgard Group	Candidatus Lokiarchaeota		*Lokiarchaeum* sp. GC14_75	2	KKK41096	688	98%	9e-134	34%	55%
				2	KKK43027	686	98%	7e-130	34%	55%
Eukaryota	Amoebozoa	Discosea	*Acanthamoeba castellanii* str. Neff	2	ELR12921	695	99%	5e-118	34%	54%
				2	ELR12919	819	98%	1e-90	31%	47%

Table 3-4 MXAN0657 homologs are widespread among bacteria.
A selection of species with homologs of MXAN0657 identified from the non-redundant protein sequences database using BLASTp, showing their similarity with MXAN0657. Note that some species have multiple paralogs. Surprisingly, homologs were found in Eukaryotes and Archaea. Entry for *Myxococcus xanthus* is presented in red font. Taxonomy information was gathered from the NCBI Taxonomy database and taxonomical categories are coloured for ease of identification.

SubOrder	Family	Genus	Species	Present	Sporulating	Fruiting body	Gliding	Rods	Aerobic	Genbank	Length	Coverage	E-value	Identity	Similarity
Cystobacterineae	Myxococcaceae	*Corallococcus*	*Corallococcus coralloides* DSM 2259	Y	Y	Y	Y	Y	Y	AFE03569	674	100%	0.0	72%	84%
		Myxococcus	*Myxococcus fulvus* HW-1	Y	Y	Y	Y	Y	Y	AEI63025	671	100%	0.1	92%	94%
			Myxococcus hansupus	Y	Y	Y	Y	Y	Y	AKQ69437	668	100%	0.2	90%	93%
			Myxococcus macrosporus DSM-14697	Y	Y	Y	Y	Y	Y	ATB45085	671	100%	0.3	93%	95%
			Myxococcus stipitatus DSM-14675	Y	Y	Y	Y	Y	Y	AGC42011	666	100%	0.4	78%	87%
			Myxococcus virescens	Y	Y	Y	Y	Y	Y	SDD46301	681	100%	0.5	99%	99%
			Myxococcus xanthus DK 1622	Y	Y	Y	Y	Y	Y	SDW56963	668	100%	0.0	100%	100%
	Anaeromyxobacteraceae	*Anaeromyxobacter*	*Anaeromyxobacter dehalogenans*	N	Y	N	Y	Y	N						
	Archangiaceae	*Archangium*	*Archangium gephyra*	N	Y	Y	Y	Y	Y						
		Cystobacter	*Cystobacter ferrugineus*	Y	Y	Y	Y	Y	Y	OJH36176	659	99%	0.0	67%	82%
			Cystobacter fuscus DSM 2262	Y	Y	Y	Y	Y	Y	EPX60099	661	99%	0.0	66%	82%
		Hyalangium	*Hyalangium minutum*	Y	Y	Y	Y	Y	Y	KFE71052	662	99%	0.0	68%	80%
		Melittangium	*Melittangium boletus* DSM 14713	Y	Y	Y	Y	Y	Y	ATB30669	666	100%	0.0	69%	82%
		Stigmatella	*Stigmatella aurantiaca* DW4/3-1	Y	Y	Y	Y	Y	Y	ADO75377	667	100%	0.0	71%	83%
			Stigmatella erecta	Y	Y	Y	Y	Y	Y	SEU34043	667	100%	0.0	72%	82%
		Vitiosangium	*Vitiosangium* sp. GDMCC 1.1324	Y	Y	Y	Y	Y	Y	PTL79960	677	100%	0.0	73%	84%
	Vulgatibacteraceae	*Vulgatibacter*	*Vulgatibacter incomptus*	N	?	N	N*	Y	Y						
Nannocystineae	Kofleriaceae	*Haliangium*	*Haliangium ochraceum*	N	Y	Y	Y	Y	Y						
	Nannocystaceae	*Nannocystis*	*Nannocystis exedens*	N	Y	Y	Y	Y	Y						
		Plesiocystis	*Plesiocystis pacifica*	N	Y	Y	Y	Y	Y						
Sorangiineae	Labilitrichaceae	*Labilithrix*	*Labilithrix luteola*	N	?	N	Y	Y	Y						
	Polyangiaceae	*Chondromyces*	*Chondromyces apiculatus*	N	Y	Y	Y	Y	Y						
			Chondromyces crocatus	N	Y	Y	Y	Y	Y						
		Pajaroellobacter	*Pajaroellobacter abortibovis*	N	?	?	?	Y	?						
		Sorangium	*Sorangium cellulosum* So0157-2	Y	Y	Y	Y	Y	Y**	AGP37946.1	667	98%	1e-76	31%	49%
		Polyangiaceae	*Polyangiaceae* bacterium UTPRO1	N	Y	Y	Y	Y	Y						
	Sandaracinaceae	*Sandaracinus*	*Sandaracinus amylolyticus*	N	Y	Y	Y	Y	Y						
	Unclassified	*Minicystis*	*Minicystis rosea*	N	Y	Y	Y	Y	Y						
Unclassified		*Enhygromyxa*	*Enhygromyxa salina*	N	Y	Y	Y	Y	Y						

Table 3-5 MXAN0657 homologs are not found in all Myxobacteria.
This table features all fully sequenced and studied myxobacteria (species in the order of Myxococcales). MXAN0657 homologs were identified from the non-redundant protein sequences database using BLASTp, specifically searching within the Myxococcales order only. Information shown includes whether homologs to *mxan0657* are present; whether individual species shares characteristics with those typical for Myxobacteria; and similarity of homologs with MXAN0657 obtained with BLASTp. Entry for *Myxococcus xanthus* is presented in red font. Taxonomical categories are coloured for ease of identification. General information of species obtained from (148) and (149). Specific information was obtained from: *Anaeromyxobacter dehalogenans* (147); *Vulgatibacter incomptus* & *Labilithrix luteola* (150); *Haliangium ochraceum* (151); *Chondromyces* (152); *Pajaroellobacter abortibovis* (153); *Sorangium cellulosum* So0157-2 (154); *Polyangiaceae* bacterium UTPRO1 (155); *Sandaracinus amylolyticus* (156); *Minicystis rosea* (157); *Enhygromyxa salina* (158).

Genes that are functionally linked often reside adjacent to each other and/or are in the same operon. If the link is strong, this spatial relationship would be conserved among phylogenetically distant related species[159]. Therefore, by investigating genes surrounding MXAN0657 in *M. xanthus* and in other homolog-containing genomes, one may be able to find clues about the function of MXAN0657. OperonDB[146] predicted that MXAN0657 is a single gene operon. Artemis[144] was used to assist in identifying surrounding conserved genes. It became apparent that the gene neighbourhood of MXAN0657 is poorly conserved (**Table 3-6**). Even within the same genus, insertions were found up- and downstream of MXAN0657. This high gene neighbour variability suggests that MXAN0657 and its homologs are unlikely to function with their surrounding genes.

An interesting finding is that there are four other proteins in *M. xanthus* containing the DUF4139 domain, found by searching through the NCBI database (**Figure 3-3**). Each of these DUF4139-containing proteins has two adjacent coiled-coil domain, as predicted by LOGICOIL[145]. But unlike MXAN0657, these coiled-coil domains are towards the N-terminus of the protein, in front of the DUF4139 domain. Both MXAN0939 and MXAN0940 have been annotated as part of the Mucoidy Inhibitor MuiA family. The DUF4139 domain of MXAN0940 is truncated and covers only around 60 amino acids, and contains a predicted carboxypepD_reg domain. The other two proteins, MXAN3400 and MXAN3401, are annotated as hypothetical proteins, and it is interesting that these DUF4139 proteins exist as a gene-pair.

Delta-proteobacteria	Myxococcus xanthus DK1622		MXAN_0654	MXAN_0655	MXAN_0656	MXAN_0657	MXAN_0658	MXAN_0659	MXAN_0660
		Putative function	MarR family transcriptional regulator	Organic hydroperoxide resistance protein	Hypothetical Protein		Hypothethical Protein	Amidohydrolase	Hypothetical lipoprotein
	Myxococcus stipitatus DSM 14675		MYSTI_RS03270	MYSTI_RS41510	MYSTI_RS03280	**MYSTI_RS03285**	MYSTI_RS03290	MYSTI_RS03295	MYSTI_RS03300
		Putative function	Hypothetical protein	Hypothetical protein	Hypothetical protein		Amidohydrolase	Alpha/beta hydrolase Putative epoxide hydrolase	Hypothetical protein
		M.x. homolog	*No homolog*	*No homolog*	*No homolog*	MXAN_0657	MXAN_0659	MXAN_1644	MXAN_0662
	Stigmatella aurantiaca DW4/3-1		STAUR_RS37485	STAUR_RS37480	STAUR_RS37475	STAUR_RS37470	STAUR_RS37465	STAUR_RS37460	STAUR_RS37455
		Putative function	Esterase/endoglucanase, SGNH hydrolase-type	Organic hydroperoxide resistance protein	Hypothetical Protein		Serine hydrolase / beta lactamase	Hypothetical Protein	Hypothetical protein
		M.x. homolog	MXAN_2225	MXAN_0655	MXAN_0656	MXAN_0657	*No homolog*	*No homolog*	MXAN_2270
	Hyalangium minutum DSM 14724		DB31_RS03970	DB31_RS03975	DB31_RS03980	DB31_RS03985	DB31_RS03990	DB31_RS03995	DB31_RS04000
		Putative function	Hypothetical protein	Putative Lipoprotein	Hypothetical protein		Type IV fimbrial assembly, ATPase PilB	PEGA domain-containing protein	Hypothetical protein
		M.x. homolog		MXAN_0656		MXAN_0657	MXAN_7176	MXAN_7177	MXAN_6305
	Sorangium cellulosum So0157-2		SCE1572_RS28850	SCE1572_RS28855	SCE1572_RS28860	SCE1572_RS28865	SCE1572_RS28870	SCE1572_RS59425	SCE1572_RS55885
		Putative function	Hypothetical protein	Hypothetical protein	Peroxiredoxin		Hypothetical	Unknown - incomplete / pseudogene	SUMF1/EgtB/PvdO family nonheme iron enzyme
		M.x. homolog	*No homolog*	*No homolog*	MXAN_6536	MXAN_0657	*No homolog*	N/A	MXAN_2077
Plantomycetia	Fimbriiglobus ruber SP7		FRUB_RS14900	FRUB_RS14905	FRUB_RS14910	FRUB_RS14915	FRUB_RS14920	FRUB_RS14925	FRUB_RS14930
		Putative function	Hypothetical protein	Hypothetical protein	Hypothetical protein		Type I glutamate--ammonia ligase	Unknown - incomplete / pseudogene	Unknown - incomplete / pseudogene
		M.x. homolog	*No homolog*	*No homolog*	*No homolog*	MXAN_0657	MXAN_0912	N/A	N/A
Beta-proteobacteria	Beggiatoa sp. 4572_84		B6247_31940	B6247_31945	B6247_31950	B6247_25715	B6247_25720	B6247_25725	B6247_25730
		Putative function	Hypothetical protein	Hypothetical protein	Hypothetical protein		ATP-binding protein	Hypothetical protein	Unknown - incomplete / pseudogene
		M.x. homolog	MXAN_7127	*No homolog*	*No homolog*	MXAN_0657	MXAN_2750	MXAN_6702	N/A
Alpha-proteobacteria	Azospirillum brasilense sp245		AZOBR_RS30925	AZOBR_RS30930	AZOBR_RS30935	AZOBR_RS30940	AZOBR_RS30945	AZOBR_RS30950	AZOBR_RS30955
		Putative function	Two-component response transcriptional regulator	Hypothetical protein	Hypothetical protein		Putative NnrU protein	Hypothetical protein	PaaI family thioesterase
		M.x. homolog	MXAN_5313	*No homolog*	MXAN_5993	MXAN_0657	*No homolog*	*No homolog*	*No homolog*

Table 3-6 Neighbouring genes of *mxan0657* homologs in different organisms.
This figure lists the three genes upstream and downstream from *mxan0657* and its counterpart in different species. Putative functions of surrounding genes are listed for comparison, as with their homologs in *M. xanthus*. Green background denotes genes coded in the same direction as *mxan_0657* and homologs, whereas beige denotes genes coded in the opposite direction.

3.3.2 Divalent cations and pH changes induce polymerisation and aggregation of MXAN0657

In TEM preparations, the lengths of natively isolated MXAN0657 filaments varies widely, and bundling is sometimes observed. As little was known about the conditions governing filament elongation and bundling, natively isolated MXAN0657 was subjected to buffers at different pH values containing various additives.

As previously observed by Dr David Zuckerman, the addition of divalent salts i.e. $CaCl_2$ and $MgCl_2$ caused MXAN0657 filaments to bundle through lateral association of filaments and through elongation by polymerisation (**Figure 3-4**). The degree of elongation of individual protofilaments within the bundle was difficult to discern as it is unclear where each began and terminated. The addition of NaCl had no observable effects at the concentration tested, suggesting that Cl^- was not responsible for the bundling observed. Next, a range of anions were introduced as potassium salts, both organic and inorganic. No effects were observed at the concentration tested. Finally, divalent cation chelating agents EDTA and EGTA were added to assess whether the length of filaments would be affected, or whether total disassembly could occur when elongation and bundling agents are removed. Again, their addition did not have any observable effects at the concentration tested.

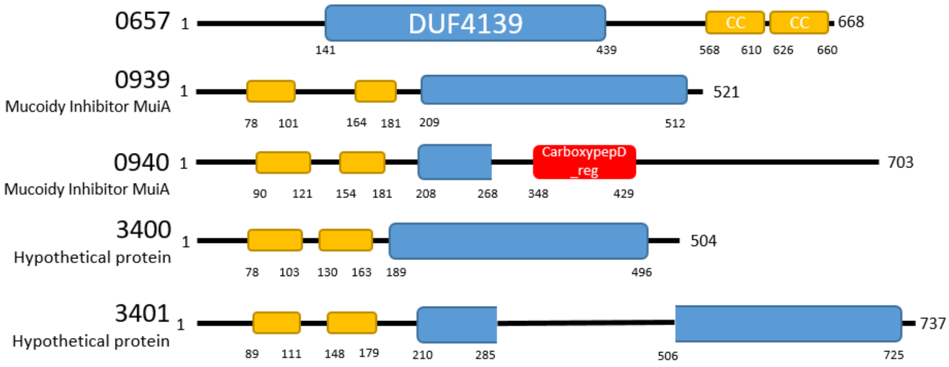

Figure 3-3 Domain composition of DUF4139 containing proteins in *M. xanthus.*
MXAN locus tag of proteins are listed. Blue boxes represent predicted DUF4139 domains. Yellow boxes represent coiled-coil domains. Red box represents a predicted carboxypepD_reg domain. Amino acid positions of start and end of domains are given. DUF4139 domain of mxan3401 has a ~220 aa long insertion near the centre. The DUF4139 domain in mxan0940 is truncated.

Many types of cytoskeletal filaments require nucleotides to polymerise, and this process is dependent on Mg^{2+} as a cofactor for nucleotide binding and hydrolysis[24]. Since Mg^{2+} causes MXAN0657 to bundle and elongate, nucleotides may also contribute to this. To test this, ATP was added at 10 mM with or without Mg^{2+}. In the absence of Mg^{2+}, ATP alone did not have any observable effects on MXAN0657. In the presence of Mg^{2+}, the degree of lateral bundling and elongation was comparable to Mg^{2+} alone.

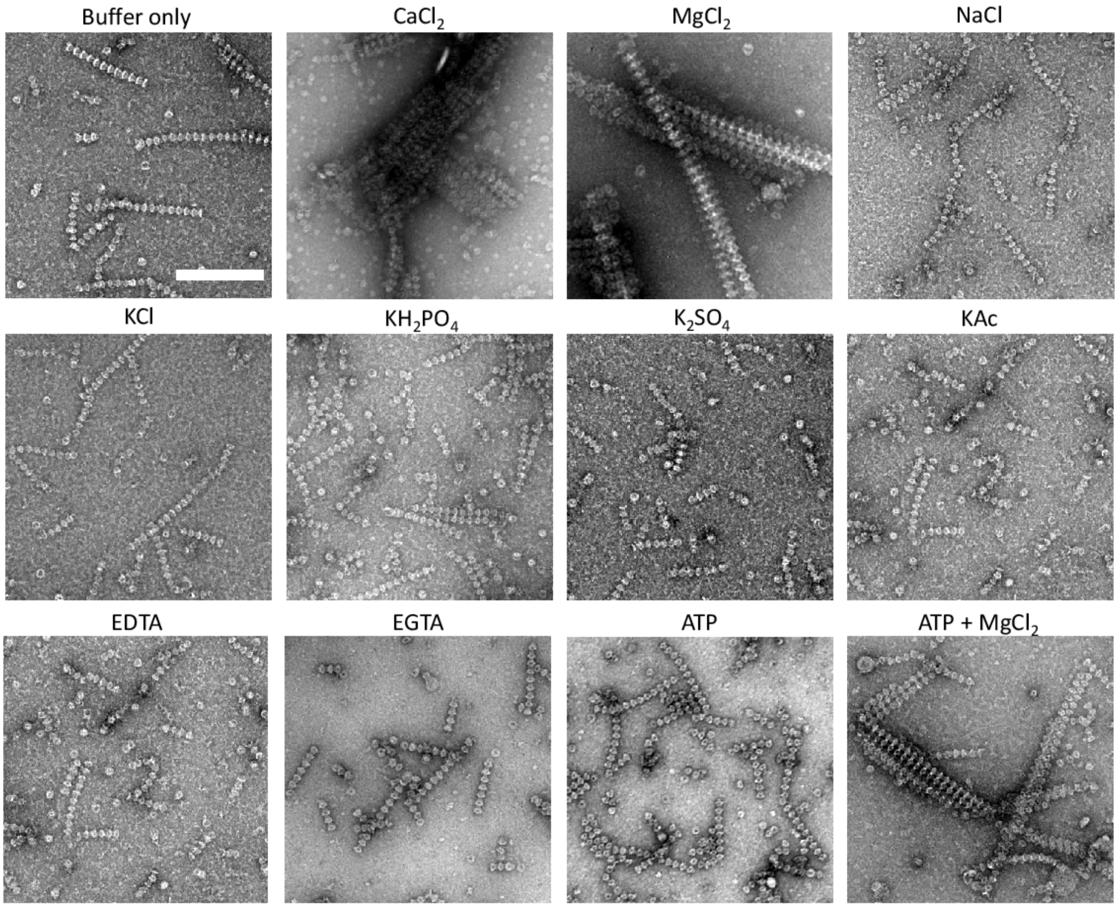

Figure 3-4 TEM micrographs of MXAN0657 responding to different additives.
MXAN0657 reacts strongly to the addition of divalent ions i.e. Ca^{2+} and Mg^{2+} by lateral association and elongation. Buffer used was Tris-HCl, at a concentration of 20 mM, pH 8. ATP was used at 10 mM with pH adjusted to 8. All other salts were used at 50 mM. Scale bar 200 = nm.

To test the effect of different pH values on MXAN0657, natively isolated filaments were dialysed in different buffers overnight and inspected with electron microscopy. Results showed that the pH has a dramatic effect on the structure of MXAN0657 filaments (**Figure 3-5**). At the low pH of 3.5 in glycine-HCl buffer, filaments were not visible at all, and only single filament units were seen. At mildly acidic conditions of pH 4.8 – 6.5 in citric acid and imidazole-HCl buffer respectively, strong bundling and elongation was observed. At pH 10.5 in NaH_2PO_4-Na_2HPO_4 buffer, no effects were seen when compared to Tris-HCl at pH 8. Finally, at a stronger basic pH of 11.5 in Na_2HPO_4-NaOH buffer, strong bundling and elongation was observed.

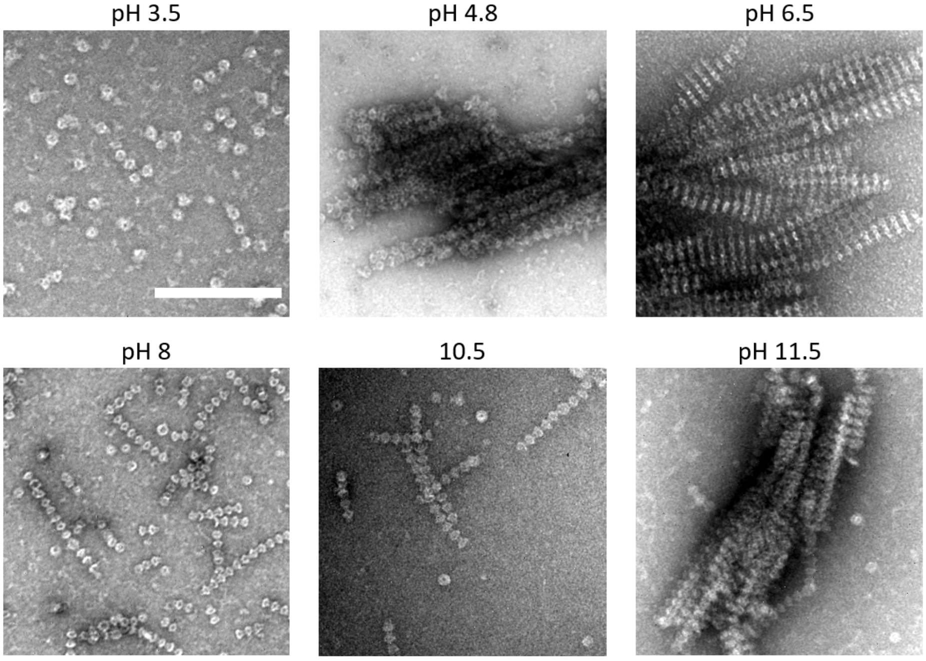

Figure 3-5 TEM micrographs of MXAN0657 responding to pH changes.
MXAN0657 structural morphology responds drastically to changing pH. At pH 3.5, MXAN0657 filaments fall part, along with some distortion and disassembly of ring structures. At mildly acidic and strongly basic pH, MXAN0657 exhibits lateral bundling and elongation. Buffers used, clockwise from top left, were glycine-HCl, citric acid buffer, imidazole-HCl, Na_2HPO_4-NaOH, $NaHPO_4$-Na_2HPO_4, and Tris-HCl. Scale bar = 200 nm.

3.3.3 MXAN0657 is sensitive to tag-attachments

The yield for natively isolated MXAN0657 filament was low. From 30 grams of cells collected from agar surfaces, only 3 mg ± 1 mg is obtained, even from using an overexpression *M. xanthus* strain. To improve the quantity and quality of MXAN0657 isolations and to further understand its intracellular behaviour and characteristics, a number of tags were introduced at various locations (**Figure 3-6 A&B**).

Previously, Dr. David Zuckerman had introduced FLAG 6xHis tags at various positions, including N- and C- terminus, and at two internal sites – amino acid positions 171 and 244. These internal positions were sites of proteolytic cleavage during purification, suggesting that these sites might be disordered and are/or surface accessible, and hence they were chosen for tag insertion.

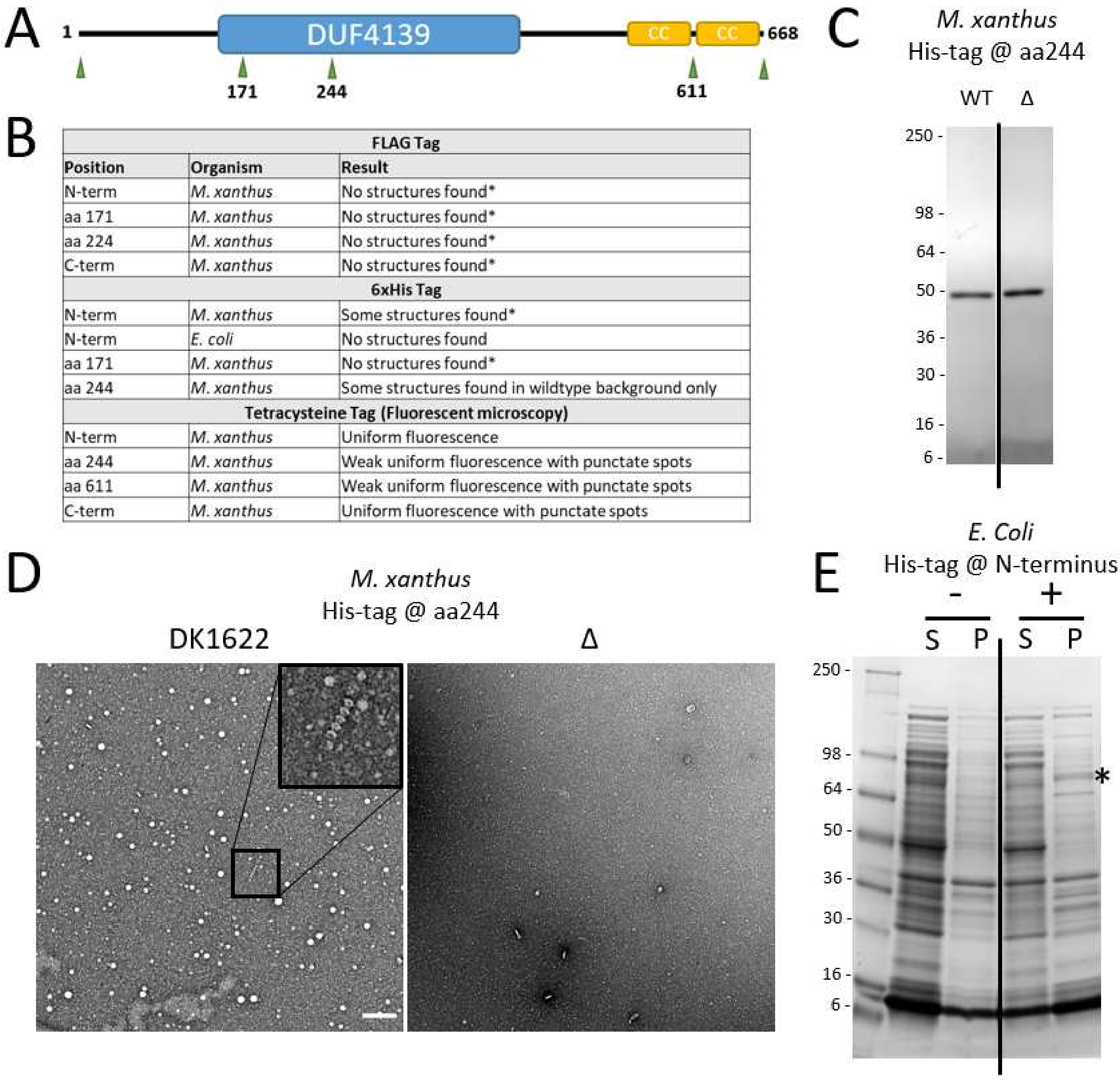

FLAG Tag		
Position	**Organism**	**Result**
N-term	*M. xanthus*	No structures found*
aa 171	*M. xanthus*	No structures found*
aa 224	*M. xanthus*	No structures found*
C-term	*M. xanthus*	No structures found*
6xHis Tag		
N-term	*M. xanthus*	Some structures found*
N-term	*E. coli*	No structures found
aa 171	*M. xanthus*	No structures found*
aa 244	*M. xanthus*	Some structures found in wildtype background only
Tetracysteine Tag (Fluorescent microscopy)		
N-term	*M. xanthus*	Uniform fluorescence
aa 244	*M. xanthus*	Weak uniform fluorescence with punctate spots
aa 611	*M. xanthus*	Weak uniform fluorescence with punctate spots
C-term	*M. xanthus*	Uniform fluorescence with punctate spots

positions are presented. (B) Types and positions of tags inserted into MXAN0657 and their results. Asterisk denotes experiment performed by Dr. David Zuckerman. *M. xanthus* strains used here were DK1622 and DMZ30 (*Δmxan0657*). Rosetta was used for expression in *E. coli*. (C) SDS-PAGE of Ni^{2+}-NTA elution fraction from *M. xanthus* cells expressing MXAN0657 with His-tag at position aa244 in wildtype (DK1622) and *Δmxan0657* (Δ) background. (D) TEM micrographs of elution fractions from (C). WT elution presented very few filaments, shown in insert. Δ elution did not show any filaments. Scale bar = 200 nm. (E) SDS-PAGE of raw lysate of *E. coli* expressing (+) N-term His tagged MXAN0657 and negative control (-). Lysate was subjected to centrifugation to separate soluble and insoluble material. Supernatant (S) and pellet (P) fractions are shown. Asterisk labels band representing His-MXAN0657.

When expressed in *M. xanthus*, he found that no FLAG-tagged MXAN0657 filaments could be isolated, and no filaments could be seen with TEM from the *Δmxan0657* background (**Figure 3-6 B**). Expressing MXAN0657 with 6xHis-tag gave more varied results. In *M. xanthus*, placing the His-tag at position aa171 gave no visible filaments. Tagging at the N-terminus did give some filaments, even in the deletion mutant, although at a low yield.

In experiments for this study, insertion of His-tag at aa244 in MXAN0657 did result in expression in both wild-type (DK1622) and deletion background, as shown in SDS-PAGE (**Figure** 3-6 **C**). However, the product isolated using Ni^{2+} NTA was not at the expected size of around 72 kDa, but was instead at 50 kDa, indicating proteolytic degradation. Under TEM, filaments from wild-type background were rarely found, and non-were seen from the deletion mutant (**Figure 3-6 D**). The few filaments seen were therefore likely indigenously expressed native MXAN0657 filaments that were unspecifically bound to the Ni^{2+} NTA matrix. Induction of N-terminally His-tagged MXAN0657 production in *E. coli* did result in weak expression. However, most of the product were found in the insoluble fraction of the lysate (**Figure 3-6 E**). No filaments could be found from the soluble and insoluble fractions under TEM.

In an attempt to visualise MXAN0657 *in vivo*, the small six amino acid tetracysteine (TC) tag was chosen to minimise disruption to the structure and function of the protein (**Figure 3-6 B**). Again, the N- and C- terminus, and position aa244 were targeted for the generation of the MXAN0657 derivatives. Additionally, position aa611 was chosen also, as it is located between two predicted coiled-coil regions and could be a flexible, disordered region. Positions just after the DUF4139 domain and just in front of the first coiled-coil region were also attempted, but were unsuccessful. Expression constructs were introduced into DK1622 and *Δmxan0657* cells. To image the cells under conditions under which they normally assemble the filaments, they were placed on agarose surfaces (**Figure 3-7**). Cells not expressing TC-tagged MXAN0657 (negative control) showed low levels of homogenous fluorescence under these conditions. In contrast, all cells expressing TC-tagged MXAN0657 showed increased homogenous fluorescence. This whole-cell fluorescence was weaker with internally TC-tagged constructs. Although punctate spots could be seen occasionally, no filamentous structures could be observed from either genetic background indicating that the TC-tagged MXAN0657 proteins appeared to fail to assemble into filaments.

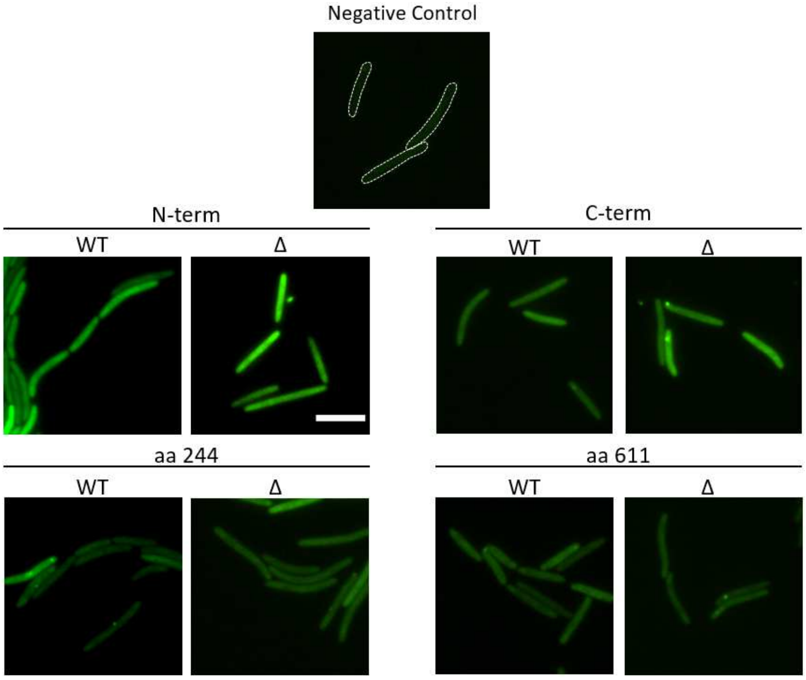

Figure 3-7 Fluorescence microscopy images of tetracysteine tagged MXAN0657 in *Myxococcus xanthus.*
Cells expressing TC-tagged MXAN0657 in DK1622 (WT) and *Δmxan0657* (Δ) backgrounds were incubated with FlAsH reagent, then washed thoroughly before imaging. All cells appear to have fluorescence throughout the cell, with some cells having additional punctate spots. Scale bar = 5 µm

3.3.4 MXAN0657 filaments can be assembled from two separately expressed fragments

Improvements in the method for isolating MXAN0657 were made throughout this study, aided by the increased understanding of characteristics of this protein. SDS-PAGE analysis of initial isolations of filaments never resulted in a single major band that corresponds to the size of MXAN0657, despite observing many filaments in TEM. As isolation purity improved, it became apparent that two major bands, at around 38 kDa and 40 kDa, represented the isolated filaments (**Figure 3-8 A&B**). To discover which parts of MXAN0657 these bands corresponds to, they were sent for Edman degradation sequencing. The upper band (band I) (**Figure 3-8 C**) gave a single unambiguous position, which represents the start of the protein with the N-terminal N-formylmethionine removed. The lower band (band II) (**Figure 3-8 C**) gave two possible positions that were two amino acids apart, at aa339 and aa341, approximately in the middle of the protein. The resulting fragments should have sizes of 37 kDa and 38 kDa, as seen in **Figure 3-8 A**.

With this information, we investigated whether MXAN0657 could be expressed and assembled as two fragments in *E. coli*. For this, the pET-DUET-1 vector was used as it allows simultaneous expression of two constructs. Two constructs were made (**Figure 3-9 A**). Construct 1 had the His-tag at the C-terminus of the amino-terminal fragment (aa1 – aa338), and the carboxyl-terminal fragment (aa339 – aa 668) was expressed with no tags. Construct 2 has no tag on the front fragment, and has a His-tag at the N-terminus of the rear fragment. Inclusion bodies were initially seen in expressing *E. coli* cells. Lowering the induction temperature alleviated this problem for construct 2, but not construct 1 (**Figure 3-9 B**). Soluble fraction of cell lysate showed short fragments of assembled MXAN0657 filaments under TEM (**Figure 3-9 C**). This fraction was purified with a Ni^{2+}-NTA column. In the TEM, eluted fractions gave mostly single filament units, with short fragments rarely found (**Figure 3-9 D**). SDS-PAGE analysis showed two closely positioned major bands (**Figure 3-9 E**), suggesting that the two fragments are able to assemble and form ring structures and filaments.

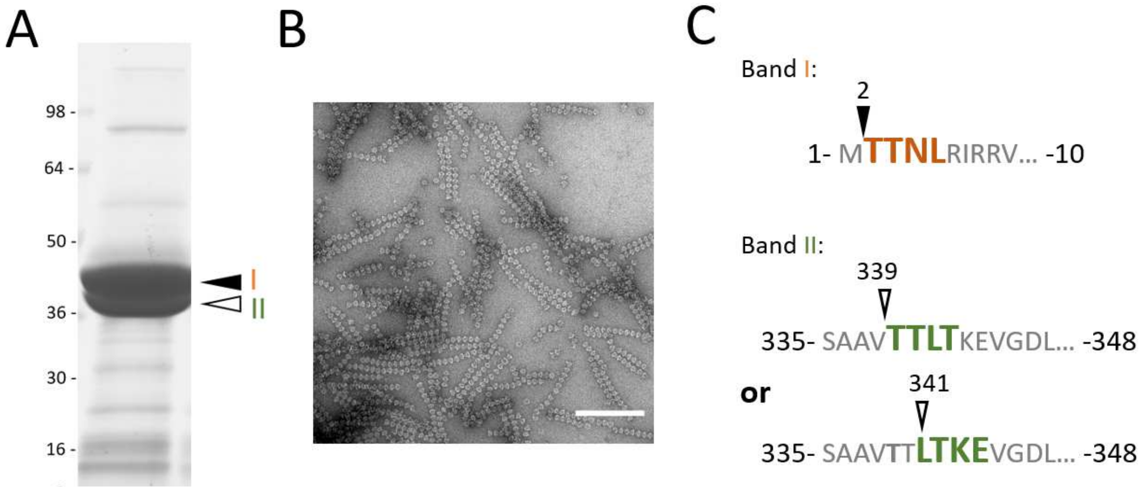

Figure 3-8 Identification of MXAN0657 cleavage site with Edman degradation.
(A)Two major bands from enriched MXAN0657, labelled here as band I and band II, were sent for Edman degradation analysis. (B) TEM micrograph of the sample from (A). Scale bar = 200 nm (C) Sequences obtained from sample bands by Edman degradation. Coloured letters in bold are amino acids sequenced. Arrowheads points at positions of cleavage, and the numbers above denote the amino acid positions leading the sequenced fragments. Band I gave one unambiguous sequence matching the beginning of MXAN0657, whereas Band II gave two overlapping sequences at the centre of the protein.

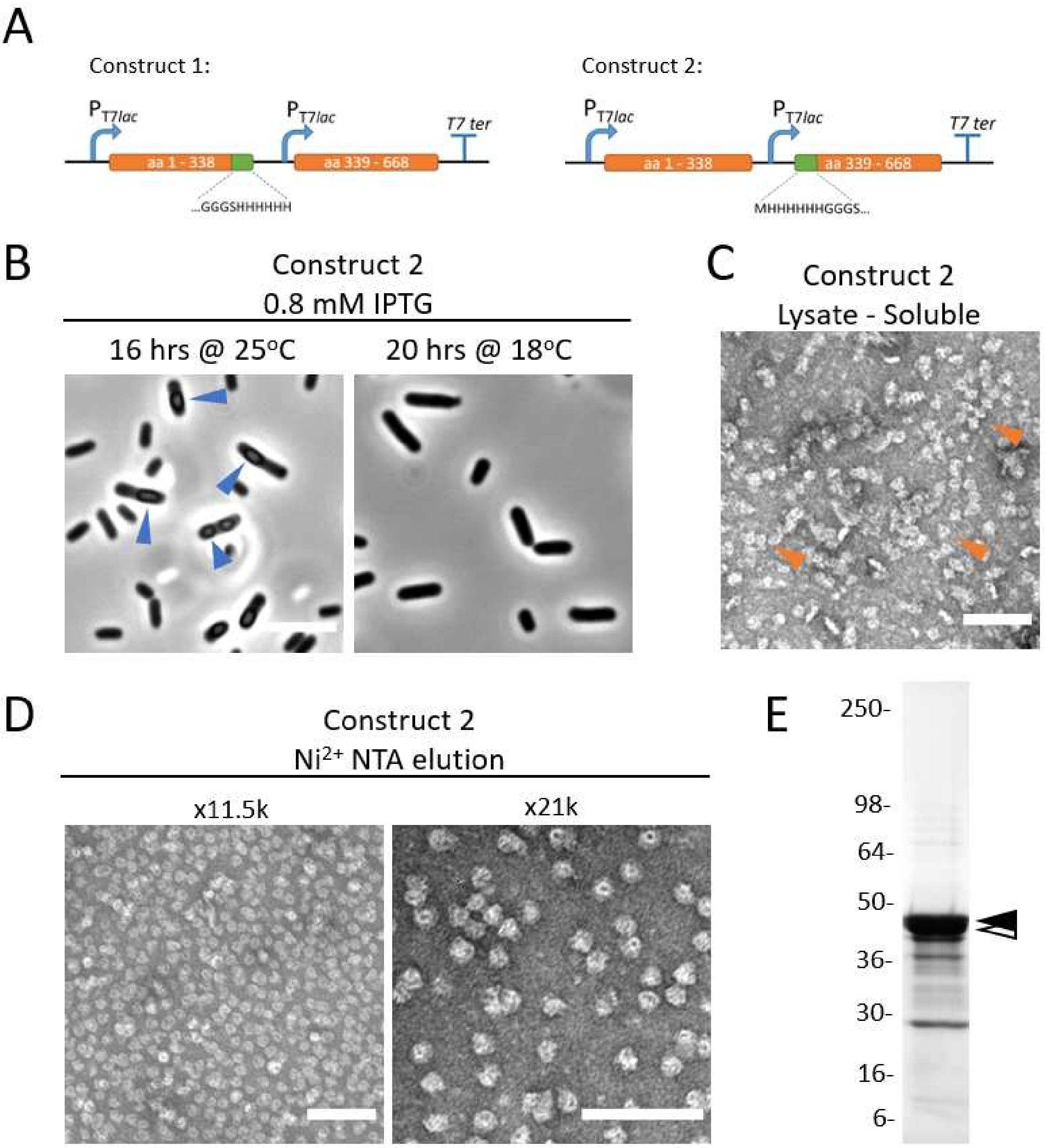

Figure 3-9 MXAN0657 can be expressed as two separate fragments to form filament units. (A) Schematic of the MSCs of the dual-expression pET-DUET-1 plasmids used. This vector containsed two IPTG-inducible T7 promoters, and downstream of each a fragment of MXAN0657 was inserted. A 6xHis tag and a short linker was inserted either into the front or the rear fragment. (B) Phase contrast light microscopy images of Rosetta cells expressing His-tagged MXAN0657 of construct 2 under different conditions. Blue arrowheads point to phase-bright inclusion bodies. Scale bar = 5 µm. (C) TEM micrographs of the soluble fraction of *E. coli* lysate after expressing His-tagged MXAN0657 of construct 2. Orange arrowheads point to MXAN0657 structures. (D) TEM Micrographs of nickel column-purified His-tagged MXAN0657, imaged at two different magnifications. Individual filament units are clearly visible, and appearing to be in a wide range of orientations. Scale bar = 100nm. (E) SDS-PAGE of the sample in D. Black and white arrowheads points to bands that represents MXAN0657. Scale bar = 100nm.

The purified His-tagged MXAN0657, like the natively purified filaments, responded to the addition of divalent cations and acidification (**Figure 3-10**). However, in these conditions, the degree of elongation and bundling seen was at a much smaller level then natively isolated filaments. Moreover, the majority of filament units remained as single particles and did not take part in polymerisation or bundling.

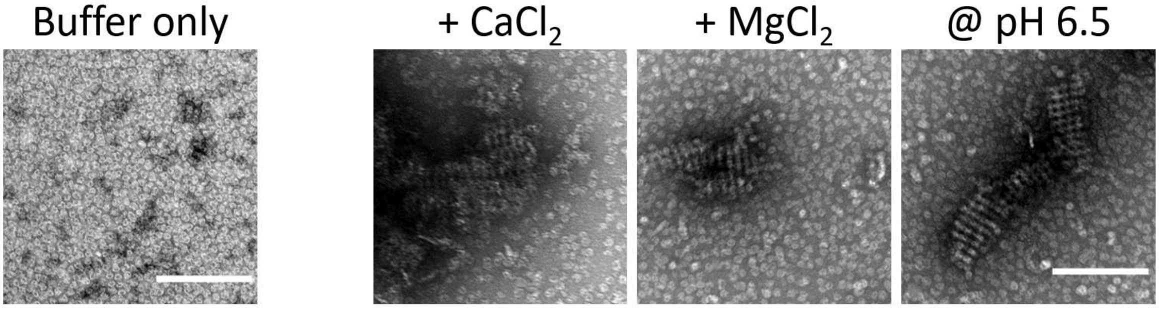

Figure 3-10 His-tagged purified fragmented MXAN0657 responds to change in pH and divalent cations.
Purified His-tagged MXAN0657 appear mostly as single filament units and occasionally as short filaments. Adding 50 mM $CaCl_2$ or $MgCl_2$ at pH 8, or dialysing into imidazole buffer at pH 6.5 caused bundling to some degree, although shorter and at a much lower scale than natively isolated filaments.

3.3.5 Development and purification of polyclonal anti-MXAN0657 antibody

A reliable anti-MXAN0657 antibody was required to further the investigation of the characteristics of MXAN0657. A native isolation of MXAN0657 was used for the immunisation of a rabbit. The resulting raw serum gave unsatisfactory results, as it recognised multiple bands from both wild-type and *Δmxan0657 M. xanthus* cells boiled in SDS buffer (**Figure 3-11**, left-most lane). To remove off-target binding antibodies, affinity depletion was performed. The raw serum was incubated in fixed and permeabilised *Δmxan0657 M. xanthus* cells. The resulting solution continued to exhibit off-target binding (**Figure 3-11**, centre left lane). To solve this, affinity purification was attempted. Purified His-tagged MXAN0657 from construct 2 (**Section 3.3.4**) was crosslinked to a CNBr-activated sepharose matrix. The affinity depleted solution was run through this matrix. Antibodies bound to the His-tagged MXAN0657 were eluted with basic and acidic buffers. The resulting antibody solution was concentrated and proved highly specific. A single band at the size of 75 kDa was detected from boiled wild-type cells and none from the deletion mutant (**Figure 3-11**, centre right lane). The antibody solution was also able to specifically recognise natively isolated MXAN0657 (**Figure 3-11**, right-most lane).

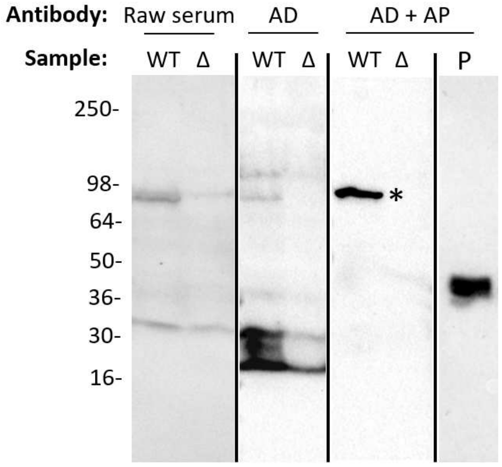

Figure 3-11 Purified αMXAN0657 antibody is specific to MXAN0657.
This figure presents the progress of antibody purification using western blot. Boiled samples of DK1622 (WT) and *Δmxan0657* (Δ) cells were ran on SDS-PAGE gel before transferring to nitrocellulose membrane for western blotting. Starting from the left, the raw serum of the immunised rabbit showed non-specific labelling. After affinity depletion (AD), a procedure that involved incubating the raw serum with fixed *Δmxan0657* cells to remove unwanted antibodies. The resulting antibody solution still exhibited unspecific labelling. The antibody was affinity purified (AP) by running the solution through a matrix coated with MXAN0657, and eluting the bound antibody. This eluted antibody was highly specific as shown by the single band in the WT lane (asterisk), and lack of bands in the Δ lane. The purified antibody recognises purified MXAN0657 (lane P).

3.3.6 Immunofluorescence of MXAN0657 in *Myxococcus xanthus*

With a highly specific antibody, immunofluorescence of MXAN0657 could be performed to gain information on the intracellular location and morphology of MXAN0657 structures. To do this, DK1622 and *Δmxan0657* cells were grown on CTT agar, collected and fixed, and probed with purified anti-MXAN0657 antibody and labelled with AlexaFluor 488-coupled antibody. An Airyscan confocal microscope was used as it offered higher resolution compared to a conventional widefield microscope.

Immunofluorescence images showed that MXAN0657 formed many small structures ranging from punctate spots to short filaments of up to around 500 nm long (**Figure 3-12 A**). Both straight and slightly bent filaments can be seen. Filaments could be found orientated along the longitudinal and lateral axis of the cells, but the majority of these structures seemed to align more closely to the lateral axis. The width of these filaments could not be determined as they are beyond the lateral resolution limit of the imaging system, meaning that they could be below 140 nm. By taking Z-stacks through the cells, one could see that some of the punctate spots are filaments extending down the *z*-axis (**Figure 3-12 B**). These structures could be seen in almost all cells viewed, and could be found throughout the whole cell. There did not appear to be any order in the distribution of MXAN0657 structures, and they did not appear to be confined to the membrane.

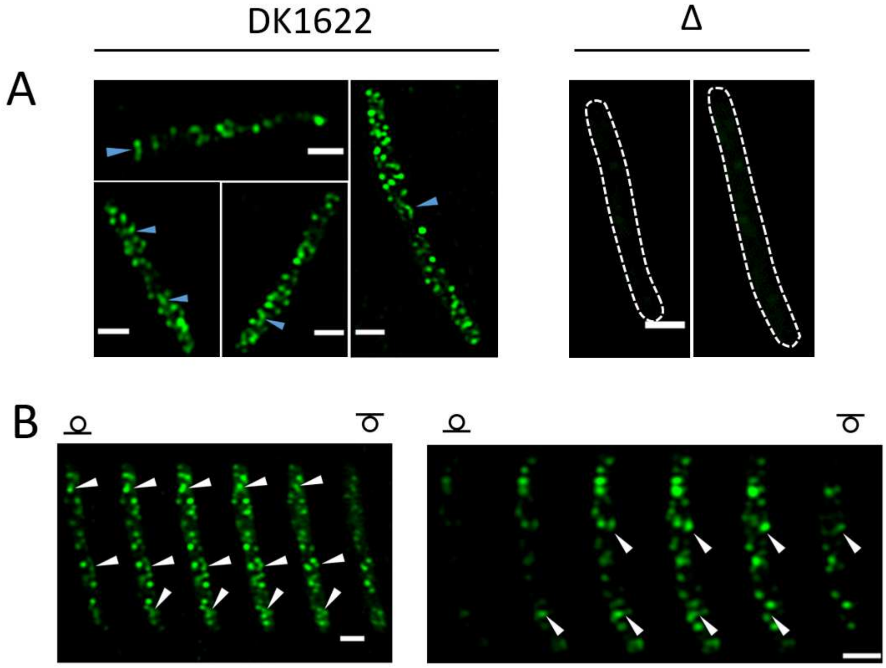

Figure 3-12 Airyscan immunofluorescence microscopy images of *M.* xanthus cells treated with anti-MXAN0657 antibody and AlexaFluor 488-coupled anti-rabbit IgG as secondary antibody. (A) Collage of different DK1622 cells showing subcellular localisation of MXAN0657. Punctate spots were visible, and short filament-like structures are also found (blue arrowheads). Scale bar = 1 μm. (B) Z-stack series of anti-MXAN0657 labelled cells at 190 nm intervals. White arrowheads points to structures that appear to span the volume of the series. Scale bar = 1 μm.

3.3.7 Deletion of *mxan0657* disrupts germination of spores

To investigate possible output pathways of MXAN0657, development assays were performed with DK1622 and *Δmxan0657* cells (**Figure 3-13 A**). Cells were grown to mid-log phase, washed, and spotted onto TPM starvation agar surfaces to induce development. Cells of the deletion mutant did successfully aggregate, and the morphology of resulting fruiting bodies appeared normal and comparable to that of the wild-type (**Figure 3-13 B**). Spores were collected from these fruiting bodies, and were sonicated and heat treated. Spores from the deletion mutant appeared morphologically normal. They were round to oval shaped and were phase bright, comparable to spores from DK1622 (**Figure 3-13 C**). These

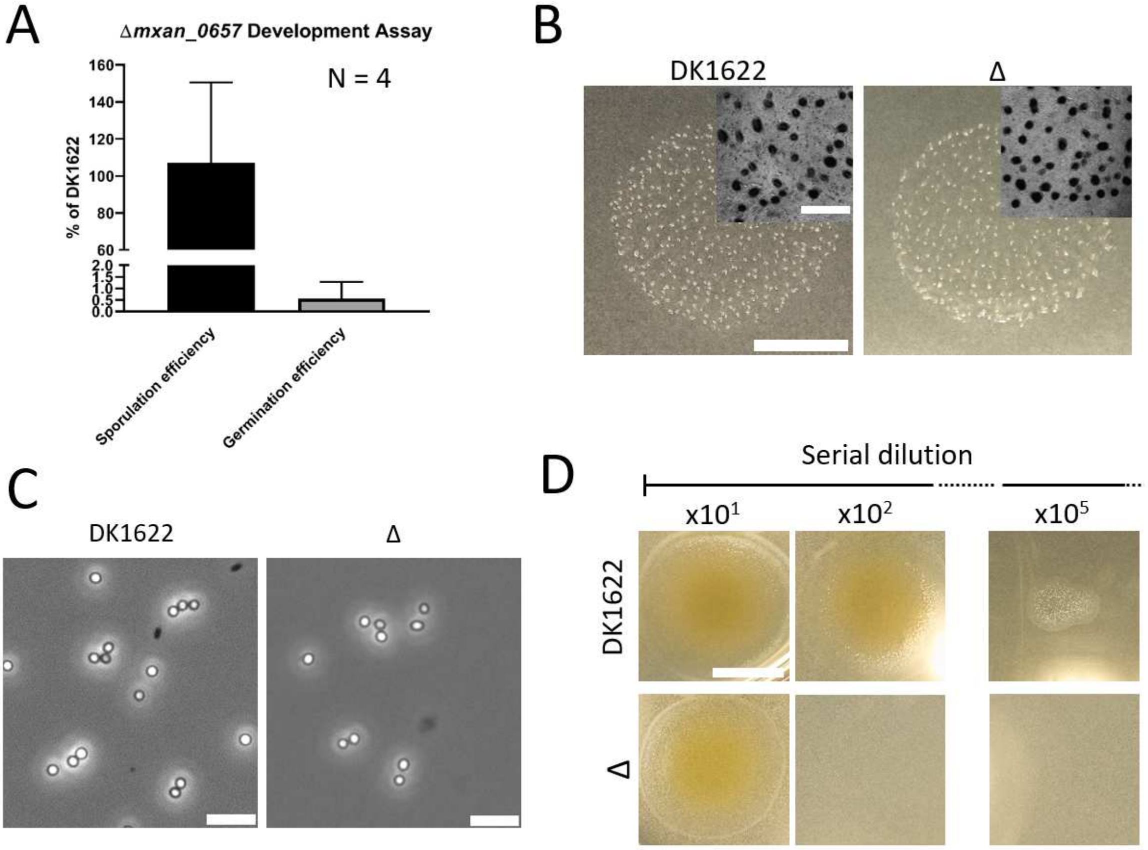

Figure 3-13 Δ*mxan0657* are defective in germination at lowered spore concentrations.
(A) Bar graph showing sporulation and germination efficiency of *Δmxan0657* compared to DK1622 from four separate experiments. Sporulation efficiency varied widely in different repeats, but averaged close to that of DK1622. Germination efficiency was consistently much lower than that of DK1622. (B) Photos of fruiting bodies after 5 days of starvation on agar. *Δmxan0657* fruiting bodies appear normal. Inserts are magnified images of fruiting bodies. Scale bar = 5 mm, insert scale bar = 1 mm. (C) Morphology of DK1622 and Δ*mxan0657* spores. Mutant spores showed normal morphology. (D) Photos of colonies arising from serial dilution of spores. At dilution of $x10^1$, size and density of mutant colony was comparable to DK1622 (WT). At $x10^2$, no growth at all was observed was observed from Δ*mxan0657*. Scale bar = 10 mm.

spores were counted to measure sporulation efficiency. This varied widely in different repeats, as shown by the large standard deviations, but averaged close to that of DK1622 (**Figure 3-13 A**). These spores were then serially diluted and spotted onto CTT nutrient agar, and germination efficiency was measured by counting the number of colonies that arose. The difference in germination efficiency was marked (**Figure 3-13 A**) as the deletion mutant had a much lower germination rate when compared to DK1622, which suggests a severe defect in the germination process. However, when looking at the morphology of the colonies that arose, the drop in colony density in the deletion mutant was very different to that of the DK1622 (**Figure 3-13 D**). For the wild-type, the density of colonies decreased gradually over the serial dilution, with germination taking place still at $x10^5$ dilution. However, for the deletion mutant, although the density of colony at x10^1 dilution was comparable to the wild-type, no germination could be observed from x10^2 dilution onwards. This interestingly hints at a density-dependent germination defect, although a population size-dependent defect could not be ruled out, as the development assay carried out here did not account for changes in the total number of spores present when density was changed.

3.3.8 MXAN0657 interaction assay

In order to identify potential interacting partners of MXAN0657, an interaction assay was performed. Natively isolated MXAN0657 filaments were cross-linked to a column of CNBr-activated Sepharose matrix (**Figure 3-14 A**). For control, the MXAN0657 isolation protocol was performed on *Δmxna_0657* cells, and the resulting isolation was cross-linked to the Sepharose matrix, so impurities in the native isolation could be accounted for. Pure buffer alone was also 'cross-linked' to the matrix. DK1622 *M. xanthus* cells were grown and collected from agar surfaces, the soluble fraction of the lysate was run through the cross-linked Sepharose columns. After gentle washing, the population of proteins that remained on the matrix were visualised with SDS-PAGE (**Figure 3-14 B**). A number of bands were found to be specific to MXAN0657 cross-linked beads, and these were sent for MS analysis. The thick bands at around 38 kDa and 40 kDa (**Figure 3-14 B**) were possibly additional MXAN0657 from cell lysate that were collected by the filaments beads, suggesting that these filaments are still capable of assembly after cross-linking. Additionally, bands that were found to be co-isolated with native filaments were also sent for MS analysis, as these may be interaction partners of MXAN0657 (**Figure 3-14 B**, far right lane).

Figure 3-14 C shows the highest scoring candidates from the MS analysis for each band. Band A, with the highest molecular weight, was reported to be MXAN1162, a putative lipoprotein, and MXAN2967, a RND (resistance/nodulation/cell division) transporter of the HAE-1 (hydrophobe/amphiphile efflux 1) family. Little information on the former protein exists in the literature, but it was found to be a tetratricopeptide repeat-containing outer membrane lipoprotein[160]. As for the latter, RND HAE-1 transporter is the major drug efflux pump in Gram-negative bacteria responsible for the removal of antimicrobial from the cytoplasm[161]. Band B also gave two candidates: MXAN6106, a zinc metalloprotease FibA and MXAN2710, a hypothetical protein. FibA is an extracellular matrix (ECM) associated protein involved in lipid chemotaxis and fruiting body morphology[162]. Although the function of MXAN2710 is unknown, it is also a putative ECM protein, and has been shown that its gene disruption in a *ΔpilA* (the structural component of Type IV pili) mutant caused a 10-fold decrease in spore viability[162]. The two candidates for band C were MXAN6923, the beta subunit of the ATP synthase F1 complex, and MXAN4389, the catalase KatB. In the tan variant of *Myxococcus xanthus*, KatB has been shown to increase in expression relative to the yellow variant[138].

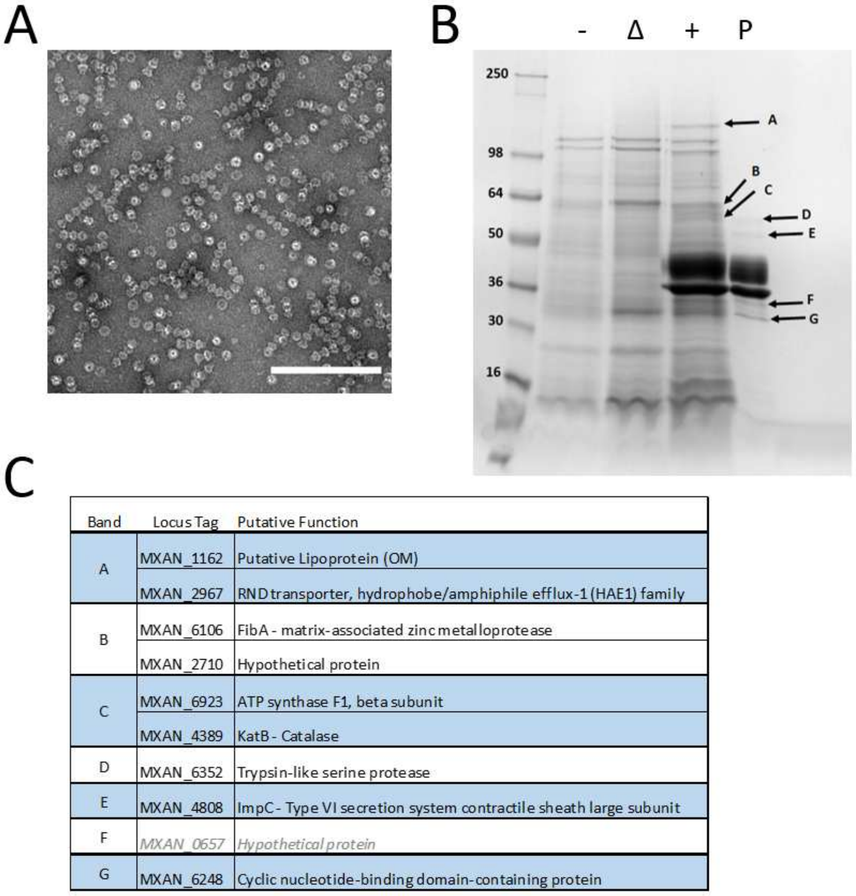

Band	Locus Tag	Putative Function
A	MXAN_1162	Putative Lipoprotein (OM)
	MXAN_2967	RND transporter, hydrophobe/amphiphile efflux-1 (HAE1) family
B	MXAN_6106	FibA - matrix-associated zinc metalloprotease
	MXAN_2710	Hypothetical protein
C	MXAN_6923	ATP synthase F1, beta subunit
	MXAN_4389	KatB - Catalase
D	MXAN_6352	Trypsin-like serine protease
E	MXAN_4808	ImpC - Type VI secretion system contractile sheath large subunit
F	*MXAN_0657*	*Hypothetical protein*
G	MXAN_6248	Cyclic nucleotide-binding domain-containing protein

Figure 3-14 MXAN0657 interaction assay.
(A) is the TEM micrograph of the natively isolated MXAN0657 sample used for cross-linking. Scale bar = 200 nm. (B) SDS-PAGE of MXAN0657 interaction assay candidates sent for mass-spectrometry (MS) analysis. Lane (-) are proteins bound to matrix coupled to buffer only. Lane Δ are proteins bound to matrix coupled to sample of Δ*MXAN0657* cells subjected to MXAN0657 purification procedure. Lane (+) are proteins bound to purified MXAN0657. Lane P is the sample of purified MXAN0657 used for coupling to the matrix. Arrows point to bands sent for MS. Asterisks denote MXAN0657 from cell lysate. (C) Table of MS results. Only high scoring candidates are shown for each band.

The bands from lane P gave less ambiguous results (**Figure 3-14**). Band D is MXAN6352, a trypsin-like serine protease. Band E is MXAN4808, which is the large subunit of the contractile sheath of the Type VI secretion system ImpC/ TssC. Band F is a degradation product of MXAN0657. Band G is MXAN_6248, a cyclic nucleotide-binding domain protein that is found enriched in outer membrane vesicles (OMV)[163].

3.4 Discussion

The lack of annotated information on the DUF4139 domain and the apparently ubiquitous MXAN0657 homologs hampered research into their functions. In fact, *M. xanthus* has around 30% of proteins annotated as merely hypothetical proteins on the NCBI database. Moreover, the quality of the annotation of genes is also a matter of concern, as the predicted start site of MXAN0657 in strain DK1622 was incorrectly positioned. These issues highlight the need to experimentally characterise the large set of proteins with unknown functions.

The finding that MXAN0657 homologs are widespread points at an underlying broad requirement for these structures. From the list of organisms found with homologs so far, there does not appear to be a universal characteristic that could hint towards the reason for the requirement of this filamentous protein. Indeed, the function that homologs play may differ across different clades, and may also be the case in organisms where multiple paralogs exist, although these paralogs may also provide functional redundancies. This is seen in different cytoskeleton elements. For instance, bacterial actin homologs have taken up function as a cell wall synthesis apparatus (MreB) as well as a scaffold for intracellular organelles (MamK), and bactofilin paralogs in *M. xanthus* have different functions.

Gene neighbourhood studies can be a powerful technique when studying uncharacterised proteins, as gene order is poorly conserved in prokaryotes unless the genes are functionally linked[159]. In our case, gene neighbours of MXAN0657 homologs showed high variability, suggesting that their interaction and association partners are elsewhere in the genome. A gene co-occurrence and anti-co-occurrence study could be performed to identify these partners[164]. Doing so may also answer why some members of the myxobacteria family lack a MXAN0657 homolog. It would also be interesting to verify whether the homologs found here form structures similar to those found in *M. xanthus*.

Of the five DUF4139 domain containing proteins, only MXAN0939 and MXAN0940 have predicted functions. They share homology with mucoidy inhibitor gene A MuiA which has been studied in *Pseudomonas aeruginosa*. MuiA has been found to inhibit overproduction of alginate[165], an exopolysaccharide required for biofilm formation. MuiA has also been implicated in the inhibition of swarming motility[166], a form of motility requiring flagella and pili in *P. aeruginosa*. How the DUF4139 domain in MuiA relays these effects was not studied. It is unlikely the MXAN0657 has the same downstream effects, as *M. xanthus* does not produce alginate; *Δmxan0657* mutant colonies appear identical to that of wild-type; and no defect in swarming has been observed from the deletion mutant. The conserved presence of the coiled-coil domain suggests that it is an important feature in DUF4139-containing proteins. Our hypothesis for MXAN0657 is that the C-terminal coiled-coil domain forms the arms linking individual filament units together. What role it plays in the other proteins is unclear, as coiled-coil domains have a variety of roles[167].

The addition of divalent cations caused the elongation and lateral bundling of isolated MXAN0657 filaments, whereas monovalent ions appeared to have no effects. Addition of ATP also appeared to have no effects on MXAN0657, perhaps unsurprisingly, as no conserved nucleotide binding motif has been predicted in its sequence. In other cytoskeletons, the addition of ions can have a range of effects, apart from the fact that nucleotide-dependent cytoskeletal proteins require Mg^{2+} for functioning. For FtsZ from multiple bacterial species, the addition of millimolars levels of Ca^{2+} ions initiates a nucleotide-dependent assembly and bundling of protofilaments[22], which could be mimicked by elevated concentration of Mg^{2+} ions[168]. In eukaryotes, however, micromolars concentrations of free Ca^{2+} destabilises microtubules and causes disassembly. Ca^{2+} can also affect microtubules indirectly *via* calmodulin, providing higher orders of regulation through other microtubule-interacting proteins[169]. For the bacterial actin homolog MamK from *Magnetospirillum magneticum,* rate of filament assembly increases when K^+ is added, bundling of filaments is induced with elevated K^+ concentrations. *E. coli* MreB has been shown to assemble into sheets when ATP/GTP and Ca^{2+} are present[32]. Like MXAN0657, the intermediate filament-like crescentin from *Caulobacter crescentus* has been shown to aggregate at millimolar concentrations of Mg^{2+} and Ca^{2+} in the absence of nucleotides, and also the slightly acidic pH of 6.5 without divalent cations[170].

Whether the aggregating and elongating response of MXAN0657 in the presence of divalent cation has any biological role is unclear. Since both Mg^{2+} and Ca^{2+} have similar effects, it is likely that bundling is an unspecific effect, for example, by the neutralisation of charges on the surface of filaments by the divalent counter-ions. It is unclear whether the bundling of MXAN0657 at mildly acidic and strongly basic conditions is physiologically relevant, as the pH of cytoplasm is tightly controlled.

The sensitivity of MXAN0657 to insertion of tags is perhaps unsurprising. The assembly of individual MXAN0657 monomeric peptides into filament units, and further into chain-like filaments likely require numerous interactions between conserved specific interaction surfaces. Small inserts like the poly-histidine and tetracysteine tags, although commonly used, could still interfere with these interactions, by steric hindrance or by surface charge/hydrophobicity disruptions. Many other cytoskeletal proteins have disrupted assembly characteristics and function by the insertion of tags, for instance MreB[40], crescentin[54], FtsZ[171], and bactofilins[59,111] (see **Section 2.3.3**).

Identification of the cleavage site of isolated MXAN0657 aided in the tagging of the protein. It was very surprising that the two fragments of MXAN0657 overexpressed in a foreign organism were able to assemble into filament units, and into short filaments. The lack of structures seen in *E. coli* expressing N-terminally tagged full-length MXAN0657 made it even more remarkable. It is possible that the tertiary structure of MXAN0657 is separated into distinctive domains, and that these domains are able to fold separately prior to assembly with the complementary fragment. Such a pre-folded domain-based assembly is observed for the catalytic domain of adenylate cyclase (CyaA) from *Bordatella pertussis*, commonly used for bacterial two hybrid systems[172]. The T25 and T18 fragment of the catalytic domains can be expressed separately attached to proteins-of-interest (POIs), and upon coupling via association of POIs, are able convert ATP to cAMP. It should be noted that for MXAN0657 the site of cleavage is near the centre of the DUF4139 domain. Since no structural information for DUF4139 exists, the mechanism of assembly is completely speculative. Only single filament units, and at most short fragments of around four chains long were found in cell lysate and purified samples. These filament units largely failed to polymerise when added with divalent cations and acidic buffers. Any bundling that took place was at a much smaller scale than seen in natively isolated filaments. It is possible that the His-tag, or indeed fragmentation disrupts parts of the protein that are involved in polymerisation and bundling. There may also be heterogeneity in the structure of His-tagged assembled rings, which may explain why only a subset of filament units polymerise and bundle.

Although many proteins require proteolytic cleavage for maturation, the proteolytic cleavage seen in isolated MXAN0657 is likely to be of an unspecific nature. This is evident from western blots of whole cells grown on agar boiled in reducing conditions, as the antibody recognised a single band at around the size of a full length MXAN0657. Due to the large number of proteolytic enzymes in the proteome of *Myxococcus xanthus*, thanks partly to its predatory life style, it is perhaps unsurprising there was degradation of isolated MXAN0657 occurring even in the presence of protease inhibitors.

Immunofluorescence of MXAN0657 gave the first glimpse of the localisation of these filaments in the cell. The structures seen in cells are generally from around half to the whole width of a cell, i.e. 200 nm to 500 nm. Exact distribution of length of filaments cannot be assessed as the images lack adequate axial resolution (around 400 nm). There were variations in the width of filaments seen in the immunofluorescence images, which may suggest that filament bundling takes place inside cells and has a physiological function. Again, the distribution of filament width is unknown as they are diffraction limited (<140 nm). For comparison, intracellular MreB filaments in *Bacillus subtilis* are on average 1.7 μm long with a width of on 75 nm on average[38], which required both Structured Illumination Microscopy and Gated Stimulated Emission Depletion microscopy – two very powerful techniques – to deduce. Although predicted to be positioned in the periplasm, no evidence was observed that the structures are confined to the periphery of the cells. In fact, the necessity for thorough cell breakage during isolation of native filaments strongly suggests that the structures are rather located in the cytoplasm of the cells than the periplasm. In order to study the behaviour of MXAN0657 *in vivo*, a functional fluorescently-tagged MXAN0657 is required. Structural information for MXAN0657 is needed for the rational design of a tagged construct that could function *in vivo*, taking advantage of possible unstructured loop regions that are solvent accessible and are not involved in inter-subunit interactions. The abovementioned cleavage site is currently being tested as a fluorescent label insertion site, but in a full-length protein construct.

Deletion of *mxan0657* appeared to affect germination in a spore-density-dependent or quorum-dependent manner, whereby spores failed to germinate at low spore concentrations or number, respectively. Performing the germination assay with a constant number of spores but at varying densities could reveal which of these factors are responsible for the effect observed. Myxospores germinate in response to increase in certain nutrients in the environment, namely calcium ions and amino acids[173].

Spore density and population density have so far not been described as a determinant for germination efficiency in myxobacteria, nor has it been described for the spores of the well-studied orders of *Bacillales* and *Clostridiales*. Acyl homoserine lactone (AHL), a mediator of quorum signal used by Gram-negative bacteria but not in Myxobacteria, can function as an external signal that promotes the germination of myxospores[174]. However, Density-dependent germination, however, has been described in the amoeba *Dictyostelium discoideum*. The similarity between *M. xanthus* and *D. discoideum* is striking - both organisms exhibit social behaviours, and upon starvation can aggregate to form fruiting bodies in which sporulation takes place. In *D. discoideum*, the cytokinin discadenine is a specific inhibitor of germination[175,176]. Discadenine is produced and secreted during culmination – a process that leads to fruiting body maturation, and its concentration correlates with cell density. Spores of *D. discoideum* therefore only germinate when removed from the high density environment of the fruiting body where discadenine is abundant. Although this phenomenon is the inverse of what we have observed in *Δmxan0657* cells, it might be advantageous if myxospores only germinate when a quorum or density is reached, which may ensure population survival in the competitor-rich soil habitat. Alternatively, the presence of MXAN0657 could have mitigated the need for a low spore density environment for germination, providing a selective advantage over ancestors that required it. There is currently no published study of germination efficiency with varying spore density or number in spore-forming myxobacteria that lack MXAN0657 homologs (**Table 3-5**), so this hypothesis remain speculative. How a filament forming protein could assist in the regulatory process of germination is currently unclear. A transcriptome study of *M. xanthus* cells found that MXAN0657 is not actively regulated during glycerol-induced sporulation[177]. It is unclear whether it is upregulated during germination, or during starvation-induced sporulation.

Of all the MS analysis candidates from the interaction study, only MXAN2710 causes a phenotype that affects germination when disrupted in the *ΔpilA* background, as described in a study performed by Curtis and colleagues[162]. The effect was a 10-fold decrease in germination, although they did not report any spore-density dependent effects or what the mechanism could be. MXAN2710 is predicted to be an ECM-associated protein and has a predicted signal sequence for Sec-mediated secretion, and so it could only be expected to interact with MXAN0657 as an unfolded peptide in the cytoplasm. The study of a *Δmxan0657 ΔpilA* or *Δmxan2710* strain could help reveal the relationship between MXAN0657 and germination.

One aspect that this study has not addressed is the requirement for surface grown cells for the isolation of filamentous structures. As a tantalising thought, MXAN0657 may polymerise when the cell senses that it is in contract with a surface, and MXAN-0657 filaments, being relatively rigid especially after bundling, could provide some form of structural support for the cell. Generally, the peptidoglycan and turgor pressure are sufficient for maintaining the rigidity of a cell. A study by Wang et al[178] did suggest that the filamentous cytoskeleton protein MreB could contribute to stiffness of *E. coli* cells. They found that A22-induced MreB disassembly is coupled with a detectable decrease in cell stiffness. However, their subsequent analytical model from this study relied on an outdated cell-spanning helical model of MreB. Nonetheless, *M. xanthus* is often observed to bend during surface motility, and in some occasion to extreme degrees[179], which would require a saccule formed of a uniquely flexible arrangement of PG. MXAN0657 filaments could therefore provide rigidity that such a saccule would lack. In previous studies by Freese, Lünsdorf and Reichenbach[109,110], structures were successfully obtained from *M. fulvus* cultures grown in a fermenter. This suggests that some environmental property sensed by the cell undergoing surface growth can be replicated in a fermenter, which could possibly be aeration levels. The study of surface sensing in bacteria is very active, but mechanisms are yet to be fully established. One hypothesis for *P. aeruginosa* is the use of T4P for surface engagement and sensing[180]. This perhaps calls for the study of the relationship between T4P and MXAN0657.

In summary, the reported data further characterise a novel cytoskeleton filament found in *M. xanthus* and in many members of the Bacteria kingdom. Two new isolation protocols were developed during the course of this work: one for the isolation of filaments from the native organism, and the other from *E. coli* which gave a high yield of single filament units. TEM studies of the isolates showed that the filaments respond to the addition of divalent cations and specific pH changes by large-scale bundling and elongation. Whether these processes also occur *in vivo* is currently unclear. Nonetheless, the development of an antibody specific to MXAN0657 allowed the observation of cellular structures that appeared to be formed by short filaments inside the cell. Finally, spore germination studies revealed that the deletion of *mxan_0657* caused a spore density-dependent germination defect.

Chapter 4

Cryo-electron microscopy of BacM and MXAN0657

4.1 Background

4.1.1 Advances in cryo-electron microscopy and single particle analysis

There is no doubt that X-ray crystallography and NMR have been the main driving forces behind the study of protein structural biology, making enormous contributions towards our knowledge of how the molecular architectures of proteins determine their functions. As of mid-2019, there were around 139,000 structures solved with X-ray crystallography deposited on the Protein Data Bank (PDB)[181], and around 12,500 by NMR. These techniques are not without their limitations, however. For X-ray crystallography, the POI must form a well ordered 3D crystal, and the conditions of crystallisation are seldom physiological. NMR is mostly limited to small and medium sized peptides and proteins, and isotope labelling of POI is essential. Moreover, the POI has to be soluble at high concentrations of up to several mg/ml.

Early attempts at using electron microscopy to solve protein structures were confined to samples arranged in crystalline orders, including two-dimensional crystals or filaments with helical symmetry, which provides high redundancies in structural information, improving SNR. For this reason, spherical viruses were also favoured due to their high symmetry[182]. Historical examples include the helical tail of bacteriophage T4[183] and spherical viruses like human wart virus[184], both serving as proof of concept studies for three-dimensional structure reconstruction with electron microscopy. Further examples are flagella from *Salononella typhimurium*[185]; and the unstained 2D lattice of bacteriorhodopsin[186], which was solved to the resolution of 3.5 Å in the *xy*-plane by Henderson and colleagues.

Proteins are primarily formed of light elements like hydrogen, oxygen, carbon, and nitrogen. Their ability to scatter electrons is very low, resulting in low contrast between protein particles and the underlying support – typically carbon film. Their susceptibility to radiation damage from the illuminating electron beam calls for low electron dose for imaging which further reduces contrast and SNR. Salts of heavy elements, for instance uranyl acetate, could be dried onto samples to form a mould around the protein. This results in much higher contrast and resistance to radiation damage. Since the stronger scattering stain is deposited around the protein particles, the particles appear 'lighter' than the background, hence it was called 'negative staining'. However, staining can mask fine structural features of the proteins due to the size of the formed grain, limiting resolution. Uneven staining, drying of the sample, and absorption into sample support may also introduce artefacts.

It was recognised that if the potential of EM to study native biological complexes at high resolution was to be realised, samples must be imaged in an unstained, frozen-hydrated condition. Taylor and Glaeser achieved this with thin crystals of catalase and obtained diffraction spots out to a resolution of 4.5 Å[187]. This led to the development by Dubochet and colleagues of a practical technique to prepare frozen-hydrated biological samples so that particles are suspended in a thin sheet of electron-transparent vitreous ice[188,189]. This process of vitrification required rapid freezing of the aqueous solution to prevent formation of strongly diffracting crystalline ice[190], and the sample must be kept below -150 °C at all times. Vitrification is often called 'plunge freezing', as the sample-bearing grid is plunged into a cryogen at high speed. This laid the foundations for cryo-electron microscopy.

Non-ordered particles can adopt many possible orientations and each micrograph only presents a 2D projection of the specimen. To distinguish useful signal from noisy low-exposure micrographs, averaging could be used. Before this could be done, the many different projections of molecules have to be classified and aligned before averaging. Performing this by eye would be highly subjective and extremely difficult due to the low SNR of individual projections. Moreover, sample heterogeneity caused by conformational differences further complicated this problem. Frank and colleague developed a computational quantitative method to identify and sort micrographs of individual particles into subsets with similar appearances and hence orientations[191,192]. Averaging within these subsets greatly improved SNR, and structural features were retained at higher resolutions.

The next step is to find the spatial relationship between all the averaged projections of particles so that a 3D model can be formed. The method developed by Frank and colleagues[193] is based on the Central-Section theorem, also known as the Fourier-Slice theorem, which states that the Fourier transform of any two 2D projections of an object in 3D space will share a common 1D projection[194]. If the directions of three of these common lines are known, then the relative orientations of the three associated projections would also be known. This is much more complicated in practice due to low SNR and errors in averaged projections. This method also required a 3D model as a reference to find the orientations of projections. Existing models that share resemblance with the POI could be used. If none is available, one could image the same particles at different tilt angles to gain 3D information on the protein.

With these keystone methods established, single-particle analysis (SPA) with cryo-EM became a reality. Resolutions of structures solved remained low for some time, and Henderson's proposed theoretical ability for cryo-EM to resolve proteins below 100 kDa at atomic resolutions with only 10,000 projections was far from reality[195]. Still, a plethora of improvements were made, including the quality and the operation of microscopes; the usage of the field-emission gun (FEG); sample preparation equipment; and computation resources. Several software packages for EM data processing were also developed, for example SPIDER[196], EMAN[197], FREALIGN[198], IMAGIC[199], and XMIPP[200], and each have been improved continuously.

The onset of the so-called 'Resolution Revolution' for cryo-EM in the first half of this decade saw a significant increase in the number of structures solved by cryo-EM and the resolution of their maps. To illustrate, the cumulative number of maps deposited on the Electron Microscopy Data Bank (EMDB)[201] in 2002 and 2012 were 8 and 1,566 respectively, and the average resolution remained around 16.5 Å. In 2015, the cumulative number jumped to 3,365, with an average resolution of 12.5 Å, which further increased to around 9,000 maps and 5.6 Å by mid-2019. This was thanks to a number of contributing factors, most notably the advent of commercially available direct electron detectors (DED) and EM data analysis software. The high level of technical and scientific support offered by the cryo-EM community should also be mentioned here, notably the Collaborative Computational Project for Electron cryo-Microscopy (CCPEM)[202].

To record EM micrographs, film or Charged-Coupled Device (CCD) cameras have both been used. Film needed to be developed and then digitised for image analysis, but offered high resolution. CCD cameras required electron signals to be converted to photons *via* a scintillator before detection. Electrons can scatter upon arriving at the scintillator, which causes spatial inaccuracy in photon emission and detection, reducing resolution and increasing noise. In 2007, Faruqi and Henderson stated that with the developments in microelectronics, the use of DED could be possible for use in an electron microscope, with which individual incident electrons could be counted during imaging. This promised high detective quantum efficiency (DQE), high SNR, preservation of high resolution information, automation of image acquisition, and high readout speed[203]. They then went on to form a consortium of engineers and scientists, and collaborated with the industrial partner FEI to produce a commercial DED. Concurrently, Peter Denes and David Agard also designed a DED with Gatan, Inc. Nguyen-Huu Xuong from Direct Electron company also rolled out a DED at around the same time[204].

The power of using DED for cryo-EM was also realised by taking advantage of its high readout speed and DQE. During imaging, apart from a constant and systematic stage-induced drift, the ice in which the POI is suspended in can move and warp due to electron beam-induced motion. Individual particles can also rotate, causing blurring of micrographs[205]. With the DED, micrographs could be taken as a time series, or 'movie', at a frame rate of up to 1,500 per second (K3 Camera, Gatan, Inc., USA), so that these motions could be tracked and corrected during image analysis[206,207]. This way, high resolution information is preserved, pushing the resolution boundary of cryo-EM.

An image acquired in the electron microscope is convoluted with a contrast transfer function (CTF), which is dictated by the defocus setting, astigmatism, drift, spherical aberration, and acceleration voltage[208,209]. Defocusing is usually necessary in order to increase contrast of images so to allow identification of particles in the field of view (**Figure 4-1A**). The CTF manifests in the reciprocal-space as a quasi-periodic sine function with circular intensity oscillations termed Thon rings[209] (**Figure 4-1 A**). Its decline in intensity along the frequency axis increases with defocus, hence the higher the defocus, the lower the amount of high resolution information. The CTF also crosses zero multiple times, meaning the loss of information at those frequencies (**Figure 4-1 B**), which is why a defocus series where images are taken at different defocus values is required in order to sample information at the whole frequency range[208]. 'Phase flipping' occurs when the CTF crosses into negative amplitude, further degrading information of projections. It was realised that the CTF must be corrected for to achieve high resolutions of 3D reconstruction[208]. Programs like ACE[210] and CTFFIND[211] can automatically estimate the CTF and corrects phase flipping and intensity decline. Astigmatism can also be corrected for, and defocus values accurately determined. This was a critical development towards the atomic resolution capabilities of cryo-EM.

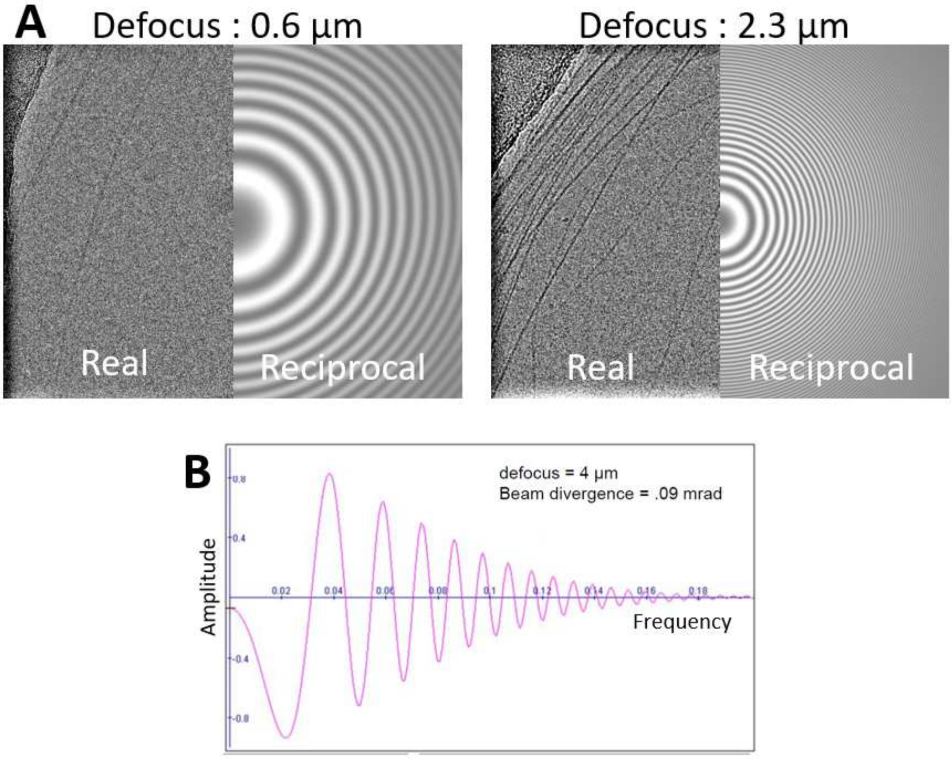

Figure 4-1 Defocus and the contrast transfer function.
(A) Cryo-EM micrographs of BacM_{TR} imaged at different defocus values. At low defocus (left), the contrast in the real-space image is much lower, and the CTF envelope in reciprocal-space has a slower decline, with Thon rings spaced further apart than at higher defocus (right). (B) An example from (212) of a cross-section of the CTF at a defocus of 4 µm. Note the multiple zero crossings and phase flipping.

The recent development of powerful and sophisticated analysis software not only increased accuracy and resolution of resolved structures, but also improved ease of use. A notable example, and one that is used in this report, is RELION, developed by Scheres and colleagues[214]. This software utilises a Bayesian approach for SPA, and implemented many aspects of developments made in EM data

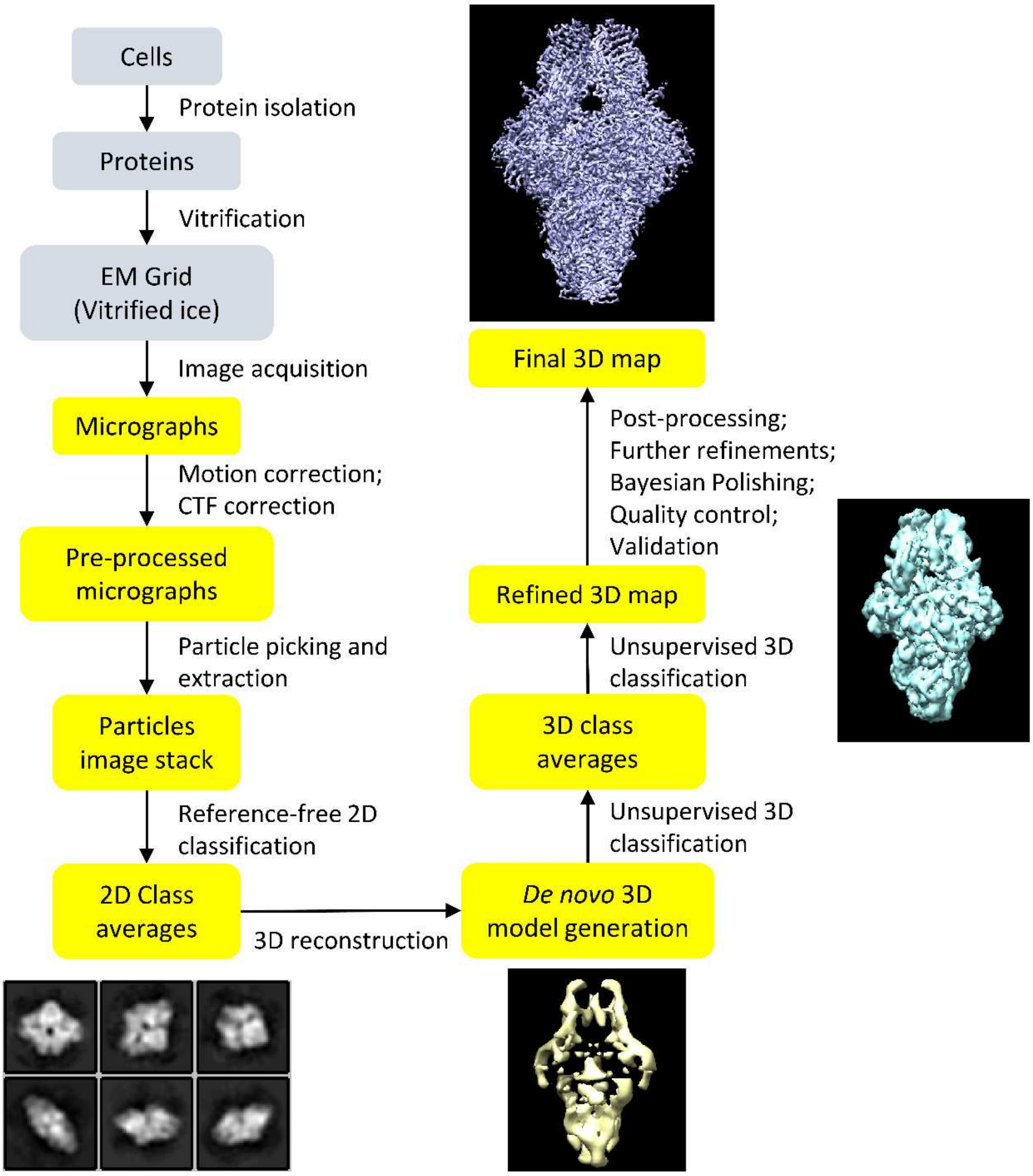

Figure 4-2 Workflow of 3D reconstruction of β-galactosidase using RELION.
Before attempting SPA, the experimenter must first refine methods of sample preparations to ensure protein homogeneity and quality. Protein vitrification conditions must also be optimised. Steps in yellow are performed with RELION. Much of the processes are automated and are unsupervised to reduce subjective inputs from a human user. However, at each step, the user should inspect the output and consider the quality and validity of the processing, and ensure the biological relevance of the results. Data of β-galactosidase was provided as part of user training guide for RELION 3.0[213].

processing, including particle detection, motion correction, CTF correction, and 3D model generation. It also takes advantage of modern computing resources, allowing highly accelerated parallel processing of data on widely available graphic processing units (GPU). Its efficient pipeline approach made it accessible to non-specialised research groups and non-expert users[210]. The workflow of cryo-EM SPA using RELION is presented in (**Figure 4-2**).

The method of sample preparations has also been improved. There is now a range of available equipment for the vitrification of samples on cryo-EM grids. The general principles have not altered much from the method of Dubochet and colleagues[188]. Briefly, it requires the suspension of sample solution across a hole made in the carbon support, which is in turn attached to a stronger, metal grid. The sample should adopt random orientations in the suspension (**Figure 4-3**). Excess liquid is blotted away, leaving only a thin film of liquid to reduce background signals during imaging and ensure a uniform layer of POI. This is quickly plunged into a cryogen for vitrification, usually liquid ethane. Many types of grids are available, with different metal supports, hole sizes and spacing, and shapes of holes, allowing thorough optimisation of sample preparations.

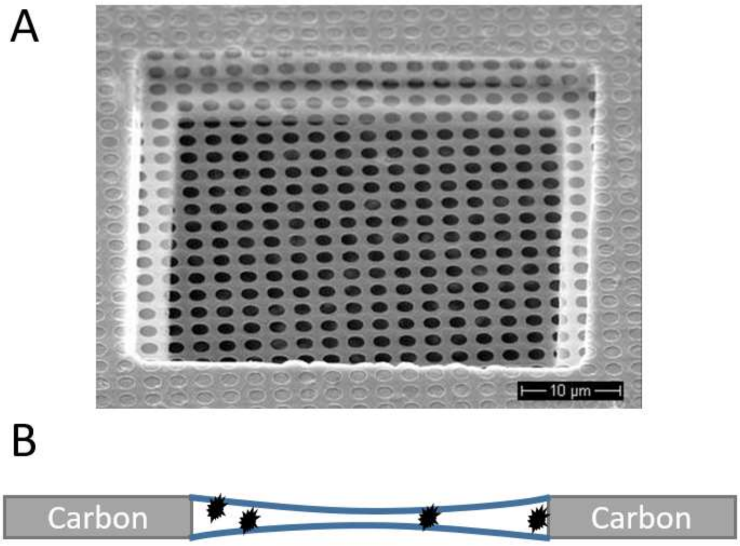

Figure 4-3 Suspension of protein in ice formed in holes on a carbon support film.
(A) Scanning electron microscopy micrograph of a holey carbon support on a copper grid (EM Resolutions Ltd, UK). (B) Schematic showing the suspension of proteins (black spots) in a thin sheet of ice (area between blue lines), suspended by a carbon support.

The developments and improvements in hardware and software greatly increased the routinely achievable resolution with cryo-EM. The sensitivity of current cryo-EM methods also allows the identification and classification of different protein conformations in a specimen, for instance, the open and closed states of the potassium channel Slo2.2[215]. The new phase-plate technology promises increased contrast even at no defocus, thus allowing detection of small proteins previously not possible and remove the necessity for a defocus series[210]. This makes cryo-EM a powerful technique to use alongside or as an alternative to other structure determining methods.

4.1.2 Helical reconstruction

As mentioned above, helical objects are favourable for structural determination by EM. The helical arrangement of asymmetric units in the object means that a projection of this object can provide many different orientations of subunits at once, greatly facilitating 3D reconstruction. An object with helical symmetry can be described as a 2D lattice of subunits with a defined and repeated horizontal and vertical spacing. Rolling up this 2D lattice gives a helical filament where the horizontal and vertical spacing becomes twist and rise (**Figure 4-4**). Helical structures may have *n* number of strands, making them *n*-start helices. However, they can still be described as 1-start helices given that they do not start at the same plane in the *z*-axis (**Figure 4-4**). The diffraction pattern of a helix gives a series of distinctive 'layer lines'. These lines are caused by the convolution of Bessel function[216], an effect induced by the cylindrical shape of the helix. The diffraction pattern and positions of these layer lines could be used to obtain the parameters of the 2D lattice. This method is called Fourier-Bessel indexing. With this information, 3D reconstruction could take place. Historically, Fourier-Bessel indexing was used widely to solve the structures of helical biological objects. However, it is laborious and requires straight, flat and long filaments that are perfectly assembled. Few samples can achieve this, as filaments can bend and assembly errors are not un-common.

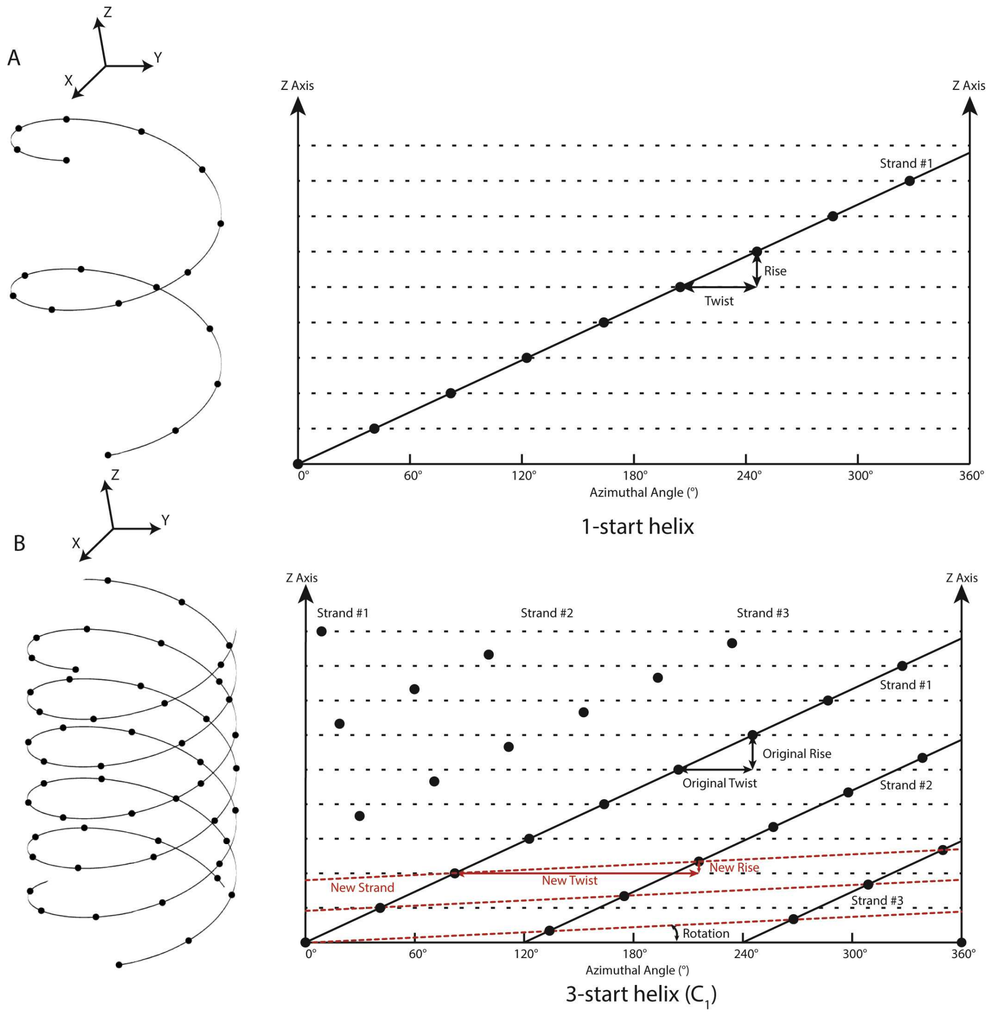

Figure 4-4 A helical object can be thought of as a rolled-up 2D lattice with a defined twist and rise.
(A) A 1-start helix 'unrolled' to give the 2D lattice on the right. The relationship between the subunits can be defined with twist and rise. (B) A 3-start helix with C_1 point group symmetry. The twist and rise of the 3-start helix can also be defined as a 1-start helix (red dotted line), and is mathematically, though not biologically, equivalent. Diagram from taken from (217).

A different approach utilises the abovementioned SPA method. Overlapping segments of the helical filament can be extracted and aligned with a 3D reference model in real-space. This approach was introduced by Egelman, termed iterative helical real-space reconstruction (IHRSR). An implementation of this was incorporated into RELION[217]. Like in SPA, RELION can deduce orientation parameters of the extracted filament segments and define the in- and out-of-plane rotation and translation required for alignment before averaging. In this method of helical reconstruction, it is very important that the helical twist and rise of the filament is well defined. RELION can robustly converge towards optimal helical parameters, even when given a large search range. Knowing the helical symmetry of the filament is also very important, and must be user-defined. If the incorrect helical symmetry is imposed during processing, the resulting map would be completely meaningless, even if RELION reports a high nominal resolution value. This also illustrates the importance of continual validation of outputs at each step by the experimenter despite the highly automated nature of cryo-EM processing with RELION.

4.1.3 Cryo-electron tomography

Cryo-electron tomography involves the imaging of a cryo-sample at a range of tilt angles to sample three-dimension information. This series of 2D projections of the sample can be used to reconstruct the 3D object, and since the relative orientation of each projection is known, the process is relatively straight forward[218] (**Figure 4-5**). This technique is particularly useful if the object of interest is unique, for example, an individual cell, or a particular biological process that needs to be imaged *in situ*[2,37,218–220].

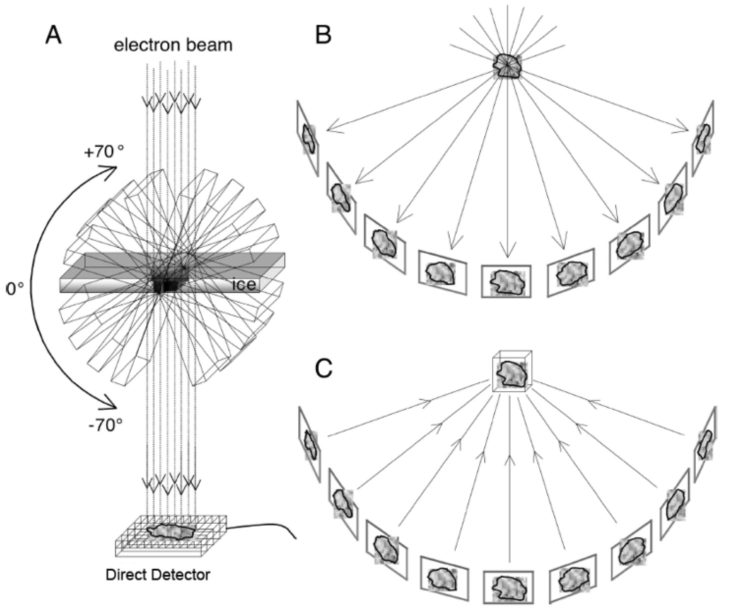

Figure 4-5 Schematic of cryo-electron tomography.
(A) The ice-embedded sample is tilted at regular intervals during imaging. (B) This allow the collection of projections of the object at different angles, sampling the Fourier-space. (C) The projections can then be back projected to form a 3D reconstruction, or a tomogram. Diagram taken from (218).

An important concept to understand about tomography is the ‘missing wedge’ effect[221]. The Fourier slice theorem mentioned above dictates that in order to completely reconstruct a 3D object, the whole Fourier-space needs to be sampled, or in other words, every angle of the object needs to be imaged around an axis. This is not possible in practice, as the stage holding the sample will inevitability block the incident electrons from the sample, and also the effective thickness of ice will increase during tilting. This incomplete sampling of information manifests as missing 'wedges' of information in reciprocal-space (**Figure 4-6 A**), or as streaking artefacts in real-space[222] (**Figure 4-6 B**). Fourier sampling can be improved by multi-axis tilting of the sample, but it requires special microscope stages, and is also prone to drift and instability during imaging[222]. Another limitation of tomography is that it requires repeated imaging of the same sample, so that electron dose has to be very low at each tilt angle to minimise radiation damage throughout the acquisition. This greatly reduces the SNR and contrast of each image, limiting the overall resolution of the 3D model.

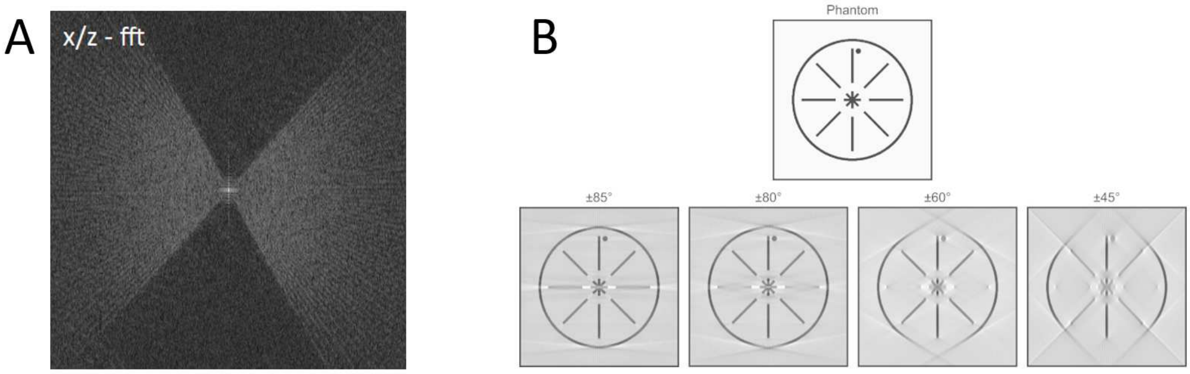

Figure 4-6 The effects of incomplete Fourier-space sampling.
(A) The fast-Fourier transform of a reconstructed tomogram in the *xz*-plane. Missing information can be seen as low information areas towards the top and bottom. (B) Incomplete sample causes artefacts in the reconstructed model in real-space, and the severity is dependent on the amount of information missing. Diagrams adapted from (222).

4.1.4 Utilising cryo-EM for the study of BacM and MXAN0657

With solid-state NMR, Shi and colleagues[60] were able to solve the structure of BacA from *C. crescentus* to atomic resolution. As predicted by our research group[62], the bactofilin domain is a β-solenoid[125]. It consists of six right-handed windings of β-strands that form a triangular core (**Figure 4-7 A**). The β-strands are parallel and engage in hydrogen bonding between the amide and carboxyl groups on the peptide backbone. Typical of a β-solenoid, hydrophobic side chains are buried tightly in the core of the solenoid, and charged residues are arranged on the solvent facing side, with opposite charges stacked on top of each other, further increasing structural stability. Although very informative, the solid-state NMR-solved structure did not offer information of how bactofilins polymerise. It was predicted that the hydrophobic surfaces at the top and bottom of the core domain engage in polymerisation, as the mutation of hydrophobic residues at these sites abolished polymerisation[62] (**Figure 4-7 B**). In order to further understand the polymerisation mechanism of bactofilins, and also the overall structure of bactofilin filaments, cryo-EM helical reconstruction was the method of choice, using BacM as the model system.

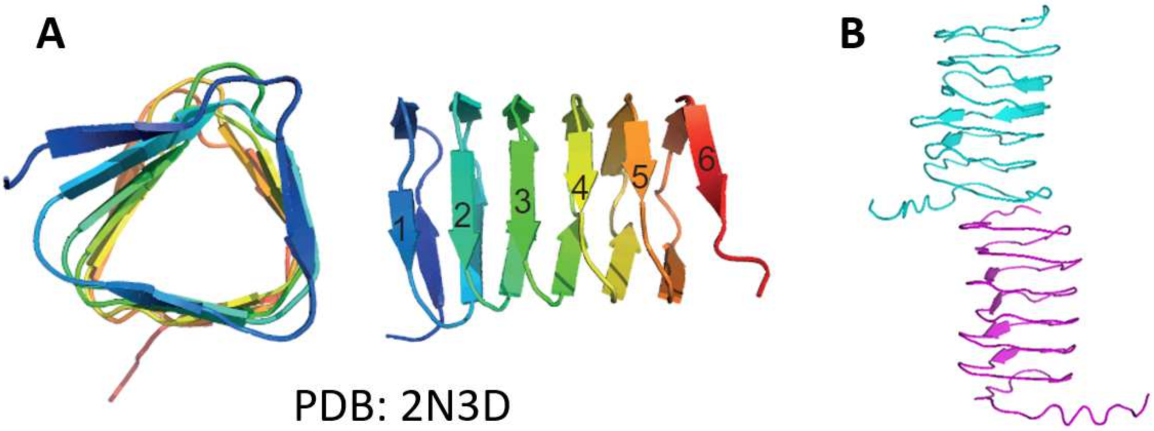

Figure 4-7 Ribbon diagram of the bactofilin domain.
(A) Solid-state NMR-solved structure of the core of BacA[60], showing the triangular arrangement of the β-windings from a top-down view (left), and a side view of the six windings of β-strands that forms the core (right). D(B) *In silico* prediction of BacM polymerisation, where the top and bottom of the bactofilin core engage in interactions[62].

For MXAN0657, the only structural information available so far were from low resolution negative stained micrographs. By using cryo-EM, this study aimed to gain insight into the domain organisation of individual subunits and the number of subunits in a filament unit. It also aimed to verify whether the arms of the filament units are indeed formed of the coiled-coil domain as predicted. Should a high resolution map be achieved, it was hoped that the information could also be used to design a tagged derivative of MXAN0657 for *in vivo* fluorescent imaging.

4.2 Materials and methods

4.2.1 Cryo-grid preparations

Conditions attempted for cryo-grid preparations are listed in **Table 4-1**. To generate cryo-grids, a range of holey carbon or ultra-thin carbon covered lacey carbon grids (Quantifoil) were glow-discharged in Agar TEM Turbo glow-discharge system for 30 seconds. A Leica EM GP Automatic Plunge Freezer was used for vitrification of grids. Three microliters of protein samples of BacM$_{TR}$, native MXAN0657, and his-tagged MXAN0657 at various concentrations were added onto freshly glow discharged grids in the preparation chamber held at constant humidity and temperatures. For cryo-electron tomography, native MXAN0657 was mixed with BSA-coated 10 nm colloidal gold at 1:1 ratio. For multi-blots, samples were applied to grids outside the chamber and blotted with filter paper by hand, and the final blot takes place in the chamber. Various pre-blot and blotting durations were attempted, after which grids were

	BacM$_{TR}$	**MXAN0657 - Native**
Microscope	FEI Tecnai Arctica	FEI Tecnai T12
Voltage	200 kV	120 kV
Electron Source	FEG	LaB$_6$
Energy filtre	-	+
Detector	Falcon III Direct Electron Detector	Charge-coupled device (CCD) camera
Acquisition mode	Counting	-
Electron Dose	$40\ e^-/A^2$	$70\text{-}80\ e^-/A^2$
Defocus	-1.4 to -2.6 µm (@ 0.2 µm steps)	3 µm
Pixel Size	0.98 Å	5.59 Å
Image Size	4096 x 4096 pixels	2048 x 2048 pixels
Tilt range	-	-60^o to $+60^o$
Increments	-	3^o
Software	FEI EPU	SerialEM

Table 4-1 Trial conditions for the cryo-grid preparations of BacMTR, native MXAN0657, or His-tagged MXAN0657.

plunged into a container of liquid ethane. Grids were stored in liquid nitrogen storage dewars until imaging.

4.2.2 Cryo-electron microscopy

Grids were screened at 300kV using a FEI Titan Krios at the Astbury Centre for Structural Molecular Biology, UK, at 200 kV using a FEI Tecnai Arctica with a Falcon III DED at the University of Sheffield, UK, or at 120 kV using a FEI Tecnai T12 with a CCD camera at the Laboratory of Structural Biology Research, USA, at various magnifications. Software used were FEI EPU automatic data collection software and SerialEM, respectively. For data collection, parameters are listed in **Table 4-2**. For data acquisition of BacM$_{TR}$ the FEI Tecnai Arctic was used and imaging was performed with counting mode at 30 seconds of total exposure with 20 – 60 fractions. For cryo-electron tomography of native MXAN0657, FEI Tecnai T12 was used at 0.5 second of exposure at each tilt angle.

	BacM$_{TR}$	**MXAN0657 - Native**
Microscope	FEI Tecnai Arctica	FEI Tecnai T12
Voltage	200 kV	120 kV
Electron Source	FEG	LaB_6
Energy filtre	-	+
Detector	Falcon III Direct Electron Detector	Charge-coupled device (CCD) camera
Acquisition mode	Counting	-
Electron Dose	40 e-/A2	70-80 e^-/A^2
Defocus	-1.4 to -2.6 µm (@ 0.2 µm steps)	3 µm
Pixel Size	0.98 Å	5.59 Å
Image Size	4096 x 4096 pixels	2048 x 2048 pixels
Tilt range	-	-60^o to $+60^o$
Increments	-	3^o
Software	FEI EPU	SerialEM

Table 4-2 Data collection parameters for BacMTR and Native MXAN0657

4.2.3 Cryo-EM data processing

For general visualisations of cryo-EM micrographs and tilt series, IMOD[223] and FIJI[115] image processing software were used. For data processing of BacM$_{TR}$ micrographs, RELION[213,214,217].

Micrographs were first pre-processed and filaments were picked and grouped into three groups depending on appearance (see text). Particles were extracted and parameters attempted are listed in Table 4-3. After particle extraction, 2D classification was performed and the resulting classes were analysed with FIJI.

For tomographic reconstruction, tilt series micrographs were pre-processed, aligned and reconstructed using Bsoft[224,225] or the Etomo tomography processing package from IMOD[226]. From the reconstructed tomogram, particles were picked using Bsoft, and extracted particles were aligned and averaged, also using Bsoft. UCSF Chimera software[227] was used for the visualisation of 3D maps of reconstructed filaments and 3D maps of subtomogram averaged filament units. Mass and resolution estimation of averaged maps were performed with Bsoft.

	Thick	**Double**	**Thin**
Particle box size (pix)	80 - 376	152 - 376	152 - 376
Tube diameter (Å)	35 - 120	35 - 62	35 -65
Number of asymmetrical units	1 - 4.5	1 - 1.5	1 - 10
Helical rise (Å)	30 - 58	31 - 65	30 - 65

Table 4-3 Range of parameters tested for BacMTR particle extraction from micrographs.

4.3 Results

4.3.1 BacM$_{TR}$ filament morphology with negative staining

As mentioned in **Section 2.3.4**, a protocol for isolating BacM$_{TR}$ filaments was developed. To assess whether this sample would be suitable for cryo-EM analysis, the isolated filaments were first inspected with negative staining. TEM micrographs in (**Figure 4-8**) showed that filaments adopted two major forms. First is what appeared to be single filaments of 3 nm in width with a smooth exterior. Second is parallel filaments that appeared to have a small gap in between. These double filaments also showed the ability to twist, which could indicate an inherent helical property and could greatly assist in structure determination. A potential problem was the high flexibility of the filaments, as it may affect quality of classifications. Regardless, this sample was used for cryo-grid preparations.

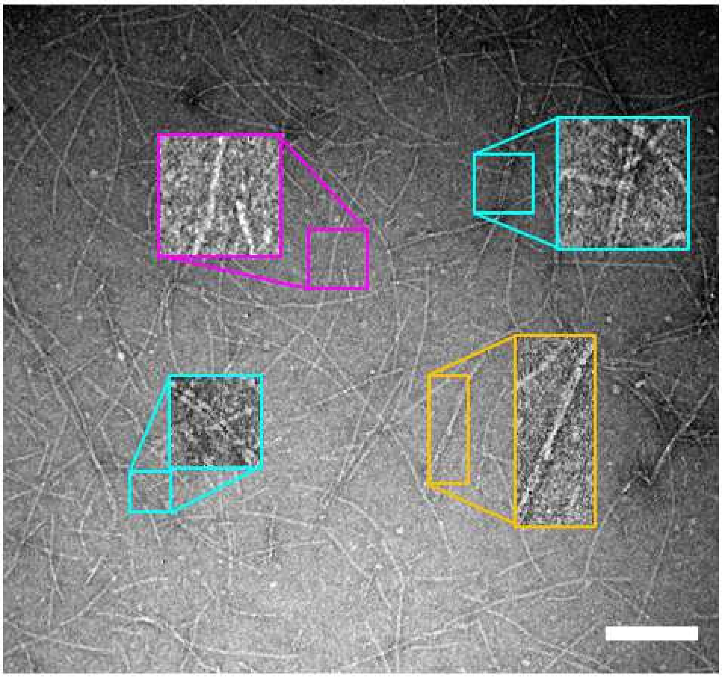

Figure 4-8 TEM micrograph showing morphology of BacM filaments in negative staining. The micrograph shows that BacM can adopt single (lilac insert) and double filament (cyan insert) conformations. The double filaments can also be seen to twist (orange insert). Scale bar = 50 nm.

4.3.2 Screening of BacM$_{TR}$ cryo-grid preparation conditions

The major criterion of a successfully prepared cryo-grid are the ice thickness and the sample distribution. To achieve these for BacM$_{TR}$, a range of conditions were tested, as listed in (**Table 4-1**). Since BacM$_{TR}$ forms long filaments very readily, it made a solution of high viscosity when dissolved, even at the low concentration of around 0.4 mg/ml. This greatly increased difficulty of liquid handling, and caused inconsistent blotting results, ice thickness, and sample distribution. To solve this, the sample was diluted to 0.05, 0.1, or 0.2 mg/ml. To alleviate the problem of decreased sample deposition on the grid due to the decreased concentrations, multiple blotting was performed, involving multiple applications of sample and blotting. This has been shown to increase sample density to an even greater effect than increasing sample concentration[228]. It also has the added benefit of improving sample distribution to the ice holes.

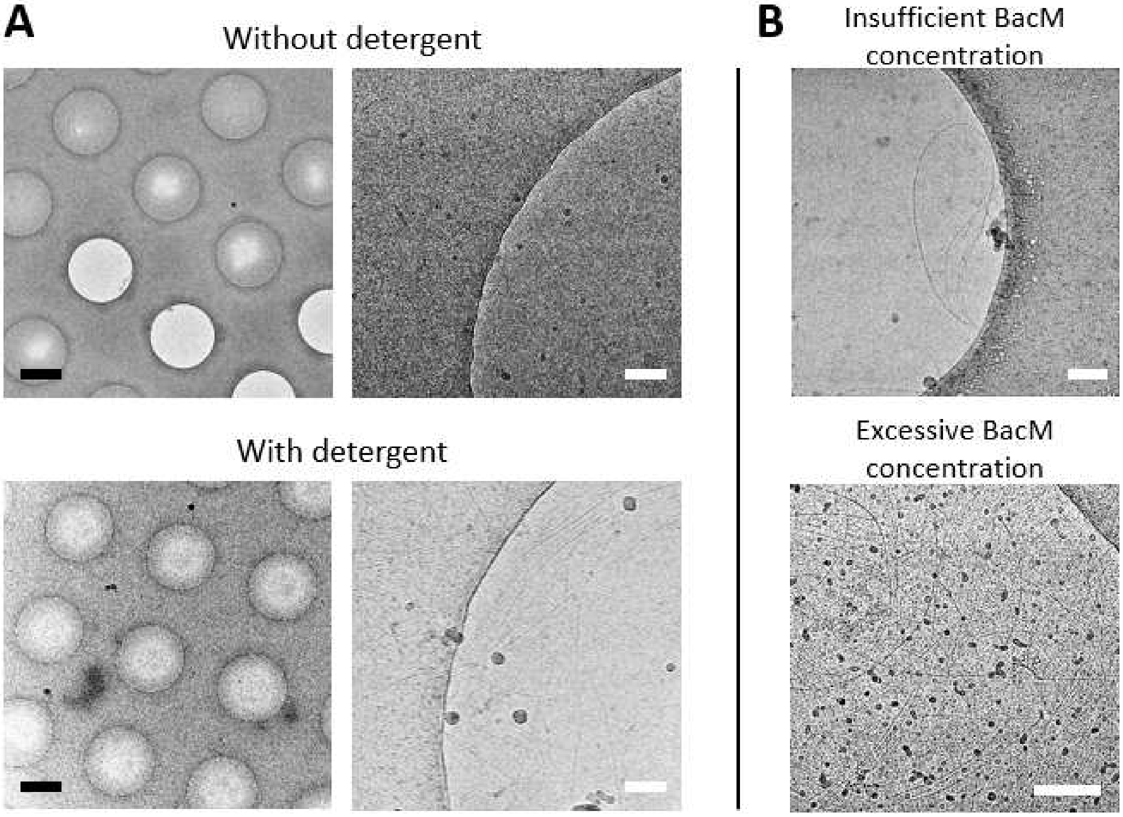

Figure 4-9 Cryo-TEM micrographs showing examples of BacM cryo-grid preparations
(A) Micrographs showing the effects of the addition of β-DDM into BacM samples before vitrification. Ice thickness was highly variable and undesirable without β-DDM, and thick ice reduces SNR and contrast (top). With β-DDM at 0.05%, ice thickness was much more reproducible, and BacM filaments were able to distribute into ice holes at ideal ice thicknesses (bottom). (B) Micrographs showing examples of sample distribution. Top micrographs show insufficient filaments visible in the ice holes, and bottom micrograph shows overly abundant filaments in the ice hole. Black scale bar = 1.5 μm. White scale bar = 100 nm

Another problem encountered was the non-uniform distribution of ice after freezing, with holes with thick ice, and holes that were ice free (**Figure 4-9 A,** top). Thick ice is undesirable as it reduces SNR, reducing contrast. This might be due to the uneven distribution of the networks of BacM$_{TR}$ filaments on the grid surface, causing uneven dewetting after blotting[229]. This was solved by the addition of a low concentration of detergent n-dodecyl β-D-maltoside (β-DDM) at 0.05%. Surfactants have been shown to promote uniform ice thickness, and BacM has been shown to be resistant to detergent treatment[62]. Major improvements were indeed seen in ice thickness distribution (**Figure 4-9 A**, bottom).

Other parameters were varied, including grid types, blot number and duration, sample concentrations and additives, which gave varying quality of filament distribution and density (**Figure**

4-9 **B**). Eventually, a condition that gave satisfactory ice thickness, ice coverage, filament distribution and density was found, and the resulting grid was chosen for data acquisition.

4.3.3 BacM$_{TR}$ cryo-EM data acquisition and processing

Parameters for data acquisition are listed in (**Table 4-2**). From the acquired micrographs, it could be observed that BacM$_{TR}$ adopts three major conformations: thin filaments; double filaments, and thick filaments (**Figure 4-10 A**). It was originally thought that the thick filaments were a different form of higher ordered arrangement of BacM filaments, for instance a helical arrangement of protofilaments. At areas of very high filament density, 2D lattices could sometimes be seen (**Figure 4-10 B**), which has been reported for C-terminally His-tagged BacA[126] and CcmA from *H. pylori*[66]. Performing Fourier transform of a patch of lattice gave signal peaks at 56 Å in two directions, which agrees completely with measurements from CcmA. The lattices appear to be formed of 3 nm filaments 'woven' together at spacing of 5.6 nm, and may be able to form sheets of indefinite sizes given high enough concentrations of BacM$_{TR}$.

To begin helical reconstruction of the BacM$_{TR}$, filaments in the collected micrographs have to be picked, using RELION[213,214,217], a program for EM data processing and structure refinement. Filaments were grouped into 'thick', 'double', and 'thin' classes. More detailed observations of the filaments in the dataset revealed that the thick filaments are likely multiple filaments stacked in the *z*-axis, giving the thicker, darker appearance. This caused complications in filament classification as it was difficult to determine how many filaments formed a given thick filament, increasing group heterogeneity, which negatively affects the subsequent step of 2D classification. Moreover, at low defocus values, thick filaments could appear as thin filaments due to the lowered contrast, further increasing group heterogeneity.

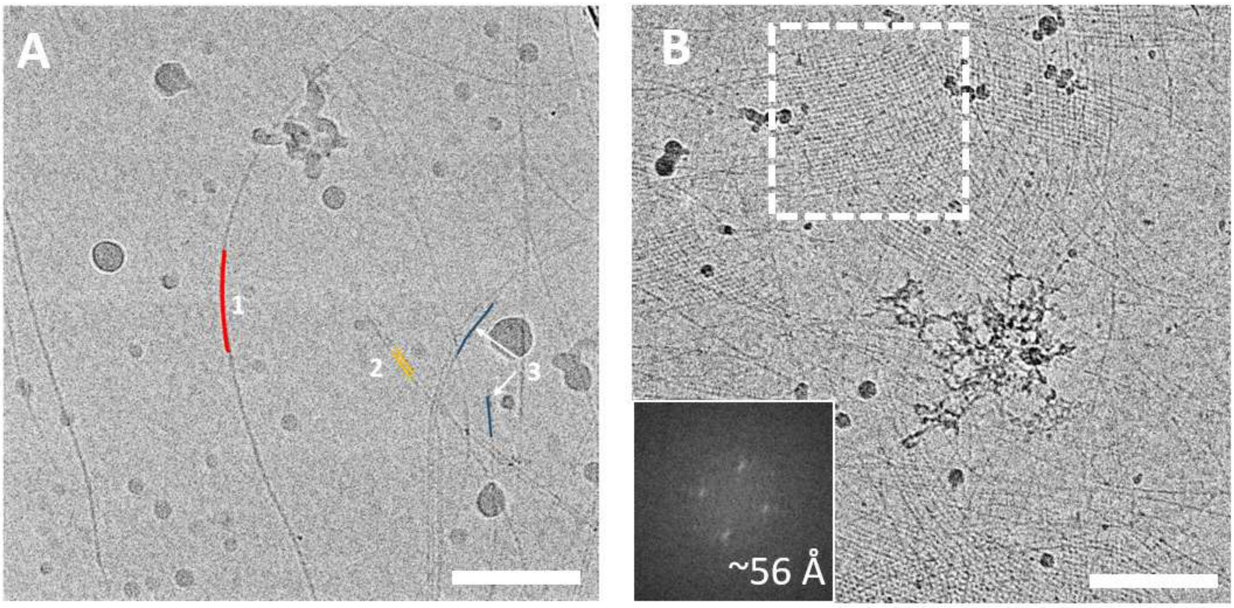

Figure 4-10 Cryo-TEM micrographs exhibiting morphology of BacM filaments in ice.
(A) BacM adopts three major forms. Thick filaments (1, red line)), double filament (2, orange lines), and thin filaments (3,). (B) BacM can also form a 2D lattice at high concentrations. Insert is the Fourier transform of the area in dashed box. The frequency domain showed maxima at a frequency of around 56 Å in two directions. Scale bars = 50 nm

To increase efficiency of filament picking, the auto-picking function of RELION was attempted[217]. Templates for auto-picking were generated by manually picking filaments for the three groups and performing 2D classification on the extracted filament particles. Inspection of the picked coordinates showed that the auto-picking function was not able to distinguish the different groups of filaments from a micrograph, and further adjustments of auto-picking parameters did not generate satisfactory results. Therefore, filaments had to be manually picked.

4.3.4 Filament segment extraction and 2D classification of BacM$_{TR}$

Once filaments start and end coordinates were picked, the next procedure was particle extraction, where segments of filaments were extracted in boxes, after which they could be treated as single particles for further processing. A number of parameters are important for this step including helical rise and number of new asymmetrical units per box. These parameters calculated the inter-box distance with this formula[217] (**Figure 4-11 A**):

$$Inter\text{-}box\ distance\ (pixel) = \frac{Helical\ rise\ (\text{Å}) \cdot No.asymetrical\ units}{Pixel\ size\ (\text{Å}\ /pixel)}$$

RELION requires prior knowledge of how many new asymmetrical units each box offers to calculate SNR. It also requires it for calculating the rotation and phase shift needed in 3D Fourier-space for each filament segment to perform 3D reconstruction[217]. Helical rise for BacM$_{TR}$ could be estimated, at least for the thin filaments, from height of the solid-state NMR-solved structure of BacA monomer from *C. crescentus*[60], which is approximately 29 Å. Inter-box distance is an important consideration, as more flexible filaments requires smaller inter-box distance to compensate for curvatures, but could increase computational costs as it increases extract filament segments too. Different combinations of parameters for particle extraction were tried (**Table 4-3**) (**Figure 4-11 B**), and 2D classifications were performed on the extracted segment.

The nature of β-solenoid core of BacM is a point of concern for further data processing. If bactofilin subunits do polymerise in the direction of β-sheet stacking, as suggested in previous studies[59,126], the repeating and similar appearances of the β-strands may result in inaccurate assignment of filament segment translation. To explain further, to perform 2D classification or 3D model, RELION needs to determine how much each filament segment should be translated along the filament axis so that each asymmetric unit can be averaged. The repeating nature of β-sheets may cause local probability maxima during translational searches, causing BacM$_{TR}$ subunits to be aligned out-of-register (**Figure** 4-11 **C**).

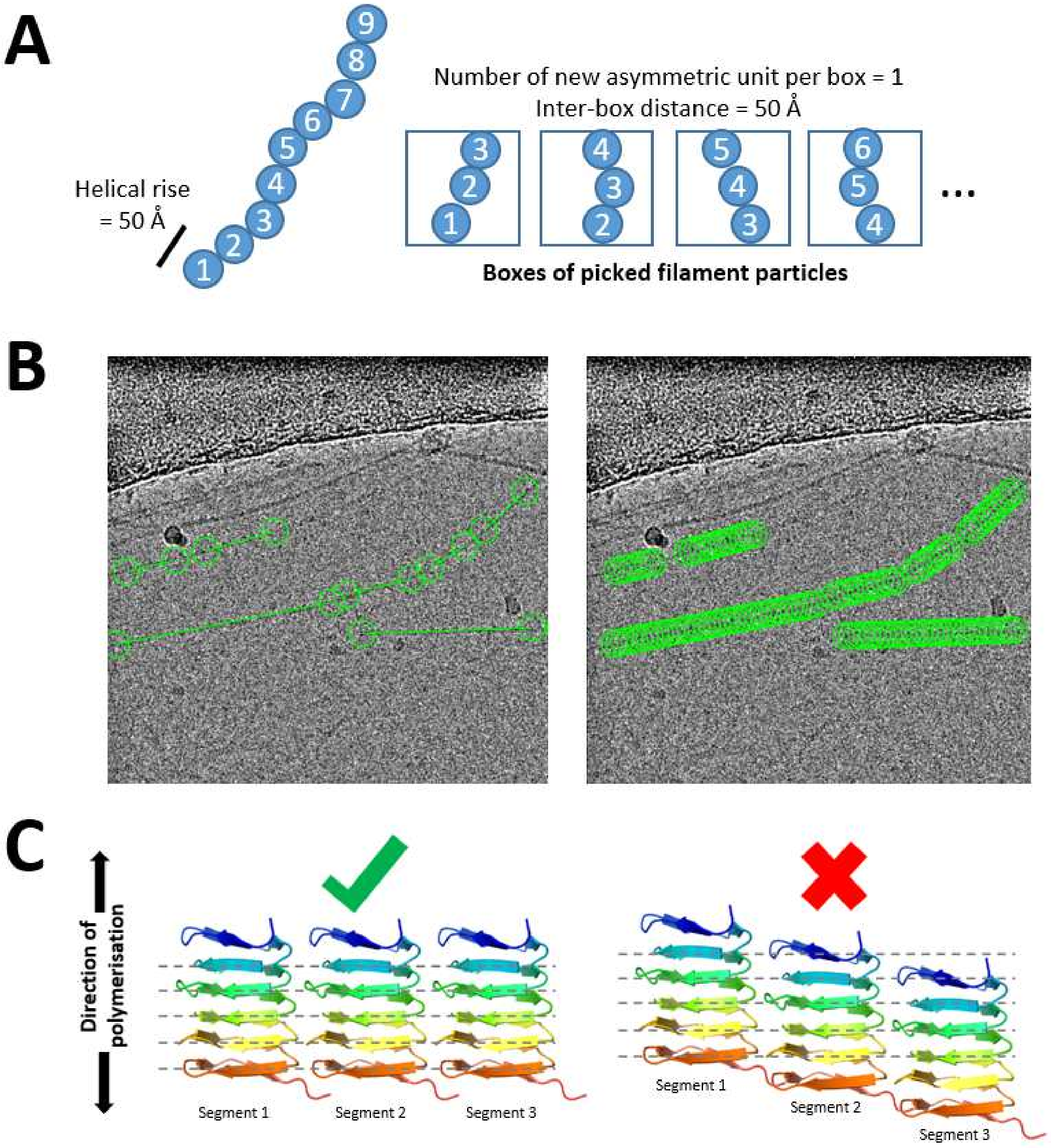

Figure 4-11 Considerations for particle extraction and 2D classification.
(A) The relationship between helical rise, number of asymmetrical units, and inter-box distance. Left is an imaginary filament with a helical rise of 50 Å. If the asymmetric unit value is to 1, inter-box distance will be 50 Å. (B) Example of filament picking and particle extraction from micrographs of vitrified BacM$_{TR}$ filaments. First, filament start and end coordinates are selected (left), then after extraction parameters are defined, RELION will extract filament particles (right). (C) The β-strands in the bactofilin domain may be too similar for accurate determination of translational shift during 2D classification. This would lead to undesired out-of-phase averaging of asymmetrical units (right). Grey dashed lines highlight the 'register' of the β-strands. Cartoon model of BacA (PDB: 2N3D) (60).

In total, 22,091 segments were extracted for thick filaments, 29,345 segments were extracted for thin filaments, and 4,428 segments were extracted for double filaments. The best 2D class of thick filaments showed periodic intensity variations with a frequency of around 29 Å, and finer striations could be seen at intervals of approximately 4.9 Å (**Figure 4-12 A**). Visualising this 2D class with an intensity profile along the filament axis gave very similar measurements (**Figure 4-12 B**). Measuring the full width at half maximum of the intensity profile in the orthogonal axis gave a value of approximately

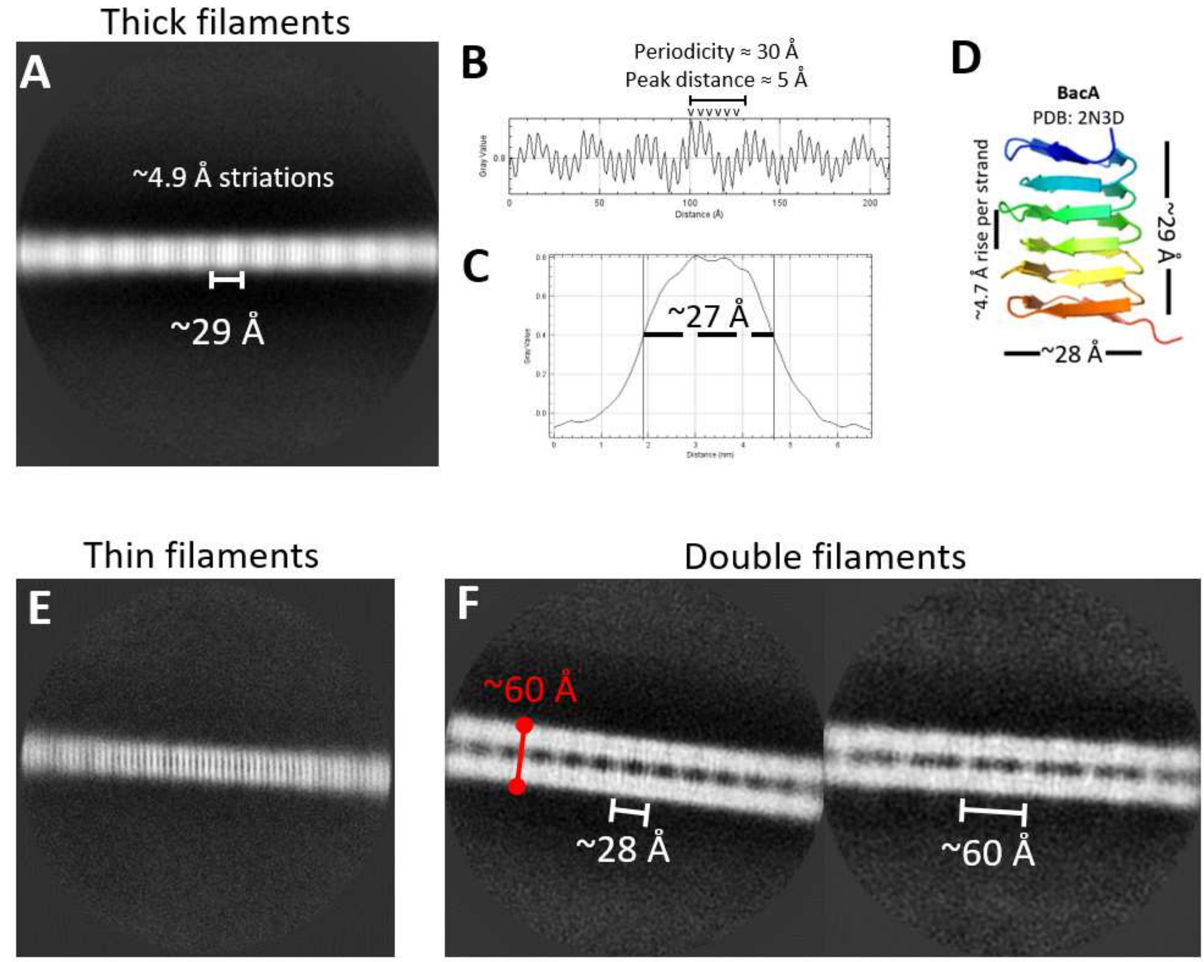

Figure 4-12 2D classification of the different classes of picked BacM filaments.
(A) 2D classification of picked thick filaments gave fine striations 4.9 Å apart, and intensity periodicity of around 29 Å. (B) Intensity profile down the longitudinal axis of the filament in the 2D class, showing very similar measurements to (A). It also showed that there are six peaks in each repeating period. (C) Intensity profile down the lateral axis of the filament in the 2D class. Measurement of full width at half maximum gave 27 Å. (D) Measurements of published structure of BacA gave very similar measurements to the thick filament 2D class (60). There were also six β-strands per bactofilin domain, agreeing with observations from (B). PDB: 2N3D. (E) 2D class of thin filaments showed striations similar to (A). (F) Double filament 2D classes showed connecting densities between strands at either 28 Å or 60 Å apart. The full width at half maximum was around 60 Å.

27 Å (**Figure 4-12 C**). These measurements were in agreement with those of the published BacA monomer structure[60] (**Figure 4-12 D**). The periodic intensity variation may correspond to the repeated stacking of BacM_{TR} monomers, which was surprising to see given the abovementioned possible alignment problem. The intervals of the finer striations were in agreement with the distance between β-strands measured from BacA, and also from cryo-EM solved structures of amyloid filaments, which are also formed of parallel β-strands[230,231]. Additionally, it could be seen that there are six striations in every intensity period, which matches the number of helical turns per bactofilin unit. The width of the filament also agreed with the approximated width of the bactofilin core of BacA. These results suggest that the BacM do indeed polymerise in the direction of β-strand stacking. The fussy edges of the filament could be due to the unresolved solvent-accessible side chains of the bactofilin core. The blurring of the ends of the filament in the 2D class was mostly likely due to the flexibility of BacM_{TR} filaments.

The best thin filament 2D class gave the fine striations seen in the thick filament 2D class above, but no intensity periodicity could be seen (**Figure 4-12 E**). An explanation for this could be the fact that thick filaments are formed of multiple filaments in alignment. This may boost the signal of individual β-strands, allowing RELION to perform translational searches more accurately. In thin, single filaments however, the signal is much weaker, so that the out-of-register problem takes place.

For double filaments, much less detail could be seen from their 2D classes, which was partly due to the lower number of segments extracted for this group. It was striking to see densities bridging the approximately 13 Å gap between the thinner filaments (**Figure 4-12 F**). Two different periodicity of the 'bridges' could be seen, at 28 Å, or 60 Å. It is likely that the C-terminal tail of BacM_{TR} is responsible for the densities. It could not be determined which was the correct or biologically relevant 2D class. If the former is correct, this would suggest that BacM is a polar filament in which subunits polymerise by interactions of the N-terminal side and C-terminal side of the bactofilin domain. If the latter is correct, this would suggest that the subunits interact in a N- to N-terminus and C- to C-terminus manner, giving a non-polar filament. The width of the double filament was approximately 60 Å, which was slightly higher than the repeating frequency of the 2D lattice observed above, possibly suggesting that filaments are packed more tightly in the 2D lattice

Because no twist could be observed in the thick or double filaments, and that thin filament segments could not be averaged in register, helical reconstruction could not proceed. A different method of sample preparation is possibly required.

4.3.5 Cryo-electron tomography of MXAN0657

Early attempts to natively isolate MXAN0657 gave very low yields of filaments and had many impurities. Cryo-grids prepared had very few filaments and it was apparent that filaments had one single preferred orientation in ice as on carbon with negative stain (**Figure 4-13**). It is known that some protein particles exhibit major orientation preferences when exposed to the water-air interface prior to vitrification[220,232]. Since a SPA approach requires particles to adopt random orientations, cryo-electron tomography (cryo-ET) was the most suitable technique to compensate for the lack of orientation diversity.

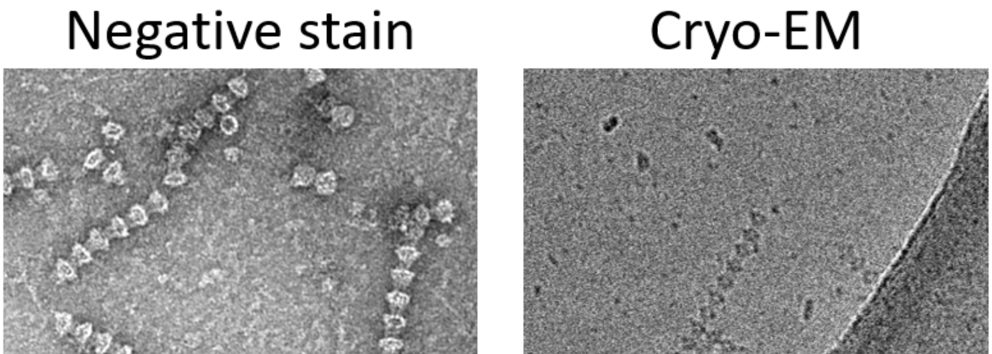

Figure 4-13 MXAN0657 filaments showed only a single orientation.
TEM micrograph of MXAN0657 filaments visualised with negative staining (left) and cryo-EM micrograph of vitrified MXAN0657 show lack of orientation variety. Scale bars = 100 nm.

MXAN0657 filaments were mixed with 10 nm colloidal gold particles as fiducial markers for tilt alignment before vitrification. Cryo-grids were screened for ice thickness and crystalline ice contamination, and areas with filaments and more than 10 gold particles in the field of view were selected. Data collection parameters are listed in **Table 4-2.** The tilt scheme used was the bidirectional tilt scheme, starting at 0° tilt angle, moving to -60° at 3° increments, and then proceeding to +3° to +60° (**Figure** 4-14). This scheme has the disadvantage of dose asymmetry, where the dose of electrons experienced by the sample is lower at negative angles than at positive angles, leading to asymmetrical sample degradation. An example of a tilt series is shown in (**Figure 4-14**).

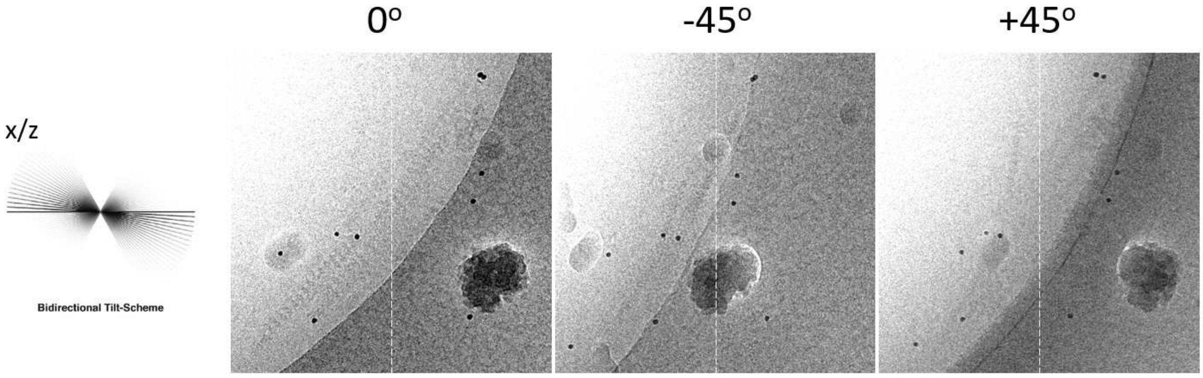

Figure 4-14 Example micrographs at different tilt angles of the tilt series.
Schematic on the left shows the tilt-scheme used (adapted from (233)). Since the scheme began at 0° toward -60°, then from +3° to +60°, sample quality shown here is the highest at 0° and the lowest at +45° as seen by the degrading contrast. Tilt axis is depicted by the dashed white line.

4.3.6 Tomographic reconstruction of MXAN0657 cryo-tilt-series

Two different programs were available during this study for tomographic reconstruction. One is Bsoft[224,225], and the other was Etomo[223,226]. Their difference lays in the method in which reconstruction is performed. Bsoft operates in the reciprocal-space during reconstruction, and Etomo performs back-projection in real-space. This gives Bsoft the advantage of having a dampened missing wedge ray artefact due to missing information beyond certain tilt angles (**Figure 4-15**). Therefore, Bsoft was chosen for further data processing, but for ease of visualisation in this report, images from Etomo are shown as they have higher contrasts (**Figure 4-15**).

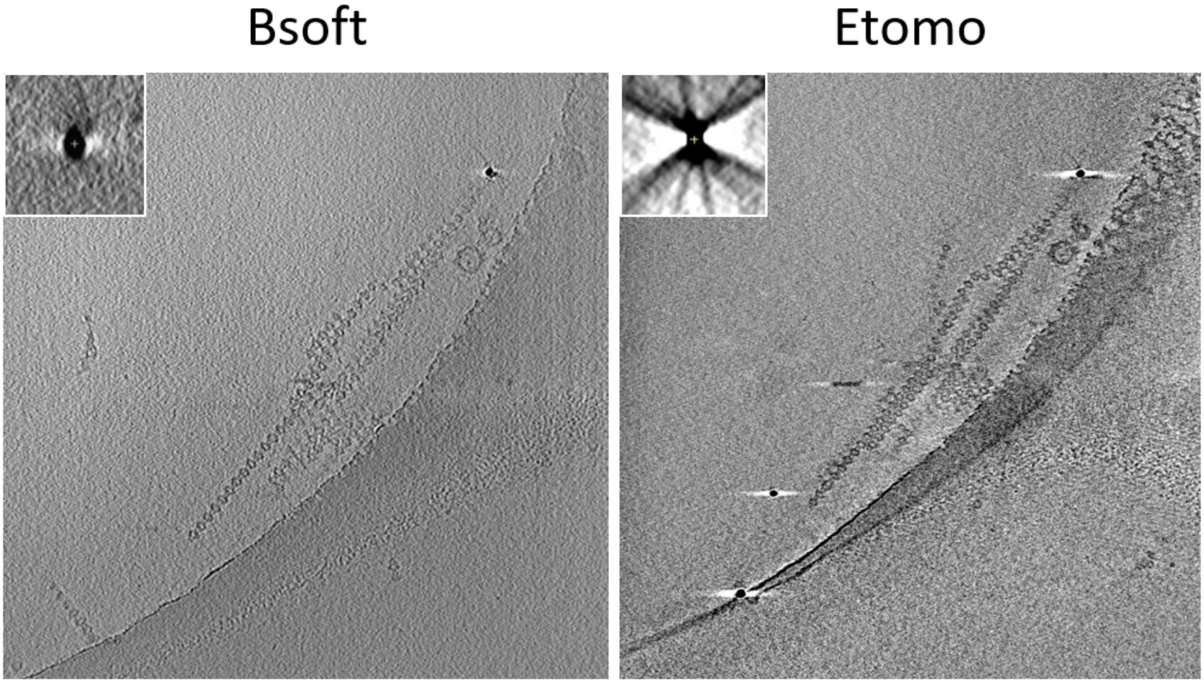

Figure 4-15 Differences in tomograms generated by Bsoft and Etomo.
Bsoft performs tomographic reconstruction in reciprocal-space, which gave less streaking artefacts than the reconstruction from Etomo, which performs it with back-projection in real-space. Inserts are gold particles viewed in the *xz*-plane.

After successful tomographic reconstruction, filaments could be seen as multi layered bundles (**Figure 4-16 A**). Observation of the space-filling 3D density map of filaments suggests that the ring-shaped globular heads are in-plane with the arms (**Figure 4-16 B**). Filaments could be seen to associate with each other at the base of the arms, or at the globular heads (**Figure 4-16 C**). Filament have also been observed to associate in an anti-parallel fashion. In this report, filament direction is determined by the end leading with the globular head. It appeared that filaments could laterally associate with the globular heads in the neighbouring filament in register or in staggered formation, where the heads are positioned at the recess created by the arms in the adjacent filaments (**Figure 4-16 C**). These have been also observed on carbon film with negative staining. Parallel filaments have not been observed in the hydrated frozen state, but were seen in negative staining. It was not clear what filament arrangements are found inside cells, but it should be noted that when protein samples are absorbed into the carbon film and dried for negative staining, protein structure and arrangements could change.

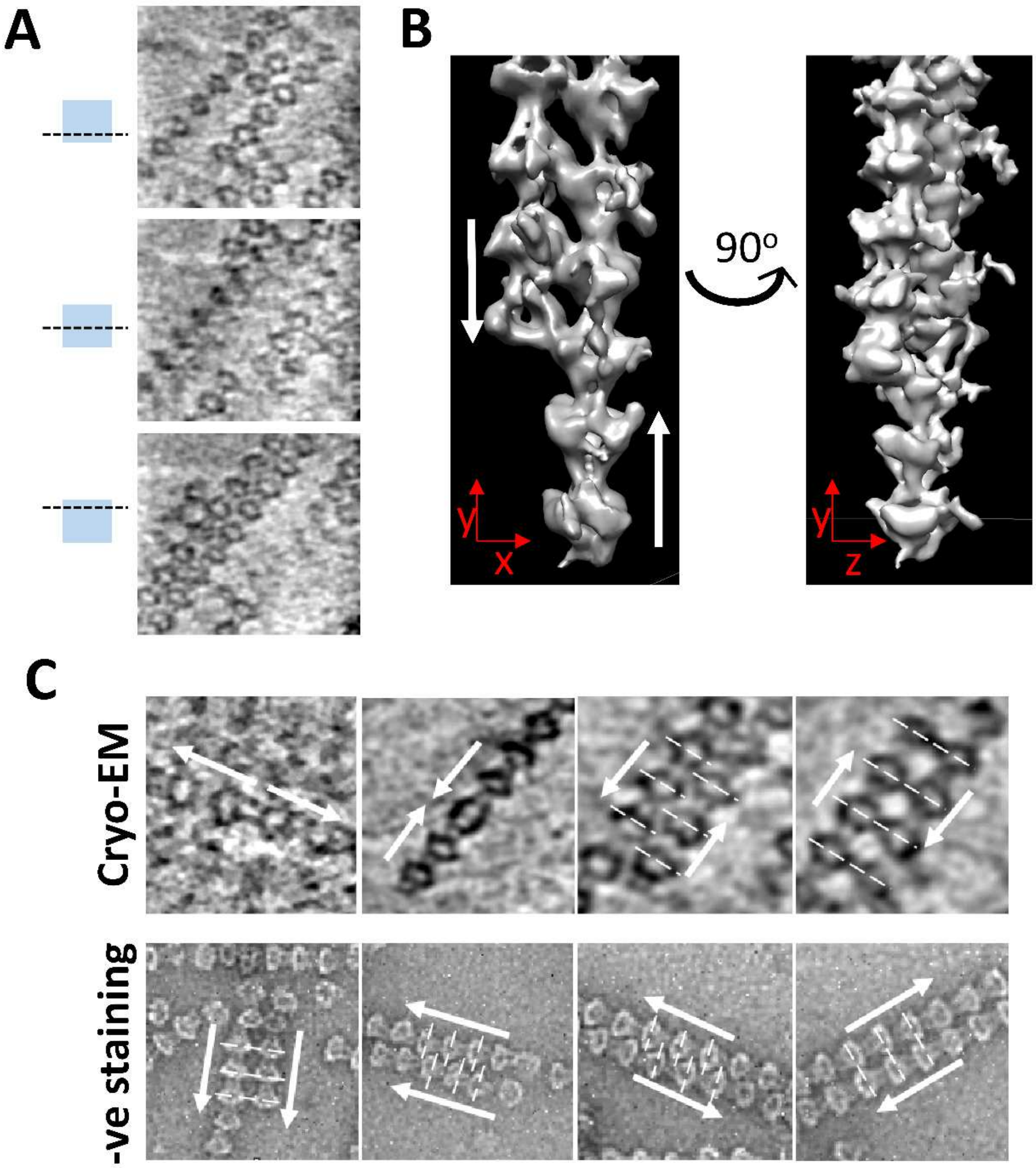

Figure 4-16 Tomograms of vitrified MXAN0657 filaments.
(A) A section of a tomogram containing MXAN0657 filaments shown at different z-depth. (B) Space-filling 3D map of MXAN0657 filaments in a tomogram, seen down the *z*-axis (left) and the *x*-axis (right). Notice the anti-parallel direction of the filaments (white arrows). In this report, the direction of the arrow depicts the direction leading with the globular head of MXAN0657 filament segment. (C) Comparison of MXAN0657 in cryo-conditions, and in negative stain. In ice (top), filaments can be seen in contact with each other's globular heads, or at the arms. They can also be seen to associate laterally in an anti-parallel fashion, either in register, or staggered, as shown by the doted white lines. In negative stain on carbon film (bottom), The above could be seen, but also filaments in parallel, in register and in staggered formation

4.3.7 Subtomogram averaging of MXAN0657

To gain more information on the structure of the MXAN0657 filament unit, subtomogram averaging was performed. This involved the picking and extracting of individual filament unit in 3D space (**Figure 4-17 A**). Bsoft then calculated the 3D rotation and translation required for proper alignment, and averaged the signal from each segment. A mask was used to compensate for the missing information within the missing wedge to avoid alignment bias[225]. In total, around 262 segments were extracted, and the resulting average map had a resolution of 36 Å to 50 Å, taken at Fourier shell correlation (FSC) value of 0.143 or 0.5, respectively (**Figure 4-17 B&C**). In the average map of the filament unit, the ring-shaped head could clearly be seen to be in plane of the arms. The estimated size of a single filament unit was around 0.6 – 0.8 MDa, equivalent to around 8 to 10 MXAN0657 polypeptides. This was likely an over estimate, however, due to the smearing and elongation of the average map in the *z-axis* as a result of the missing wedge effect, and also the presence of extra densities at the top and bottom of the map included from the preceding and succeeding filament unit (**Figure 4-17 C)**.

From the 3D density map of the tomogram (**Figure 4-16 B**), and the subtomogram average map above, it became clear that the data here did not agree with the previously suggested architecture of MXAN0657. The existing model proposed that the plane of the ring-shaped globular head is perpendicular to that of the arms' direction (**Figure 4-17 D,** left)[110]. Presumably, the globular domains of individual subunits would form the ring, and the coiled-coil domains would form the arms. This implies that each subunit would be experiencing identical environments. The model suggested from average maps in this study places the ring-shaped head in-plane with the arms' direction (**Figure 4-17 D,** right). This may point towards a mechanism were half of the subunits assembles into half of a filament unit, and then further associates with another 'half-filament unit' to form a complete filament unit, which could then polymerise to filaments. At the low resolution of the average maps, little more information could be derived, and it was disappointing that outlines of individual subunit globular domain could not be observed.

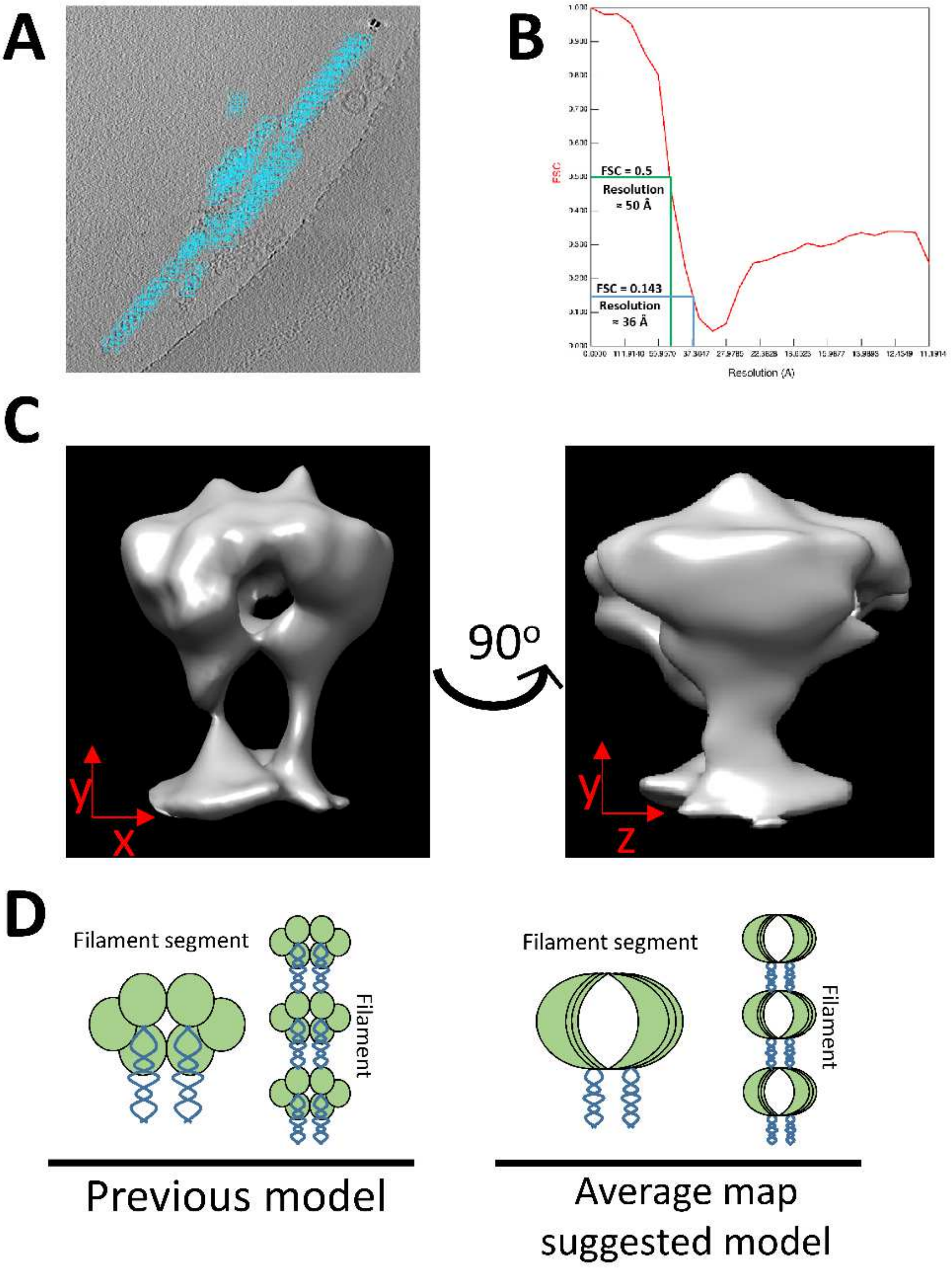

Figure 4-17 Subtomogram averaging of MXAN0657 filament unit.
(A) Individual filament units were picked manually. (B) Fourier-shell correlation plot with estimated average map resolution at FSC = 0.5 (green lines) or 0.143 (blue lines). Note the secondary 'bump' in the plot. (C) The average map of a filament unit. The ring-shaped globular head appeared to be in plane with the arms of the unit. Note the elongation in the z-direction is due to the missing wedge effect. Extra densities can be seen at the top and bottom of the average map due to the way units were picked, the extra densities belonged to the units above and below the one shown. (D) Comparison of MXAN0657 models. The original model shows that the plane of the ring-shaped globular heads is perpendicular to the direction of the arms. The subtomogram averaged map suggests the ring-shaped globular heads are in-plane with the arms. The number of subunits in one filament unit shown here is arbitrary.

It should be noted that the resolution of the subtomogram averaged map is difficult to assess. The quality and resolution of information varies throughout the tilt series, affected by factors such as ice thickness at high tilt angles, and accumulated irradiation damage. From the Fourier-shell correlation plot in (**Figure 4-17 B**), a secondary 'bump' could be seen towards the right-hand side of the graph giving a bilobal appearance. This could be a sign for over fitting, or problems in reconstruction or averaging. In this situation, it was likely due to the high amount of box-overlapping during particle picking, and also the highly similar angle of rotation of particles during alignment search caused by the strong directionality of filaments[234]. These problems however are inconsequential due to the low expected resolution of the average map.

4.3.8 Further cryo-grid preparations of MXAN0657

With the improved isolation protocol of native MXAN0657 filaments developed for this study, additional cryo-grids were prepared in an attempt to increase sample density on the cryo-grid. This way a recently described tilt-based strategy could be utilised to alleviate problems associated with the preferentially oriented MXAN0657[235]. This strategy requires micrographs to be taken at a range of tilt angles, e.g. at 0°, 10°, 20°, 30°, 40°, and 50° of different filaments orientated in different directions in the *xy*-plane. This way, each filament would only be exposed once, instead of multiple low doses in conventional tomography. The authors reporting this strategy obtained a near-atomic resolution structure of a preferentially orientated protein particle using this method[235]. As with BacM$_{TR}$, a range of conditions were trialled (**Table 4-1**). MXAN0657 filaments had a strong tendency to aggregate at edges of holes regardless of concentrations (**Figure 4-18,** top), and the addition of detergent did not solve this problem. Since MXAN0657 could be observed as unbundled and non-aggregated filaments on carbon films during negative staining, ultra-thin amorphous carbon-coated lacey carbon grids were used to replicate this condition. Bundling and aggregation could still be observed regardless of concentration (**Figure** 4-18**,** bottom). Clearly, a radically different strategy was called for to achieve satisfactory filament distribution.

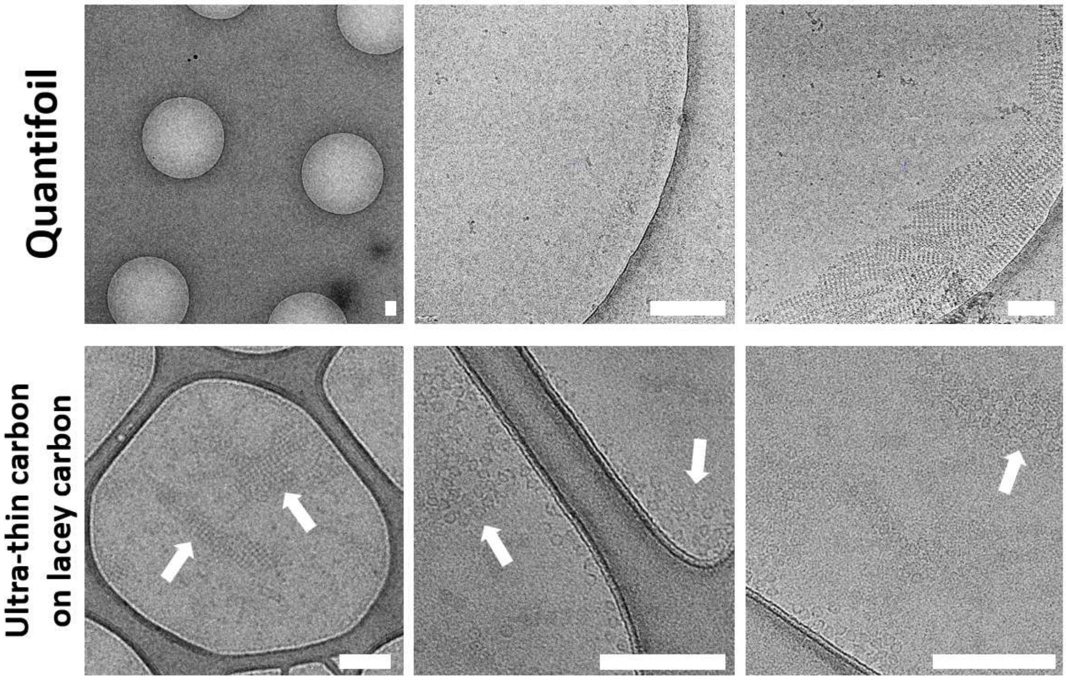

Figure 4-18 Further cryo-preparations of MXAN0657.
(Top) Detergent was used for further trials with Quantifoil grids, at different concentrations of MXAN0657. Although ice thicknesses were ideal, the filaments have the tendency to bundle at the carbon hole edge. (Bottom) Trials with ultra-thin carbon coated lacey carbon grids showed heavy bundling, as indicated by the white arrows. Scale bars = 200 nm.

4.3.9 Cryo-grid preparations of His-tagged MXAN0657

As described in **Section 3.3.4**, when MXAN0657 was expressed as two fragments in *E. coli* with a His-tag attached to the latter half, single filament units were formed, which appeared to have a range of orientations when imaged with negative staining under TEM. Therefore, it would be appropriate to generate cryo-grids for his-MXAN0657 so that single particle analysis could be attempted. Again, the conditions for grid preparations are listed here (**Table 4-1**). The use of detergent appeared to have the opposite effect previously stated, as his-MXAN0657 seldom spread into ice holes, and was preferentially positioned on the carbon support (**Figure 4-19 A**). Without detergent, the filament units did distribute into ice holes, but closer inspection revealed that many units appeared denatured or unfolded (**Figure** 4-19 **B**). It is known that proteins are susceptible to denaturing or folding when absorbed to the water-air interface[232,236]. This was not observed during negative staining visualisations. Strands of densities could be seen which formed arcs or even full circles. The diameter of these were larger than the dimensions of individual filament units, indicating a high level of unfolding. One possibility is that since the protein was expressed as two fragments, the fragments could dissociate upon denaturation, and fragments with the coiled-coil domain could associate to form long, thin structures. Another possibility, which may indicate that the previously published model is accurate, is that the separation of the two fragments reduced the integrity of the ring-shaped head, leaving some of them 'opened' hence forming the arcs observed (**Figure 4-19 B,** second from right). Additionally, some of these opened rings could interact with their now exposed interaction surfaces, forming larger rings (**Figure 4-19 B,** far right). Indeed, some of the larger rings have a beaded appearance which could represent individual globular subunits (**Figure 4-19 B,** far right).

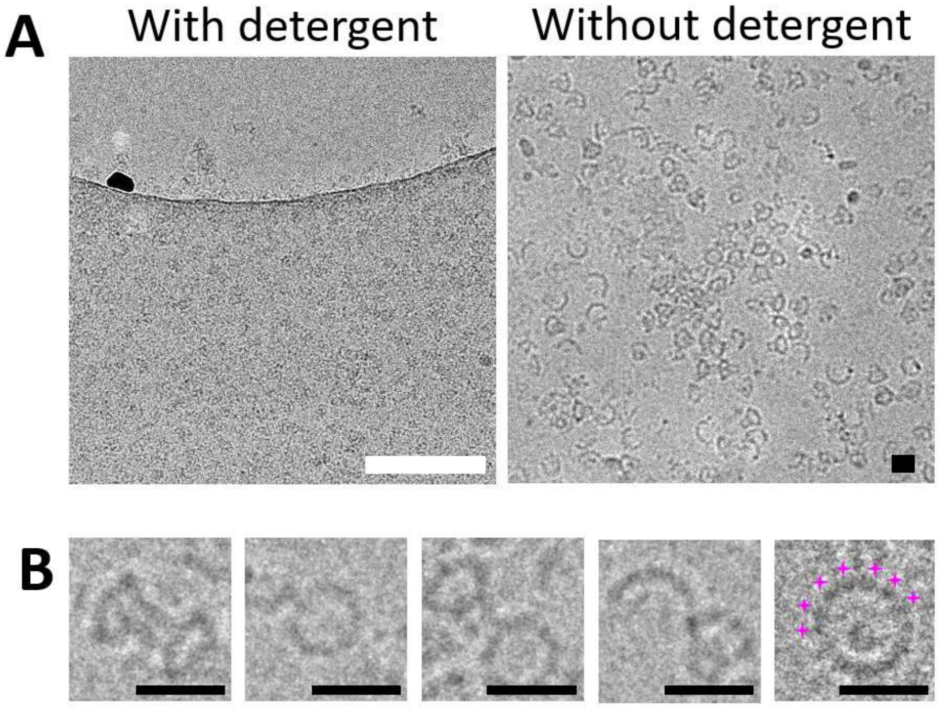

Figure 4-19 Cryo-preparations of his-MXAN0657
(A) His-MXAN0657 have the tendency to remain at the carbon film when detergent is added (left). Without detergent, his-MXAN0657 do spread to the ice, but appear denatured and unfolded. (B) Micrographs of his-MXAN0657 conformations. Assemblies could be seen to be unfolded and could form arcs or circles. Some repeating 'beads' could be seen in some of the circles. White scale bar = 200 nm. Black scale bars = 20 nm.

4.4 Discussion

4.4.1 On sample preparation

As demonstrated from this study, sample preparation remains to be a major bottleneck for cryo-EM structural studies of proteins[220,229,232,236]. Current methods for grid preparations still rely mostly on the method by Dubochet and colleagues from 1984[188], where sample solution is applied to a carbon film-covered grid, excess liquid blotted away with filter paper, and the remaining solution allowed to form an inherently unstable thin aqueous film[229] before rapid vitrification by plunge freezing into a cryogen. This means that cryo-grid preparations often have low reproducibility, consistency, and scalability. These have partially been addressed by recent improvements in commercially available equipment. Indeed, sample optimisation should take place before attempts are made for generating cryo-grids, but as seen above for BacM$_{\mathrm{TR}}$, native MXAN0657 and his-MXAN0657, samples could appear optimal for cryo-grid preparations, but proteins could behave very differently on any given cryo-grid and it is difficult to predict beforehand how to counteract this deficiency.

There are a number of methods that could be attempted to solve the issues of non-ideal distribution, preferred orientation, and denaturation of BacM$_{\mathrm{TR}}$, native and his-tagged MXAN0657. One is the use of continuous graphene-coated grids[236]. Graphene is extremely strong and electron transparent, and although highly hydrophobic, it can be hydrophilised with 1-pyrene carboxylic acid. This layer of graphene prevented fatty acid synthase (FAS) particles from *Saccharomyces cerevisiae* from denaturing by interacting with air-water interface interactions, and instead attracted the protein particles to the graphene-water interface. Graphene support could also affect particle distribution positively[232]. Alternatively, graphene oxide could also be used, which is more hydrophobic than pristine graphene. It has been shown with the fragile 26S proteasome that with graphene oxide support, the protein assembly remained intact after freezing[237]. Additionally, with this hydrophilic support, much of the excessive solution could be blotted away without excessive surface dewetting, allowing a very thin layer of vitreous ice to be formed. Drulyte and colleagues[232] also showed that the use of graphene oxide could increase angular distribution of β-galactosidase, which usually has a strong preferred orientation in ice. Another method used to improve sample distribution into ice holes is the introduction of a hydrophilic self-assembled monolayer (SAM) of thiolated polyethylene glycol (PEG) on gold-coated holey carbon grids. These PEG groups render the grid surface much more hydrophilic than glow-discharging, so that protein solution can flow through the holes in the carbon film. Good particle distribution was observed with the kainite receptor GluK2 from rats after vitrification, which are usually excluded from holes[238]. Moreover, PEGylation has also been shown to improve angular distribution of complex I from mouse heart mitochondria (Jamie Blaza personal communication. Results could be assessed here[239]).

Much work is being done to improve sample preparation workflow, and completely novel systems are being developed to improve throughput and reproducibility. One such system is named the Vitrojet[240]. This system integrates the glow-discharger, sample applicator, plunge freezer and storage in one unit. Sample application is done by pin-printing, allowing sub-nanolitre of sample applied in a pre-defined pattern per grid, reducing amount of precious sample wasted. An integrated camera allows real-time inspection of liquid film thickness and quality. Vitrification is performed by a jet of cryogen directly sprayed onto the grid, minimising cooling time gradients across the grid. Another exciting development is a microfluidic method that allow cell lysis, protein isolation, and sample preparation all with a single capillary tube[241,242]. This method utilises biotinylated antibody 'fragment antigen binder' (Fab) bound to magnetic beads that can extract proteins-of-interest from cell lysates. The antigen-Fab-magnetic bead complexes are held in the capillary by electromagnets whilst cell debris is washed away, after which the antigen-Fab are released by photo-cleavage and printed onto a grid. There are also attempts to use microfluidics to achieve time-resolved cryo-EM (TrEM) structural studies of proteins dynamics and interactions at the ~10 milliseconds scale[243]. This is achieved by the mixing of protein solutions or reagents in micro-capillaries, rapidly spraying the mixture onto a grid with a voltage-assisted sprayer, and immediate vitrification by plunge freezing, all performed within 15 ms. This rapid vitrification has the added benefits of minimising air-water interface interactions of proteins, reducing preferential orientations and protein denaturation[243]. Together, all these automated sample preparation approaches allow much higher throughput, and many conditions could be tested in a relatively short time. However, these systems are yet to be made commercially available and will likely remain inaccessible but to specialised laboratories for some time.

4.4.2 BacM$_{TR}$ filament analysis with cryo-EM

Although the cryo-EM data obtained during this study did not result in a 3D structure of BacM filaments the 2D classes did confirm existing knowledge and models on bactofilins, and they were also in agreement with a very recently published report on the structure of bactofilin filaments from *Thermus thermophilus* (TtBac) solved by cryo-EM and X-ray crystallography[135]. In the published report, the authors found that natively isolated TtBac had the tendency to bundle over a range of conditions, to an extent that was not observed in BacM$_{TR}$. The authors subsequently prepared filaments at pH 11 which gave mostly unbundled filaments that were very straight and were not confined to areas close to hole edges[135]. This condition was repeated here for BacM$_{TR}$ but no improvements could be seen. Similar to BacM$_{TR}$, these filaments were made of different numbers of protofilaments. Many of these filaments were formed of three protofilaments arranged in a C3 symmetry not observed for BacM$_{TR}$. The 2D classification of these filaments yielded striations measuring 4.7 Å apart, which was very close to measurements of BacM$_{TR}$. Additionally, they observed connected densities between the filaments, like those reported in this study, but only at a frequency of around 6 nm, and none at 3 nm that was also observed here. The authors also proposed that the 6 nm spacing hinted at the non-polar arrangement of bactofilin subunits. The authors did face the problem of incorrect β-strand indexing, and could not process further other than a low resolution 3D model of the three-start helically arranged filaments, where subunit boundaries could not be resolved[135].

The authors subsequently used modified monoclonal nanobodies to identify the register of bactofilins in cryo-EM The resulting TtBac-nanobody complex formed ideal two-start filaments with a constant helical twist, they were able to solve the structure of the complex to a nominal resolution of 3.4 Å (**Figure 4-20 A**), but only 4.2 Å when FSC was performed against the structure of BacA, due to the prominent repeating β-strands decreasing confidence of amino acid conformation assignment[135]. The structure indeed showed non-polar arrangement of subunits, where they engage in N-N and C-C termini interactions (**Figure 4-20 A**). The authors also found that TtBac filaments had a very low helical twist of 4.89° per dimer, or 57 Å rise (**Figure 4-20 B**), in agreement with the non-observable helical twist of BacM$_{TR}$ single filaments. To validate the cryo-EM structure, the authors also performed X-ray crystallography on TtBac mutated at an equivalent site at the C-terminal polymerisation interface identified by our lab for BacM[62], rendering it unable to polymerise into filaments. They also removed ten amino acids from the N-terminal for ease of handling. As part of this study BacM$_{TR}$ with amino acid substitutions at the N- and C- terminal, and at both polymerisation interfaces were also sent for crystallisation trials, but were unsuccessful. Amazingly, the mutated ΔN-TtBac was still able to form filaments in the crystal structure (**Figure 4-20 C**). The sixth winding of β-strands at the C-terminus unfolded, which allowed the fifth winding of β-strands to engage in subunit interaction, and hence polymerisation[135]. This is a testament to the repeatedly reported resilience of the bactofilin domain's ability to polymerise.

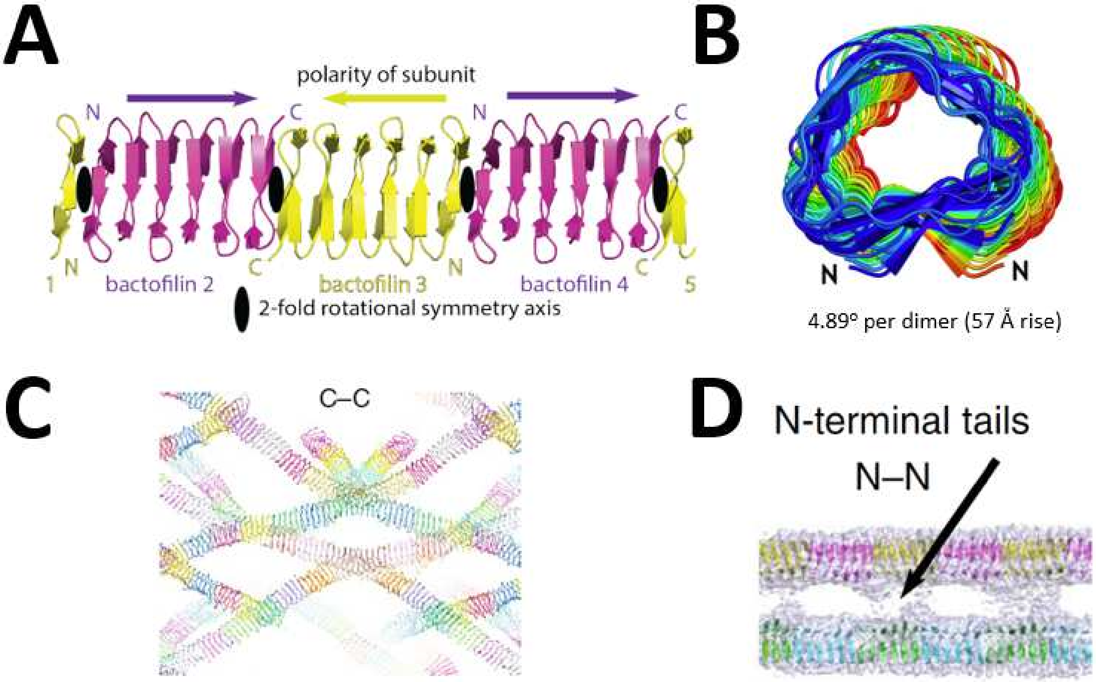

Figure 4-20 Figures from a study performed by Deng and colleagues on the structure of a bactofilin from *Thermus thermophilus* (TtBac).
(A) Ribbon diagram of TtBac showing the mode of subunit interactions, forming a non-polar filament. (B) Viewing down the filament axis of TtBac shows the low helical twist rate of TtBac. (C) Crystal unit cell of mutated ΔN-TtBac, which was still able to form filaments. There are 32 molecules per asymmetric unit. (D) The density between protofilaments are formed by the N-terminal tail of TtBac. Figures from this panel adapted from (135).

An interesting discrepancy is that the authors reported that the N-terminus tails are responsible for the bridging densities observed between protofilament as evident in their final atomic model (**Figure** 4-20 **D**) and in the lack of bundling seen in the ΔN-TtBac derivative. The authors also claimed that the N-terminal tail of TtBac would be reserved for membrane binding *in vivo*, and that TtBac would therefore exist as single filaments in the cell. Evidence include the presence of two conserved hydrophobic amino acids at the N-terminal tail, and cryo-tomography of TtBac mixed with liposomes that showed the ability of TtBac to bind and deform liposomes.

It is possible that the situation for BacM is different. In *M. xanthus*, the majority of BacM subunits have the N-terminal twenty-seven amino acids cleaved including the conserved pair of hydrophobic amino acids, leaving only five amino acids leading the predicted bactofilin domain[59] (the exact number varies depending on prediction program used). The C-terminus tail, however, is more than twenty amino acids long (again, this number varies), which makes it a more likely candidate for the interfilament densities. The effects of C-terminal tail manipulation on filament bundling and appearance support this idea (**Section 2.3.4**). Moreover, thick filaments could be observed in the cell like the polar rod-like structures (**Section 2.3.6**) indicating that BacM can interact laterally and form bundles in the cell. The minority full-length BacM isoform with the putative membrane-binding hydrophobic amino acids could help tether BacM filaments to the membrane. This could not yet be confirmed, as the short N-terminal tail remaining in $\mathrm{BacM_{TR}}$ could theoretically bridge the 13 Å gap between filaments if position and conformation were optimal. It could also be that the C-terminal tail is responsible for tethering filaments to the membrane, as suggested by the localisation of mCherry fused with the poly-proline region of BacM (**Section 2.3.7**). The C-terminal tail could be highly dynamic and unstructured so that it could not be resolved in 2D classification, as no additional densities could be seen. As reported earlier in **Section 2.3.7**, the accessibility of the C-terminal PP region could be important for the function of BacM, so it is conceivable that this tail is indeed highly dynamic.

As an interesting note, the C-terminal tail of FtsZ from *B. subtilis* determines the spacing between neighbouring filaments, as demonstrated by cryo-EM study of BsFtsZ with varying C-terminal tail lengths[22]. The authors of this study proposed that the tail allow flexible interactions between filaments during cell division for unhindered but spatially coordinated treadmilling. Whether the C-terminal tail of

BacM could play such a role may be difficult to assess, as any manipulation to that region causes bundling unamenable for cryo-EM studies.

The 2D lattice observed for BacM_{TR} could have functional implications. Other bactofilins, e.g. BacAB and BacEF, have been reported to form patches *in vivo.* In the fluorescent microscopy experiments of BacM in *M. xanthus* performed for this study (**Sections 2.3.2 & 2.3.6**), certain BacM morphologies found in the cell could correspond to structures formed by 2D lattices, like the amorphous structures seen with superresolution microscopy. If BacM 2D lattices do interact with the membrane, it would be conceivable that they may be less motile, hence they may be responsible for the very slow FRAP recovery rate observed for non-polar structures (**Section 2.3.2**).

The 2D lattices of BacM_{TR} could be a candidate for 2D electron crystallography studies, so that the mechanism of filament interaction that form these arrays could be understood. Briefly, this method involves the collection of micrographs of these arrays at different tilt angles, so that 3D information could be collected. Sections of micrographs containing the lattice could be extracted and treated as single particles for further processing[244]. Judging the sample quality seen in **Figure 4-10 B**, the amount of these lattice has to be increased, which could be achievable by increasing BacM_{TR} concentration or number of sample applications and blots during cryo-grid preparations. Individual lattices should not overlap, and there should be minimal distortion of the arrays, contrary to what is seen in the figure. Further sample improvements should therefore be performed before 2D electron crystallography studies could take place.

4.4.3 Analysis of MXAN0657 with cryo-EM

This study only achieved a low resolution map from cryo-tomography of native MXAN0657 filaments. The resulting average map contradicts the existing model of subunit arrangement in a filament unit. It is not immediately clear what the biological consequences are for these models. It is also not clear how filaments bundle *in vivo*, or indeed whether they bundle at all. If they do laterally associate in the cell, it also begs the question of whether they are parallel (polar) or anti parallel (non-polar). This may have implications on the whether MXAN0657 exhibit cytomotive behaviours, for example, by treadmilling. But the lack of observed nucleotide-dependent polymerisation, or other mechanisms for intrinsic dynamic instability makes it unlikely. It is also not clear whether the observation that filaments can laterally associate in-register or in a staggered manner has any functional significance as has been historically proposed.

One of the questions this study aimed to answer with cryo-EM was how many subunits are there in a filament unit. Although no individual subunit globular domains could be seen in the average maps, it could be estimated that the size of the filament unit must be under 0.8 mDa, or under 10 subunits. Another clue could have come from the predictions of the oligomeric state of the C-terminal coiled-coil domain. Prediction programs used were LOGICOIL[145], a program developed to predict the oligomeric state of coiled-coils *ab initio* combined with MARCOIL[245], a Hidden Markov Model (HMM) based program that predicts the locations of coiled-coil domains; MULTICOIL 2[246,247], a program that combines window-based-probabilistic methods with HMM to determine sites and oligomer states of coiled-coil domains; and PrOCoil[248], a tool developed with a machine learning approach that distinguishes oligomer states of coiled-coil domains combined with PAIRCOIL[249], which uses pairwise residue correlation to predict locations of coiled-coils. All these programs, chosen for the variety of methods employed, failed to reach a consensus, as states from dimer to tetramer have been predicted, which could also vary depending on user-defined probabilistic thresholds.

Another possible approach is by using available protein structure prediction programs that also predict oligomer structures[250–252]. Although remarkable advancements have been made in this field, in terms of computational methods and power, the problem is that the workflow requires first the generation of a predicted structure of a monomer before oligomeric properties can be explored. For MXAN0657, the structure of the monomer is likely heavily influenced by the neighbouring subunits, and may not be stable in isolation, making accurate monomer structure prediction difficult. Another level of complication arises from the lack of structures solved from MXAN0657 homologs, so there is limited resources for prediction programs for model building. Using COTH[251], only the structure of the C-terminal coiled-coil domain was presented, and HOMOCO[250] gave no results. Using GalaxyHomomer[252], suggested structures of the globular heads were presented, but none of the overall predicted oligomeric structures matched EM observations, regardless of user-defined oligomeric state input. Unsurprisingly, templates used for model building were coiled-coil rich proteins, meaning that the coiled-coil regions are weighted disproportionally for structure prediction.

A method that has yet to be attempted is mass measurement with scanning transmission electron microscope (STEM)[253,254]. This method detects the electrons elastically scattered by the unstained POI to estimate the mass of the protein. A mass standard, usually tobacco mosaic virus (TMV) is mixed with the sample for intensity-mass ratio calibration. This allows the mass-per-length of a filament to be measured, and the mass of visible structures could also be assigned *in situ*. This method was used for early research on filamentous proteins before the advent of high resolution electron microscopy and associated computational analysis packages[255,256], but is no longer widely available.

A future goal as an extension to this study is to perform whole cell cryo-ET, a powerful technique that could be used to observe the native arrangement and localisation of MXAN0657 filaments. Interacting protein complexes may also be observed. This has been performed with vitrified, unfixed *M. xanthus* cells for the study of T4P machinery[88] and the type VI secretion system[257]. The size and the distinct shape of MXAN0657 should make them resolvable and identifiable with this method. For the same reason, it is puzzling why they have not been reported in *M. xanthus* or other organisms. A recent jointly published report by a number of cryo-EM groups have compiled many uncharacterised and mysterious structures observed in tomograms of different bacterial cells[258]. No structures similar to MXAN0657 were found, however. The reason could be that cryo-ET has so far only been performed on liquid grown *M. xanthus* cells[257,258] (Lotte Søgaard-Andersen personal communication). *M. xanthus* cells could be made to grow on the surface of a holey carbon-coated gold grid before vitrification and visualisation.

Chapter 5

Final remarks

Two different cytoskeletal elements from *M. xanthus* were investigated in this work; the first was BacM, a member of the bactofilin family, while the second was MXAN0657, an enigmatic chain-like filament.

Through the use of various microscopy techniques, this study has found that BacM forms a range of structures inside the cell and displayed high variability within a population of cells in its distribution and morphology. This is unusual for bacterial cytoskeletons described so far. The sensitivity of BacM to tag insertion made it difficult for *in vivo* studies. Using a low expression of fluorescent protein-tagged BacM, it was found that BacM has low intra-filament dynamics, but can be static or highly motile in the cell. The manipulation of the proline-rich C-terminus tail caused drastic changes in the morphology of filaments *in vitro*, and the poly-proline motif within the tail appeared to be important for function and localisation of BacM. Further physiological questions remain, including the identification of the enzyme responsible for N-terminal cleavage of BacM and the function of this process; the control mechanism of BacM dynamics and its polymerisation state; and the output pathway of BacM.

The observations from cryo-EM of $\mathrm{BacM_{TR}}$ were mostly consistent with structural studies of bactofilins in the literature. There were differences, namely in the proposed role of the N- and C-terminal tails. As these regions are highly variable between bactofilin, and given that bactofilins play such a diverse range of roles, discrepancies may perhaps be unsurprising. The continuation of the study of BacM filament structures may provide insight into the mechanisms that define structural, behavioural, and functional differences between bactofilins.

MXAN0657 remains an enigmatic novel structure. It was found to be sensitive to pH value changes and divalent cations, responding by large scale bundling and elongation. Using immunofluorescence, it was observed that MXAN0657 formed short filaments distributed across the cell, but attempts at introducing a fluorescent tag into MXAN0657 has so far been unsuccessful, preventing *in vivo* visualisation. It was highly interesting to find that deletion of *mxan0657* prevented germination of spores in a density dependent manner, but the exact function of MXAN0657 is still unclear. The ubiquitous presence of its homologs in different organisms suggests a fundamental requirement for this structure, and possibly functional diversification also.

Using cryo-EM tomography, a low resolution 3D map of a MXAN0657 filament unit was obtained. The average map contradicts the current idea of subunit arrangement, but without higher resolution information it was not possible to confirm the validity of either model. The surprise finding that fragmented expression of MXAN0657 in *E. coli* led to monomeric filament units gave the possibility of SPA of MXAN0657 using cryo-EM. However, obtaining a satisfactory cryo-sample remained a challenge, and further optimisation is required.

Over the last two decades, many new bacterial cytoskeleton proteins have come to light. Although the progress of their research falls well behind that of the eukaryotes, it is still apparent that their functions encompass many cellular process. Further research into novel cytoskeletal elements will no doubt be rewarded with novel and existing knowledge on the physiology and morphology of prokaryotes.

Reference

1. Xiong, Y., Rangamani, P., Fardin, M.-A., Lipshtat, A., Dubin-Thaler, B., Rossier, O., Sheetz, M. P. & Iyengar, R. Mechanisms controlling cell size and shape during isotropic cell spreading. *Biophys. J.* **98**, 2136–2146 (2010).

2. Celler, K., Koning, R. I., Koster, A. J. & van Wezel, G. P. Multidimensional view of the bacterial cytoskeleton. *J. Bacteriol.* **195**, 1627–1636 (2013).

3. Fischer, R. S. & Fowler, V. M. Thematic minireview series: The state of the cytoskeleton in 2015. *J. Biol. Chem.* **290**, 17133–17136 (2015).

4. Miller, N. G. & Wilson, R. B. *In vivo* and *in vitro* observation of *Leptospira promona* by electron microscopy. *J. Bacteriol.* **84**, 569–76 (1962).

5. Williamson, D. L. Unusual fibrils from the spirochete-like sex ratio organism. *J. Bacteriol.* **117**, 904–6 (1974).

6. Cabeen, M. T. & Jacobs-Wagner, C. Bacterial cell shape. *Nat. Rev. Microbiol.* **3**, 601–610 (2005).

7. Bi, E. & Lutkenhaus, J. FtsZ ring structure associated with division in *Escherichia coli. Nature* **354**, 161–164 (1991).

8. Bork, P., Sander, C. & Valencia, a. An ATPase domain common to prokaryotic cell cycle proteins, sugar kinases, actin, and hsp70 heat shock proteins. *Proc. Natl. Acad. Sci.* **89**, 7290–4 (1992).

9. Ausmees, N., Kuhn, J. R. & Jacobs-Wagner, C. The bacterial cytoskeleton: An intermediate filament-like function in cell shape. *Cell* **115**, 705–713 (2003).

10. Cho, H. The role of cytoskeletal elements in shaping bacterial cells. *J. Microbiol. Biotechnol.* **25**, 307–316 (2015).

11. Mukherjee, A., Dai, K. & Lutkenhaus, J. Escherichia coli cell division protein FtsZ is a guanine nucleotide binding protein. *Proc. Natl. Acad. Sci.* **90**, 1053–7 (1993).

12. Erickson, H. P., Taylor, D. W., Taylor, K. A. & Bramhill, D. Bacterial cell division protein FtsZ assembles into protofilament sheets and minirings, structural homologs of tubulin polymers. *Proc. Natl. Acad. Sci.* **93**, 519–23 (1996).

13. Löwe, J. & Amos, L. A. Crystal structure of the bacterial cell-division protein FtsZ. *Nature* **391**, 203–206 (1998).

14. Varma, A. & Young, K. D. FtsZ Collaborates with penicillin binding proteins to generate bacterial cell shape in *Escherichia coli*. *J. Bacteriol.* **186**, 6768–6774 (2004).

15. Aaron, M., Charbon, G., Lam, H., Schwarz, H., Vollmer, W. & Jacobs-Wagner, C. The tubulin homologue FtsZ contributes to cell elongation by guiding cell wall precursor synthesis in *Caulobacter crescentus*. *Mol. Microbiol.* **64**, 938–952 (2007).

16. Varma, A., De Pedro, M. A. & Young, K. D. FtsZ directs a second mode of peptidoglycan synthesis in *Escherichia coli*. *J. Bacteriol.* **189**, 5692–5704 (2007).

17. Adams, D. W. & Errington, J. Bacterial cell division: assembly, maintenance and disassembly of the Z ring. *Nat Rev Micro* **7**, 642–653 (2009).

18. de Boer, P., Crossley, R. & Rothfield, L. The essential bacterial cell-division protein FtsZ is a GTPase. *Nature* **359**, 254–256 (1992).

19. Osawa, M., Anderson, D. E. & Erickson, H. P. Reconstitution of contractile FtsZ rings in liposomes. *Science* **320**, 792–4 (2008).

20. Daley, D. O., Skoglund, U. & Söderström, B. FtsZ does not initiate membrane constriction at the onset of division. *Sci. Rep.* **6**, 33138 (2016).

21. den Blaauwen, T., Hamoen, L. W. & Levin, P. A. The divisome at 25: the road ahead. *Curr. Opin. Microbiol.* **36**, 85–94 (2017).

22. Huecas, S., Ramírez-Aportela, E., Vergoñós, A., Núñez-Ramírez, R., Llorca, O., Díaz, J. F., Juan-Rodríguez, D., Oliva, M. A., Castellen, P. & Andreu, J. M. Self-organization of ftsz polymers in solution reveals spacer role of the disordered C-terminal tail. *Biophys. J.* **113**, 1831–1844 (2017).

23. Yang, X., Lyu, Z., Miguel, A., McQuillen, R., Huang, K. C. & Xiao, J. GTPase activity-coupled treadmilling of the bacterial tubulin FtsZ organizes septal cell wall synthesis. *Science* **355**, 744–747 (2017).

24. Cabeen, M. T. & Jacobs-Wagner, C. The bacterial cytoskeleton (2010). *Annu. Rev. Genet.* **44**, 365–392 (2010).

25. Martin-Galiano, A. J., Oliva, M. A., Sanz, L., Bhattacharyya, A., Serna, M., Yebenes, H., Valpuesta, J. M. & Andreu, J. M. Bacterial tubulin distinct loop sequences and primitive assembly properties support its origin from a eukaryotic tubulin ancestor. *J. Biol. Chem.* **286**, 19789–19803 (2011).

26. Löwe, J. & Amos, L. A. Evolution of cytomotive filaments: The cytoskeleton from prokaryotes to eukaryotes. *Int. J. Biochem. Cell Biol.* **41**, 323–329 (2009).

27. Fink, G. & Löwe, J. Reconstitution of a prokaryotic minus end-tracking system using TubRC centromeric complexes and tubulin-like protein TubZ filaments. *Proc. Natl. Acad. Sci. U. S. A.* **112**, E1845-50 (2015).

28. Doi, M., Wachi, M., Ishino, F., Tomioka, S., Ito, M., Sakagami, Y., Suzuki, A. & Matsuhashi, M. Determinations of the DNA sequence of the mreB gene and of the gene products of the mre region that function in formation of the rod shape of *Escherichia coli* cells. *J. Bacteriol.* **170**, 4619–4624 (1988).

29. Jones, L. J. F., Carballido-López, R. & Errington, J. Control of cell shape in bacteria: Helical, actin-like filaments in *Bacillus subtilis*. *Cell* **104**, 913–922 (2001).

30. Van den Ent, F., Amos, L. A., Löwe, J., Ent, F. Van Den, Amos, L. A. & Lo, J. Prokaryotic origin of the actin cytoskeleton. *Nature* **413**, 39–44 (2001).

31. van den Ent, F., Izoré, T., Bharat, T. A. M., Johnson, C. M. & Löwe, J. Bacterial actin MreB forms antiparallel double filaments. *Elife* **2014**, 1–22 (2014).

32. Nurse, P. & Marians, K. J. Purification and characterization of *Escherichia coli* MreB protein. *J. Biol. Chem.* **288**, 3469–75 (2013).

33. Bean, G. J., Flickinger, S. T., Westler, W. M., McCully, M. E., Sept, D., Weibel, D. B. & Amann, K. J. A22 disrupts the bacterial actin cytoskeleton by directly binding and inducing a low-affinity state in MreB. *Biochemistry* **48**, 4852–4857 (2009).

34. Salje, J., van den Ent, F., de Boer, P. & Löwe, J. Direct membrane binding by bacterial actin MreB. *Mol. Cell* **43**, 478–487 (2011).

35. Garner, E. C., Bernard, R., Wang, W., Zhuang, X., Rudner, D. Z. & Mitchison, T. Coupled, circumferential motions of the cell wall synthesis machinery and MreB filaments in *B. subtilis*. *Science* **333**, 222–5 (2011).

36. Domínguez-Escobar, J., Chastanet, A., Crevenna, A. H., Fromion, V., Wedlich-Söldner, R., Carballido-López, R., J, D.-E., A, C., AH, C., V, F., R, W.-S. & R., C.-L. Processive movement of Mreb-associated cell wall biosynthetic complexes in Bacteria. *Science* **333**, 225–228 (2011).

37. Swulius, M. T., Chen, S., Jane Ding, H., Li, Z., Briegel, A., Pilhofer, M., Tocheva, E. I., Lybarger, S. R., Johnson, T. L., Sandkvist, M. & Jensen, G. J. Long helical filaments are not seen encircling cells in electron cryotomograms of rod-shaped bacteria. *Biochem. Biophys. Res. Commun.* **407**, 650–655 (2011).

38. Reimold, C., Defeu Soufo, H. J., Dempwolff, F. & Graumann, P. L. Motion of variable-length MreB filaments at the bacterial cell membrane influences cell morphology. *Mol. Biol. Cell* **24**, 2340–9 (2013).

39. Chastanet, A. & Carballido-Lopez, R. The actin-like MreB proteins in *Bacillus subtilis*: a new turn. *Front. Biosci. (Schol. Ed).* **4**, 1582–1606 (2012).

40. Swulius, M. T. & Jensen, G. J. The helical Mreb cytoskeleton in *Escherichia coli* MC1000/pLE7 is an artifact of the N-terminal yellow fluorescent protein tag. *J. Bacteriol.* **194**, 6382–6386 (2012).

41. Billaudeau, C., Yao, Z., Cornilleau, C., Carballido-López, R. & Chastanet, A. MreB Forms Subdiffraction Nanofilaments during Active Growth in *Bacillus subtilis*. *MBio* **10**, e01879-18 (2019).

42. Figge, R. M., Divakaruni, A. V & Gober, J. W. MreB, the cell-shape determining bacterial actin

homolog, coordinates cell wall morphogenesis in. *Genomics* **51**, 1–47 (2004).

43. Bratton, B. P., Shaevitz, J. W., Gitai, Z. & Morgenstein, R. M. MreB polymers and curvature localization are enhanced by RodZ and predict *E. coli*'s cylindrical uniformity. *Nat. Commun.* **9**, 2797 (2018).

44. Shi, H., Bratton, B. P., Gitai, Z. & Huang, K. C. How to build a bacterial cell: MreB as the foreman of *E. coli* construction. *Cell* **172**, 1294–1305 (2018).

45. Mauriello, E. M. F., Mouhamar, F., Nan, B., Ducret, A., Dai, D., Zusman, D. R. & Mignot, T. Bacterial motility complexes require the actin-like protein, MreB and the Ras homologue, MglA. *EMBO J.* **29**, 315–326 (2010).

46. Treuner-Lange, A., Macia, E., Guzzo, M., Hot, E., Faure, L. M., Jakobczak, B., Espinosa, L., Alcor, D., Ducret, A., Keilberg, D., Castaing, J. P., Gervais, S. L., Franco, M., Søgaard-Andersen, L. & Mignot, T. The small G-protein MglA connects to the MreB actin cytoskeleton at bacterial focal adhesions. *J. Cell Biol.* **210**, 243–256 (2015).

47. Bharat, T. a. M., Murshudov, G. N., Sachse, C. & Löwe, J. Structures of actin-like ParM filaments show architecture of plasmid-segregating spindles. *Nature* 1–5 (2015). doi:10.1038/nature14356

48. Pilhofer, M. & Jensen, G. J. The bacterial cytoskeleton: More than twisted filaments. *Curr. Opin. Cell Biol.* **25**, 1–9 (2013).

49. Barber-Zucker, S., Keren-Khadmy, N. & Zarivach, R. From invagination to navigation: The story of magnetosome-associated proteins in magnetotactic bacteria. *Protein Science* **25**, 338–351 (2016).

50. Toro-Nahuelpan, M., Müller, F. D., Klumpp, S., Plitzko, J. M., Bramkamp, M. & Schüler, D. Segregation of prokaryotic magnetosomes organelles is driven by treadmilling of a dynamic actin-like MamK filament. *BMC Biol.* **14**, 88 (2016).

51. Löwe, J., He, S., Scheres, S. H. W. & Savva, C. G. X-ray and cryo-EM structures of monomeric and filamentous actin-like protein MamK reveal changes associated with polymerization. *Proc. Natl. Acad. Sci.* **113**, 13396–13401 (2016).

52. Bergeron, J. R. C., Hutto, R., Ozyamak, E., Hom, N., Hansen, J., Draper, O., Byrne, M. E., Keyhani, S., Komeili, A. & Kollman, J. M. Structure of the magnetosome-associated actin-like MamK filament at subnanometer resolution. *Protein Sci.* **26**, 93–102 (2017).

53. Cabeen, M. T., Charbon, G., Vollmer, W., Born, P., Ausmees, N., Weibel, D. B. & Jacobs-Wagner, C. Bacterial cell curvature through mechanical control of cell growth. *EMBO J.* **28**, 1208–19 (2009).

54. Charbon, G., Cabeen, M. T. & Jacobs-Wagner, C. Bacterial intermediate filaments: *In vivo* assembly, organization, and dynamics of crescentin. *Genes Dev.* **23**, 1131–1144 (2009).

55. Esue, O., Rupprecht, L., Sun, S. X. & Wirtz, D. Dynamics of the bacterial intermediate filament crescentin *in vitro* and *in vivo*. *PLoS One* **5**, e8855 (2010).

56. Fuchino, K., Bagchi, S., Cantlay, S., Sandblad, L., Wu, D., Bergman, J., Kamali-Moghaddam, M., Flärdh, K. & Ausmees, N. Dynamic gradients of an intermediate filament-like cytoskeleton are recruited by a polarity landmark during apical growth. *Proc. Natl. Acad. Sci.* **110**, E1889-97 (2013).

57. Hay, N. A., Tipper, D. J., Gygi, D. & Hughes, C. A novel membrane protein influencing cell shape and multicellular swarming of *Proteus mirabilis*. *J. Bacteriol.* **181**, 2008–2016 (1999).

58. Kühn, J., Briegel, A., Mörschel, E., Kahnt, J., Leser, K., Wick, S., Jensen, G. J. & Thanbichler, M. Bactofilins, a ubiquitous class of cytoskeletal proteins mediating polar localization of a cell wall synthase in *Caulobacter crescentus*. *EMBO J.* **29**, 327–39 (2010).

59. Koch, M. K., Mchugh, C. A. & Hoiczyk, E. BacM, an N-terminally processed bactofilin of *Myxococcus xanthus*, is crucial for proper cell shape. *Mol. Microbiol.* **80**, 1031–1051 (2011).

60. Shi, C., Fricke, P., Lin, L., Chevelkov, V., Wegstroth, M., Giller, K., Becker, S., Thanbichler, M. & Lange, A. Atomic-resolution structure of cytoskeletal bactofilin by solid-state NMR. *Sci. Adv.* **1**, e1501087 (2015).

61. Kassem, M. M., Wang, Y., Boomsma, W. & Lindorff-Larsen, K. Structure of the bacterial cytoskeleton protein bactofilin by NMR chemical shifts and sequence variation. *Biophys. J.* **110**,

2342–2348 (2016).

62. Zuckerman, D. M., Boucher, L. E., Xie, K., Engelhardt, H., Bosch, J. & Hoiczyk, E. The bactofilin cytoskeleton protein BacM of *Myxococcus xanthus* forms an extended β-Sheet structure likely mediated by hydrophobic interactions. *PLoS One* **10**, e0121074 (2015).

63. El Andari, J., Altegoer, F., Bange, G. & Graumann, P. L. *Bacillus subtilis* bactofilins are essential for flagellar hook- and filament assembly and dynamically localize into structures of less than 100 nm diameter underneath the cell membrane. *PLoS One* **10**, 1–22 (2015).

64. Blair, K. M., Mears, K. S., Taylor, J. A., Fero, J., Jones, L. A., Gafken, P. R., Whitney, J. C. & Salama, N. R. The *Helicobacter pylori* cell shape promoting protein Csd5 interacts with the cell wall, MurF, and the bacterial cytoskeleton. *Mol. Microbiol.* **110**, 114–127 (2018).

65. Yang, D. C., Blair, K. M., Taylor, J. A., Petersen, T. W., Sessler, T., Tull, C. M., Leverich, C. K., Collar, A. L., Wyckoff, T. J., Biboy, J., Vollmer, W. & Salama, N. R. A Genome-wide *Helicobacter pylori* morphology screen uncovers a membrane-spanning helical cell shape complex. *J. Bacteriol.* **201**, (2019).

66. Holtrup, S., Heimerl, T., Linne, U., Altegoer, F., Noll, F. & Waidner, B. Biochemical characterization of the Helicobacter pylori bactofilin-homolog HP1542. *PLoS One* **14**, e0218474 (2019).

67. Jackson, K. M., Schwartz, C., Wachter, J., Rosa, P. A. & Stewart, P. E. A widely conserved bacterial cytoskeletal component influences unique helical shape and motility of the spirochete *Leptospira biflexa*. *Mol. Microbiol.* **108**, 77–89 (2018).

68. Lin, L. & Thanbichler, M. Nucleotide-independent cytoskeletal scaffolds in bacteria. *Cytoskeleton* **70**, 409–423 (2013).

69. Halbedel, S., Kawai, M., Breitling, R. & Hamoen, L. W. SecA is required for membrane targeting of the cell division protein DivIVA in vivo. *Front. Microbiol.* **5**, 1–12 (2014).

70. Ptacin, J. L., Gahlmann, A., Bowman, G. R., Perez, A. M., von Diezmann, A. R. S., Eckart, M. R.,

Moerner, W. E. & Shapiro, L. Bacterial scaffold directs pole-specific centromere segregation. *Proc. Natl. Acad. Sci. U. S. A.* **111**, E2046-55 (2014).

71. Hwang, L. C., Vecchiarelli, A. G., Han, Y.-W., Mizuuchi, M., Harada, Y., Funnell, B. E. & Mizuuchi, K. ParA-mediated plasmid partition driven by protein pattern self-organization. *EMBO J.* **32**, 1238–1249 (2013).

72. Busiek, K. K. & Margolin, W. Bacterial actin and tubulin homologs in cell growth and division. *Curr. Biol.* **25**, R243–R254 (2015).

73. Rosenberg, E. Myxobacteria: Development and cell Interactions. (Springer New York, 1984).

74. Dworkin, M. & Kaiser, D. Myxobacteria II. (American Society for Microbiology, 1993).

75. Zusman, D. R., Scott, A. E., Yang, Z. & Kirby, J. R. Chemosensory pathways, motility and development in *Myxococcus xanthus*. *Nat. Rev. Microbiol.* **5**, 862–872 (2007).

76. Berleman, J. & Keane, R. The predatory life cycle of *Myxococcus xanthus*. *Microbiology* **162**, 1–11 (2016).

77. Berleman, J. E., Chumley, T., Cheung, P. & Kirby, J. R. Rippling Is a Predatory Behavior in *Myxococcus xanthus*. *J. Bacteriol.* **188**, 5888–5895 (2006).

78. Tzeng, L. & Singer, M. DNA replication during sporulation in *Myxococcus xanthus* fruiting bodies. *Proc. Natl. Acad. Sci. U. S. A.* **102**, 14428–33 (2005).

79. Bui, N. K., Gray, J., Schwarz, H., Schumann, P., Blanot, D. & Vollmer, W. The peptidoglycan sacculus of *Myxococcus xanthus* has unusual structural features and is degraded during glycerol-induced myxospore development. *J. Bacteriol.* **191**, 494–505 (2009).

80. Müller, F. D., Schink, C. W., Hoiczyk, E., Cserti, E. & Higgs, P. I. Spore formation in *Myxococcus xanthus* is tied to cytoskeleton functions and polysaccharide spore coat deposition. *Mol. Microbiol.* **83**, 486–505 (2012).

81. Lee, B., Holkenbrink, C., Treuner-Lange, A. & Higgs, P. I. *Myxococcus xanthus* developmental cell fate production: heterogeneous accumulation of developmental regulatory proteins and

reexamination of the role of MazF in developmental lysis. *J. Bacteriol.* **194**, 3058–68 (2012).

82. Lobedanz, S. & Søgaard-Andersen, L. Identification of the C-signal, a contact-dependent morphogen coordinating multiple developmental responses in *Myxococcus xanthus*. *Genes Dev.* **17**, 2151–2161 (2003).

83. Jelsbak, L. & Søgaard-Andersen, L. Cell behavior and cell-cell communication during fruiting body morphogenesis in *Myxococcus xanthus*. *J. Microbiol. Methods* **55**, 829–839 (2003).

84. Boynton, T. O. & Shimkets, L. J. *Myxococcus* CsgA, Drosophila sniffer, and human HSD10 are cardiolipin phospholipases. *Genes Dev.* **29**, 1903–1914 (2015).

85. Muñoz-Dorado, J., Marcos-Torres, F. J., García-Bravo, E., Moraleda-Muñoz, A. & Pérez, J. Myxobacteria: moving, killing, feeding, and surviving together. *Front. Microbiol.* **7**, 1–18 (2016).

86. Zhang, Y., Franco, M., Ducret, A. & Mignot, T. A bacterial ras-like small GTP-binding protein and its cognate GAP establish a dynamic spatial polarity axis to control directed motility. *PLoS Biol.* **8**, 1–12 (2010).

87. Szadkowski, D., Harms, A., Carreira, L. A. M., Wigbers, M., Potapova, A., Wuichet, K., Keilberg, D., Gerland, U. & Søgaard-Andersen, L. Spatial control of the GTPase MglA by localized RomR–RomX GEF and MglB GAP activities enables *Myxococcus xanthus* motility. *Nat. Microbiol.* **4**, 1344–1355 (2019).

88. Chang, Y.-W., Rettberg, L. A., Treuner-Lange, A., Iwasa, J., Søgaard-Andersen, L., Jensen, G. J., Korotkov, K. V., Sandkvist, M., Hol, W. G. J., Jarrell, K. F., Albers, S.-V., Mattick, J. S., Craig, L., Pique, M. E., Tainer, J. A., Evans, K. J., Lambert, C., Sockett, R. E., Chen, I., *et al.* Architecture of the type IVa pilus machine. *Science* **351**, aad2001 (2016).

89. Bulyha, I., Lindow, S., Lin, L., Bolte, K., Wuichet, K., Kahnt, J., van der Does, C., Thanbichler, M. & Sögaard-Andersen, L. Two small gtpases act in concert with the bactofilin cytoskeleton to regulate dynamic bacterial cell polarity. *Dev. Cell* **25**, 119–131 (2013).

90. Hu, W., Yang, Z., Lux, R., Zhao, M., Wang, J., He, X., Shi, W., Behmlander, R., Dworkin, M.,

Campos, J., Geisselsoder, J., Zusman, D., Chang, B., Dworkin, M., Clausen, M., Jakovljevic, V., Sogaard-Andersen, L., Maier, B., Collins, T., *et al.* Direct visualization of the interaction between pilin and exopolysaccharides of *Myxococcus xanthus* with eGFP-fused PilA protein. *FEMS Microbiol. Lett.* **326**, 23–30 (2012).

91. Pathak, D. T., Wei, X. & Wall, D. Myxobacterial tools for social interactions. *Res. Microbiol.* **163**, 579–591 (2012).

92. Wolgemuth, C., Hoiczyk, E., Kaiser, D. & Oster, G. How myxobacteria glide. *Curr. Biol.* **12**, 369–377 (2002).

93. Hoiczyk, E. & Baumeister, W. The junctional pore complex, a prokaryotic secretion organelle, is the molecular motor underlying gliding motility in cyanobacteria. *Curr. Biol.* **8**, 1161–1168 (1998).

94. Yu, R. & Kaiser, D. Gliding motility and polarized slime secretion. *Mol. Microbiol.* **63**, 454–467 (2007).

95. Ducret, A., Valignat, M.-P., Mouhamar, F., Mignot, T. & Theodoly, O. Wet-surface-enhanced ellipsometric contrast microscopy identifies slime as a major adhesion factor during bacterial surface motility. *Proc. Natl. Acad. Sci.* **109**, 10036–10041 (2012).

96. Nan, B., Chen, J., Neu, J. C., Berry, R. M., Oster, G. & Zusman, D. R. Myxobacteria gliding motility requires cytoskeleton rotation powered by proton motive force. *Proc. Natl. Acad. Sci.* **108**, 2498–503 (2011).

97. Nan, B., McBride, M. J., Chen, J., Zusman, D. R. & Oster, G. Bacteria that glide with helical tracks. *Curr. Biol.* **24**, R169–R173 (2014).

98. Tam, M., Shaevitz, J. W., Hartzell, P. L. & Zusman, D. R. Evidence that focal adhesion complexes power bacterial gliding motility. *Science (80-.).* **315**, 853–856 (2007).

99. Balagam, R., Litwin, D. B., Czerwinski, F., Sun, M., Kaplan, H. B., Shaevitz, J. W. & Igoshin, O. A. *Myxococcus xanthus* gliding motors are elastically coupled to the substrate as predicted by the focal adhesion model of gliding motility. *PLoS Comput. Biol.* **10**, (2014).

100. Nan, B., Mauriello, E. M. F., Sun, I. H., Wong, A. & Zusman, D. R. A multi-protein complex from *Myxococcus xanthus* required for bacterial gliding motility. *Mol. Microbiol.* **76**, 1539–1554 (2010).

101. Patryn, J., Allen, K., Dziewanowska, K., Otto, R. & Hartzell, P. L. Localization of MglA, an essential gliding motility protein in *Myxococcus xanthus*. *Cytoskeleton* **67**, 322–337 (2010).

102. Islam, S. T. & Mignot, T. The mysterious nature of bacterial surface (gliding) motility: A focal adhesion-based mechanism in *Myxococcus xanthus*. *Semin. Cell Dev. Biol.* **46**, 143–154 (2015).

103. Mauriello, E. M. F., Nan, B. & Zusman, D. R. AglZ regulates adventurous (A-) motility in *Myxococcus xanthus* through its interaction with the cytoplasmic receptor, FrzCD. *Mol. Microbiol.* **72**, 964–977 (2009).

104. Luciano, J., Agrebi, R., Valé Rie Le Gall, A., Wartel, M., Fiegna, F., Ducret, A., Line Brochier-Armanet, C. & Mignot, T. M. Emergence and modular evolution of a novel motility machinery in bacteria. *PLoS Genet* **7**, (2011).

105. Faure, L. M., Fiche, J.-B., Espinosa, L., Ducret, A., Anantharaman, V., Luciano, J., Lhospice, S., Islam, S. T., Tréguier, J., Sotes, M., Kuru, E., Van Nieuwenhze, M. S., Brun, Y. V., Théodoly, O., Aravind, L., Nollmann, M. & Mignot, T. The mechanism of force transmission at bacterial focal adhesion complexes. *Nature* **539**, 530–535 (2016).

106. Fu, G., Bandaria, J. N., Le Gall, A. V., Fan, X., Yildiz, A., Mignot, T., Zusman, D. R. & Nan, B. MotAB-like machinery drives the movement of MreB filaments during bacterial gliding motility. *Proc. Natl. Acad. Sci.* **115**, 2484–2489 (2018).

107. Vassallo, C., Pathak, D. T., Cao, P., Zuckerman, D. M., Hoiczyk, E. & Wall, D. Cell rejuvenation and social behaviors promoted by LPS exchange in myxobacteria. *Proc. Natl. Acad. Sci.* **112**, E2939-46 (2015).

108. Diez, J., Martinez, J. P., Mestres, J., Sasse, F., Frank, R. & Meyerhans, A. Myxobacteria: natural pharmaceutical factories. *Microb. Cell Fact.* **11**, 52 (2012).

109. Lünsdorf, H. & Reichenbach, H. Ultrastructural Details of the Apparatus of Gliding Motility of

Myxococcus fulvus (Myxobacterales). *J. Gen. Microbiol.* **135**, 1633–1641 (1989).

110. Freese, A., Reichenbach, H. & Lünsdorf, H. Further characterization and in situ localization of chain-like aggregates of the gliding bacteria *Myxococcus fulvus* and *Myxococcus xanthus*. *J. Bacteriol.* **179**, 1246–1252 (1997).

111. Lin, L., Osorio Valeriano, M., Harms, A., Søgaard-Andersen, L. & Thanbichler, M. Bactofilin-mediated organization of the ParABS chromosome segregation system in *Myxococcus xanthus*. *Nat. Commun.* **8**, 1817 (2017).

112. Kaiser, D. Social gliding is correlated with the presence of pili in *Myxococcus xanthus*. **76**, (1979).

113. Iniesta, A. A., García-Heras, F., Abellón-Ruiz, J., Gallego-García, A. & Elías-Arnanz, M. Two systems for conditional gene expression in *Myxococcus xanthus* inducible by isopropyl-β-D-thiogalactopyranoside or vanillate. *J. Bacteriol.* **194**, 5875–5885 (2012).

114. Gómez-Santos, N., Treuner-Lange, A., Moraleda-Muñoz, A., García-Bravo, E., García-Hernández, R., Martínez-Cayuela, M., Pérez, J., Søgaard-Andersen, L. & Muñoz-Dorado, J. Comprehensive set of integrative plasmid vectors for copper-inducible gene expression in *Myxococcus xanthus*. *Appl. Environ. Microbiol.* **78**, 2515–2521 (2012).

115. Schindelin, J., Arganda-Carreras, I., Frise, E., Kaynig, V., Longair, M., Pietzsch, T., Preibisch, S., Rueden, C., Saalfeld, S., Schmid, B., Tinevez, J.-Y., White, D. J., Hartenstein, V., Eliceiri, K., Tomancak, P. & Cardona, A. Fiji: an open-source platform for biological-image analysis. *Nat. Methods* **9**, 676–682 (2012).

116. Hartmann, R., Teeseling, M. C. F. van, Thanbichler, M. & Drescher, K. BacStalk: a comprehensive and interactive image analysis software tool for bacterial cell biology. *bioRxiv* 360230 (2018). doi:10.1101/360230

117. Ovesný, M., Křížek, P., Borkovec, J., Svindrych, Z. & Hagen, G. M. ThunderSTORM: a comprehensive ImageJ plug-in for PALM and STORM data analysis and super-resolution imaging. *Bioinformatics* **30**, 2389–90 (2014).

118. Shaner, N. C., Campbell, R. E., Steinbach, P. A., Giepmans, B. N. G., Palmer, A. E. & Tsien, R. Y. Improved monomeric red, orange and yellow fluorescent proteins derived from *Discosoma* sp. red fluorescent protein. *Nat. Biotechnol.* **22**, 1567–1572 (2004).

119. Moraleda-Muñoz, A., Pérez, J., Fontes, M., Murillo, F. J. & Muñoz-Dorado, J. Copper induction of carotenoid synthesis in the bacterium *Myxococcus xanthus*. *Mol. Microbiol.* **56**, 1159–1168 (2005).

120. Shaner, N. C., Lambert, G. G., Chammas, A., Ni, Y., Cranfill, P. J., Baird, M. A., Sell, B. R., Allen, J. R., Day, R. N., Israelsson, M., Davidson, M. W. & Wang, J. A bright monomeric green fluorescent protein derived from *Branchiostoma lanceolatum*. *Nat. Methods* **10**, 407–409 (2013).

121. Hoffmann, C., Gaietta, G., Zürn, A., Adams, S. R., Terrillon, S., Ellisman, M. H., Tsien, R. Y. & Lohse, M. J. Fluorescent labeling of tetracysteine-tagged proteins in intact cells. *Nat. Protoc.* **5**, 1666–1677 (2010).

122. Griffin, B. A., Adams, S. R. & Tsien, R. Y. Specific covalent labeling of recombinant protein molecules inside live cells. *Science* **281**, 269–272 (1998).

123. Martin, B. R., Giepmans, B. N. G., Adams, S. R. & Tsien, R. Y. Mammalian cell–based optimization of the biarsenical-binding tetracysteine motif for improved fluorescence and affinity. *Nat. Biotechnol.* **23**, 1308–1314 (2005).

124. Zarrinpar, A., Bhattacharyya, R. P. & Lim, W. A. The structure and function of proline recognition domains. *Sci. Signal.* **2003**, re8 (2003).

125. Kajava, A. V. & Steven, A. C. β-rolls, β-helices, and other β-solenoid proteins. *Adv. Protein Chem.* **73**, 55–96 (2006).

126. Vasa, S., Lin, L., Shi, C., Habenstein, B., Riedel, D., Kühn, J., Thanbichler, M. & Lange, A. β-Helical architecture of cytoskeletal bactofilin filaments revealed by solid-state NMR. *Proc. Natl. Acad. Sci. U. S. A.* **112**, E127-36 (2015).

127. Allen, J. R., Silfies, J. S., Schwartz, S. A. & Davidson, M. Single-molecule super-resolution imaging. *Nikon MicroscopyU* Available at: https://www.microscopyu.com/techniques/super-

resolution/single-molecule-super-resolution-imaging.

128. Pollithy, A., Romer, T., Lang, C., Müller, F. D., Helma, J., Leonhardt, H., Rothbauer, U. & Schüler, D. Magnetosome expression of functional camelid antibody fragments (nanobodies) in *Magnetospirillum gryphiswaldense*. *Appl. Environ. Microbiol.* **77**, 6165–71 (2011).

129. Klein, A., Hank, S., Raulf, A., Joest, E. F., Tissen, F., Heilemann, M., Wieneke, R. & Tampé, R. Live-cell labeling of endogenous proteins with nanometer precision by transduced nanobodies. *Chem. Sci.* **9**, 7835–7842 (2018).

130. Melak, M., Plessner, M. & Grosse, R. Actin visualization at a glance. *J. Cell Sci.* **130**, 525–530 (2017).

131. Tiede, C., Bedford, R., Heseltine, S. J., Smith, G., Wijetunga, I., Ross, R., AlQallaf, D., Roberts, A. P., Balls, A., Curd, A., Hughes, R. E., Martin, H., Needham, S. R., Zanetti-Domingues, L. C., Sadigh, Y., Peacock, T. P., Tang, A. A., Gibson, N., Kyle, H., *et al.* Affimer proteins are versatile and renewable affinity reagents. *Elife* **6**, (2017).

132. Robert, A., Hookway, C. & Gelfand, V. I. Intermediate filament dynamics: What we can see now and why it matters. *Bioessays* **38**, 232–43 (2016).

133. Nguyen, L. T., Gumbart, J. C., Beeby, M. & Jensen, G. J. Coarse-grained simulations of bacterial cell wall growth reveal that local coordination alone can be sufficient to maintain rod shape. *Proc. Natl. Acad. Sci.* **112**, E3689–E3698 (2015).

134. Sycuro, L. K., Wyckoff, T. J., Biboy, J., Born, P., Pincus, Z., Vollmer, W. & Salama, N. R. Multiple peptidoglycan modification networks modulate *Helicobacter pylori*'s cell shape, motility, and colonization potential. *PLoS Pathog.* **8**, (2012).

135. Deng, X., Gonzalez Llamazares, A., Wagstaff, J. M., Hale, V. L., Cannone, G., McLaughlin, S. H., Kureisaite-Ciziene, D. & Löwe, J. The structure of bactofilin filaments reveals their mode of membrane binding and lack of polarity. *Nat. Microbiol.* 1–12 (2019). doi:10.1038/s41564-019-0544-0

136. Campos, M., Surovtsev, I. V, Kato, S., Paintdakhi, A., Beltran, B., Ebmeier, S. E. & Jacobs-Wagner, C. A constant size extension drives bacterial cell size homeostasis. *Cell* **159**, 1433–46 (2014).

137. Lambert, A., Vanhecke, A., Archetti, A., Holden, S., Schaber, F., Pincus, Z., Laub, M. T., Goley, E. & Manley, S. Constriction rate modulation can drive cell size control and homeostasis in C. crescentus. *iScience* **4**, 180–189 (2018).

138. Furusawa, G., Dziewanowska, K., Stone, H., Settles, M. & Hartzell, P. Global analysis of phase variation in *Myxococcus xanthus*. *Mol. Microbiol.* **81**, 784–804 (2011).

139. Goldman, B. S., Nierman, W. C., Kaiser, D., Slater, S. C., Durkin, A. S., Eisen, J. A., Ronning, C. M., Barbazuk, W. B., Blanchard, M., Field, C., Halling, C., Hinkle, G., Iartchuk, O., Kim, H. S., Mackenzie, C., Madupu, R., Miller, N., Shvartsbeyn, A., Sullivan, S. A., *et al.* Evolution of sensory complexity recorded in a myxobacterial genome. *Proc. Natl. Acad. Sci.* **103**, 15200–15205 (2006).

140. Wu, S. S. & Kaiser, D. Genetic and functional evidence that Type IV pili are required for social gliding motility in M*yxococcus xanthus*. *Mol. Microbiol.* **18**, 547–558 (1995).

141. Altschul, S. F., Gish, W., Miller, W., Myers, E. W. & Lipman, D. J. Basic local alignment search tool. *J. Mol. Biol.* **215**, 403–410 (1990).

142. Altschul, S. F., Madden, T. L., Schäffer, A. A., Zhang, J., Zhang, Z., Miller, W. & Lipman, D. J. Gapped BLAST and PSI-BLAST: a new generation of protein database search programs. *Nucleic Acids Res.* **25**, 3389–402 (1997).

143. Kurtz, S., Phillippy, A., Delcher, A. L., Smoot, M., Shumway, M., Antonescu, C. & Salzberg, S. L. Versatile and open software for comparing large genomes. *Genome Biol.* **5**, R12 (2004).

144. Carver, T. J., Rutherford, K. M., Berriman, M., Rajandream, M.-A. M. A., Barrell, B. G. & Parkhill, J. ACT: The Artemis comparison tool. *Bioinformatics* **21**, 3422–3423 (2005).

145. Vincent, T. L., Green, P. J. & Woolfson, D. N. LOGICOIL—multi-state prediction of coiled-coil oligomeric state. *Bioinformatics* **29**, 69–76 (2013).

146. Taboada, B., Estrada, K., Ciria, R. & Merino, E. Operon-mapper: a web server for precise operon identification in bacterial and archaeal genomes. *Bioinformatics* **34**, 4118–4120 (2018).

147. Sanford, R. A., Cole, J. R. & Tiedje, J. M. Characterization and description of Anaeromyxobacter dehalogenans gen. nov., sp. nov., an aryl-halorespiring facultative anaerobic myxobacterium. *Appl. Environ. Microbiol.* **68**, 893–900 (2002).

148. *Bergey's Manual® of Systematic Bacteriology: Volume Two: The Proteobacteria (Part C).* (Springer US, 2005). doi:10.1007/0-387-29298-5

149. Dawid, W. Biology and global distribution of myxobacteria in soils. *FEMS Microbiol. Rev.* **24**, 403–427 (2000).

150. Yamamoto, E., Muramatsu, H. & Nagai, K. Vulgatibacter incomptus gen. nov., sp. nov. and *Labilithrix luteola* gen. nov., sp. nov., two myxobacteria isolated from soil in Yakushima Island, and the description of *Vulgatibacteraceae* fam. nov., *Labilitrichaceae* fam. nov. and Anaeromyxobacteraceae fam. nov. *Int. J. Syst. Evol. Microbiol.* **64**, 3360–3368 (2014).

151. Ivanova, N., Daum, C., Lang, E., Abt, B., Kopitz, M., Saunders, E., Lapidus, A., Lucas, S., Glavina Del Rio, T., Nolan, M., Tice, H., Copeland, A., Cheng, J.-F., Chen, F., Bruce, D., Goodwin, L., Pitluck, S., Mavromatis, K., Pati, A., *et al.* Complete genome sequence of Haliangium ochraceum type strain (SMP-2T). *Stand. Genomic Sci.* **2**, 96–106 (2010).

152. Nellis, L. F. & Garner, H. R. Methods for isolation and purification of Chondromyces. *J. Bacteriol.* **87**, 230–1 (1964).

153. Brooks, R. S., Blanchard, M. T., Clothier, K. A., Fish, S., Anderson, M. L. & Stott, J. L. Characterization of *Pajaroellobacter abortibovis* , the etiologic agent of epizootic bovine abortion. *Vet. Microbiol.* **192**, 73–80 (2016).

154. Han, K., Li, Z., Peng, R., Zhu, L., Zhou, T., Wang, L., Li, S., Zhang, X., Hu, W., Wu, Z., Qin, N. & Li, Y. Extraordinary expansion of a *Sorangium cellulosum* genome from an alkaline milieu. *Sci. Rep.* **3**, 2101 (2013).

155. Awal, R. P., Müller, R. & Garcia, R. *Racemicystis crocea* gen. nov., sp. nov., a soil myxobacterium in the family Polyangiaceae. *Int. J. Syst. Evol. Microbiol.* **66**, 2389–2395 (2016).

156. Mohr, K. I., Garcia, R. O., Gerth, K., Irschik, H. & Muller, R. *Sandaracinus amylolyticus* gen. nov., sp. nov., a starch-degrading soil myxobacterium, and description of Sandaracinaceae fam. nov. *Int. J. Syst. Evol. Microbiol.* **62**, 1191–1198 (2012).

157. Garcia, R., Gemperlein, K. & Muller, R. *Minicystis rosea* gen. nov., sp. nov., a polyunsaturated fatty acid-rich and steroid-producing soil myxobacterium. *Int. J. Syst. Evol. Microbiol.* **64**, 3733–3742 (2014).

158. Iizuka, T., Jojima, Y., Fudou, R., Tokura, M., Hiraishi, A. & Yamanaka, S. *Enhygromyxa salina* gen. nov., sp. nov., a slightly halophilic myxobacterium isolated from the coastal areas of Japan. *Syst. Appl. Microbiol.* **26**, 189–196 (2003).

159. Rogozin, I. B., Makarova, K. S., Wolf, Y. I. & Koonin, E. V. Computational approaches for the analysis of gene neighbourhoods in prokaryotic genomes. *Brief. Bioinform.* **5**, 131–149 (2004).

160. Bhat, S., Zhu, X., Patel, R. P., Orlando, R. & Shimkets, L. J. Identification and localization of Myxococcus xanthus porins and lipoproteins. *PLoS One* **6**, e27475 (2011).

161. Nikaido, H. RND transporters in the living world. *Res. Microbiol.* **169**, 363–371 (2018).

162. Curtis, P. D., Atwood, J., Orlando, R., Shimkets, L. J. & Shimkets, L. J. Proteins associated with the *Myxococcus xanthus* extracellular matrix. *J. Bacteriol.* **189**, 7634–42 (2007).

163. Berleman, J. E., Allen, S., Danielewicz, M. A., Remis, J. P., Gorur, A., Cunha, J., Hadi, M. Z., Zusman, D. R., Northen, T. R., Witkowska, H. E. & Auer, M. The lethal cargo of *Myxococcus xanthus* outer membrane vesicles. *Front. Microbiol.* **5**, 1–11 (2014).

164. Saha, C. K., Pires, R. S., Brolin, H. & Atkinson, G. C. Predicting functional associations using flanking genes (FlaGs). *bioRxiv* 362095 (2018). doi:10.1101/362095

165. Withers, T. R., Yin, Y. & Yu, H. D. Identification and characterization of a novel inhibitor of alginate overproduction in *Pseudomonas aeruginosa*. *Pathog. Dis.* **70**, 185–8 (2014).

166. McGuffie, B. A., Vallet-Gely, I. & Dove, S. L. σ factor and anti-σ factor that control swarming motility and biofilm formation in *Pseudomonas aeruginosa*. *J. Bacteriol.* **198**, 755–65 (2015).

167. Truebestein, L. & Leonard, T. A. Coiled-coils: The long and short of it. *Bioessays* **38**, 903–16 (2016).

168. Marrington, R., Small, E., Rodger, A., Dafforn, T. R. & Addinall, S. G. FtsZ fiber bundling is triggered by a conformational change in bound GTP. *J. Biol. Chem.* **279**, 48821–9 (2004).

169. Kölling, M., Kumari, P. & Bürstenbinder, K. Calcium- and calmodulin-regulated microtubule-associated proteins as signal-integration hubs at the plasma membrane–cytoskeleton nexus. *J. Exp. Bot.* **70**, 387–396 (2019).

170. Cabeen, M. T., Herrmann, H. & Jacobs-Wagner, C. The domain organization of the bacterial intermediate filament-like protein crescentin is important for assembly and function. *Cytoskeleton (Hoboken).* **68**, 205–19 (2011).

171. Ma, X., Ehrhardt, D. W. & Margolin, W. Colocalization of cell division proteins FtsZ and FtsA to cytoskeletal structures in living *Escherichia coli* cells by using green fluorescent protein. *Proc. Natl. Acad. Sci. U. S. A.* **93**, 12998–3003 (1996).

172. Ladant, D. & Ullmann, A. *Bordetella pertussis* adenylate cyclase: a toxin with multiple talents. *Trends Microbiol.* **7**, 172–176 (1999).

173. Elias, M. & Murillo, F. J. Induction of germination in *Myxococcus xanthus* fruiting body spores. *J. Gen. Microbiol.* **137**, 381–388 (1991).

174. Lloyd, D. G. & Whitworth, D. E. The myxobacterium *Myxococcus xanthus* can sense and respond to the quorum signals secreted by potential prey organisms. *Front. Microbiol.* **8**, 439 (2017).

175. Kessin, R. H. *Dictyostelium: Evolution, Cell Biology, and the Development of Multicellularity.* (Cambridge University Press, 2001).

176. Anjard, C., Loomis, W. F., Iranfar, N., Fuller, D. & Loomis, W. F. Cytokinins induce sporulation in Dictyostelium. *Development* **135**, 819–27 (2008).

177. Müller, F.-D., Treuner-Lange, A., Heider, J., Huntley, S. M. & Higgs, P. I. Global transcriptome analysis of spore formation in *Myxococcus xanthus* reveals a locus necessary for cell differentiation. *BMC Genomics* **11**, 264 (2010).

178. Wang, S., Arellano-Santoyo, H., Combs, P. A. & Shaevitz, J. W. Actin-like cytoskeleton filaments contribute to cell mechanics in bacteria. *Proc. Natl. Acad. Sci.* **107**, 9182–5 (2010).

179. Wolgemuth, C. W. Force and flexibility of flailing myxobacteria. *Biophys. J.* **89**, 945–950 (2005).

180. O'Toole, G. A. & Wong, G. C. Sensational biofilms: surface sensing in bacteria. *Curr. Opin. Microbiol.* **30**, 139–146 (2016).

181. Berman, H. M., Westbrook, J., Feng, Z., Gilliland, G., Bhat, T. N., Weissig, H., Shindyalov, I. N. & Bourne, P. E. The protein data bank. *Nucleic Acids Res.* **28**, 235–242 (2000).

182. Frank, J. Generalized single-particle cryo-EM--a historical perspective. *Reprod. Syst. Sex. Disord.* **65**, 3–8 (2016).

183. De Rosier, D. J. & Klug, A. Reconstruction of three dimensional structures from electron micrographs. *Nature* **217**, 130–134 (1968).

184. Crowther, R. A., Amos, L. A., Finch, J. T., De Rosier, D. J. & Klug, A. Three dimensional reconstructions of spherical viruses by fourier synthesis from electron micrographs. *Nature* **226**, 421–425 (1970).

185. O'Brien, E. J. & Bennett, P. M. Structure of straight flagella from a mutant *Salmonella*. *J. Mol. Biol.* **70**, 133–152 (1972).

186. Henderson, R., Baldwin, J. M., Ceska, T. A., Zemlin, F., Beckmann, E. & Downing, K. H. Model for the structure of bacteriorhodopsin based on high-resolution electron cryo-microscopy. *J. Mol. Biol.* **213**, 899–929 (1990).

187. Matricardi, V. R., Moretz, R. C. & Parsons, D. F. Electron diffraction of wet proteins: catalase. *Science* **177**, 268–270 (1972).

188. Adrian, M., Dubochet, J., Lepault, J. & McDowall, A. W. Cryo-electron microscopy of viruses.

Nature **308**, 32–36 (1984).

189. Dubochet, J., Lepault, J., Freeman, R., Berriman, J. A. & Homo, J.-C. Electron microscopy of frozen water and aqueous solutions. *J. Microsc.* **128**, 219–237 (1982).

190. Dubochet, J. & Lepault, J. Cryo-electron microscopy of vitrified water. *Le J. Phys. Colloq.* **45**, C7-85-C7-94 (1984).

191. Frank, J. Averaging of low exposure electron micrographs of non-periodic objects. *Ultramicroscopy* **1**, 159–162 (1975).

192. van Heel, M. & Frank, J. Use of multivariates statistics in analysing the images of biological macromolecules. *Ultramicroscopy* **6**, 187–194 (1981).

193. Penczek, P. A., Grassucci, R. A. & Frank, J. The ribosome at improved resolution: New techniques for merging and orientation refinement in 3D cryo-electron microscopy of biological particles. *Ultramicroscopy* **53**, 251–270 (1994).

194. Crowther, R. A. Procedures for three-dimensional reconstruction of spherical viruses by fourier synthesis from electron micrographs. *Philos. Trans. R. Soc. B Biol. Sci.* **261**, 221–230 (1971).

195. Henderson, R. The potential and limitations of neutrons, electrons and X-rays for atomic resolution microscopy of unstained biological molecules. *Q. Rev. Biophys.* **28**, 171–93 (1995).

196. Frank, J., Radermacher, M., Penczek, P., Zhu, J., Li, Y., Ladjadj, M. & Leith, A. SPIDER and WEB: processing and visualization of images in 3D electron microscopy and related fields. *J. Struct. Biol.* **116**, 190–199 (1996).

197. Ludtke, S. J., Baldwin, P. R. & Chiu, W. EMAN: semiautomated software for high-resolution single-particle reconstructions. *J. Struct. Biol.* **128**, 82–97 (1999).

198. Grigorieff, N. Three-dimensional structure of bovine NADH:ubiquinone oxidoreductase (complex I) at 22 Å in ice. *J. Mol. Biol.* **277**, 1033–1046 (1998).

199. van Heel, M., Harauz, G., Orlova, E. V., Schmidt, R. & Schatz, M. A new generation of the IMAGIC image processing system. *J. Struct. Biol.* **116**, 17–24 (1996).

200. Marabini, Masegosa, San Martin MC, Marco, Fernandez, de la Fraga LG, Vaquerizo & Carazo. Xmipp: an image processing package for electron microscopy. *J. Struct. Biol.* **116**, 237–40 (1996).

201. Patwardhan, A. Trends in the electron microscopy data bank (EMDB). *Acta Crystallogr. Sect. D Struct. Biol.* **73**, 503–508 (2017).

202. Wood, C., Burnley, T., Patwardhan, A., Scheres, S., Topf, M., Roseman, A., Winn, M. & IUCr. Collaborative computational project for electron cryo-microscopy. *Acta Crystallogr. Sect. D Biol. Crystallogr.* **71**, 123–126 (2015).

203. Faruqi, A. & Henderson, R. Electronic detectors for electron microscopy. *Curr. Opin. Struct. Biol.* **17**, 549–555 (2007).

204. Kuhlbrandt, W. The Resolution Revolution. *Science* **343**, 1443–1444 (2014).

205. Brilot, A. F., Chen, J. Z., Cheng, A., Pan, J., Harrison, S. C., Potter, C. S., Carragher, B., Henderson, R. & Grigorieff, N. Beam-induced motion of vitrified specimen on holey carbon film. *J. Struct. Biol.* **177**, 630–7 (2012).

206. Li, X., Mooney, P., Zheng, S., Booth, C. R., Braunfeld, M. B., Gubbens, S., Agard, D. A. & Cheng, Y. Electron counting and beam-induced motion correction enable near-atomic-resolution single-particle cryo-EM. *Nat. Methods* **10**, 584–590 (2013).

207. Zheng, S. Q., Palovcak, E., Armache, J.-P., Verba, K. A., Cheng, Y. & Agard, D. A. MotionCor2: anisotropic correction of beam-induced motion for improved cryo-electron microscopy. *Nat. Methods* **14**, 331–332 (2017).

208. Zhu, J., Penczek, P. A., Schröder, R. & Frank, J. Three-dimensional reconstruction with contrast transfer function correction from energy-filtered cryoelectron micrographs: procedure and application to the 70S *Escherichia coli* ribosome. *J. Struct. Biol.* **118**, 197–219 (1997).

209. Cheng, Y., Grigorieff, N., Penczek, P. A. & Walz, T. A primer to single-particle cryo-electron microscopy. *Cell* **161**, 438–449 (2015).

210. Fernandez-Leiro, R., Scheres, S. H. W. & IUCr. A pipeline approach to single-particle processing

in *RELION*. *Acta Crystallogr. Sect. D Struct. Biol.* **73**, 496–502 (2017).

211. Rohou, A. & Grigorieff, N. CTFFIND4: Fast and accurate defocus estimation from electron micrographs. *J. Struct. Biol.* **192**, 216–221 (2015).

212. Saibil, H. Contrast transfer and CTF correction. Available at: http://embo2015.cryst.bbk.ac.uk/embo2015/course/Lectures/Lecture-6-Helen-Saibil-4-Sept-15.pdf (2015).

213. Zivanov, J., Nakane, T., Forsberg, B. O., Kimanius, D., Hagen, W. J., Lindahl, E. & Scheres, S. H. New tools for automated high-resolution cryo-EM structure determination in RELION-3. *Elife* **7**, (2018).

214. Scheres, S. H. W. RELION: Implementation of a Bayesian approach to cryo-EM structure determination. *J. Struct. Biol.* **180**, 519–530 (2012).

215. Rubinstein, J. L. Cryo-EM Captures the dynamics of ion channel opening. *Cell* **168**, 341–343 (2017).

216. Diaz, R., Rice, W. J., Stokes, D. L. & Stokes, D. L. Fourier-Bessel reconstruction of helical assemblies. *Methods Enzymol.* **482**, 131–65 (2010).

217. He, S. & Scheres, S. H. W. Helical reconstruction in RELION. *J. Struct. Biol.* **198**, 163–176 (2017).

218. Steven, A. & Belnap, D. Electron microscopy and image processing: an essential tool for structural analysis of macromolecules. in *Current Protocols in Protein Science* **42**, 17.2.1-17.2.39 (John Wiley & Sons, Inc., 2005).

219. Trachtenberg, S., Dorward, L. M., Speransky, V. V., Jaffe, H., Andrews, S. B. & Leapman, R. D. Structure of the cytoskeleton of *Spiroplasma melliferum* BC3 and its interactions with the cell membrane. *J. Mol. Biol.* **378**, 776–787 (2008).

220. Noble, A. J., Dandey, V. P., Wei, H., Brasch, J., Chase, J., Acharya, P., Tan, Y. Z., Zhang, Z., Kim, L. Y., Scapin, G., Rapp, M., Eng, E. T., Rice, W. J., Cheng, A., Negro, C. J., Shapiro, L., Kwong, P. D., Jeruzalmi, D., des Georges, A., *et al.* Routine single particle CryoEM sample and grid

characterization by tomography. *Elife* **7**, e34257 (2018).

221. Kováčik, L., Kerïeche, S., Höög, J. L., Jůda, P., Matula, P. & Raška, I. A simple Fourier filter for suppression of the missing wedge ray artefacts in single-axis electron tomographic reconstructions. *J. Struct. Biol.* **186**, 141–152 (2014).

222. Palmer, C. M. & Löwe, J. A cylindrical specimen holder for electron cryo-tomography. *Ultramicroscopy* **137**, 20–9 (2014).

223. Kremer, J. R., Mastronarde, D. N. & McIntosh, J. R. Computer visualization of three-dimensional image data using IMOD. *J. Struct. Biol.* **116**, 71–6 (1996).

224. Heymann, J. B. & Belnap, D. M. Bsoft: Image processing and molecular modeling for electron microscopy. *J. Struct. Biol.* **157**, 3–18 (2007).

225. Heymann, J. B., Cardone, G., Winkler, D. C. & Steven, A. C. Computational resources for cryo-electron tomography in Bsoft. *J. Struct. Biol.* **161**, 232–242 (2008).

226. Mastronarde, D. N. & Held, S. R. Automated tilt series alignment and tomographic reconstruction in IMOD. *J. Struct. Biol.* **197**, 102 (2017).

227. Pettersen, E. F., Goddard, T. D., Huang, C. C., Couch, G. S., Greenblatt, D. M., Meng, E. C. & Ferrin, T. E. UCSF Chimera- A visualization system for exploratory research and analysis. *J. Comput. Chem.* **25**, 1605–1612 (2004).

228. Snijder, J., Borst, A. J., Dosey, A., Walls, A. C., Burrell, A., Reddy, V. S., Kollman, J. M. & Veesler, D. Vitrification after multiple rounds of sample application and blotting improves particle density on cryo-electron microscopy grids. *J. Struct. Biol.* **198**, 38–42 (2017).

229. Glaeser, R. M., Han, B.-G., Csencsits, R., Killilea, A., Pulk, A. & Cate, J. H. D. Factors that influence the formation and stability of thin, cryo-EM specimens. *Biophys. J.* **110**, 749–755 (2016).

230. Fitzpatrick, A. W. P., Falcon, B., He, S., Murzin, A. G., Murshudov, G., Garringer, H. J., Crowther, R. A., Ghetti, B., Goedert, M. & Scheres, S. H. W. Cryo-EM structures of tau filaments from Alzheimer's disease. *Nature* **547**, 185–190 (2017).

231. Radamaker, L., Lin, Y.-H., Annamalai, K., Huhn, S., Hegenbart, U., Schönland, S. O., Fritz, G., Schmidt, M. & Fändrich, M. Cryo-EM structure of a light chain-derived amyloid fibril from a patient with systemic AL amyloidosis. *Nat. Commun.* **10**, 1103 (2019).

232. Drulyte, I., Johnson, R. M., Hesketh, E. L., Hurdiss, D. L., Scarff, C. A., Porav, S. A., Ranson, N. A., Muench, S. P. & Thompson, R. F. Approaches to altering particle distributions in cryo-electron microscopy sample preparation. *Acta Crystallogr. Sect. D Struct. Biol.* **74**, 560–571 (2018).

233. Hagen, W. J. H., Wan, W. & Briggs, J. A. G. Implementation of a cryo-electron tomography tilt-scheme optimized for high resolution subtomogram averaging. *J. Struct. Biol.* **197**, 191–198 (2017).

234. Penczek, P. A. Resolution measures in molecular electron microscopy. in *Methods in Enzymology: Cryo-EM Part B: 3-D Reconstruction* (ed. Jensen, G. J.) 73–100 (Academic Press, 2010).

235. Tan, Y. Z., Baldwin, P. R., Davis, J. H., Williamson, J. R., Potter, C. S., Carragher, B. & Lyumkis, D. Addressing preferred specimen orientation in single-particle cryo-EM through tilting. *Nat. Methods* **14**, 793–796 (2017).

236. D'Imprima, E., Floris, D., Joppe, M., Sánchez, R., Grininger, M. & Kühlbrandt, W. Protein denaturation at the air-water interface and how to prevent it. *Elife* **8**, (2019).

237. Pantelic, R. S., Meyer, J. C., Kaiser, U., Baumeister, W. & Plitzko, J. M. Graphene oxide: A substrate for optimizing preparations of frozen-hydrated samples. *J. Struct. Biol.* **170**, 152–156 (2010).

238. Meyerson, J. R., Rao, P., Kumar, J., Chittori, S., Banerjee, S., Pierson, J., Mayer, M. L. & Subramaniam, S. Self-assembled monolayers improve protein distribution on holey carbon cryo-EM supports. *Sci. Rep.* **4**, 1–5 (2014).

239. Agip, A.-N. A., Blaza, J. N., Bridges, H. R., Viscomi, C., Rawson, S., Muench, S. P. & Hirst, J. Cryo-EM structures of complex I from mouse heart mitochondria in two biochemically defined states. *Nat. Struct. Mol. Biol.* **25**, 548–556 (2018).

240. Ravelli, R. B. G., Nijpels, F. J. T., Henderikx, R. J. M., Weissenberger, G., Thewessem, S.,

Gijsbers, A., Beulen, B. W. A. M. M., López-Iglesias, C. & Peters, P. J. Automated cryo-EM sample preparation by pin-printing and jet vitrification. *bioRxiv* 651208 (2019). doi:10.1101/651208

241. Arnold, S. A., Albiez, S., Bieri, A., Syntychaki, A., Adaixo, R., McLeod, R. A., Goldie, K. N., Stahlberg, H. & Braun, T. Blotting-free and lossless cryo-electron microscopy grid preparation from nanoliter-sized protein samples and single-cell extracts. *J. Struct. Biol.* **197**, 220–226 (2017).

242. Schmidli, C., Albiez, S., Rima, L., Righetto, R., Mohammed, I., Oliva, P., Kovacik, L., Stahlberg, H. & Braun, T. Microfluidic protein isolation and sample preparation for high-resolution cryo-EM. *Proc. Natl. Acad. Sci. U. S. A.* **116**, 15007–15012 (2019).

243. Kontziampasis, D., Klebl, D. P., Iadanza, M. G., Scarff, C. A., Kopf, F., Sobott, F., Monteiro, D. C. F., Trebbin, M., Muench, S. P. & White, H. D. A cryo-EM grid preparation device for time-resolved structural studies. *IUCrJ* **6**, (2019).

244. Righetto, R. D., Biyani, N., Kowal, J., Chami, M. & Stahlberg, H. Retrieving high-resolution information from disordered 2D crystals by single-particle cryo-EM. *Nat. Commun.* **10**, 1722 (2019).

245. Delorenzi, M. & Speed, T. An HMM model for coiled-coil domains and a comparison with PSSM-based predictions. *Bioinformatics* **18**, 617–625 (2002).

246. Wolf, E., Kim, P. S. & Berger, B. MultiCoil: a program for predicting two- and three-stranded coiled coils. *Protein Sci.* **6**, 1179 (1997).

247. Trigg, J., Gutwin, K., Keating, A. E. & Berger, B. Multicoil2: predicting coiled coils and their oligomerization states from sequence in the twilight zone. *PLoS One* **6**, e23519 (2011).

248. Mahrenholz, C. C., Abfalter, I. G., Bodenhofer, U., Volkmer, R. & Hochreiter, S. Complex networks govern coiled-coil oligomerization – predicting and profiling by means of a machine learning approach. *Mol. Cell. Proteomics* **10**, M110.004994 (2011).

249. Berger, B., Wilson, D. B., Wolf, E., Tonchev, T., Milla, M. & Kim, P. S. Predicting coiled coils by

use of pairwise residue correlations. *Proc. Natl. Acad. Sci. U. S. A.* **92**, 8259–63 (1995).

250. Fukuhara, N. & Kawabata, T. HOMCOS: a server to predict interacting protein pairs and interacting sites by homology modeling of complex structures. *Nucleic Acids Res.* **36**, W185-9 (2008).

251. Mukherjee, S. & Zhang, Y. Protein-protein complex structure predictions by multimeric threading and template recombination. *Structure* **19**, 955–66 (2011).

252. Baek, M., Park, T., Heo, L., Park, C. & Seok, C. GalaxyHomomer: a web server for protein homo-oligomer structure prediction from a monomer sequence or structure. *Nucleic Acids Res.* **45**, W320–W324 (2017).

253. Wall, J. S. & Hainfeld, J. F. Mass mapping with the scanning transmission electron microscope. *Annu. Rev. Biophys. Biophys. Chem.* **15**, 355–376 (1986).

254. Müller, S. A. & Engel, A. Mass measurement in the scanning transmission electron microscope: a powerful tool for studying membrane proteins. *J. Struct. Biol.* **121**, 219–230 (1998).

255. Sosinsky, G. E., Francis, N. R., DeRosier, D. J., Wall, J. S., Simon, M. N. & Hainfeld, J. Mass determination and estimation of subunit stoichiometry of the bacterial hook-basal body flagellar complex of Salmonella typhimurium by scanning transmission electron microscopy. *Proc. Natl. Acad. Sci. U. S. A.* **89**, 4801–5 (1992).

256. Watts, N. R., Misra, M., Wingfield, P. T., Stahl, S. J., Cheng, N., Trus, B. L., Steven, A. C. & Williams, R. W. Three-dimensional structure of HIV-1 Rev protein filaments. *J. Struct. Biol.* **121**, 41–52 (1998).

257. Oikonomou, C. M. & Jensen, G. J. Electron cryotomography of bacterial secretion systems. *Microbiol. Spectr.* **7**, (2019).

258. Dobro, M. J., Oikonomou, C. M., Piper, A., Cohen, J., Guo, K., Jensen, T., Tadayon, J., Donermeyer, J., Park, Y., Solis, B. A., Kjær, A., Jewett, A. I., McDowall, A. W., Chen, S., Chang, Y.-W. W., Shi, J., Subramanian, P., Iancu, C. V., Li, Z., *et al.* Uncharacterized bacterial structures revealed by electron cryotomography. *J. Bacteriol.* **199**, 1–14 (2017).